

# **Final Report**

## **Title: Exploration of New Principles in Spintronics Based on Topological Insulators (Option 1)**

**AFOSR/AOARD Reference Number:** AOARD-10-4103

**AFOSR/AOARD Program Manager:** Seng Hong, Ph.D.

**Period of Performance:** 10 June 2010 - 05 May 2012

**Submission Date:** 14 May 2012

**PI: Yoichi Ando**, Professor, Institute of Scientific and Industrial Research (ISIR), Osaka University

8-1 Mihogaoka, Ibaraki, Osaka 567-0047, Japan

Tel: +81-6-6879-8440 / Fax: +81-6-6879-8444

Report Documentation Page			Form Approved OMB No. 0704-0188		
Public reporting burden for the collection of information is estimated to average 1 hour per response, including the time for reviewing instructions, searching existing data sources, gathering and maintaining the data needed, and completing and reviewing the collection of information. Send comments regarding this burden estimate or any other aspect of this collection of information, including suggestions for reducing this burden, to Washington Headquarters Services, Directorate for Information Operations and Reports, 1215 Jefferson Davis Highway, Suite 1204, Arlington VA 22202-4302. Respondents should be aware that notwithstanding any other provision of law, no person shall be subject to a penalty for failing to comply with a collection of information if it does not display a currently valid OMB control number.					
1. REPORT DATE <b>07 JUN 2012</b>		2. REPORT TYPE <b>Final</b>		3. DATES COVERED <b>06-05-2010 to 05-05-2012</b>	
4. TITLE AND SUBTITLE <b>Exploration of New Principles in Spintronics Based on Topological Insulators</b>			5a. CONTRACT NUMBER <b>FA23861014103</b>		
			5b. GRANT NUMBER		
			5c. PROGRAM ELEMENT NUMBER		
6. AUTHOR(S) <b>Yoichi Ando</b>			5d. PROJECT NUMBER		
			5e. TASK NUMBER		
			5f. WORK UNIT NUMBER		
7. PERFORMING ORGANIZATION NAME(S) AND ADDRESS(ES) <b>Osaka University,8-1 Mohogaoka, Ibaraki,Osaka 567-0047,Japan,NA,NA</b>			8. PERFORMING ORGANIZATION REPORT NUMBER <b>N/A</b>		
9. SPONSORING/MONITORING AGENCY NAME(S) AND ADDRESS(ES) <b>AOARD, UNIT 45002, APO, AP, 96338-5002</b>			10. SPONSOR/MONITOR'S ACRONYM(S) <b>AOARD</b>		
			11. SPONSOR/MONITOR'S REPORT NUMBER(S) <b>AOARD-104103</b>		
12. DISTRIBUTION/AVAILABILITY STATEMENT <b>Approved for public release; distribution unlimited</b>					
13. SUPPLEMENTARY NOTES					
14. ABSTRACT <b>This is the final report of a project to develop techniques to prepare topological-insulator single crystals with sufficiently low bulk carrier density, and use them for the investigation of novel quantum phenomena in topological insulators for conceiving devices with unprecedented functionalities.</b>					
15. SUBJECT TERMS <b>Physics, Spintronics, Magnetic materials, Quantum Spin Hall insulator</b>					
16. SECURITY CLASSIFICATION OF:			17. LIMITATION OF ABSTRACT <b>Same as Report (SAR)</b>	18. NUMBER OF PAGES <b>79</b>	19a. NAME OF RESPONSIBLE PERSON
a. REPORT <b>unclassified</b>	b. ABSTRACT <b>unclassified</b>	c. THIS PAGE <b>unclassified</b>			

### Objectives:

This project explores new avenues of the spintronics to utilize the “helically spin-polarized” metallic state that exist on the surface of a *topological insulator*, which is a new state of matter discovered just a few years ago. In the helically spin-polarized surface state, the current direction and the spin polarization is directly coupled; namely, right- and left-moving electrons carry up and down spins, respectively. This allows completely new ways to generate and control spins with minimal energy dissipation. However, the topological insulator samples available today contain too much bulk carriers that hinder exploiting their surface properties in device forms. In this project, the PI will develop techniques to prepare topological-insulator single crystals with sufficiently low bulk carrier density, and use them for the investigation of novel quantum phenomena in topological insulators for conceiving devices with unprecedented functionalities. This option 1 builds on the basic part (which was finished on 05 May 2011) by expanding efforts to various topological insulator materials.

### Status of effort (200 words or less):

The project went on very well and produced a number of results. Here, we focus on the results obtained after the previous final report for the basic part (dated 03 June 2011) was written. Most notably, we discovered that the superconducting topological insulator  $\text{Cu}_x\text{Bi}_2\text{Se}_3$  is the first concrete example of a topological superconductor to host surface Majorana fermions. This achievement was publicized in a news article in the US media *Science News*. Also, we discovered an unexpected mass acquisition of the surface Dirac fermions near the topological phase transition, which provides a new route to realize the topological magnetoelectric effect. This result was published in *Nature Physics* and was featured on the cover of its November 2011 issue. In addition, there has been a steady progress in our investigations of the fundamental physical properties of the topological surface state, as well as in our device fabrications for the spin-current detection.

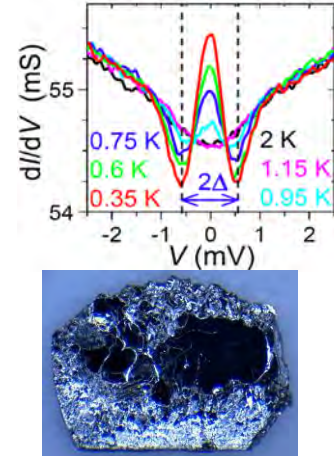
### Abstract of important results:

#### 1) Discovery of Topological Superconductivity in a Superconducting Topological Insulator

The recent discovery of the topological insulator stimulated the search for an even more exotic state of matter, the topological superconductor, which is characterized by the topologically-protected gapless surface state that is essentially an Andreev bound state consisting of Majorana fermions. Recently, the doped topological insulator  $\text{Cu}_x\text{Bi}_2\text{Se}_3$ , which superconducts below  $\sim 3$  K, was predicted to possess a topological superconducting state, and its confirmation was an urgent issue. We performed point-contact spectroscopy on a cleaved surface of superconducting  $\text{Cu}_x\text{Bi}_2\text{Se}_3$  and observed a pronounced zero-bias conductance peak (ZBCP) which signifies unconventional superconductivity. Theoretical considerations of all possible superconducting states help us conclude that this ZBCP is due to Majorana Fermions and gives evidence for a topological superconductivity in  $\text{Cu}_x\text{Bi}_2\text{Se}_3$ .

While the notion of topological superconductivity has been around for some time, its experimental confirmation has been elusive. The problem was that an unconventional superconducting state (*i.e.*, non-s-wave state) can be both topological and non-topological. However, in the case of  $\text{Cu}_x\text{Bi}_2\text{Se}_3$  that was studied in the present work, thanks to the simple band structure governed by the strong spin-orbit coupling, it can be shown that if the superconductivity is unconventional, it can only be topological.

[*Physical Review Letters* **107**, 217001 (2011)].

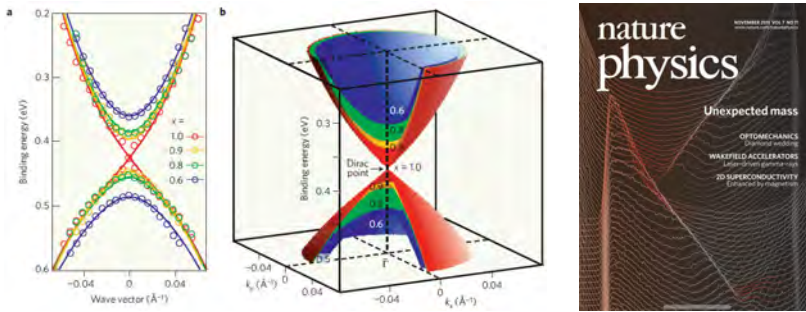


This work was publicized in a news article in the US media *Science News* (31 Dec. 2012 issue, p 18).

#### 2) Unexpected Mass Acquisition of the Surface Dirac Fermions near the Topological Phase Transition

The three-dimensional (3D) topological insulator is a novel quantum state of matter where an insulating bulk hosts a linearly-dispersing surface state, which can be viewed as a sea of massless Dirac fermions protected by the time-reversal symmetry (TRS). Breaking the TRS by a magnetic order leads to the opening of a gap in the surface state and consequently the Dirac fermions become massive. It has been proposed theoretically that such a mass acquisition is necessary for realizing novel topological phenomena, but achieving a sufficiently

large mass is an experimental challenge. Quite unexpectedly, we discovered that the surface Dirac fermions in a solid-solution system  $\text{TlBi}(\text{S}_{1-x}\text{Se}_x)_2$  acquires a mass *without* explicitly breaking the TRS. This system goes through a quantum phase transition from the topological to the non-topological phase, and by tracing the evolution of the electronic states using the angle-resolved photoemission, we observed that the massless Dirac state in  $\text{TlBiSe}_2$  switches to a massive state before it disappears in the non-topological phase. This result suggests the existence of a condensed-matter version of the “Higgs mechanism” where particles acquire a mass through spontaneous symmetry breaking. [Nature Physics 7, 840-844 (2011)].

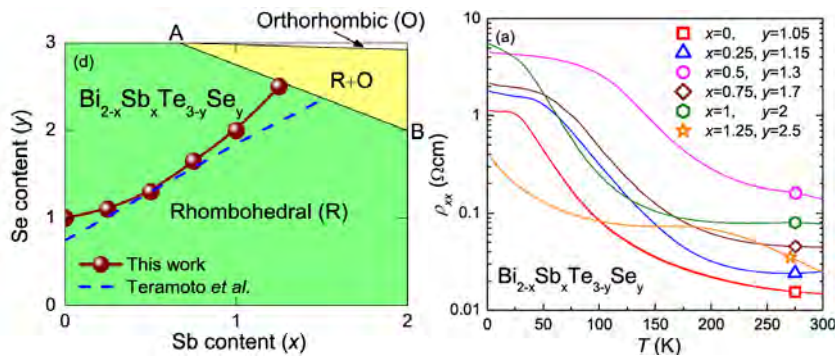


This work was featured on the cover of the November 2011 issue of Nature Physics.

### 3) Optimizing Topological Insulator

To optimize the bulk-insulating behavior in the topological insulator materials having the tetradymite structure, we have synthesized and characterized single-crystal samples of  $\text{Bi}_{2-x}\text{Sb}_x\text{Te}_{3-y}\text{Se}_y$  (BSTS) solid solution at various compositions. We have elucidated that there are a series of “intrinsic” compositions where the acceptors and donors compensate each other and present a maximally bulk-insulating behavior. At such compositions, the resistivity can become as large as several  $\Omega\text{cm}$  at low temperature and one can infer the role of the surface-transport channel in the non-linear Hall effect. In particular, the composition of  $\text{Bi}_{1.5}\text{Sb}_{0.5}\text{Te}_{1.7}\text{Se}_{1.3}$  achieves the lowest bulk carrier density and appears to be best suited for surface-transport studies.

[Physical Review B 84, 165311 (2011)].

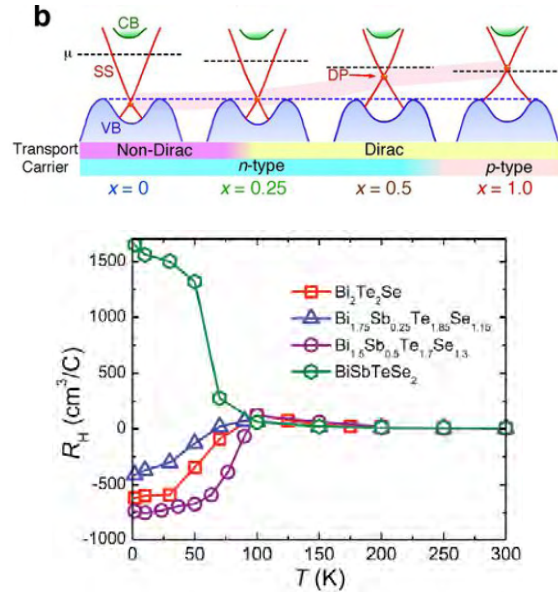


This paper was selected as **Editors' Suggestion** and was also featured in *Physics Synopsis* as an important development.

### 4) Achieving Dirac-Cone Engineering in Bulk-Insulating Topological Insulators

The three-dimensional topological insulator is a novel quantum state of matter where the insulating bulk hosts gapless topological surface states characterized by a Dirac-cone energy dispersion. The realization of topological-insulator devices to utilize the peculiar surface-transport properties requires a highly insulating bulk together with a tunability of the Dirac carriers. To achieve the latter, it is desirable to be able to control the energy location of the Dirac cone in the band gap, because the chemical potential in bulk insulators is

difficult to tune. We show that the tetradymite solid-solution  $\text{Bi}_{2-x}\text{Sb}_x\text{Te}_{3-y}\text{Se}_y$  is the first topological-insulator system that simultaneously satisfies the above requirements, which was elucidated by directly measuring its electronic states with angle-resolved photoemission spectroscopy. Upon increasing the Sb content  $x$  while tuning the Se content  $y$  to maintain the bulk-insulating character, we observed that the chemical potential is always located in the bulk gap and the surface Dirac point, which separates the hole- and electron-like regimes and is buried in the bulk band in  $\text{Bi}_2\text{Te}_2\text{Se}$  ( $x = 0$ ;  $y = 1$ ), starts to be isolated from the bulk band above  $x \sim 0.25$ ; furthermore, a sign change of the Dirac carriers was observed at  $x \sim 0.9$ . Such a tunable Dirac cone in the bulk-insulating platform opens a promising pathway to the development of novel topological-insulator devices. [*Nature Communications* **3**, 636 (2012)].



This paper was selected as a “Hot Paper” by the Nature Asia-Pacific, which published the Japanese translation of its abstract in their webpage (<http://www.natureasia.com/japan/ncomms/highlights/detail.php?id=1109>).

#### Personnel Supported:

Kazuma Eto, Graduate Student, ISIR, Osaka University (Part-time)

#### Publications:

1. Unexpected mass acquisition of Dirac fermions at the quantum phase transition of a topological insulator, T. Sato, K. Segawa, K. Kosaka, S. Souma, K. Nakayama, K. Eto, T. Minami, Y. Ando, and T. Takahashi, **Nature Physics** **7**, 840-844 (2011).
2. Tunable Dirac cone in the topological insulator  $\text{Bi}_{2-x}\text{Sb}_x\text{Te}_{3-y}\text{Se}_y$ , T. Arakane, T. Sato, S. Souma, K. Kosaka, K. Nakayama, M. Komatsu, T. Takahashi, Z. Ren, K. Segawa, and Y. Ando, **Nature Communications** **3**, 636-(1-5) (2012).
3. Topological Superconductivity in  $\text{Cu}_x\text{Bi}_2\text{Se}_3$ , S. Sasaki, M. Kriener, K. Segawa, K. Yada, Y. Tanaka, M. Sato, and Y. Ando, **Phys. Rev. Lett.** **107**, 217001-(1-5) (2011).
4. Topological Surface States in Lead-Based Ternary Telluride  $\text{Pb}(\text{Bi}_{1-x}\text{Sb}_x)_2\text{Te}_4$ , S. Souma, K. Eto, M. Nomura, K. Nakayama, T. Sato, T. Takahashi, K. Segawa, and Y. Ando, **Phys. Rev. Lett.** **108**, 116801-(1-5) (2012).
5. Observation of Dirac Holes and Electrons in a Topological Insulator, A. A. Taskin, Z. Ren, S. Sasaki, K. Segawa, and Y. Ando, **Phys. Rev. Lett.** **107**, 016801-(1-4) (2011).
6. Optimizing  $\text{Bi}_{2-x}\text{Sb}_x\text{Te}_{3-y}\text{Se}_y$  solid solutions to approach the intrinsic topological insulator regime, Z. Ren, A. A. Taskin, S. Sasaki, K. Segawa, and Y. Ando, **Phys. Rev. B** **84**, 165311-(1-6) (Editors' Suggestion, featured in *Physics Synopsis*) (2011).
7. Fermi level tuning and a large activation gap achieved in the topological insulator  $\text{Bi}_2\text{Te}_2\text{Se}$  by Sn doping, Zhi Ren, A. A. Taskin, Satoshi Sasaki, Kouji Segawa, and Yoichi Ando, **Phys. Rev. B** **85** (2012) 155301-(1-6) (Editors' Suggestion).
8. Electrochemical synthesis and superconducting phase diagram of  $\text{Cu}_x\text{Bi}_2\text{Se}_3$ , M. Kriener, K. Segawa, Z. Ren, S. Sasaki, S. Wada, S. Kuwabata, and Y. Ando, **Phys. Rev. B** **84**, 054513-(1-5) (Editors' Suggestion) (2011).

9. Topological transition in  $\text{Bi}_{1-x}\text{Sb}_x$  studied as a function of Sb doping, F. Nakamura, Y. Kousa, A. A. Taskin, Y. Takeichi, A. Nishide, A. Kakizaki, M. D'Angelo, P. Lefevre, F. Bertran, A. Taleb-Ibrahimi, F. Komori, S. Kimura, H. Kondo, Y. Ando, and I. Matsuda, **Phys. Rev. B** **84** 235308-(1-8) (2011).
  10. Observations of two-dimensional quantum oscillations and ambipolar transport in the topological insulator  $\text{Bi}_2\text{Se}_3$  achieved by Cd doping, Z. Ren, A. A. Taskin, S. Sasaki, K. Segawa, and Y. Ando, **Phys. Rev. B** **84** 075316-(1-6) (2011).
  11. Berry phase of nonideal Dirac fermions in topological insulators, A. A. Taskin and Y. Ando, **Phys. Rev. B** **84** 035301-(1-6) (2011).
  12. Additional Evidence for the Surface Origin of the Peculiar Angular-Dependent Magnetoresistance Oscillations Discovered in a Topological Insulator  $\text{Bi}_{1-x}\text{Sb}_x$ , A. A. Taskin, K. Segawa and Y. Ando, **J. Phys.: Conf. Ser.** **334** (2011) 012012-(1-5) (2011). [Proceedings of the 19th International Conference on the Application of High Magnetic Fields in Semiconductor Physics and Nanotechnology (HMF-19), Fukuoka, August 1-6, 2010]
  13. Electrical Transport Properties of Topological Insulators, Yoichi Ando, **Hyomen Kagaku (Journal of the Surface Science Society of Japan)** **35**, 189-195 (2011) [in Japanese].
- (The papers listed below were included in the previous final report for the basic part of this project.)
14. Direct Measurement of the Out-of-Plane Spin Texture in the Dirac Cone Surface State of a Topological Insulator, S. Souma, K. Kosaka, T. Sato, M. Komatsu, A. Takayama, T. Takahashi, M. Kriener, K. Segawa, and Y. Ando, **Phys. Rev. Lett.** **106** 216803-(1-4) (2011).
  15. Bulk Superconducting Phase with a Full Energy Gap in the Doped Topological Insulator  $\text{Cu}_x\text{Bi}_2\text{Se}_3$ , M. Kriener, Kouji Segawa, Zhi Ren, Satoshi Sasaki, and Yoichi Ando, **Phys. Rev. Lett.** **106**, 127004 (2011).
  16. Large bulk resistivity and surface quantum oscillations in the topological insulator  $\text{Bi}_2\text{Te}_2\text{Se}$ , Zhi Ren, A. A. Taskin, S. Sasaki, K. Segawa, and Y. Ando, **Phys. Rev. B** (Rapid Comm.) **82**, 241306(R) (2010).
  17. Direct Evidence for the Dirac-Cone Topological Surface States in the Ternary Chalcogenide  $\text{TlBiSe}_2$ , T. Sato, K. Segawa, H. Guo, K. Sugawara, S. Souma, T. Takahashi, and Y. Ando, **Phys. Rev. Lett.** **105**, 136802 (2010).
  18. Oscillatory angular dependence of the magnetoresistance in a topological insulator  $\text{Bi}_{1-x}\text{Sb}_x$ , A.A. Taskin, K. Segawa, and Y. Ando, **Phys. Rev. B** (Rapid Comm.) **82**, 121302(R) (2010).
  19. Electrical Transport Properties of Topological Insulators, Yoichi Ando, **Hyomen Kagaku (Journal of the Surface Science Society of Japan)** **35**, 189-195 (2011) [in Japanese].
  20. Experimental studies of topological insulators, Yoichi Ando, **KOTAIBUTSURI (Solid State Physics)** **45**, 667-680 (2010) [in Japanese].
  21. Spin-polarized surface bands of a three-dimensional topological insulator studied by high-resolution spin- and angle-resolved photoemission spectroscopy, A. Nishide, Y. Takeichi, T. Okuda, A. A. Taskin, T. Hirahara, K. Nakatsuji, F. Komori, A. Kakizaki, Y. Ando, and I. Matsuda, **New J. Phys.** **12**, 065011 (2010).
  22. Additional Evidence for the Surface Origin of the Peculiar Angular-Dependent Magnetoresistance Oscillations Discovered in a Topological Insulator  $\text{Bi}_{1-x}\text{Sb}_x$ , A. A. Taskin, Kouji Segawa and Yoichi Ando, **J. Phys.: Conference Series** [Proceedings manuscript for the 19th International Conference on the Application of High Magnetic Fields in Semiconductor Physics and Nanotechnology (HMF-19)], in press (arXiv:1009.4005).

#### Invited Talks:

1. Y. Ando, "Probing the Exotic Surface States in Topological Insulators and Superconductors", CNAM Colloquium, Department of Physics, University of Maryland, March 14, 2012.

2. Y. Ando, "Transport Studies of Topological Insulators and Superconductors", American Physical Society March Meeting, Boston, February 29, 2012. **[Invited]**
3. Y. Ando, "Probing the Exotic Surface States in Topological Insulators and Superconductors", FIRST-QS2C Workshop on *Emergent Phenomena of Correlated Materials*, Okinawa, December 13, 2011. **[Invited]**
4. Y. Ando, "Probing the Exotic Surface States in Topological Insulators and Superconductors", Condensed Matter Physics Seminar, MIT, Boston, December 1, 2011. **[Invited]**
5. Y. Ando, "Materials-Oriented Research of Topological Insulators and Superconductors", 2011 MRS Fall Meeting, Boston, November 29, 2011. **[Invited]**
6. Y. Ando, "Cutting-Edge Experiments on Topological Insulators and Superconductors", International Workshop on Novel Quantum States in Condensed Matter: Correlation, Frustration and Topology (NQS2011), Yukawa Institute, Kyoto University, November 18, 2011. **[Invited]**
7. Y. Ando, "Materials-Oriented Research of Topological Insulators and Superconductors", LT26 Satellite Conference on Topological Insulators and Superconductors", Tsinghua University, Beijing, August 19, 2011. **[Invited]**
8. Y. Ando, "Topological Insulators and Superconductors", RIKEN Seminar, RIKEN, Saitama, June 13, 2011. **[Invited]**
9. Y. Ando, "Topological Insulators and Superconductors, Seminar, Walther-Meissner-Institut, Garching, May 6, 2011. **[Invited]**
10. Y. Ando, "Materials Studies of Topological Insulators and Superconductors", International Meeting on High-Accuracy, Hierarchical and Many-Body Schemes for Materials Simulations, University of Tokyo, March 11, 2011. **[Invited]**
11. Y. Ando, "Unusual Quantum Magnetotransport in a Topological Insulator Bi<sub>1-x</sub>Sb<sub>x</sub>", The 19th International Conference on the Application of High Magnetic Fields in Semiconductor Physics and Nanotechnology (HMF19), Fukuoka, August 5, 2010. **[Invited]**
12. Y. Ando, "Novel transport properties of Bi-Sb and other topological insulators", Workshop on Topological Insulators and Superconductors, The Princeton Center for Theoretical Science, Princeton University, November 4, 2010. **[Invited]**
13. Y. Ando, "Developments and Prospects of the Studies of Topological Insulators", Seminar, Yukawa Institute for Theoretical Physics, Kyoto University, May 19, 2010. **[Invited]**

**Inventions:**

- (a) Discoveries, inventions, or patent disclosures: None.
- (b) DD Form 882, "Report of Inventions and Subcontractors": Submitted separately.

**Honors/Awards:** None.

**Software and/or Hardware (if they are specified in the contract as part of final deliverables):** None.



# Unexpected mass acquisition of Dirac fermions at the quantum phase transition of a topological insulator

T. Sato<sup>1\*</sup>, Kouji Segawa<sup>2</sup>, K. Kosaka<sup>1</sup>, S. Souma<sup>3</sup>, K. Nakayama<sup>1</sup>, K. Eto<sup>2</sup>, T. Minami<sup>2</sup>, Yoichi Ando<sup>2\*</sup> and T. Takahashi<sup>1,3</sup>

**The three-dimensional (3D) topological insulator is a novel quantum state of matter where an insulating bulk hosts a linearly dispersing surface state, which can be viewed as a sea of massless Dirac fermions protected by the time-reversal symmetry (TRS). Breaking the TRS by a magnetic order leads to the opening of a gap in the surface state<sup>1</sup>, and consequently the Dirac fermions become massive. It has been proposed theoretically that such a mass acquisition is necessary to realize novel topological phenomena<sup>2,3</sup>, but achieving a sufficiently large mass is an experimental challenge. Here we report an unexpected discovery that the surface Dirac fermions in a solid-solution system  $\text{TlBi}(\text{S}_{1-x}\text{Se}_x)_2$  acquire a mass without explicitly breaking the TRS. We found that this system goes through a quantum phase transition from the topological to the non-topological phase, and, by tracing the evolution of the electronic states using the angle-resolved photoemission, we observed that the massless Dirac state in  $\text{TlBiSe}_2$  switches to a massive state before it disappears in the non-topological phase. This result suggests the existence of a condensed-matter version of the ‘Higgs mechanism’ where particles acquire a mass through spontaneous symmetry breaking.**

Whether a band insulator is topological or not is determined by the parity of the valence-band wave function, which is described by the  $Z_2$  topological invariant. Strong spin–orbit coupling can lead to an inversion of the character of valence- and conduction-band wave functions, resulting in an odd  $Z_2$  invariant that characterizes the topological insulator<sup>4,5</sup>. All known topological insulators<sup>6–14</sup> are based on this band-inversion mechanism<sup>4,5,15–18</sup>, but the successive evolution of the electronic state across the quantum phase transition (QPT) from trivial to topological has not been well studied in 3D topological insulators owing to the lack of suitable materials.  $\text{TlBi}(\text{S}_{1-x}\text{Se}_x)_2$  is therefore the first system where one can investigate the 3D topological QPT (ref. 19). The advantage of this system is that it always maintains the same crystal structure (Fig. 1a), irrespective of the S/Se ratio. Low-energy, ultrahigh-resolution angle-resolved photoemission spectroscopy (ARPES), which has recently become available, is particularly suited to trace such a QPT in great detail.

The bulk band structures of the two end members,  $\text{TlBiSe}_2$  and  $\text{TlBiS}_2$ , are shown in Fig. 1b, where one can see several common features, such as the prominent hole-like band at the binding energy  $E_B$  of 0.5–1 eV and a weaker intensity at the Fermi level ( $E_F$ ), both being centred at the  $\bar{\Gamma}$  point (Brillouin-zone centre). These features

correspond to the top of the bulk valence band (VB) and the bottom of the bulk conduction band (CB), respectively, demonstrating that both  $\text{TlBiSe}_2$  and  $\text{TlBiS}_2$  samples are originally insulators with a bandgap of 0.3–0.4 eV, but electron carriers are doped in the naturally-grown crystals<sup>10–12</sup>. Besides the wider VB width in  $\text{TlBiSe}_2$ , which is naturally expected from its smaller lattice constant, the VB structures in the two systems are very similar (Fig. 1c).

A critical difference in the electronic states of the two compounds is recognized by looking at the band dispersion in the vicinity of  $E_F$  around the  $\bar{\Gamma}$  point (Fig. 1d). An ‘X’-shaped surface band that traverses the bulk bandgap is clearly recognized in  $\text{TlBiSe}_2$  (ref. 10), whereas such a surface state is completely absent in  $\text{TlBiS}_2$ . This indicates a topologically distinct nature between the two, despite the similar overall bulk band structure. One can thus conclude that the band parity is inverted in  $\text{TlBiSe}_2$ , whereas it is not in  $\text{TlBiS}_2$ .

What would happen if we mixed the topologically non-trivial  $\text{TlBiSe}_2$  and trivial  $\text{TlBiS}_2$  phases? One natural consequence of such an alloying would be that the bulk bandgap closes owing to the switching of the parity of the VB wave function at a certain Se content  $x_c$ , marking a topological QPT across which the massless Dirac-cone surface band appears (vanishes) once the system enters into the topological (non-topological) phase. The surface band in the topological phase would retain the Kramers degeneracy at the Dirac point and retain the massless character, as long as the alloying disorder does not break the TRS. It turns out that the electronic-structure evolution in  $\text{TlBi}(\text{S}_{1-x}\text{Se}_x)_2$  indeed presents the topological QPT, but it bears a feature that is totally unexpected.

Figure 2a shows the near- $E_F$  ARPES intensity around the zone centre for a series of  $x$  values, including  $\text{TlBiSe}_2$  ( $x = 1.0$ ) and  $\text{TlBiS}_2$  ( $x = 0.0$ ). One can immediately see that the surface state is seen for  $x \geq 0.6$ , whereas it is absent for  $x \leq 0.4$  (see also Supplementary Information), which points to the topological QPT occurring at  $x_c \approx 0.5$ . In fact, the bulk bandgap estimated from our data approaches zero on both sides of the QPT (see Fig. 3d), suggesting that a band inversion takes place across the QPT, in accordance with the natural expectation and also with a recent ARPES study independently done on  $\text{TlBi}(\text{S}_{1-x}\text{Se}_x)_2$  (ref. 19).

The unexpected physics manifests itself at the Dirac point. The bright intensity peak at  $\sim 0.4$  eV at  $x = 1.0$  is no longer visible at  $x = 0.9$  and is markedly suppressed at  $x = 0.6$ , suggesting that the Kramers degeneracy is lifted on S substitution whereas the surface state is still present. In fact, a closer look at the energy-distribution curves (EDCs) in Fig. 2b shows that the originally X-shaped surface

<sup>1</sup>Department of Physics, Tohoku University, Sendai 980-8578, Japan, <sup>2</sup>Institute of Scientific and Industrial Research, Osaka University, Ibaraki, Osaka 567-0047, Japan, <sup>3</sup>WPI Research Center, Advanced Institute for Materials Research, Tohoku University, Sendai 980-8577, Japan.

\*e-mail: t-sato@arpes.phys.tohoku.ac.jp; y-ando@sanken.osaka-u.ac.jp.



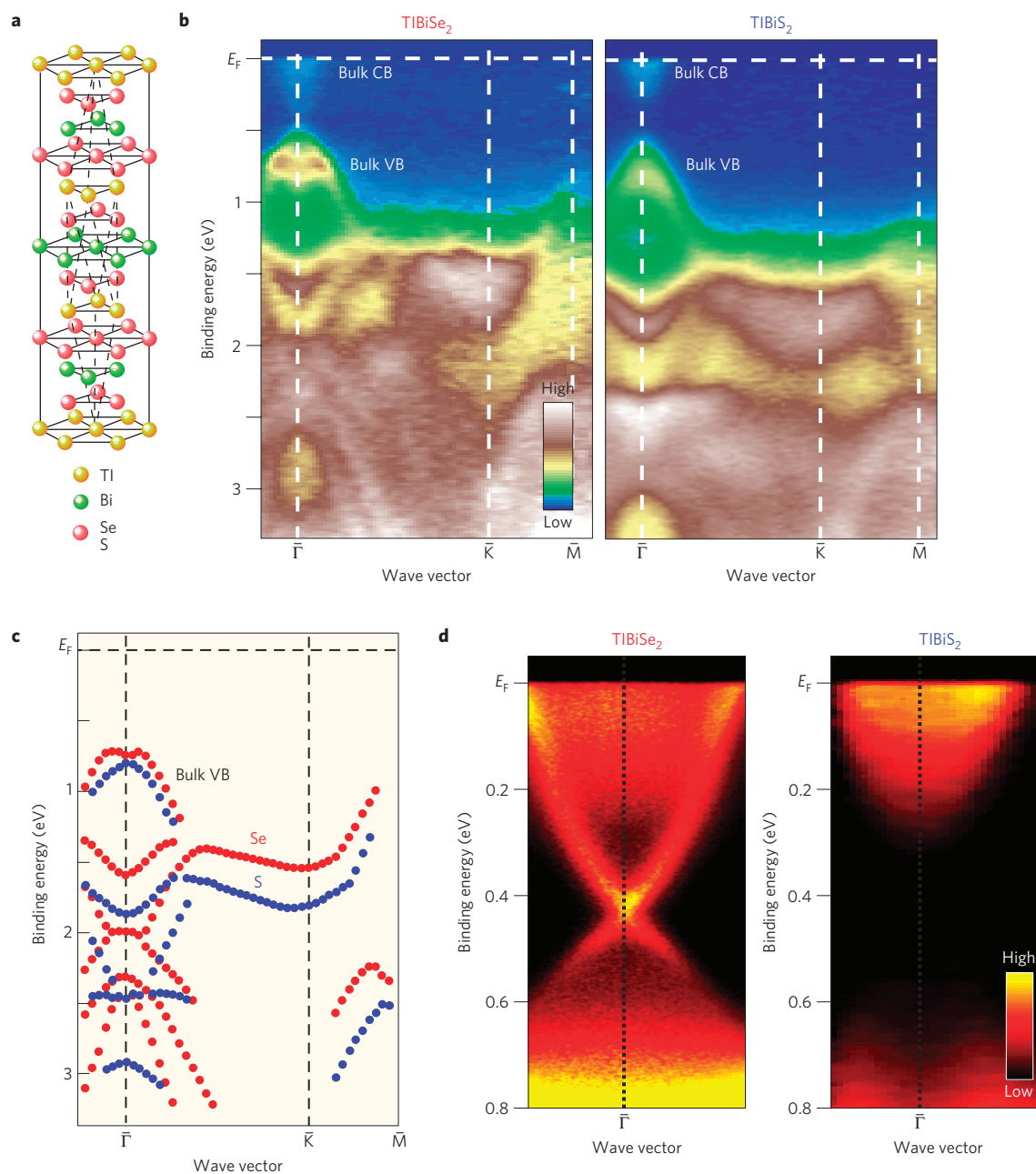


**Figure 1 | Comparison of the valence-band structure between TlBiSe<sub>2</sub> and TlBiS<sub>2</sub>.** **a**, Crystal structure of TlBi(S<sub>1-x</sub>Se<sub>x</sub>)<sub>2</sub>. **b**, Valence-band ARPES intensity along the  $\bar{\Gamma}$ - $\bar{K}$ - $\bar{M}$  direction of the surface Brillouin zone for TlBiSe<sub>2</sub> and TlBiS<sub>2</sub>, plotted as a function of wave vector and binding energy, measured using the He I  $\alpha$  resonance line ( $h\nu = 21.218$  eV) at  $T = 30$  K. **c**, Direct comparison of the valence-band dispersions between TlBiSe<sub>2</sub> and TlBiS<sub>2</sub>. The energy positions of the bands are determined by tracing the peak position of the second derivatives of the ARPES spectra. Several branches of dispersive bands in both compounds are found at  $E_B$  higher than 1 eV; these are attributed to the hybridized states of Tl 6p, Bi 6p and Se 4p (S 3p) orbitals<sup>16–18</sup>. Clearly, the bands in TlBiS<sub>2</sub> are shifted towards higher  $E_B$  with respect to those in TlBiSe<sub>2</sub>, with the energy shift being more enhanced in deeper-lying bands, indicating the relative expansion of the VB width in TlBiS<sub>2</sub>. **d**, Comparison of the near- $E_F$  ARPES intensity around the  $\bar{\Gamma}$  point between TlBiSe<sub>2</sub> and TlBiS<sub>2</sub>, measured using the Xe I resonance line ( $h\nu = 8.437$  eV). The absence of the surface band in TlBiS<sub>2</sub> was also confirmed by varying the photon energy and light polarization of the synchrotron radiation.

band at  $x = 1.0$ , where the EDC at the  $\bar{\Gamma}$  point is well fitted by a slightly asymmetric Lorentzian, splits into lower and upper branches at  $x = 0.9$ , with a finite energy gap at the  $\bar{\Gamma}$  point. Further substitution of S results in the reduction and the broadening of the intensity of the surface band (see EDCs for  $x = 0.6$ ), but the energy position of the surface band can be still traced, as illustrated in the second-derivative intensity plots in Fig. 2c. The surface-state nature of this band was confirmed by the stationary nature of its energy position with respect to the photon energy (Supplementary

Information), so this band evidently represents massive Dirac fermions on the surface. As a result of the gapped nature, this phase cannot be called topological in the strict sense, but the massive Dirac fermions are obviously of topological origin, suggesting that the bulk bands are kept inverted. On the other hand, the photon-energy dependence of the ARPES spectra for  $x = 0.4$  signifies the absence of the surface state, in contrast to the clear signature of it for  $x = 0.6$  (Supplementary Information). The disappearance of the surface state and the very narrow bulk gap at  $x = 0.4$  (which can be inferred

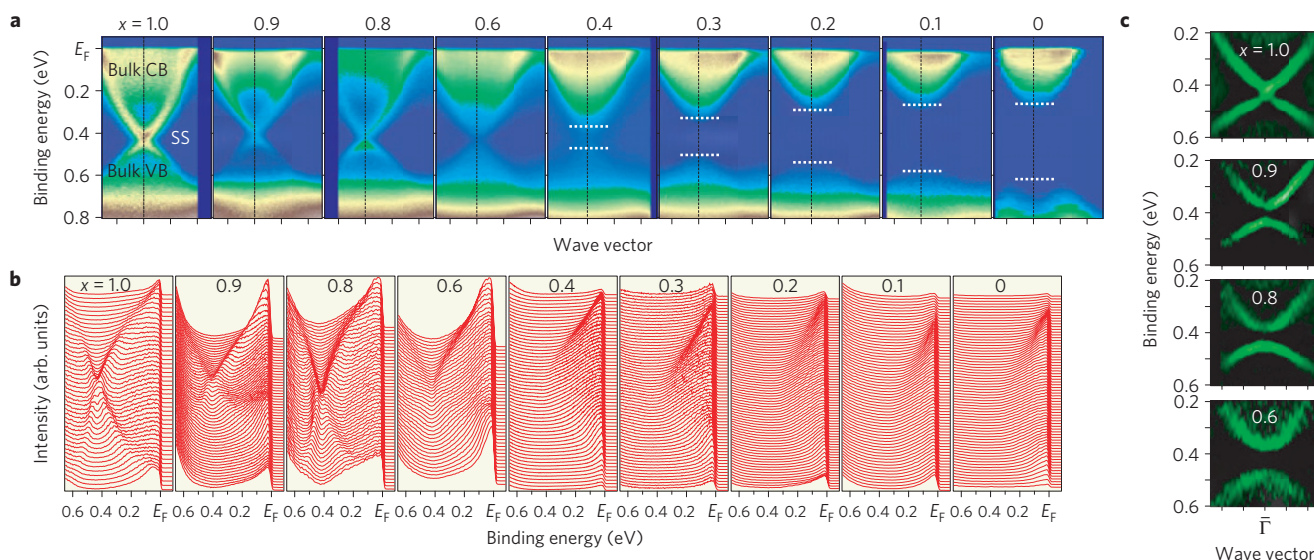


**Figure 2 | Mass acquisition of surface Dirac fermions in  $\text{TlBi}(\text{S}_{1-x}\text{Se}_x)_2$ .** **a**, Near- $E_F$  ARPES intensity around the  $\bar{\Gamma}$  point as a function of wave vector and binding energy in  $\text{TlBi}(\text{S}_{1-x}\text{Se}_x)_2$  for a series of Se concentrations, measured using the Xe I line with the same experimental geometry. White dotted lines for  $x \leq 0.4$  represent the top of the VB and the bottom of the CB, thus highlighting the bandgap; owing to the  $k_z$  dispersion of the bulk bands, the true gap is likely to be smaller than these estimates, as is reflected in the error bars in Fig. 3d. **b**, Energy distribution curves (EDCs) of the data shown in **a**. **c**, Second-derivative plots of the ARPES intensity for  $x = 1.0, 0.9, 0.8$  and  $0.6$ .

from Supplementary Fig. S2) point to the topological QPT being located between  $x = 0.6$  and  $0.4$ . Interestingly, the surface bandgap, called here the Dirac gap, grows with decreasing  $x$  (less than  $0.1$  eV at  $x = 0.9$  and  $0.8$ , and greater than  $0.1$  eV at  $x = 0.6$ ), indicating that the S content is closely related to the magnitude of the Dirac gap. We also found that the magnitude of the Dirac gap does not diminish with increasing temperature (Supplementary Information), which argues against a magnetic-order origin of the gap. We note that in a recent independent work<sup>19</sup> the Dirac cone was reported to remain gapless for  $x > 0.5$ , in contrast to the gapped surface states for  $0.6 \leq x \leq 0.9$  observed here. This discrepancy may be due to the difference in the energy resolution ( $15$  meV in ref. 19, as opposed to  $2\text{--}4$  meV in the present experiment).

One may wonder if the bulk bandgap really closes at  $x_c \approx 0.5$ . If the bandgap never closes, the samples for both  $x = 1.0$  and  $0.0$  should be in the same topological phase. Apparently, this is inconsistent with our ARPES data in Fig. 1d. According to the fundamental principle of the topological band theory, the QPT must always be accompanied by a bandgap closing. Hence, based on our data, the bandgap closing must be happening either at  $0.4 < x < 0.6$  or at  $0.9 < x < 1.0$  (at which the Dirac gap starts to open). Taking into account the gradual reduction of the bandgap size on approaching  $x = 0.5$ , it is most sensible to conclude that the inevitable closing of the gap takes place at  $x = 0.5$ .

One may also question if the observed Dirac gap might be an artefact of an inhomogeneous S distribution in the sample. To address this question, we employed electron-probe microanalysis (EPMA) on the surface and found that our crystals are exceedingly homogeneous (Supplementary Information). The persistently narrow X-ray diffraction peaks, together with a systematic change of the lattice constants, further corroborate this conclusion (Supplementary Information).

To quantify the magnitude of the Dirac gap, we use the theoretical surface-band dispersion to account for the finite mass term<sup>20</sup> (which was originally proposed to explain the  $\text{Bi}_2\text{Se}_3$  ultrathin-film data<sup>21</sup>) and numerically simulate the experimentally obtained surface band dispersion near the  $\bar{\Gamma}$  point; although the origin of the mass term in  $\text{TlBi}(\text{S}_{1-x}\text{Se}_x)_2$  is not clear at the moment. As shown in Fig. 3a, the simulated curves reasonably well reproduce

the experimental data, and the obtained Dirac gaps for  $x = 0.9, 0.8$  and  $0.6$  are  $50 \pm 10$ ,  $70 \pm 10$  and  $130 \pm 20$  meV, respectively. The evolution of the massive Dirac cone is schematically illustrated in 3D images of the band dispersions in Fig. 3b. We have confirmed that the obtained sizes of the Dirac gap are highly reproducible by measuring more than five samples for each composition and also by varying the incident photon energy. Taking into account that all the elements contained in  $\text{TlBi}(\text{S}_{1-x}\text{Se}_x)_2$  are nonmagnetic and also that the sample shows no obvious magnetic order (Supplementary Information), our result is a strong indication that the substitution of Se with S in  $\text{TlBi}(\text{S}_{1-x}\text{Se}_x)_2$  leads to an unconventional mass acquisition of the surface Dirac fermions without explicitly breaking the TRS.

Based on the present ARPES results, one may draw the electronic phase diagram of  $\text{TlBi}(\text{S}_{1-x}\text{Se}_x)_2$ , as shown in Fig. 3d. The massless Dirac topological phase is achieved only near  $x = 1.0$ . Once a small amount of S is substituted for Se, the Dirac gap opens, growing almost linearly as a function of the S content,  $1-x$ . Such a massive Dirac phase is present until the topological QPT occurs at  $x_c \approx 0.5$ , where the bulk gap closes and the band parity is interchanged.

The mass acquisition of the Dirac fermions indicates that the Kramers degeneracy is lifted, which means that the TRS must be broken on the surface. Given that there is no explicit TRS breaking, the only possibility is that a spontaneous symmetry breaking takes place on the S substitution, which is reminiscent of the Higgs mechanism in particle physics. Therefore,  $\text{TlBi}(\text{S}_{1-x}\text{Se}_x)_2$  may serve as a model system to bridge condensed-matter physics and particle physics. The exact mechanism of the mass acquisition is not clear at the moment, but an interesting possibility is that it originates from some exotic many-body effects that can lead to an electronic order, although a simple mechanism like the spin-density wave does not seem to be relevant (Supplementary Information). When the top and bottom surface states coherently couple and hybridize, a Dirac gap can open<sup>21</sup>, but the sufficiently large thickness ( $>10\text{ }\mu\text{m}$ ) of our samples precludes this origin. Another possibility is that critical fluctuations associated with the QPT are responsible for the mass acquisition, but it is too early to speculate along this line. From the application point of view, the Dirac gap can be much larger than that of the

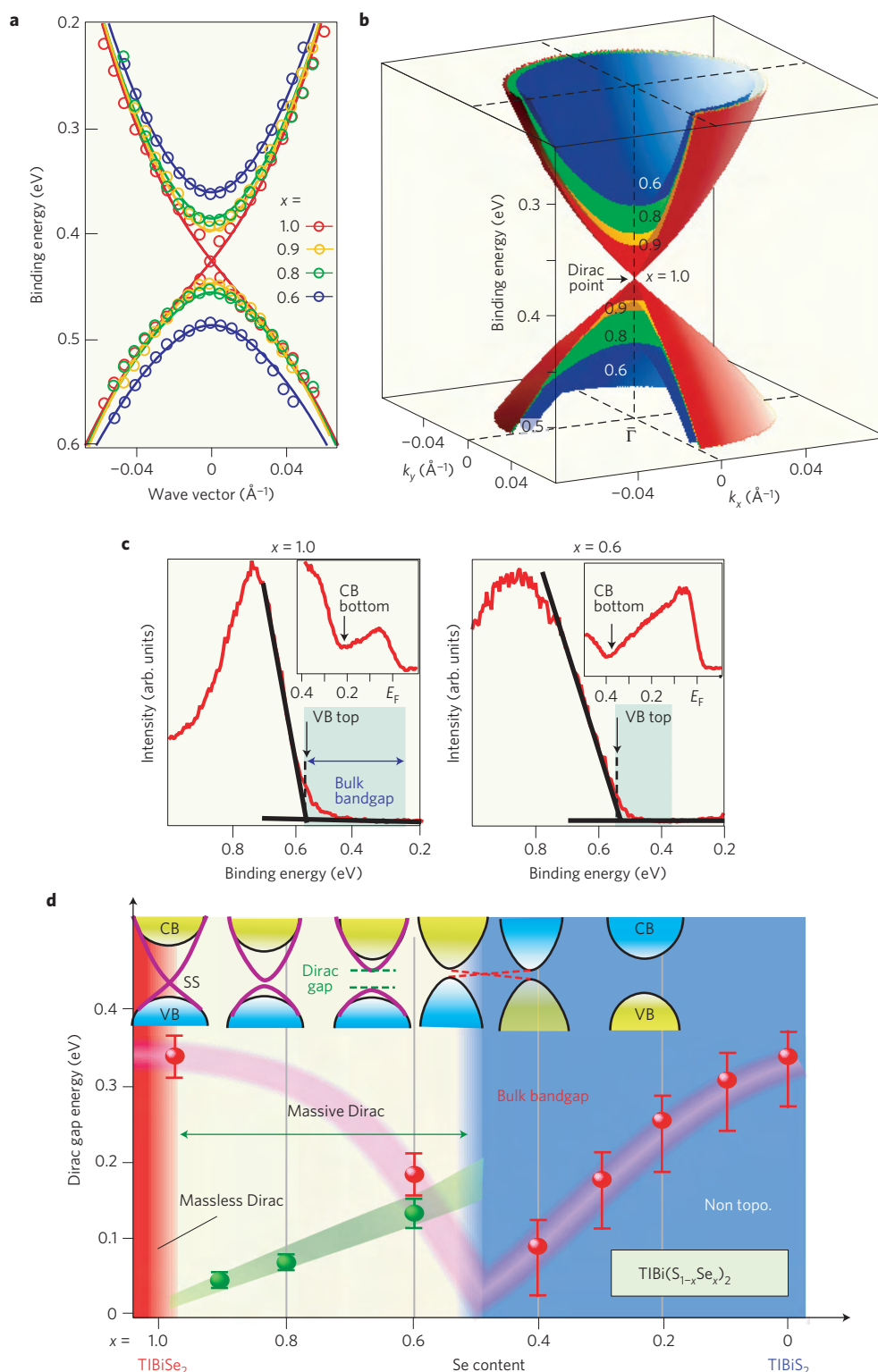


**Figure 3 | Massive Dirac fermions and the electronic phase diagram across the topological quantum phase transition.** **a**, Numerical fittings of the ARPES-determined surface band dispersion (open circles) using the theoretical band dispersion which incorporates the finite mass term<sup>20</sup>. Note that the Dirac energy for  $x = 0.9$  is shifted downward by 0.015 eV for clarity. **b**, Schematic 3D image of the surface Dirac cone and its energy-gap evolution at low sulphur concentrations. **c**, ARPES spectra around the VB and CB edges for  $x = 1.0$  and  $0.6$ , which are used for the bandgap determination for  $x > 0.5$ , as was done in ref. 10; the photon energies of the synchrotron radiation were chosen to optimally probe the VB top and the CB bottom respectively<sup>10</sup>. **d**, Electronic phase diagram of  $\text{TlBi}(\text{S}_{1-x}\text{Se}_x)_2$  showing the surface Dirac gap (green symbols) and the bulk bandgap (red symbols), together with a schematic picture of the band evolution (top) summarizing the present ARPES experiment. Error bars for the Dirac gap energy correspond to the experimental uncertainty in determining the energy position of the band dispersion at the  $\bar{\Gamma}$  point in **a**, whereas those for the bulk bandgap originate from the experimental uncertainty in determining the energy difference between the top of the valence band and the bottom of the conduction band in Figs 2 and 3c.

magnetically doped topological insulator  $\text{Bi}_2\text{Se}_3$  (ref. 1) and is tunable by means of the S/Se ratio, making the  $\text{TlBi}(\text{S}_{1-x}\text{Se}_x)_2$  system a prime candidate for device applications that require a gapped surface state.

## Methods

High-quality single crystals of  $\text{TlBi}(\text{S}_{1-x}\text{Se}_x)_2$  were grown by a modified Bridgman method (see Supplementary Information for details). X-ray diffraction measurements indicated the monotonic shrinkage of  $a$  and  $c$  axis lengths on substitution of S for Se, without any apparent change in the relative atomic position with respect to the unit cell. ARPES measurements were performed at Tohoku University using VG-SCIENIA SES2002 and MBS-A1 spectrometers with high-flux He and Xe discharge lamps and a toroidal/spherical grating monochromator. The He I $\alpha$  ( $h\nu = 21.218$  eV) line and one of the Xe I ( $h\nu = 8.437$  eV) lines<sup>22</sup> were used to excite photoelectrons. Samples were cleaved *in situ* along the (111) crystal plane in an ultrahigh vacuum of  $5 \times 10^{-11}$  torr. The energy resolutions for the measurement of the VB and near- $E_F$  regions were set at 15 and 2–4 meV, respectively. The angular resolution was  $0.2^\circ$ , corresponding to a  $k$  resolution of 0.007 and  $0.004 \text{ \AA}^{-1}$  for the He I $\alpha$  and Xe I photons, respectively. The Fermi level of the samples was referenced to that of a gold film evaporated onto the sample holder. A shiny mirror-like surface was obtained after cleaving samples, confirming its high quality.

Received 30 December 2010; accepted 8 July 2011;  
published online 14 August 2011

## References

- Chen, Y.-L. *et al.* Massive Dirac fermion on the surface of a magnetically doped topological insulator. *Science* **329**, 659–662 (2010).
- Qi, X.-L., Hughes, T. L. & Zhang, S.-C. Topological field theory of time-reversal invariant insulators. *Phys. Rev. B* **78**, 195424 (2008).
- Qi, X.-L., Li, R.-D., Zang, J.-D. & Zhang, S.-C. Inducing a magnetic monopole with topological surface states. *Science* **323**, 1184–1187 (2009).
- Bernevig, B. A., Hughes, T. L. & Zhang, S.-C. Quantum spin Hall effect and topological phase transition in HgTe quantum wells. *Science* **314**, 1757–1761 (2006).
- Fu, L. & Kane, C. L. Topological insulators with inversion symmetry. *Phys. Rev. B* **76**, 045302 (2007).
- König, M. *et al.* Quantum spin Hall insulator state in HgTe quantum wells. *Science* **318**, 766–770 (2007).
- Hsieh, D. *et al.* A topological Dirac insulator in a quantum spin Hall phase. *Nature* **452**, 970–974 (2008).
- Xia, Y. *et al.* Observation of a large-gap topological-insulator class with a single Dirac cone on the surface. *Nature Phys.* **5**, 398–402 (2009).
- Chen, Y. L. *et al.* Experimental realization of a three-dimensional topological insulator,  $\text{Bi}_2\text{Te}_3$ . *Science* **325**, 178–181 (2009).
- Sato, T. *et al.* Direct evidence for the Dirac-cone topological surface states in ternary chalcogenide  $\text{TlBiSe}_2$ . *Phys. Rev. Lett.* **105**, 136802 (2010).
- Kuroda, K. *et al.* Experimental realization of a three-dimensional topological insulator phase in ternary chalcogenide  $\text{TlBiSe}_2$ . *Phys. Rev. Lett.* **105**, 146801 (2010).
- Chen, Y. L. *et al.* Observation of single Dirac cone topological surface state in compounds  $\text{TlBiTe}_2$  and  $\text{TlBiSe}_2$  from a new topological insulator family. *Phys. Rev. Lett.* **105**, 266401 (2010).
- Ren, Z. *et al.* Large bulk resistivity and surface quantum oscillations in the topological insulator  $\text{Bi}_2\text{Te}_2\text{Se}$ . *Phys. Rev. B* **82**, 241306 (2010).
- Xu, Y.-S. *et al.* Discovery of several large families of topological insulator classes with backscattering-suppressed spin-polarized single-Dirac-cone on the surface. Preprint at <http://arxiv.org/abs/1007.5111> (2010).
- Zhang, H. *et al.* Topological insulators in  $\text{Bi}_2\text{Se}_3$ ,  $\text{Bi}_2\text{Te}_3$  and  $\text{Sb}_2\text{Te}_3$  with a single Dirac cone on the surface. *Nature Phys.* **5**, 438–442 (2009).
- Yan, B. *et al.* Theoretical prediction of topological insulators in thallium-based III-V-VI<sub>2</sub> ternary chalcogenides. *Europhys. Lett.* **90**, 37002 (2010).
- Lin, H. *et al.* Single-Dirac-cone topological surface states in the  $\text{TlBiSe}_2$  class of topological semiconductors. *Phys. Rev. Lett.* **105**, 036404 (2010).
- Hoang, K. & Mahanti, S. D. Atomic and electronic structures of thallium-based III-V-VI<sub>2</sub> ternary chalcogenides: *Ab initio* calculations. *Phys. Rev. B* **81**, 041309(R) (2010).
- Xu, S.-Y. *et al.* Topological phase transition and texture inversion in a tunable topological insulator. *Science* **332**, 560–564 (2011).
- Lu, H.-Z., Shan, W.-Y., Yao, W., Niu, Q. & Shen, S.-Q. Massive Dirac fermions and spin physics in an ultrathin film of topological insulator. *Phys. Rev. B* **81**, 115407 (2010).
- Zhang, L. *et al.* Crossover of the three-dimensional topological insulator  $\text{Bi}_2\text{Se}_3$  to the two-dimensional limit. *Nature Phys.* **6**, 584–588 (2010).
- Souma, S., Sato, T., Takahashi, T. & Baltzer, P. High-intensity xenon plasma discharge lamp for bulk-sensitive high-resolution photoemission spectroscopy. *Rev. Sci. Instrum.* **78**, 123104 (2007).

## Acknowledgements

We thank N. Nagaosa for valuable discussions. We also thank H. Guo, K. Sugawara, M. Komatsu, T. Arakane and A. Takayama for their assistance in the ARPES experiment, and S. Sasaki for the analysis using EPMA. This work was supported by JSPS (KAKENHI 19674002 and NEXT Program), JST-CREST, MEXT of Japan (Innovative Area ‘Topological Quantum Phenomena’), AFOSR (AOARD 10-4103), and KEK-PF (Proposal number: 2009S2-005 and 2010G507).

## Author contributions

T.S., K.K., S.S., K.N., and T.T. performed ARPES measurements. K.S., K.E., T.M. and Y.A. carried out the growth of the single crystals and their characterizations. T.S., K.S. and Y.A. conceived the experiments and wrote the manuscript.

## Additional information

The authors declare no competing financial interests. Supplementary information accompanies this paper on [www.nature.com/naturephysics](http://www.nature.com/naturephysics). Reprints and permissions information is available online at <http://www.nature.com/reprints>. Correspondence and requests for materials should be addressed to T.S. or Y.A.

## ARTICLE

Received 19 Aug 2011 | Accepted 9 Dec 2011 | Published 17 Jan 2012

DOI:10.1038/ncomms1639

# Tunable Dirac cone in the topological insulator $\text{Bi}_{2-x}\text{Sb}_x\text{Te}_{3-y}\text{Se}_y$

T. Arakane<sup>1</sup>, T. Sato<sup>2</sup>, S. Souma<sup>1</sup>, K. Kosaka<sup>2</sup>, K. Nakayama<sup>2</sup>, M. Komatsu<sup>2</sup>, T. Takahashi<sup>1,2</sup>, Zhi Ren<sup>3</sup>, Kouji Segawa<sup>3</sup> & Yoichi Ando<sup>3</sup>

The three-dimensional topological insulator is a quantum state of matter characterized by an insulating bulk state and gapless Dirac cone surface states. Device applications of topological insulators require a highly insulating bulk and tunable Dirac carriers, which has so far been difficult to achieve. Here we demonstrate that  $\text{Bi}_{2-x}\text{Sb}_x\text{Te}_{3-y}\text{Se}_y$  is a system that simultaneously satisfies both of these requirements. For a series of compositions presenting bulk-insulating transport behaviour, angle-resolved photoemission spectroscopy reveals that the chemical potential is always located in the bulk band gap, whereas the Dirac cone dispersion changes systematically so that the Dirac point moves up in energy with increasing  $x$ , leading to a sign change of the Dirac carriers at  $x \sim 0.9$ . Such a tunable Dirac cone opens a promising pathway to the development of novel devices based on topological insulators.

<sup>1</sup> WPI Research Center, Advanced Institute for Materials Research, Tohoku University, Sendai 980-8577, Japan. <sup>2</sup> Department of Physics, Tohoku University, Sendai 980-8578, Japan. <sup>3</sup> Institute of Scientific and Industrial Research, Osaka University, Ibaraki, Osaka 567-0047, Japan. Correspondence and requests for materials should be addressed to T.S. (email: t-sato@arpes.phys.tohoku.ac.jp).



The surface state of a three-dimensional topological insulator (TI) is characterized by a Dirac cone dispersion showing a helical spin structure<sup>1–4</sup>, which makes the Dirac fermions immune to backward scattering and robust to non-magnetic impurities and disorder<sup>5,6</sup>. Experimental realizations of novel topological phenomena expected for such helical Dirac fermions hinge on the dominance of surface transport, but a highly insulating bulk has rarely been achieved in prototypical TIs such as  $\text{Bi}_2\text{Se}_3$  and  $\text{Bi}_2\text{Te}_3$  because of naturally occurring defects and the resulting carrier doping<sup>3,7–10</sup>. Furthermore, applications of TIs to a wide range of devices would require a means to intentionally manipulate the properties of the Dirac carriers (sign, density, velocity and so on.) while keeping the bulk sufficiently insulating. However, such a Dirac cone engineering has been difficult to achieve because of the lack of suitable materials.

Recently, it has been shown that the ternary tetradymite TI material  $\text{Bi}_2\text{Te}_2\text{Se}$ , which forms the ordered Te–Bi–Se–Bi–Te quintuple layers, has a large bulk resistivity<sup>11,12</sup> because of its chemical characteristics suitable for reducing defect formations. In this regard, the tetradymite  $\text{Bi}_{2-x}\text{Sb}_x\text{Te}_{3-y}\text{Se}_y$  (BSTS) solid solution, which has the same crystal structure as  $\text{Bi}_2\text{Te}_2\text{Se}$  (Fig. 1a), is of interest because a series of special combinations of  $x$  and  $y$  have been known to yield a high resistivity<sup>13–15</sup>. Thus, in the insulating compositions reported here ( $(x, y) = (0, 1), (0.25, 1.1), (0.5, 1.3), (1, 2)$ ), the  $y$  value is unique when  $x$  is specified (details are described in Methods (in the subsection Transport properties of BSTS)). Such a control of the material properties is an advantage of the solid-solution systems<sup>16–18</sup> and makes the BSTS system an interesting platform for investigating the Dirac band structure while keeping the insulating nature of the bulk.

Here we report our angle-resolved photoemission spectroscopy (ARPES) experiments on BSTS, which elucidated the surface and bulk electronic states in the vicinity of the Fermi level ( $E_F$ ) responsible for the peculiar physical properties. We show that simultaneous tuning of the Sb and Se contents in the BSTS crystal makes it

possible to control the energy location of the Dirac cone in the bulk band gap (and the sign of Dirac carriers) while keeping the bulk insulating character. This result demonstrates that what BSTS offers is, at present, the closest to the ultimate goal of the Dirac cone engineering, that is, being able to tune the Dirac band structure to have desired surface carrier properties without having to tune the chemical potential in bulk crystals.

## Results

**Electronic states of  $\text{Bi}_2\text{Te}_2\text{Se}$ .** We first demonstrate the ARPES data of an end member  $\text{Bi}_2\text{Te}_2\text{Se}$  ( $x=0; y=1$ ). The photon-energy dependence of the band structure near  $E_F$  is displayed in Figure 1b, where one can see several common features such as a prominent electron-like band centred at the  $\bar{\Gamma}$  point ( $k_y=0$ ) in the binding energy  $E_B$  range of 0.0–0.3 eV and rather complicated band dispersions at  $E_B > 0.3$  eV. These features correspond to the surface state (SS) and the bulk valence bands (VB), respectively, judged from the analysis shown in Figure 1c, where the energy position of the SS is stationary with the variation in  $h\nu$  unlike that of the VB. A closer look at Figure 1c also reveals that the SS has an ‘x’-shaped dispersion with its Dirac point at  $\sim 0.3$  eV, indicative of an electron-doped character of the surface. The highest lying VB at  $\sim 0.4$  eV exhibits an ‘m’-shaped dispersion and is located closest to  $E_F$  at  $h\nu = 58$  eV. We use this photon energy for comparing the electronic states at different compositions of BSTS and also for quantitatively estimating characteristic energies, as will be described later. One can see in Figure 1b that the signature of the bulk conduction band (CB) is completely absent in the ARPES intensity, confirming the insulating nature of the bulk. The two-dimensional contour plots of the ARPES intensity at various  $E_B$  shown in Figure 1d signify the hexagonal warping of the SS band structure that gradually weakens on approaching the Dirac point, as commonly observed in other TIs<sup>4,8,19</sup>. Outside the SS, the VB feature is visible as a six-fold petal-like intensity pattern at  $E_B = 0.25$ –0.3 eV.

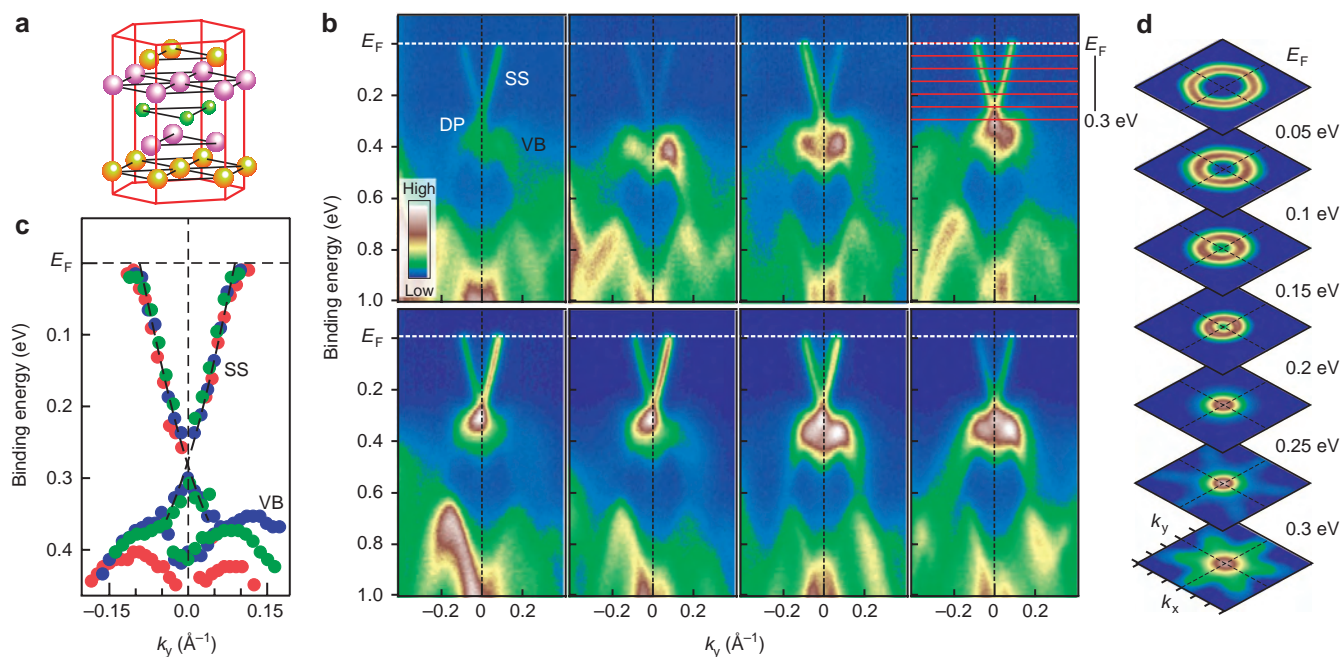


**Figure 1 | Photon energy dependence of the band structure in  $\text{Bi}_2\text{Te}_2\text{Se}$ .** (a) Crystal structure of  $\text{Bi}_{2-x}\text{Sb}_x\text{Te}_{3-y}\text{Se}_y$ . Green, purple and yellow circles represent Se, Bi/Sb and Te/Se atoms, respectively. (b) Photon energy dependence of the ARPES intensity around the  $\bar{\Gamma}$  point for  $\text{Bi}_2\text{Te}_2\text{Se}$  ( $x=0, y=1$ ) measured at  $h\nu = 46, 50, 54$  and  $58$  eV (top row) and  $62, 66, 70$  and  $74$  eV (bottom row) at  $T = 30$  K. (c) Comparison of the band dispersions of the SS and the bulk VB in  $x=0$  for 3 representative photon energies  $h\nu = 50, 58$  and  $70$  eV, as indicated by red, blue and green circles, respectively. The band dispersions were obtained by tracing the peak position of EDCs. Black dashed curves are guides to the eyes to trace the SS. (d) ARPES intensity plots for  $x=0$  as a function of two-dimensional wave vector measured with  $h\nu = 58$  eV, for various binding energies between  $E_F$  and 0.3 eV. The intensity maps were obtained by folding the ARPES intensity with the crystal symmetry taken into account.



**Evolution of electronic states in  $\text{Bi}_{2-x}\text{Sb}_x\text{Te}_{3-y}\text{Se}_y$ .** Figure 2a–c show a comparison of the Fermi surface and the near- $E_F$  band structure at different compositions, all of which belong to the bulk insulating phase as confirmed by the resistivity data shown in Figure 2d. Indeed, only the SS is present at  $E_F$  in all the samples. Interestingly, the SS Fermi surface systematically shrinks on increasing  $x$  (Fig. 2a) accompanied by an overall upward shift of the SS (Fig. 2b,c). This demonstrates that increasing  $x$  (and the simultaneous increase in  $y$ ) provides more acceptors, which is likely due to a slight change in the carrier compensation condition, while the bulk remains highly insulating as confirmed by the electrical resistivity data in Figure 2d; in particular, the resistivity for  $\text{Bi}_{1.5}\text{Sb}_{0.5}\text{Te}_{1.7}\text{Se}_{1.3}$  ( $x=0.5$ ;  $y=1.3$ ) is very high for TIs, reaching  $10\ \Omega\text{cm}$  at low temperatures, and previous magnetotransport studies elucidated the surface mobility to exceed  $1,000\ \text{cm}^2\text{Vs}^{-1}$  for this composition<sup>14</sup>. An important indication of our data is a systematic compensation of Dirac carriers that can be seen in Figure 2a–c; this trend can also be confirmed in the momentum distribution curves (MDCs) at  $E_F$  shown in Figure 2e, where the momentum separation of two peaks in the MDC, corresponding to the  $2k_F$  (Fermi vector) value, gradually decreases with increasing  $x$ . To quantitatively evaluate the evolution of the SS, we plot in Figure 2f the Dirac band dispersion determined from the peak positions of the energy distribution curves (EDCs) in Figure 2c. One can see that the energy shift of the Dirac band proceeds in a rigid-band manner, the bands for different  $x$  values essentially overlap with each other when we plot its energy position with respect to the Dirac-point energy ( $E_{\text{DP}}$ ), despite the total chemical potential ( $\mu$ ) shift of as large as  $0.3\ \text{eV}$  as seen in Figure 2g. Intriguingly, the SS band dispersion below  $E_F$  for  $x=1.0$  suggests that the Dirac point is located slightly above  $E_F$ , which can also be confirmed in the plot of the  $2k_F$  values in Figure 2h, pointing to a sign change of Dirac carriers from  $n$ - to  $p$ -type at some  $x$  value between  $0.5$  and  $1.0$ . Another important indication in Figure 2 is that the bulk VB does not show a rigid-band shift relative to the SS, as inferred from the data in Figure 2b, where the lower hole-like branch of the Dirac cone for  $x=1.0$  is more clearly visible than in  $x=0$ .

**Band diagram of  $\text{Bi}_{2-x}\text{Sb}_x\text{Te}_{3-y}\text{Se}_y$ .** Looking at Figure 2a, one notices that the Dirac point is buried in the bulk VB at  $x=0$ , which means that the putative transport properties near the Dirac point would be strongly affected by the bulk-surface interband scattering. In contrast, one can see in Figure 2b that the Dirac point for  $x=1.0$  is well isolated from the bulk, indicating a more ideal situation for applications. To depict a comprehensive picture of the evolution of the energy bands, it is necessary to determine the energy locations of the bulk-band edges. This requires the observation of the CB which becomes possible by ageing the sample surface<sup>20–22</sup>. The details of this ageing experiments are described in Methods (Surface ageing to observe the bulk CB). We have estimated  $E_{\text{CB}}$  and  $E_{\text{VB}}$  as well as the Dirac-point energy ( $E_{\text{DP}}$ ) by using the ageing technique for all compositions, and the obtained characteristic energies are shown in Figure 3a. While the magnitude of the band gap is almost independent of  $x$ , the Dirac-point energy relative to the VB top,  $E_{\text{DP}}-E_{\text{VB}}$ , is negative at  $x=0$  and turns to positive around the critical  $x$  of  $\sim 0.25$ . As illustrated in the schematic band diagram (Fig. 3b), the intrinsic transport properties near the Dirac point can be achieved in samples with  $x>0.25$ , and, therefore, this composition range is particularly suited for realizing the topological phenomena to require the tuning of  $\mu$  to the Dirac point, such as the topological magnetoelectric effect<sup>23</sup>. Another important aspect is that  $\mu$  at the native surface of our BSTS samples is located above the Dirac point in  $0 \leq x \leq 0.5$  and below it in  $x=1.0$ . This suggests that a sign change in surface Dirac carriers takes place at  $x \sim 0.9$  (estimated from a linear interpolation in Fig. 2h), and, therefore, a  $p$ - $n$  junction fabricated by a composition gradient in BSTS may be conceivable. In this regard, the Hall coefficient at low temperature is negative for  $x=0.0$ – $0.5$ , whereas

it is positive for  $x=1.0$  as described in Methods (in the subsection Transport properties of BSTS), in good agreement with the ARPES data.

## Discussion

The observed isolated nature of the Dirac cone at  $x=1$  as opposed to its buried character at  $x=0$  may be understood in terms of the difference in the Se/Te content: according to the previous ARPES studies, the Dirac point in  $\text{Bi}_2\text{Se}_3$  (ref. 3) is well isolated from the bulk bands while that in  $\text{Bi}_2\text{Te}_3$  is situated inside the bulk VB<sup>8</sup>. In BSTS, the Dirac cone is gradually isolated from the bulk band as the Se/Te ratio is increased from  $0.5$  to  $2.0$  (on which  $x$  changes from  $0.0$  to  $1.0$ ), in accordance with the natural expectation from the difference in the electronic states in  $\text{Bi}_2\text{Se}_3$  and  $\text{Bi}_2\text{Te}_3$ . This suggests the importance of controlling the orbital character of chalcogen-derived bands for the Dirac cone engineering.

The experimental realization of both Dirac holes and electrons in the BSTS system demonstrated here points to the high potential of this material for studying the various topological phenomena requiring the access to the Dirac point. Moreover, it would provide an excellent platform for the development of novel topological devices to utilize a dual-gate configuration for the electric control of spins<sup>24</sup> or  $p$ - $n$ -junction configurations that are essential for various applications, as in semiconductor technology. Another important feature of this system is that the energy location of the Dirac point in the band gap can be tuned while keeping the bulk-insulating nature and a high surface mobility, allowing one to study the effect of the bulk-surface scattering channel on the surface carriers near the Dirac point. Furthermore, the availability of the Dirac cone engineering in bulk crystals is important for the topological magnetoelectric effect, because it has been proposed that the energy gain in the bulk owing to the axion term can be crucial for realizing such an effect<sup>25</sup>. The present result provides an important step toward establishing the means to fully control of surface Dirac fermions in TIs to explore a variety of exotic physical properties proposed for this exciting class of materials.

## Methods

**Sample preparation.** High-quality single crystals of BSTS were grown by sealing stoichiometric amounts of high-purity elements in evacuated quartz tubes and melting them at  $850^\circ\text{C}$  for  $48\ \text{h}$  with intermittent shaking to ensure a homogeneity of the melt, followed by cooling slowly to  $550^\circ\text{C}$  and annealing at that temperature for  $4\ \text{days}$ . X-ray diffraction analyses confirmed that all the samples have the same crystal structure ( $R\ \bar{3}m$ ) with the desired chalcogen ordering as shown in Figure 1a. Transport properties were measured with Quantum Design PPMS using the standard AC four-probe method.

**ARPES experiments.** ARPES measurements were performed with a VG Scienta SES2002 electron analyser with a tunable synchrotron light at the beamline BL28A at Photon Factory (KEK). We used circularly polarized lights of  $36$ – $116\ \text{eV}$ . The energy and angular resolutions were set at  $15$ – $30\ \text{meV}$  and  $0.2^\circ$ , respectively. ARPES measurements were also performed with a MBS A1 electron analyzer with a high-flux Xe discharge lamp and a spherical grating monochromator ( $h\nu=8.437\ \text{eV}$ )<sup>26</sup> at Tohoku University. Samples were cleaved *in-situ* along the  $(111)$  crystal plane in an ultrahigh vacuum of  $1 \times 10^{-10}$  Torr. The Fermi level of the samples was referenced to that of a gold film evaporated onto the sample holder. A shiny mirror-like surface was obtained after cleaving the samples, confirming its high quality.

**Transport properties of BSTS.** As was reported in ref. 15, the ‘intrinsic’ compositions in the solid-solution system BSTS were recently elucidated. At such compositions, acceptors and donors maximally compensate each other, and bulk-insulating behaviour is observed. In the present ARPES experiment, we studied four combinations of  $(x, y)$  [ $= (0, 1)$ ,  $(0.25, 1.1)$ ,  $(0.5, 1.3)$ , and  $(1, 2)$ ] that all belong to such intrinsic compositions. The crystals used in the present work are obtained after careful optimization of the growth conditions for insulating behaviour, as evidenced by the resistivity data (Fig. 2d) that present even higher values for all compositions compared with those reported in ref. 15.

To corroborate our claim that all the compositions studied here possess highly bulk-insulating nature, and to elucidate the sign of the surface charge carriers, the temperature dependences of the Hall coefficient  $R_H$  for the four compositions were measured (Supplementary Fig. S1). The Hall measurements were done on the same samples as those used for the resistivity measurements. One can see that the

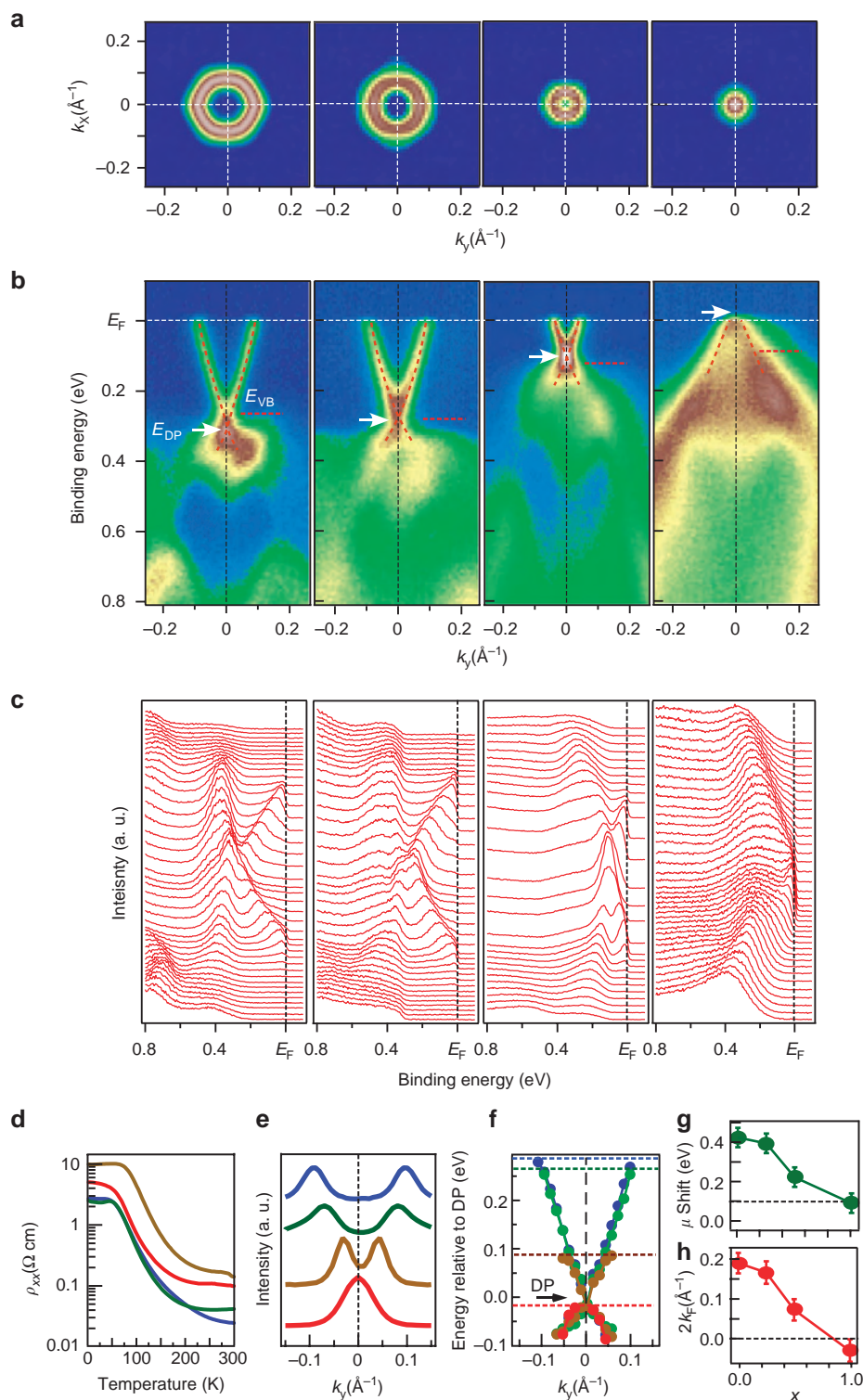


**Figure 2 | Properties of  $\text{Bi}_{2-x}\text{Sb}_x\text{Te}_{3-y}\text{Se}_y$  for various compositions.** (a–c) Comparison of (a) the Fermi surface of the SS, (b) the near- $E_F$  band dispersions, and (c) the EDCs in  $\text{Bi}_{2-x}\text{Sb}_x\text{Te}_{3-y}\text{Se}_y$  for four  $x$  values ( $x=0, 0.25, 0.5$  and  $1.0$ ) where  $y=1, 1.15, 1.3$  and  $2$ , respectively. The ARPES data were measured with  $h\nu=58$  eV at  $T=30$  K. Brown dashed curves in (b) are guides to the eyes to trace the SS. White arrows and red dashed lines indicate the energy positions of the Dirac point ( $E_{DP}$ ) and the VB top ( $E_{VB}$ ), respectively. (d) Temperature dependences of the electrical resistivity  $\rho_{xx}$  at the four compositions. (e–h) Composition dependences of (e) the MDCs at  $E_F$ , (f) the band dispersions of the SS relative to the Dirac point, (g) the shift of the chemical potential ( $\mu$ ) relative to that for  $x=1.0$  when the Dirac point is taken as the reference point, and (h) the  $2k_F$  values along  $k_y$ .  $k_F$  values were determined by fitting MDCs at  $E_F$  with two Lorentzian peaks. Blue, green, brown and red curves or dots in d–f are for  $x=0, 0.25, 0.5$  and  $1.0$ , respectively. Error bars in (g) correspond to the experimental uncertainty in determining  $E_{DP}$ , whereas those in (h) originates in the experimental uncertainty in estimating the peak position of MDCs.

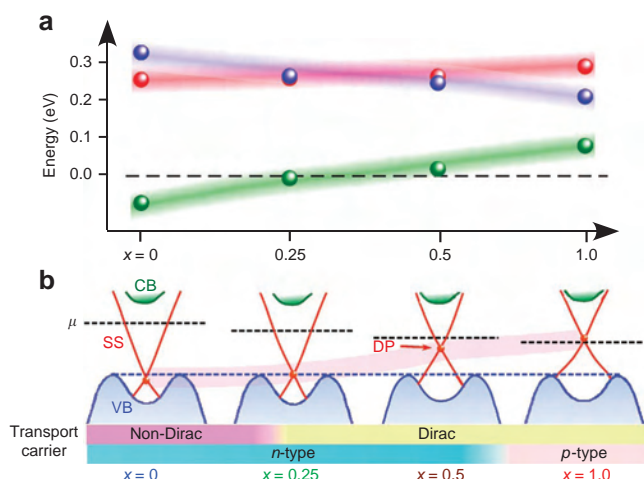


**Figure 3 | Characteristic energies and the schematic band diagram.**

(a) Plot of the three characteristic energies, the band gap  $E_{\text{gap}} (= E_{\text{CB}} - E_{\text{VB}})$ ,  $E_{\text{CB}} - E_{\text{DP}}$ , and  $E_{\text{DP}} - E_{\text{VB}}$ , as a function of  $x$ , as indicated by red, blue and green colours, respectively. (b) Schematic band diagram for changing  $x$  in BSTS derived from the present ARPES experiment. The top of the VB is aligned in this diagram for clarity.

absolute values of  $R_H$  at the lowest temperature are  $400 \text{ cm}^3 \text{ per } ^\circ\text{C}$  or larger, which indicates that the present samples are even better insulators than the  $\text{Bi}_2\text{Te}_2\text{Se}$  sample originally reported in ref. 13 (where  $|R_H|$  at the lowest temperature was  $200 \text{ cm}^3 \text{ per } ^\circ\text{C}$ ).

**Surface ageing to observe the bulk conduction band.** To determine the energy location of the bulk CB that is located above  $E_F$  in our insulating samples, we intentionally aged the sample surface in our vacuum chamber and doped electrons into the SS to enhance the surface band-bending effect, by following the ARPES studies of  $\text{Bi}_2\text{Se}_3$  and  $\text{Bi}_2\text{Te}_3$  (refs 20–22) and also a recent transport study of BSTS<sup>14</sup>. A representative result for  $x=0$  shown in Supplementary Figure S2 demonstrates that the ageing leads to an overall downward shift of the spectral feature and, simultaneously, the appearance of the CB at  $E_F$ . As shown in the right panel of Supplementary Figure S2, it is thus possible to estimate the actual locations of the bottom of the CB ( $E_{\text{CB}}$ ) and the top of the VB ( $E_{\text{VB}}$ ) by tracing the trailing/leading edges of the EDCs<sup>27</sup>.

## References

- Hasan, M. Z. & Kane, C. L. Colloquium: topological insulators. *Rev. Mod. Phys.* **82**, 3045–3067 (2010).
- Qi, X.-L. & Zhang, S.-C. Topological insulators and superconductors. *Rev. Mod. Phys.* **83**, 1057–1110 (2011).
- Xia, Y. *et al.* Observation of a large-gap topological-insulator class with a single Dirac cone on the surface. *Nature Phys.* **5**, 398–402 (2009).
- Souma, S. *et al.* Direct measurement of the out-of-plane spin texture in the Dirac-cone surface state of a topological insulator. *Phys. Rev. Lett.* **106**, 216803 (2011).
- Roushan, P. *et al.* Topological surface states protected from backscattering by chiral spin texture. *Nature* **460**, 1106–1109 (2009).
- Seo, J. *et al.* Transmission of topological surface states through surface barriers. *Nature* **466**, 343–346 (2010).
- Hsieh, D. *et al.* A topological Dirac insulator in a quantum spin Hall phase. *Nature* **452**, 970–974 (2008).
- Chen, Y.-L. *et al.* Massive Dirac fermion on the surface of a magnetically doped topological insulator. *Science* **329**, 659–662 (2010).
- Hor, Y. S. *et al.*  $p$ -type  $\text{Bi}_2\text{Se}_3$  for topological insulator and low-temperature thermoelectric applications. *Phys. Rev. B* **79**, 195208 (2009).

- Checkelsky, J. G. *et al.* Quantum interference in macroscopic crystals of nonmetallic  $\text{Bi}_2\text{Se}_3$ . *Phys. Rev. Lett.* **103**, 246601 (2009).
- Ren, Z., Taskin, A. A., Sasaki, S., Segawa, K. & Ando, Y. Large bulk resistivity and surface quantum oscillations in the topological insulator  $\text{Bi}_2\text{Te}_2\text{Se}$ . *Phys. Rev. B* **82**, 241306 (2010).
- Xiong, J., Petersen, A. C., Qu, D., Cava, R. J. & Ong, N. P. Quantum oscillations in a topological insulator  $\text{Bi}_7\text{Te}_2\text{Se}$  with large bulk resistivity ( $6 \Omega\text{cm}$ ). Preprint arXiv:1101.1315 (2011).
- Teramoto, I. & Takayanagi, S. Relations between the electronic properties and the chemical bonding of  $\text{Sb}_x\text{Bi}_{1-x}\text{Te}_{3-y}\text{Se}_y$  system. *J. Phys. Chem. Solids* **19**, 124–129 (1961).
- Taskin, A. A., Ren, Z., Sasaki, S., Segawa, K. & Ando, Y. Observation of Dirac holes and electrons in a topological insulator. *Phys. Rev. Lett.* **107**, 016801 (2011).
- Ren, Z., Taskin, A. A., Sasaki, S., Segawa, K. & Ando, Y. Optimizing  $\text{Bi}_{2-x}\text{Sb}_x\text{Te}_{3-y}\text{Se}_y$  solid solutions to approach the intrinsic topological insulator regime. *Phys. Rev. B* **84**, 165311 (2011).
- Taskin, A. A. & Ando, Y. Quantum oscillations in a topological insulator  $\text{Bi}_{1-x}\text{Sb}_x$ . *Phys. Rev. B* **80**, 085303 (2009).
- Zhang, J. *et al.* Band structure engineering in  $(\text{Bi}_{1-x}\text{Sb}_x)_2\text{Te}_3$  ternary topological insulators. *Nat. Commun.* **2**, 574 (2011).
- Kong, D. *et al.* Ambipolar field effect in topological insulator nanoplates of  $(\text{Bi}_x\text{Sb}_{1-x})_2\text{Te}_3$ . *Nat. Nanotechnol.* **6**, 705–709 (2011).
- Kuroda, K. *et al.* Hexagonally deformed Fermi surface of the 3D topological insulator  $\text{Bi}_2\text{Se}_3$ . *Phys. Rev. Lett.* **105**, 076802 (2010).
- Bianchi, M. *et al.* Coexistence of the topological state and a two-dimensional electron gas on the surface of  $\text{Bi}_2\text{Se}_3$ . *Nat. Commun.* **1**, 128 (2010).
- Wray, L. A. *et al.* Electron dynamics in topological insulator semiconductor-metal interfaces (topological p-n interface). Preprint arXiv:1105.4794 (2011).
- Benia, H. M., Lin, C., Kern, L. K. & Ast, C. R. Reactive chemical doping of the  $\text{Bi}_2\text{Se}_3$  topological insulator. *Phys. Rev. Lett.* **107**, 177602 (2011).
- Qi, X.-L., Hughes, T. L. & Zhang, S.-C. Topological field theory of time-reversal invariant insulators. *Phys. Rev. B* **78**, 195424 (2008).
- Yazyev, O. V., Moore, J. E. & Louie, S. G. Spin polarization and transport of surface states in the topological insulators  $\text{Bi}_2\text{Se}_3$  and  $\text{Bi}_2\text{Te}_3$  from first principles. *Phys. Rev. Lett.* **105**, 266806 (2010).
- Nomura, K. & Nagaosa, N. Surface-quantized anomalous Hall current and the magnetoelectric effect in magnetically disordered topological insulators. *Phys. Rev. Lett.* **106**, 166802 (2011).
- Souma, S., Sato, T., Takahashi, T. & Baltzer, P. High-intensity xenon plasma discharge lamp for bulk-sensitive high-resolution photoemission spectroscopy. *Rev. Sci. Instrum.* **78**, 123104 (2007).
- Sato, T. *et al.* Direct evidence for the Dirac-cone topological surface states in ternary chalcogenide  $\text{TlBiSe}_2$ . *Phys. Rev. Lett.* **105**, 136802 (2010).

## Acknowledgements

We thank Y. Tanaka, K. Yoshimatsu, H. Kumigashira and K. Ono for their assistance in ARPES measurements. This work was supported by JSPS (NEXT Program and KAKENHI 23224010), JST-CREST, MEXT of Japan (Innovative Area “Topological Quantum Phenomena”), AFOSR (AOARD 10-4103), and KEK-PF (Proposal number: 2010G507).

## Author contributions

T.A., T.S., S.S., K.K., K.N., M.K. and T.T. performed ARPES measurements. Z.R., K.S. and Y.A. carried out the growth of the single crystals and their characterizations. T.A., T.S., Z.R. and Y.A. conceived the experiments and wrote the manuscript.

## Additional information

**Supplementary Information** accompanies this paper at <http://www.nature.com/naturecommunications>

**Competing financial interests:** The authors declare no competing financial interests.

**Reprints and permission** information is available online at <http://npg.nature.com/reprintsandpermissions/>

**How to cite this article:** Arakane, T. *et al.* Tunable Dirac cone in the topological insulator  $\text{Bi}_{2-x}\text{Sb}_x\text{Te}_{3-y}\text{Se}_y$ . *Nat. Commun.* 3:636 doi: 10.1038/ncomms1639 (2012).



# Topological Superconductivity in $\text{Cu}_x\text{Bi}_2\text{Se}_3$

Satoshi Sasaki,<sup>1</sup> M. Kriener,<sup>1</sup> Kouji Segawa,<sup>1</sup> Keiji Yada,<sup>2</sup> Yukio Tanaka,<sup>2</sup> Masatoshi Sato,<sup>3</sup> and Yoichi Ando<sup>1,\*</sup>

<sup>1</sup>*Institute of Scientific and Industrial Research, Osaka University, Ibaraki, Osaka 567-0047, Japan*

<sup>2</sup>*Department of Applied Physics, Nagoya University, Nagoya 464-8603, Japan*

<sup>3</sup>*Institute for Solid State Physics, University of Tokyo, Chiba 277-8581, Japan*

(Received 2 August 2011; published 14 November 2011)

A topological superconductor (TSC) is characterized by the topologically protected gapless surface state that is essentially an Andreev bound state consisting of Majorana fermions. While a TSC has not yet been discovered, the doped topological insulator  $\text{Cu}_x\text{Bi}_2\text{Se}_3$ , which superconducts below  $\sim 3$  K, has been predicted to possess a topological superconducting state. We report that the point-contact spectra on the cleaved surface of superconducting  $\text{Cu}_x\text{Bi}_2\text{Se}_3$  present a zero-bias conductance peak (ZBCP) which signifies unconventional superconductivity. Theoretical considerations of all possible superconducting states help us conclude that this ZBCP is due to Majorana fermions and gives evidence for a topological superconductivity in  $\text{Cu}_x\text{Bi}_2\text{Se}_3$ . In addition, we found an unusual pseudogap that develops below  $\sim 20$  K and coexists with the topological superconducting state.

DOI: 10.1103/PhysRevLett.107.217001

PACS numbers: 74.45.+c, 03.65.Vf, 73.20.At, 74.20.Rp

The recent discovery of topological insulators [1–24] stimulated the search for an even more exotic state of matter, the topological superconductor (TSC) [25–28]. A topological state of matter is characterized by a topological structure of the quantum-mechanical wave function in the Hilbert space. In topological insulators, a nontrivial  $Z_2$  topology of the bulk valence band leads to the emergence of Dirac fermions on the surface [22,23]. Similarly, in TSCs nontrivial  $Z$  or  $Z_2$  topologies of the superconducting (SC) states lead to the appearance of Majorana fermions on the surface [25–27]. Majorana fermions are peculiar in that the particles are their own antiparticles, and they were originally conceived as mysterious neutrinos [29]. Currently their realization in condensed matter is of significant interest because of their novelty as well as the potential for quantum computing [29].

The  $\text{Cu}_x\text{Bi}_2\text{Se}_3$  superconductor [30–33] is a prime candidate of the TSC because of its peculiar band structure and strong spin-orbit coupling [34]. In this material, Cu atoms are intercalated into the layered topological insulator  $\text{Bi}_2\text{Se}_3$  and the SC state appears for the Cu concentration  $x$  of about 0.2–0.5, which causes electron doping with the density of  $\sim 10^{20} \text{ cm}^{-3}$ . This material has not been well studied because of the difficulty in preparing high-quality samples [30,31] but a recent breakthrough in the synthesis of  $\text{Cu}_x\text{Bi}_2\text{Se}_3$  by using electrochemistry [32,33] made it possible to prepare reliable junctions and perform a conductance spectroscopy in the superconducting state.

In the present work, we employed the so-called “soft” point-contact technique [35]: The contacts were prepared at room temperature in ambient atmosphere by putting a tiny ( $\sim 20 \mu\text{m}$ ) drop of silver paste on the cleaved (111) surface of a  $\text{Cu}_x\text{Bi}_2\text{Se}_3$  single crystal below a  $30\text{-}\mu\text{m}$ -diameter gold wire [Figs. 1(a) and 1(b)]. In this

type of junction, ballistic transport occurs sporadically through parallel nanometer-scale channels formed between individual grains in the silver paste and the sample surface [see Figs. 1(c) and 1(d) and Ref. [36]]. The  $dI/dV$  spectra were measured with a lock-in technique by sweeping a dc current that is superimposed with a small-amplitude ac current [ $1.35 \mu\text{A}$  (rms), corresponding to  $0.5 \text{ A/cm}^2$ ]. We used a quasi-four-probe configuration, in which the

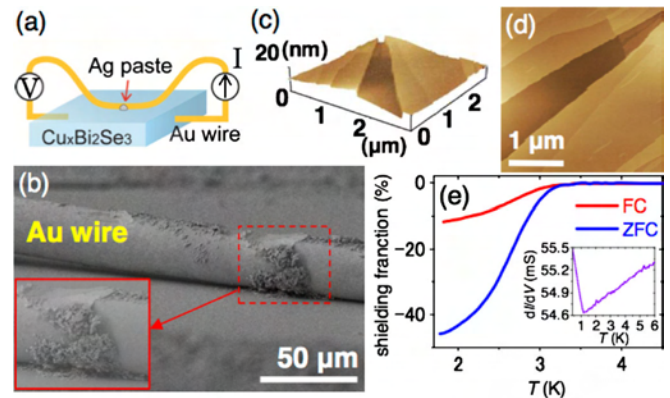


FIG. 1 (color online). Point-contact experiment and the sample. (a) Sketch of the soft point contact and the measurement circuit. (b) Scanning-electron-microscope picture of the actual sample; inset magnifies the silver-paste spot where the point contact is formed. (c) 3D presentation of nanometer-scale terraces on a typical cleaved surface of  $\text{Cu}_x\text{Bi}_2\text{Se}_3$  seen by an atomic-force microscope. Typical terrace width is  $0.5 \mu\text{m}$ . (d) A false color mapping of (c). (e) SQUID data for the SC transition in the sample ( $x = 0.3$ ) used for the point-contact measurements shown in Fig. 2. Both the zero-field-cooled (ZFC) and the field-cooled (FC) data measured in  $0.2 \text{ mT}$  are shown, and the former gives the SC shielding fraction of 46%. Inset shows the temperature dependence of the zero-bias differential conductance of the point contact reported in Fig. 2.

current was applied between a contact pad and the gold wire, and the voltage between the wire and another contact pad was measured [Fig. 1(a)]. The Quantum Design PPMS was used for cooling the samples down to 0.35 K and applying the magnetic field up to 9 T.

A set of point-contact data taken on a  $\text{Cu}_x\text{Bi}_2\text{Se}_3$  sample with the bulk onset  $T_c = 3.2$  K is shown in Fig. 2, where one can see that a pronounced zero-bias conductance peak (ZBCP) develops at low temperature [36]. The inset of Fig. 1(e) shows the temperature dependence of the zero-bias conductance, which indicates that this peak appears below 1.2 K [36]. We note that essentially the same ZBCP data have been obtained on another sample (see Fig. S2 of Ref. [36]).

Since heating effects can cause a spurious ZBCP [37], it is important to elucidate that it is not the case here. It was argued by Sheet *et al.* [37] that in samples with a large normal-state resistivity when the point contact is in the thermal regime, a spurious ZBCP could show up if the increase in the bias voltage causes the local current to exceed the critical current, which leads to a voltage-dependent decrease in the differential conductivity. If this is the case, the conductivity at zero bias (which is always measured below the critical current) should *not* change with a weak magnetic field; the role of the magnetic field in this case is primarily to reduce the critical current, so the width of the spurious ZBCP would become narrower, but the height at  $V = 0$  should be mostly unchanged as long as the superconductor is in the zero-resistivity state. In the magnetic-field dependence of our spectra shown in Fig. 2(c), by contrast, the ZBCP is strongly suppressed with a modest magnetic field while its width is little affected, which clearly speaks against the heating origin of the ZBCP. (The magnetic field was applied perpendicular to the cleaved surface.) Another well-known signature of the heating effect is a sharp, spikelike dip at energies much larger than the gap [35,37], which is caused by the local transition to normal state; in fact, when we made the point contact on a disordered surface, we observed a widening of the peak and a lot of sharp dips at relatively high energies, which are obviously caused by the heating [36]. In contrast, the data shown in Fig. 2 are free from such

features, which corroborates the intrinsic nature of the ZBCP. Therefore, one can safely conclude that the ZBCP observed here is not due to the heating effects and is intrinsic.

One should also keep in mind that, even when the ZBCP is intrinsic, it can be caused by several mechanisms in point contacts [38]: conventional Andreev reflection [39,40], reflectionless tunneling [41–43], magnetic scattering [44,45], and the unconventional Andreev bound state (ABS) [38,40]. In this respect, it is important to notice that the ZBCP shown in Fig. 2 is accompanied by pronounced dips on its sides and the peak does not split into two even at the lowest temperature (0.35 K). These features are clearly at odds with the Blonder-Tinkham-Klapwijk (BTK) theory for conventional Andreev reflection [39]. Also, the reflectionless tunneling and the magnetic scattering are obviously irrelevant, because the former is suppressed by a very small magnetic field of less than 0.1 T [46] and the latter presents a peak splitting in magnetic fields [47]. Hence, one can conclude that the ZBCP observed here is a manifestation of the ABS [38].

Previously, it was inferred [32] from the specific-heat data that the superconducting gap of  $\text{Cu}_x\text{Bi}_2\text{Se}_3$  at  $T = 0$  K,  $\Delta(0)$ , would be about 0.7 meV. In Fig. 2, one can see that the minima in the pronounced dips are located at  $\sim \pm 0.6$  meV at 0.35 K; since the ZBCP due to the ABS is usually accompanied by dips near the gap energy [38], the energy scale of the dip is assuring.

Given that the observed ZBCP is intrinsic and is due to the ABS, it is important to understand its concrete origin. The ABS is caused by the interference of the SC wave function at the surface, and it is a signature of unconventional superconductivity [38]. Its occurrence is determined by the symmetry of the SC state, which in turn is determined by the symmetry of the Hamiltonian and the pairing mechanism. Also, it has been elucidated that Majorana fermions reside in an ABS when it is spin nondegenerate [48]. Hence, we examined all possible SC states in  $\text{Cu}_x\text{Bi}_2\text{Se}_3$  and the nature of the ABS to elucidate whether the observed ZBCP is due to Majorana fermions. The microscopic model to describe the band structure of  $\text{Cu}_x\text{Bi}_2\text{Se}_3$  has already been developed [34,49–51], and

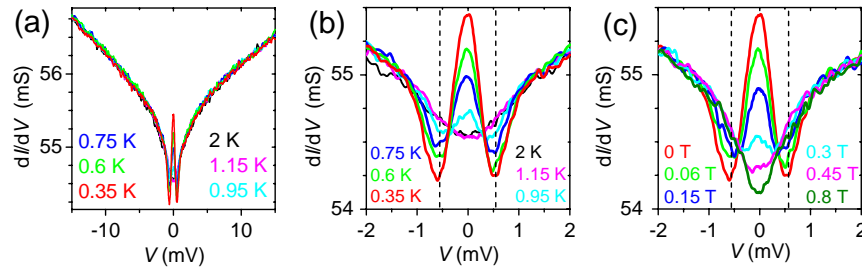


FIG. 2 (color online). Zero-bias conductance peak. (a) Point-contact spectra ( $dI/dV$  vs bias voltage) of  $\text{Cu}_x\text{Bi}_2\text{Se}_3$  with  $x = 0.3$  for 0.35–2 K measured in 0 T for a wide energy window. (b) A narrower window of (a). (c) The spectra at 0.35 K measured in perpendicular magnetic fields of 0–0.8 T. The vertical dashed lines in (b) and (c) indicate the energy position of the dips.

it was shown [34] that, if both short- and long-range interactions are considered, the symmetry of the Hamiltonian allows four different types of the SC gap function,  $\Delta_1$  to  $\Delta_4$  [36], with three of them being unconventional. Following Ref. [51], we have theoretically calculated the spectral functions of the bulk and the surface as well as the local density of states (LDOS) for all possible gap functions (see Ref. [36] for details), similar to those done in Refs. [52,53].

First, the conventional even-parity SC state  $\Delta_1$  was found to give no two-dimensional (2D) ABS [36]. While in this case the surface could become a 2D TSC due to the proximity effect as proposed by Fu and Kane [28], the surface of a three-dimensional (3D) superconductor is continuously connected and has no topological edge; hence, the one-dimensional Majorana fermions that might appear at the edge of a 2D TSC [28] would not exist in the present case.

Among the remaining three possible SC states that are all unconventional, the fully-gapped, odd-parity SC state  $\Delta_2$  gives rise to 2D helical Majorana fermions as the ABS. However, because of the Dirac-like dispersion of this ABS, the surface LDOS tends to have a minimum at zero energy [36], which does not agree well with our data; nevertheless, it was very recently proposed that the ZBCP could appear even in this fully gapped state due to a peculiar “twisting” of the ABS dispersion [54]. In the case of the other two odd-parity SC states,  $\Delta_3$  and  $\Delta_4$ , both of which have two point nodes, a single ZBCP naturally shows up in the surface LDOS [Figs. 3(a)–3(c)]; this is because the point nodes lead to a partially flat dispersion of the helical Majorana fermions, concentrating the LDOS near zero energy. Therefore, it is most likely that the observed ZBCP signifies 2D Majorana fermions due to the odd-parity bulk SC state, although it is difficult to determine the exact pairing state from the three possibilities at this stage. The fact that the ZBCP is strongly suppressed with a modest magnetic field [Fig. 2(c)] supports this conclusion, because the helical Majorana fermions are naturally suppressed as the time-reversal symmetry is broken with the

magnetic field. Note that, while there are nanometer-scale terraces on the cleaved surface (Figs. 1(c) and 1(d) and Ref. [36]), electron transmissions in the in-plane directions through the side walls of the terraces are much less likely to take place compared to the transmissions in the out-of-plane direction, because the typical terrace height ( $< 10$  nm) is much smaller than the typical Ag grain size of 50 nm [36]. Therefore, our data are expected to reflect mostly the ABS on the (111) surface.

We now discuss the topological nature of the possible SC states  $\Delta_3$  and  $\Delta_4$ . The presence of the point nodes might seem to preclude the topological superconductivity, which is usually considered to require a full gap. However, for the  $\Delta_3$  and  $\Delta_4$  states one can define a nontrivial topological invariant, “mod-2 winding number,” which is immune to weak perturbations and assures that the  $\Delta_3$  and  $\Delta_4$  states are robustly topological [36]. In fact, a time-reversal-invariant SC state with a pair of point nodes is adiabatically connected to a fully gapped state in the “mod-2 winding number” topological class, and having an odd parity is sufficient for this case to become topologically nontrivial [36].

Previously, we reported that the specific-heat data was most consistent with a fully-gapped SC state [32]. It is fair to note, however, that the entropy contribution of the quasiparticles excited near the point node of a 3D SC state is very small and, indeed, the  $T^3$  dependence of the specific heat expected for point nodes is difficult to be distinguished [55], particularly in inhomogeneous samples. Therefore, the  $\Delta_3$  or  $\Delta_4$  state with point nodes does not necessarily contradict the existing specific-heat data.

An interesting and unexpected feature in our data is that a pseudogap develops below  $\sim 20$  K [Fig. 4(a)]. As shown in Figs. 4(b)–4(g), this pseudogap appears to be enhanced by the magnetic field, and it is most pronounced at 0.35 K in high magnetic fields. This pseudogap coexists with the superconductivity below the upper critical field  $H_{c2}$  [56] and may give us a clue to understanding the pairing mechanism in  $\text{Cu}_x\text{Bi}_2\text{Se}_3$ . Finally, how the spectra change with

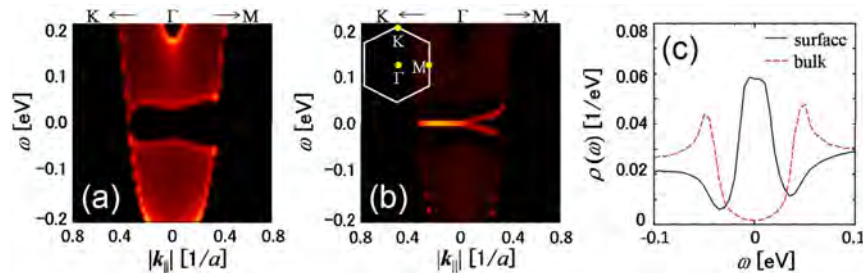


FIG. 3 (color online). Model calculations of the topological band structure in the superconducting state of  $\text{Cu}_x\text{Bi}_2\text{Se}_3$ . Theoretically calculated spectral functions  $A(\mathbf{k}, \omega)$  of the bulk (a) and the surface on the  $xy$  plane (b) in  $\Gamma$ - $M$  and  $\Gamma$ - $K$  directions in the surface Brillouin zone shown in the inset of (b), as well as the LDOS (c), in the superconducting state for the topological gap function  $\Delta_4$  ( $\Delta_{\parallel}^{12} = \Delta_{\parallel}^{21} = -\Delta_{\parallel}^{21} = -\Delta_{\parallel}^{12}$ ); the model Hamiltonian and the band parameters used are described in detail in Ref. [36]. The false color mappings of  $A(\mathbf{k}, \omega)$  in (a) and (b) are in arbitrary units.  $\Delta(0)$  was set to be 0.05 eV for the convenience of the calculations.



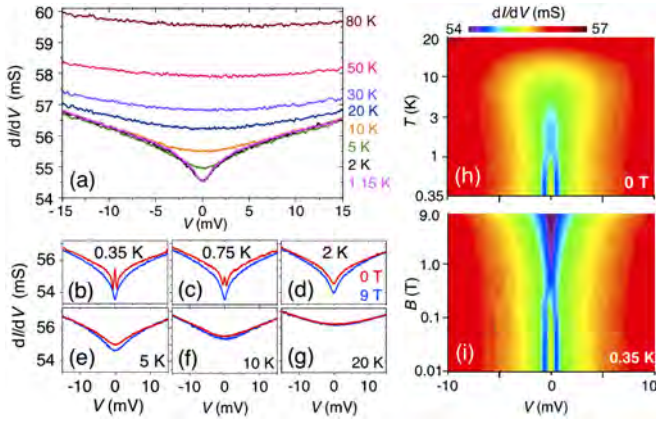


FIG. 4 (color online). Pseudogap in  $\text{Cu}_x\text{Bi}_2\text{Se}_3$ . (a)  $dI/dV$  vs bias voltage for 1.5–80 K measured in 0 T. (b)–(g) Comparisons of the spectra in 0 and 9 T. At low temperature below  $\sim 20$  K, the spectra in 9 T show smaller  $dI/dV$  near zero bias compared to that at 0 T, indicating that the pseudogap deepens with the magnetic field. (h),(i) False color mappings of  $dI/dV$  in the bias-voltage vs temperature plane in 0 T (h) and in the bias-voltage vs magnetic-field plane at 0.35 K (i), summarizing how the spectra change with temperature and magnetic field; note that the vertical axes are in logarithmic scales in both (h) and (i).

temperature and magnetic field is summarized in false color mappings shown in Figs. 4(h) and 4(i).

As is clear from the above discussions, one can conclude that the ZBCP in  $\text{Cu}_x\text{Bi}_2\text{Se}_3$  signifies an ABS consisting of 2D Majorana fermions and that  $\text{Cu}_x\text{Bi}_2\text{Se}_3$  is hosting a topological superconductivity. It is therefore an urgent task to determine the exact pairing symmetry in  $\text{Cu}_x\text{Bi}_2\text{Se}_3$ . Regarding the Majorana physics, an interesting question is the existence of the Majorana zero mode in the vortex core [57]. The 2D Majorana fermions living on the surface of a 3D TSC are different from the non-Abelian Majorana fermions of a 2D TSC proposed for topological quantum computing [22,28], but establishing a general understanding of Majorana fermions is important for both fundamental physics and future information technologies.

In summary, our point-contact spectroscopy of the  $\text{Cu}_x\text{Bi}_2\text{Se}_3$  superconductor found an unusual pseudogap below  $\sim 20$  K and a pronounced ZBCP in the SC state. The latter signifies an unconventional SC state that can only be topological in  $\text{Cu}_x\text{Bi}_2\text{Se}_3$ , and therefore our observation gives evidence for a topological superconductivity in this material. One can fully expect that  $\text{Cu}_x\text{Bi}_2\text{Se}_3$  as the first concrete example of a TSC will greatly help advance our understanding of topological states of matter and associated exotic quasiparticles.

We thank L. Fu, A. Furusaki, and S. Onoda for useful discussions, and K. Matsumoto and S. Wada for their help in the experiment. This work was supported by JSPS (NEXT Program), MEXT (Innovative Area “Topological Quantum Phenomena” KAKENHI), and AFOSR (AOARD 10-4103).

\*y\_ando@sanken.osaka-u.ac.jp

- [1] C.L. Kane and E.J. Mele, *Phys. Rev. Lett.* **95**, 146802 (2005).
- [2] B.A. Bernevig, T.L. Hughes, and S.-C. Zhang, *Science* **314**, 1757 (2006).
- [3] M. König, S. Wiedmann, C. Brüne, A. Roth, H. Buhmann, L.W. Molenkamp, X.-L. Qi, and S.-C. Zhang, *Science* **318**, 766 (2007).
- [4] L. Fu, C.L. Kane, and E.J. Mele, *Phys. Rev. Lett.* **98**, 106803 (2007).
- [5] J.E. Moore and L. Balents, *Phys. Rev. B* **75**, 121306(R) (2007).
- [6] R. Roy, *Phys. Rev. B* **79**, 195322 (2009).
- [7] X.-L. Qi, T.L. Hughes, and S.-C. Zhang, *Phys. Rev. B* **78**, 195424 (2008).
- [8] L. Fu and C.L. Kane, *Phys. Rev. B* **76**, 045302 (2007).
- [9] D. Hsieh, D. Qian, L. Wray, Y. Xia, Y.S. Hor, R.J. Cava, and M.Z. Hasan, *Nature (London)* **452**, 970 (2008).
- [10] A.A. Taskin and Y. Ando, *Phys. Rev. B* **80**, 085303 (2009).
- [11] A. Nishide, A.A. Taskin, Y. Takeichi, T. Okuda, A. Kakizaki, T. Hirahara, K. Nakatsuji, F. Komori, Y. Ando, and I. Matsuda, *Phys. Rev. B* **81**, 041309(R) (2010).
- [12] Y.L. Chen, J.G. Analytis, J.-H. Chu, Z.K. Liu, S.-K. Mo, X.L. Qi, H.J. Zhang, D.H. Lu, X. Dai, Z. Fang, S.C. Zhang, I.R. Fisher, Z. Hussain, and Z.-X. Shen, *Science* **325**, 178 (2009).
- [13] D. Hsieh, Y. Xia, D. Qian, L. Wray, F. Meier, J.H. Dil, J. Osterwalder, L. Patthey, A.V. Fedorov, H. Lin, A. Bansil, D. Grauer, Y.S. Hor, R.J. Cava, and M.Z. Hasan, *Phys. Rev. Lett.* **103**, 146401 (2009).
- [14] Y. Xia, D. Qian, D. Hsieh, L. Wray, A. Pal, H. Lin, A. Bansil, D. Grauer, Y.S. Hor, R.J. Cava, and M.Z. Hasan, *Nature Phys.* **5**, 398 (2009).
- [15] T. Sato, K. Segawa, H. Guo, K. Sugawara, S. Souma, T. Takahashi, and Y. Ando, *Phys. Rev. Lett.* **105**, 136802 (2010).
- [16] K. Kuroda, M. Ye, A. Kimura, S.V. Ereemeev, E.E. Krasovskii, E.V. Chulkov, Y. Ueda, K. Miyamoto, T. Okuda, K. Shimada, H. Namatame, and M. Taniguchi, *Phys. Rev. Lett.* **105**, 146801 (2010).
- [17] Y.L. Chen, Z.K. Liu, J.G. Analytis, J.-H. Chu, H.J. Zhang, B.H. Yan, S.-K. Mo, R.G. Moore, D.H. Lu, I.R. Fisher, S.-C. Zhang, Z. Hussain, and Z.-X. Shen, *Phys. Rev. Lett.* **105**, 266401 (2010).
- [18] Z. Ren, A.A. Taskin, S. Sasaki, K. Segawa, and Y. Ando, *Phys. Rev. B* **82**, 241306(R) (2010).
- [19] S.Y. Xu, L.A. Wray, Y. Xia, R. Shankar, A. Petersen, A. Fedorov, H. Lin, A. Bansil, Y.S. Hor, D. Grauer, R.J. Cava, and M.Z. Hasan, *arXiv:1007.5111v1*.
- [20] J. Xiong, A.C. Petersen, Dongxia Qu, R.J. Cava, and N.P. Ong, *arXiv:1101.1315*.
- [21] A.A. Taskin, Z. Ren, S. Sasaki, K. Segawa, and Y. Ando, *Phys. Rev. Lett.* **107**, 016801 (2011).
- [22] M.Z. Hasan and C.L. Kane, *Rev. Mod. Phys.* **82**, 3045 (2010).
- [23] J.E. Moore, *Nature (London)* **464**, 194 (2010).
- [24] X.-L. Wang, S.X. Dou, and C. Zhang, *NPG Asia Mater.* **2**, 31 (2010).

- [25] X.-L. Qi and S.-C. Zhang, *Rev. Mod. Phys.* **83**, 1057 (2011).
- [26] A. P. Schnyder, S. Ryu, A. Furusaki, and A. W. W. Ludwig, *Phys. Rev. B* **78**, 195125 (2008).
- [27] M. Sato, *Phys. Rev. B* **81**, 220504(R) (2010).
- [28] L. Fu and C. L. Kane, *Phys. Rev. Lett.* **100**, 096407 (2008).
- [29] F. Wilczek, *Nature Phys.* **5**, 614 (2009).
- [30] Y. S. Hor, A. J. Williams, J. G. Checkelsky, P. Roushan, J. Seo, Q. Xu, H. W. Zandbergen, A. Yazdani, N. P. Ong, and R. J. Cava, *Phys. Rev. Lett.* **104**, 057001 (2010).
- [31] L. A. Wray, S.-Y. Xu, Y. Xia, Y. S. Hor, D. Qian, A. V. Fedorov, H. Lin, A. Bansil, R. J. Cava, and M. Z. Hasan, *Nature Phys.* **6**, 855 (2010).
- [32] M. Kriener, K. Segawa, Z. Ren, S. Sasaki, and Y. Ando, *Phys. Rev. Lett.* **106**, 127004 (2011).
- [33] M. Kriener, K. Segawa, Z. Ren, S. Sasaki, S. Wada, S. Kuwabata, and Y. Ando, *Phys. Rev. B* **84**, 054513 (2011).
- [34] L. Fu and E. Berg, *Phys. Rev. Lett.* **105**, 097001 (2010).
- [35] D. Daghero and R. S. Gonnelli, *Supercond. Sci. Technol.* **23**, 043001 (2010).
- [36] See Supplemental Material at <http://link.aps.org/supplemental/10.1103/PhysRevLett.107.217001> for supplemental data and discussions.
- [37] G. Sheet, S. Mukhopadhyay, and P. Raychaudhuri, *Phys. Rev. B* **69**, 134507 (2004).
- [38] S. Kashiwaya and Y. Tanaka, *Rep. Prog. Phys.* **63**, 1641 (2000); Y. Tanaka and S. Kashiwaya, *Phys. Rev. Lett.* **74**, 3451 (1995).
- [39] G. E. Blonder, M. Tinkham, and T. M. Klapwijk, *Phys. Rev. B* **25**, 4515 (1982).
- [40] G. Deutscher, *Rev. Mod. Phys.* **77**, 109 (2005).
- [41] A. Kastalsky, A. W. Kleinsasser, L. H. Greene, R. Bhat, F. P. Milliken, and J. P. Harbison, *Phys. Rev. Lett.* **67**, 3026 (1991).
- [42] C. W. J. Beenakker, *Phys. Rev. B* **46**, 12 841 (1992); I. K. Marmorkos, C. W. J. Beenakker, and R. A. Jalabert, *Phys. Rev. B* **48**, 2811 (1993).
- [43] B. J. van Wees, P. de Vries, P. Magnée, and T. M. Klapwijk, *Phys. Rev. Lett.* **69**, 510 (1992).
- [44] J. A. Appelbaum, *Phys. Rev.* **154**, 633 (1967).
- [45] L. Y. L. Shen and J. M. Rowell, *Phys. Rev.* **165**, 566 (1968).
- [46] The footprint of our point contact is  $\sim 20 \mu\text{m}$ , which is larger than the dephasing length  $L_\phi$  of  $\sim 1 \mu\text{m}$  in Ag below 1 K [P. McConville and N. O. Birge, *Phys. Rev. B* **47**, 16667 (1993)]. This means that  $L_\phi$  governs the reflectionless tunneling [42] which would be suppressed with  $\sim 0.7$  mT.
- [47] The  $g$  factor of  $\text{Bi}_2\text{Se}_3$  is as large as 32 for  $H \parallel C_3$  [H. Köhler and E. Wöchner, *Phys. Status Solidi B* **67**, 665 (1975)], which suggests that the Zeeman splitting for  $S = 1/2$  in 0.1 T would be  $\sim 0.2$  meV. This should be observable if the magnetic scattering is relevant.
- [48] J. Linder, Y. Tanaka, T. Yokoyama, A. Sudbø, and N. Nagaosa, *Phys. Rev. Lett.* **104**, 067001 (2010).
- [49] H. Zhang, C.-X. Liu, X.-L. Qi, X. Dai, Z. Fang, and S. C. Zhang, *Nature Phys.* **5**, 438 (2009).
- [50] C.-X. Liu, X.-L. Qi, H. Zhang, X. Dai, Z. Fang, and S.-C. Zhang, *Phys. Rev. B* **82**, 045122 (2010).
- [51] L. Hao and T. K. Lee, *Phys. Rev. B* **83**, 134516 (2011).
- [52] A. P. Schnyder, P. M. R. Brydon, D. Manske, and C. Timm, *Phys. Rev. B* **82**, 184508 (2010).
- [53] K. Yada, M. Sato, Y. Tanaka, and T. Yokoyama, *Phys. Rev. B* **83**, 064505 (2011).
- [54] T. Hsieh and L. Fu, [arXiv:1109.3464](https://arxiv.org/abs/1109.3464).
- [55] H. R. Ott, H. Rudigier, T. M. Rice, K. Ueda, Z. Fisk, and J. L. Smith, *Phys. Rev. Lett.* **52**, 1915 (1984).
- [56] With resistivity measurements, we confirmed that the SC state is completely suppressed with the perpendicular magnetic field of 3 T (with the midpoint  $H_{c2}$  of 1.7 T) at 0.35 K, consistent with the reported  $H_{c2}(T)$  diagram [32].
- [57] P. Hosur, P. Ghaemi, R. S. K. Mong, and A. Vishwanath, *Phys. Rev. Lett.* **107**, 097001 (2011).

# Topological Surface States in Lead-Based Ternary Telluride $\text{Pb}(\text{Bi}_{1-x}\text{Sb}_x)_2\text{Te}_4$

S. Souma,<sup>1</sup> K. Eto,<sup>2</sup> M. Nomura,<sup>3</sup> K. Nakayama,<sup>3</sup> T. Sato,<sup>3</sup> T. Takahashi,<sup>1,3</sup> Kouji Segawa,<sup>2</sup> and Yoichi Ando<sup>2</sup>

<sup>1</sup>WPI Research Center, Advanced Institute for Materials Research, Tohoku University, Sendai 980-8577, Japan

<sup>2</sup>Institute of Scientific and Industrial Research, Osaka University, Ibaraki, Osaka 567-0047, Japan

<sup>3</sup>Department of Physics, Tohoku University, Sendai 980-8578, Japan

(Received 23 November 2011; published 12 March 2012)

We have performed angle-resolved photoemission spectroscopy on  $\text{Pb}(\text{Bi}_{1-x}\text{Sb}_x)_2\text{Te}_4$ , which is a member of lead-based ternary tellurides and has been theoretically proposed as a candidate for a new class of three-dimensional topological insulators. In  $\text{PbBi}_2\text{Te}_4$ , we found a topological surface state with a hexagonally deformed Dirac-cone band dispersion, indicating that this material is a strong topological insulator with a single topological surface state at the Brillouin-zone center. Partial replacement of Bi with Sb causes a marked change in the Dirac carrier concentration, leading to the sign change of Dirac carriers from *n* type to *p* type. The  $\text{Pb}(\text{Bi}_{1-x}\text{Sb}_x)_2\text{Te}_4$  system with tunable Dirac carriers thus provides a new platform for investigating exotic topological phenomena.

DOI: 10.1103/PhysRevLett.108.116801

PACS numbers: 73.20.-r, 71.20.-b, 75.70.Tj, 79.60.-i

Three-dimensional (3D) topological insulators are a novel state of quantum matter where the insulating bulk hosts gapless topological surface states with a Dirac-cone energy dispersion [1,2] which appear within the bulk excitation gap generated by the large spin-orbit coupling. The spin-orbit coupling is also responsible for the helical spin texture, where the spin direction is locked perpendicularly to the momentum. This peculiar spin texture [3,4] is the source of the dissipationless spin current that exists in equilibrium [5], as well as the immunity of Dirac fermions to the backward scattering [1]. Moreover, it has been predicted [6] that if superconductivity is induced in such spin-helical Dirac fermions, non-Abelian Majorana fermions that are the essential ingredient of topological quantum computing may emerge in the vortices. Angle-resolved photoemission spectroscopy (ARPES) has played a crucial role in the discovery of 3D topological insulators owing to the momentum (**k**) resolving capability and the high surface sensitivity. In fact, previous ARPES studies have identified a few types of new 3D topological insulators in the compounds containing group-V elements bismuth (Bi) and/or antimony (Sb), by observing the complex topological surface states in  $\text{Bi}_{1-x}\text{Sb}_x$  alloys [7–9] and the simpler topological surface states with a single Dirac cone in tetradymite semiconductors ( $\text{Bi}_2\text{Se}_3$  and  $\text{Bi}_2\text{Te}_3$ ) [3,10] and thallium-based ternary chalcogenides ( $\text{TlBiSe}_2$  and  $\text{TlBiTe}_2$ ) [11–13].

Recently, it has been proposed on the basis of the band structure calculations [14–16] that lead (Pb)-based layered ternary chalcogenides  $\text{PbM}_2\text{X}_4$  (*M*: Bi, Sb; *X*: Se, Te) are a promising candidate for a new class of 3D topological insulators. According to the calculations, some compounds of this system show a single Dirac cone at the Brillouin-zone center originating from the topological surface states, and a band inversion takes place at the *Z* or  $\Gamma$  point in the bulk Brillouin zone [15,16] as suggested by the parity

analysis of valence-band wave functions [16]. However, a clear experimental demonstration of the topological-insulator nature of Pb-based ternary chalcogenides has not yet been made, mainly due to the lack of high-quality single crystals. Finding a new class of 3D topological insulators with possibly tunable Dirac carrier properties is particularly important, since only a few topological-insulator materials have been found to date and it has been difficult to tune the carrier type of the Dirac fermions in bulk crystals.

In this Letter, we report a high-resolution ARPES study of Pb-based ternary chalcogenides  $\text{Pb}(\text{Bi}_{1-x}\text{Sb}_x)_2\text{Te}_4$ . We have experimentally established that this system constitutes a new family of 3D topological insulators, by observing a single Dirac-cone-like surface band structure at the Brillouin-zone center. We also demonstrate that the chemical potential  $\mu$  (and thus the sign of the Dirac carriers) is tunable by controlling the Bi/Sb ratio. We discuss the present ARPES results in relation to the band calculations as well as to previous ARPES studies of other topological insulators.

Single crystals of  $\text{Pb}(\text{Bi}_{1-x}\text{Sb}_x)_2\text{Te}_4$  with *x* = 0.0 and 0.4 were grown by melting stoichiometric amounts of high-purity elements (Pb 99.998%, Bi, Sb, and Te 99.9999%) in a sealed evacuated quartz tube at 900 °C for 1 d, followed by slow cooling to 500 °C in about 4 d, and then switching off the furnace. On the other hand, the *x* = 1.0 crystal is difficult to grow from the stoichiometric melt [17]; in the present work, we melted the high-purity elements Pb, Sb, and Te with the molar ratio of 2:6:11 in a sealed evacuated quartz tube at 900 °C for 1 d and then cooled it to room temperature at a rate of 48 °C per hour. The  $\text{PbSb}_2\text{Te}_4$  crystals were found at the bottom of the solidified rod and its crystal structure was confirmed by x-ray diffraction.  $\text{Pb}(\text{Bi}_{1-x}\text{Sb}_x)_2\text{Te}_4$  has a rhombohedral crystal structure with the layers stacked along the [111] direction as shown in Fig. 1(a). It consists of septuple layers where Pb atoms



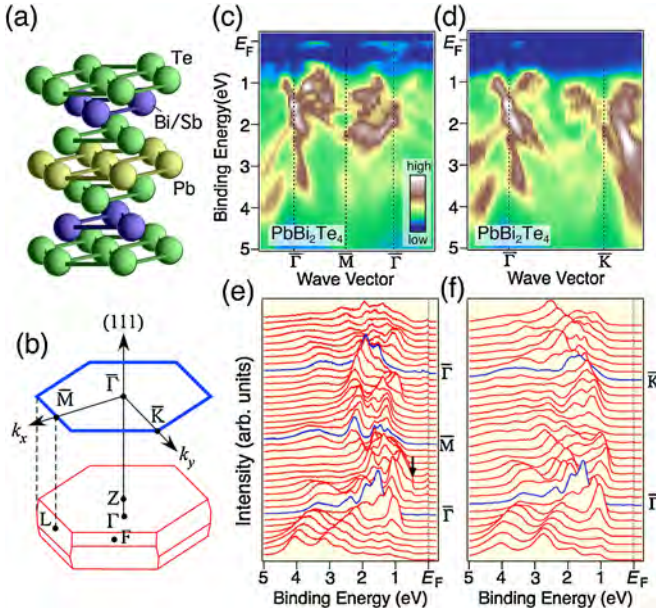


FIG. 1 (color online). (a) Crystal structure of  $\text{Pb}(\text{Bi}_{1-x}\text{Sb}_x)_2\text{Te}_4$ . (b) Bulk Brillouin zone (red thin lines) and corresponding (111) surface Brillouin zone (blue thick lines). (c),(d) ARPES intensity of  $\text{PbBi}_2\text{Te}_4$  ( $x = 0.0$ ) plotted as a function of  $E_B$  and wave vector along  $\bar{\Gamma}\bar{M}$  and  $\bar{\Gamma}\bar{K}$  high-symmetry lines, respectively, measured with  $h\nu = 80$  eV. (e), (f) Corresponding energy distribution curves of (c) and (d), respectively.

are sandwiched by Te-(Bi/Sb)-Te layers, with a real-space inversion symmetry centered at the Pb atom. Cleaving of the crystal takes place between two septuple layers which are weakly coupled by van der Waals interactions. The bulk Brillouin zone and its projected surface Brillouin zone onto the (111) plane are shown in Fig. 1(b), where the bulk Brillouin zone is shrunk along the  $[111]$  direction by  $\sim 30\%$  with respect to that of the prototypical topological insulator  $\text{Bi}_2\text{Te}_3$  owing to the longer  $c$  axis.

ARPES measurements were performed with a VG-Scienta SES2002 electron analyzer with a tunable synchrotron light at the beam line BL28A at Photon Factory (KEK). We used circularly polarized light of 36–80 eV. The energy and angular resolutions were set at 15–30 meV and  $0.2^\circ$ , respectively. Sample orientation was determined by Laue x-ray diffraction prior to the ARPES experiment. A mirrorlike (111) surface was obtained by *in situ* cleaving at  $T = 30$  K just before the measurement in an ultrahigh vacuum of  $1 \times 10^{-10}$  Torr, and kept at the same temperature during the measurement. ARPES data were obtained by rotating the sample with respect to the electron analyzer using a high-precision five-axes manipulator equipped with a liquid helium cryostat. The Fermi level ( $E_F$ ) of the samples was referenced to that of a gold film evaporated onto the sample holder. All the spectra were recorded within 12 h after cleaving, during which we did not observe any sign of degradation or contamination of the

sample surface. We have confirmed that the results are reproducible by measuring several samples.

Figures 1(c) and 1(d) show valence-band ARPES spectra of the end member  $\text{PbBi}_2\text{Te}_4$  ( $x = 0.0$ ) measured along high-symmetry lines  $\bar{\Gamma}\bar{M}$  and  $\bar{\Gamma}\bar{K}$  in the surface Brillouin zone, respectively. Corresponding energy distribution curves are also displayed in Figs. 1(e) and 1(f). We immediately notice in Figs. 1(c) and 1(d) several dispersive bands at the binding energy ( $E_B$ ) of 0.5–4.5 eV. These bands are attributed to the hybridized states of Bi/Pb 6*p* and Te 5*p* orbitals [14–16]. As seen in the energy distribution curves along the  $\bar{\Gamma}\bar{M}$  direction in Fig. 1(e), we find a holelike band with the top of dispersion slightly away from the  $\bar{\Gamma}$  point (see black arrow), which corresponds to the top of the valence band with the dominant Te 5*p* character, in agreement with the calculations which show a local maximum between  $Z$  and  $L$  points of the bulk Brillouin zone [15,16]. Such a local maximum structure is not reproduced in the calculations without including spin-orbit coupling [15], suggesting that the observed valence-band feature is a fingerprint of the strong spin-orbit coupling. One can also see in Figs. 1(c) and 1(e) a weak intensity in the vicinity of  $E_F$  in the  $k$  region between the  $\bar{\Gamma}$  and  $\bar{M}$  points, which is assigned to the bulk conduction band of the strong Bi/Pb 6*p* character that lies above  $E_F$  in the calculations [14–16]. In the present ARPES experiment, this band is shifted downward to cross  $E_F$ , possibly owing to the electron-doped nature of as-grown crystals as in the case of other 3D topological insulators [3,10–13].

Figure 2(a) displays the ARPES intensity at  $E_F$  of  $\text{PbBi}_2\text{Te}_4$  plotted as a function of 2D wave vector measured with  $h\nu = 80$  eV, which covers a wide  $\mathbf{k}$  region in the surface Brillouin zone. In both the first and second Brillouin zones, we find a circularlike Fermi surface centered at the  $\bar{\Gamma}$  point together with elongated intensity patterns extending toward the  $\bar{M}$  point. To elucidate the Fermi-surface topology and band dispersion around the  $\bar{\Gamma}$  point in more detail, we have performed ARPES measurement with higher energy resolution and finer  $\mathbf{k}$  interval with  $h\nu = 60$  eV, and the result of the Fermi-surface mapping is shown in Fig. 2(b). We also plot the band dispersions for the  $\bar{\Gamma}\bar{K}$  and  $\bar{\Gamma}\bar{M}$  directions in Figs. 2(c) and 2(d), respectively.

As clearly seen in the ARPES intensity of Fig. 2(c), we find a sharply dispersive “V”-shaped electronlike surface state (denoted SS) whose bottom is located at  $E_B \sim 0.5$  eV. A careful look at energy distribution curves in Fig. 2(e) further reveals the presence of an additional branch band showing holelike dispersion centered at the  $\bar{\Gamma}$  point (traced by dashed lines). This branch merges into the V-shaped band exactly at the  $\bar{\Gamma}$  point, satisfying the Kramers degeneracy and forming a deformed Dirac-cone dispersion as in  $\text{Bi}_2\text{Te}_3$  [10]. The surface origin of these branches was confirmed by the fact that the energy position is stationary with the variation of  $h\nu$  (not shown). Note that

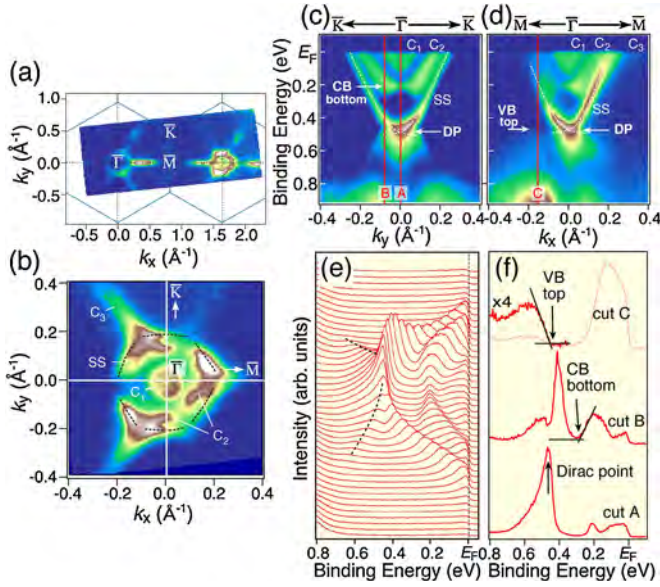


FIG. 2 (color online). (a) ARPES intensity plot at  $E_F$  of  $\text{PbBi}_2\text{Te}_4$  ( $x = 0.0$ ) as a function of 2D wave vector measured with  $h\nu = 80$  eV. (b) 2D intensity plot at  $E_F$  around the  $\bar{\Gamma}$  point measured with  $h\nu = 60$  eV. (c),(d) Near- $E_F$  ARPES intensity as a function of  $E_B$  and wave vector along  $\bar{\Gamma}\bar{K}$  and  $\bar{\Gamma}\bar{M}$  cuts, respectively [white lines in (b)]. Dashed lines are a guide for eyes to trace the surface states (SS); CB, VB, and DP stand for conduction band, valence band, and Dirac point, respectively. (e) Corresponding energy distribution curves along the  $\bar{\Gamma}\bar{K}$  direction. (f) Plot of energy distribution curves at  $\mathbf{k}$  points A–C as indicated by red lines in (c) and (d).

the energy position of other bands was also found to be insensitive to the  $h\nu$  variation in the present range of  $h\nu$ , presumably because of the quasi-two-dimensional character of electronic states due to the long  $c$  axis. Nevertheless, the observed gapless dispersion should belong to the surface states, since it does not show up in the bulk band calculations of  $\text{PbBi}_2\text{Te}_4$  [14,16].

One can also see in Figs. 2(c) and 2(d) two electronlike bands within the surface states near  $E_F$  which exhibit a parabolalike ( $C_1$ ) and “w”-shaped ( $C_2$ ) dispersions, corresponding to a small circular pocket and a larger pocket with triangularlike intensity distribution, respectively, in Fig. 2(b) [18]. Furthermore, in Figs. 2(b) and 2(d) another weak intensity ( $C_3$ ) is seen outside of the surface states which either form an elongated pocket or are connected to the  $C_2$  band along the  $\bar{\Gamma}\bar{M}$  direction, although it is hard to experimentally conclude which is the case because of the presence of multiple bands in the close vicinity of  $E_F$  as well as the possible surface resonance which smears the overall intensity distribution in this  $\mathbf{k}$  region. The  $C_1$ – $C_3$  bands are attributed to the bulk conduction band, and the bottom of the lowest-lying conduction band is located at the  $\mathbf{k}$  region where the  $C_2$  band exhibits a local minimum structure, as indicated by a red line for cut B in Fig. 2(c). Finally, in Fig. 2(d) the highest-lying bulk valence band has

its local maximum slightly away from the  $\bar{\Gamma}$  point (at cut C), suggesting an indirect nature of the bulk band gap.

We have quantitatively estimated the bulk band gap by determining the leading (trailing) edge of the valence (conduction) band, as shown by an arrow in Fig. 2(f). The energy location of the conduction-band bottom and the valence-band top are  $\sim 0.25$  and  $\sim 0.45$  eV, respectively, corresponding to the band-gap size of  $\sim 0.2$  eV, slightly larger than that of the band calculations (0.1–0.15 eV) [14–16]. Moreover, as seen in the energy distribution curve for cut A, the Dirac point (at  $E_B = 0.46$  eV) is situated at almost the same energy as the valence-band top. We have estimated the band velocity at the Dirac point,  $v_{\text{Dirac}}$ , to be  $1.0$  eV  $\text{\AA}$  along the  $\bar{\Gamma}\bar{M}$  direction, which is only about 35%–50% of the value obtained for  $\text{Bi}_2\text{Te}_3$  and  $\text{TlBiSe}_2$  (2.7 eV  $\text{\AA}$  [10] and 2.0 eV  $\text{\AA}$  [11], respectively).

We highlight in Fig. 3(a) the Fermi surface and band diagrams for the bulk and surface bands obtained from the present ARPES experiment. We recognize the complex and anisotropic nature of the conduction band, which is distinctly different from prototypical topological insulators [3,10] showing a weaker anisotropy in the conduction band, likely because of the heavily electron-doped nature of  $\text{PbBi}_2\text{Te}_4$  as apparent from the deeper energy position of the Dirac point as compared to other topological insulators [3,10–13]. To show the 2D band dispersion, we plot in

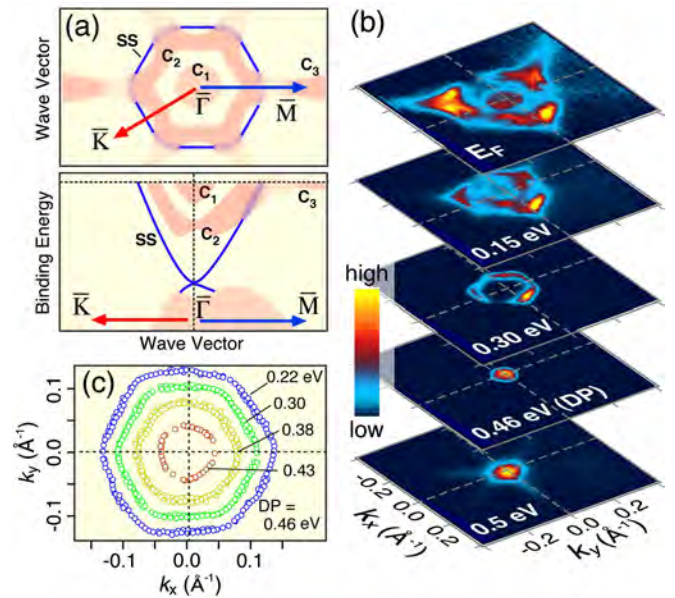


FIG. 3 (color online). (a) Schematic diagrams for (top) the Fermi surface and (bottom) the band dispersion of  $\text{PbBi}_2\text{Te}_4$  obtained from the present ARPES experiment. For the bulk conduction and valence bands, a finite  $k_z$  dispersion and momentum broadening have been taken into account. (b) ARPES intensity plots for various  $E_B$ 's between  $E_F$  and 0.5 eV. (c) Energy contour plots of the surface states for various  $E_B$ 's estimated by tracing the peak position of momentum-distribution curves.



Fig. 3(b) the ARPES intensity for  $x = 0.0$  as a function of  $k_x$  and  $k_y$  for several  $E_B$ 's. The triangular-shaped intensity pattern at  $E_F$ , which is dominated by the contribution from the  $C_2$  band, gradually diminishes upon approaching the Dirac point. At  $E_B = 0.3$  eV, we recognize a strongly deformed ringlike intensity pattern which originates from the surface states. This ringlike image shrinks and converges into a single bright spot at the Dirac point ( $E_B = 0.46$  eV), and then expands again below the Dirac point ( $E_B = 0.5$  eV), as expected from the Dirac-cone energy dispersion. At  $E_B = 0.5$  eV, we also notice an additional weak intensity extending toward the  $\bar{M}$  point, which originates from the top of the valance band as also seen in Fig. 2(d). To discuss the shape of the Dirac band in more detail, we have quantitatively estimated the  $\mathbf{k}$  location of the band crossing point in various  $E_B$  slices above the Dirac point, and a representative result is displayed in Fig. 3(c). Obviously, the contour map of the band dispersion signifies the hexagonal warping which appears to become more prominent as one moves away from the Dirac point, similarly to the case of other topological insulators [4,10,11,19].

Next we demonstrate the evolution of the electronic states upon Sb substitution for Bi in  $\text{Pb}(\text{Bi}_{1-x}\text{Sb}_x)_2\text{Te}_4$ . Figures 4(a)–4(c) display plots of near- $E_F$  ARPES intensity around the  $\bar{\Gamma}$  point as a function of  $E_B$  and  $\mathbf{k}$ , corresponding energy distribution curves, and the Fermi-surface mapping, for  $x = 0.0, 0.4$ , and  $1.0$ , respectively. The band dispersions for  $x = 0.4$  appear to be quite similar to that for  $x = 0.0$ , although the overall dispersive features are shifted upward by  $\sim 0.15$  eV. The  $C_1$  band has completely disappeared in the ARPES intensity, as one can also confirm in the absence

of the  $C_1$  pocket in Fig. 4(c). The  $C_3$  Fermi surface also vanishes at  $x = 0.4$ . At  $x = 1.0$  ( $\text{PbSb}_2\text{Te}_4$ ), on the other hand, the overall spectral feature appears to be quite different from those at  $x = 0.0$  and  $0.4$ . As seen in Fig. 4(a), we observe a holelike band with a weak intensity at  $E_B = 0-0.3$  eV, together with a less dispersive bright intensity pattern at  $\sim 0.6$  eV. The former band is assigned to the bulk valance band which is seen at  $E_B = 0.4-0.6$  eV at  $x = 0.4$ , whereas the latter band is one of the valance band which corresponds to the feature at  $\sim 1.0$  eV for  $x = 0.0$  [see Figs. 1(c)–1(f)], suggesting that the Dirac point for  $x = 1.0$  is located in the unoccupied region.

To quantitatively evaluate the evolution of the electronic states upon Sb substitution, we plot in Fig. 4(d) the band dispersions determined from the peak positions in the energy- or momentum-distribution curves. One can recognize that the energy shift of the surface states and bulk bands proceeds roughly in a rigid-band manner since the bands for different  $x$  values nearly overlap with each other when we plot their energy positions with respect to the Dirac-point energy, despite the total  $\mu$  shift of as large as 0.6 eV. Indeed, the band dispersion below  $E_F$  for  $x = 1.0$  suggests that the Dirac point is located above  $E_F$  by  $\sim 50$  meV, pointing to the sign change of Dirac carriers from  $n$  type to  $p$  type at some  $x$  between 0.4 and 1.0, in agreement with the Hall coefficient measured with our samples which exhibits a negative value at  $x = 0.0-0.4$  and a positive value at  $x = 1.0$ . The present result thus demonstrates that the substitution of Bi with Sb results in the  $\mu$  shift without significantly altering the shape of the Dirac surface state, as highlighted in the schematic band picture in Fig. 4(e).

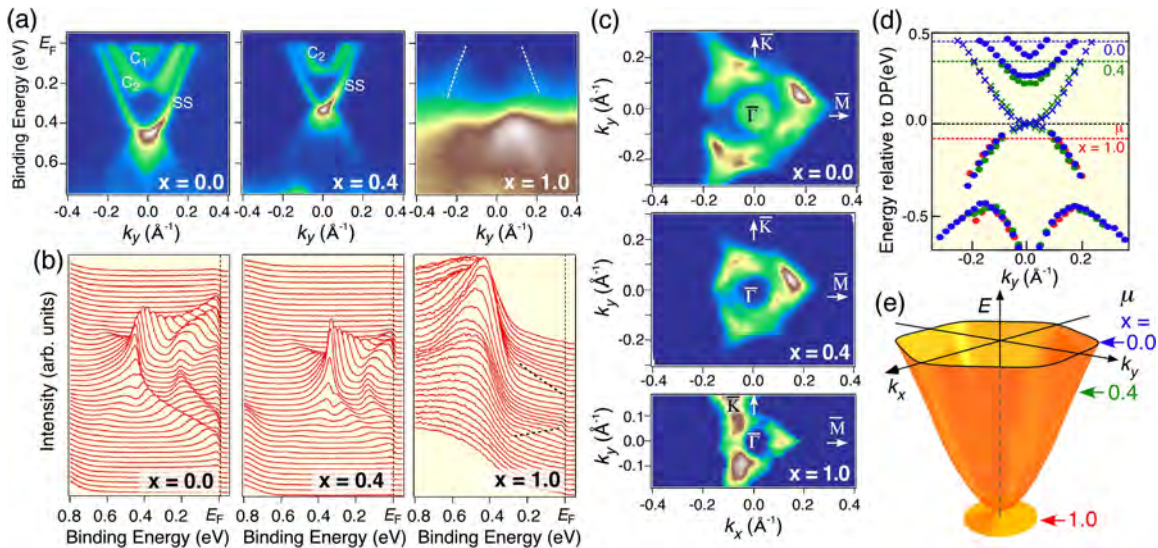


FIG. 4 (color online). (a)–(c) Comparison of (a) the near- $E_F$  band dispersions, (b) the energy distribution curves, and (c) the Fermi surface in  $\text{Pb}(\text{Bi}_{1-x}\text{Sb}_x)_2\text{Te}_4$  for three  $x$  values ( $x = 0.0, 0.4$ , and  $1.0$ ). (d) The bulk (circles) and surface (crosses) band dispersions relative to the Dirac point for the three compositions  $x = 0.0, 0.4$ , and  $1.0$ , estimated by tracing the peak positions of energy- and momentum-distribution curves. The locations of the chemical potential for the three compositions with respect to the Dirac point are shown by horizontal dashed lines. (e) Schematic 3D picture of the Dirac-band surface state and the position of  $\mu$  for each  $x$ .



The experimental realization of the sign change of Dirac carriers points to the high potential of Pb-based ternary chalcogenides for investigation of the various novel topological phenomena which requires the control of Dirac carrier conduction. It would also provide an excellent platform for the development of novel topological devices with  $p$ - $n$  junction configurations that are essential for various applications as in semiconductor technology as well as with dual-gate configuration for the electric control of spins [20]. Moreover, the observed variation in the chemical-potential value of  $\sim 0.6$  eV as achieved by the Bi/Sb replacement, which is the largest among known topological insulators, is useful for varying the Dirac carrier concentrations in a wide range, though bulk carriers coexist in most of the ranges. A next important step would be to synthesize a truly bulk insulating sample, which could be accessible by a fine control of the Bi/Sb ratio in the crystal.

In summary, we have reported the ARPES study on Pb-based ternary tellurides  $\text{Pb}(\text{Bi}_{1-x}\text{Sb}_x)_2\text{Te}_4$ . We found direct evidence for the Dirac-cone topological surface state within the indirect bulk band gap. Moreover, we have revealed a sign change of Dirac carriers from  $n$  type to  $p$  type upon variation in the Sb concentration  $x$ , demonstrating tunable Dirac carriers. The Pb-based ternary chalcogenide system is thus a promising candidate for investigating novel topological phenomena in topological insulators.

We thank Y. Tanaka, E. Ieki, K. Kosaka, K. Yoshimatsu, H. Kumigashira, and K. Ono for their assistance in ARPES measurements. This work was supported by JSPS (NEXT Program, KAKENHI 23224010, and Grant-in-Aid for

JSPS Fellows 23.4376), JST-CREST, MEXT of Japan (Innovative Area “Topological Quantum Phenomena”), AFOSR (AOARD 10-4103), and KEK-PF (Proposal No. 2010G507).

- 
- [1] M. Z. Hasan and C. L. Kane, *Rev. Mod. Phys.* **82**, 3045 (2010).
  - [2] X.-L. Qi and S.-C. Zhang, *Rev. Mod. Phys.* **83**, 1057 (2011).
  - [3] Y. Xia *et al.*, *Nature Phys.* **5**, 398 (2009).
  - [4] S. Souma *et al.*, *Phys. Rev. Lett.* **106**, 216803 (2011).
  - [5] C. L. Kane and E. J. Mele, *Science* **314**, 1692 (2006).
  - [6] L. Fu and C. L. Kane, *Phys. Rev. Lett.* **100**, 096407 (2008).
  - [7] D. Hsieh *et al.*, *Nature (London)* **452**, 970 (2008).
  - [8] D. Hsieh *et al.*, *Science* **323**, 919 (2009).
  - [9] A. Nishide *et al.*, *Phys. Rev. B* **81**, 041309(R) (2010).
  - [10] Y. L. Chen *et al.*, *Science* **325**, 178 (2009).
  - [11] T. Sato *et al.*, *Phys. Rev. Lett.* **105**, 136802 (2010).
  - [12] K. Kuroda *et al.*, *Phys. Rev. Lett.* **105**, 146801 (2010).
  - [13] Y. L. Chen *et al.*, *Phys. Rev. Lett.* **105**, 266401 (2010).
  - [14] S.-Y. Xu *et al.*, [arXiv:1007.5111](https://arxiv.org/abs/1007.5111).
  - [15] H. Jin, J. H. Song, A. J. Freeman, and M. G. Kanatzidis, *Phys. Rev. B* **83**, 041202(R) (2011).
  - [16] T. V. Menshchikova *et al.*, *JETP Lett.* **93**, 15 (2011).
  - [17] L. E. Shelimova *et al.*, *Inorg. Mater. (USSR)* **40**, 1264 (2004).
  - [18] Triangular intensity distribution is likely caused by the photoionization matrix-element effect.
  - [19] K. Kuroda *et al.*, *Phys. Rev. Lett.* **105**, 076802 (2010).
  - [20] O. V. Yazyev, J. E. Moore, and S. G. Louie, *Phys. Rev. Lett.* **105**, 266806 (2010).

# Observation of Dirac Holes and Electrons in a Topological Insulator

A. A. Taskin, Zhi Ren, Satoshi Sasaki, Kouji Segawa, and Yoichi Ando

*Institute of Scientific and Industrial Research, Osaka University, Ibaraki, Osaka 567-0047, Japan*

(Received 17 March 2011; revised manuscript received 16 May 2011; published 27 June 2011)

We show that in the new topological-insulator compound  $\text{Bi}_{1.5}\text{Sb}_{0.5}\text{Te}_{1.7}\text{Se}_{1.3}$  one can achieve a surfaced-dominated transport where the surface channel contributes up to 70% of the total conductance. Furthermore, it was found that in this material the transport properties sharply reflect the time dependence of the surface chemical potential, presenting a sign change in the Hall coefficient with time. We demonstrate that such an evolution makes us observe both Dirac holes and electrons on the surface, which allows us to reconstruct the surface band dispersion across the Dirac point.

DOI: 10.1103/PhysRevLett.107.016801

PACS numbers: 73.25.+i, 71.18.+y, 72.20.My, 73.20.At

The three-dimensional (3D) topological insulator (TI) hosts a metallic surface state that emerges due to a non-trivial  $Z_2$  topology of the bulk valence band [1,2]. This peculiar surface state offers a new playground for studying the physics of quasiparticles with unusual dispersions, such as Dirac or Majorana fermions [3,4]. However, most of the known TI materials are poor insulators in their bulk, hindering transport studies of the expected novel surface properties [3,4]. Last year, we discovered that the TI material  $\text{Bi}_2\text{Te}_2\text{Se}$  (BTS) presents a high resistivity exceeding  $1 \Omega \text{ cm}$  [5], which made it possible to clarify both the surface and bulk transport channels in detail. Also, we found that in our BTS sample the surface channel accounts for  $\sim 6\%$  of the total conductance. For this compound, Xiong *et al.* recently reported an even higher resistivity in the range of  $5\text{--}6 \Omega \text{ cm}$  [6]. Since the source of the residual bulk carriers in BTS is the acceptor states [5], reducing the number of antisite defects working as acceptors in this promising material is an important challenge for the advancement of the TI research.

In this work, we tried to optimize the composition of BTS by reducing the Te:Se ratio and introducing some Sb into Bi positions [7], while keeping the ordering of the chalcogen layers as in BTS [Fig. 1(a), [8]]. The x-ray powder diffraction patterns shown in Fig. 1(b) demonstrate that the chalcogen ordering is still present in  $\text{Bi}_{1.5}\text{Sb}_{0.5}\text{Te}_{1.7}\text{Se}_{1.3}$  (BSTS), and we focus on this compound in this Letter. We found that in BSTS one can achieve an even larger surface contribution (up to 70%) than in BTS. We also found that the surface state of BSTS changes with time, and, intriguingly, we observed quantum oscillations from Dirac holes, the negative energy state of the Dirac fermions, as well as those from Dirac electrons in the same sample at different time points. We show that this time evolution can be used to reconstruct the surface band structure across the Dirac point, providing a unique way to determine the dispersion relation of the surface state.

Single crystals of BSTS were grown by melting high-purity (99.9999%) elements of Bi, Sb, Te, and Se with a molar ratio of 1.5:0.5:1.7:1.3 at  $850^\circ\text{C}$  for 48 h in

evacuated quartz tubes, followed by cooling to room temperature over one week. For transport measurements, crystals were cut along the principal axes, and cleaved just before the measurements. Ohmic contacts were made with room-temperature cured silver paste. The resistivity  $\rho_{xx}$  and the Hall resistivity  $\rho_{yx}$  were measured simultaneously by a standard six-probe method [9] by sweeping the magnetic field  $B$  between  $\pm 14 \text{ T}$  at  $0.3 \text{ T/min}$  while stabilizing the temperature  $T$  to within  $\pm 5 \text{ mK}$ .

Freshly cleaved thin samples were used for studying the surface transport in BSTS. As shown in Fig. 1(c),  $\rho_{xx}$  in BSTS sharply increases upon lowering temperature from  $300 \text{ K}$ , which is characteristic of an insulator, but it saturates below  $\sim 100 \text{ K}$  due to the metallic surface transport

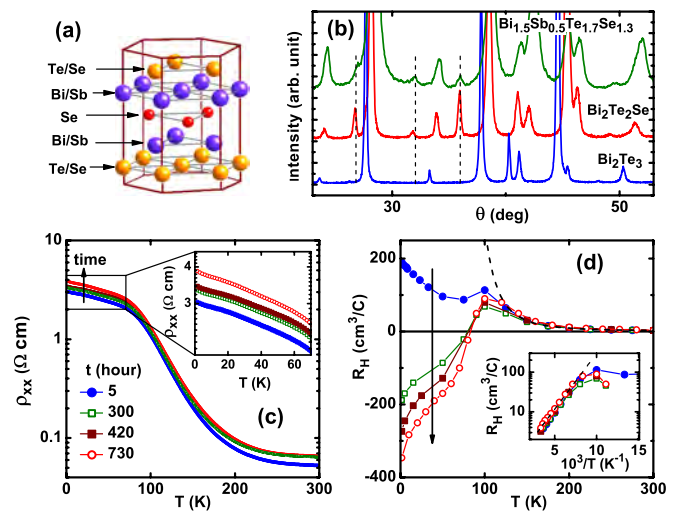


FIG. 1 (color online). (a) Basic structure unit of  $\text{Bi}_{1.5}\text{Sb}_{0.5}\text{Te}_{1.7}\text{Se}_{1.3}$  (BSTS). (b) X-ray powder diffraction patterns of BSTS,  $\text{Bi}_2\text{Te}_2\text{Se}$ , and  $\text{Bi}_2\text{Te}_3$ . Dashed lines indicate the positions of the peaks characteristic of the ordering of Se and Te (Te/Se) layers. (c)  $T$  dependence of  $\rho_{xx}$  measured repeatedly in time in a cleaved  $30\text{-}\mu\text{m}$ -thick BSTS sample. (d)  $T$  dependence of the low-field  $R_H$ , presenting a sign change with time. The dashed line represents the Arrhenius-law fitting to the data above  $150 \text{ K}$ , which is also shown in the inset.

as well as the bulk impurity-band (IB) transport [5]. This behavior is essentially the same as in BTS. What is peculiar in BSTS is that  $\rho_{xx}(T)$  increases slowly with time and, furthermore, the low-temperature Hall coefficient  $R_H$  changes sign with time in thin samples. As an example, Figs. 1(c) and 1(d) show  $\rho_{xx}(T)$  and  $R_H(T)$  data of a 30- $\mu\text{m}$ -thick BSTS sample, measured repeatedly in about one month. In contrast to the relatively small change in  $\rho_{xx}$  [Fig. 1(c)],  $R_H$  at low temperature exhibits rather drastic evolution [Fig. 1(d)] from positive to negative, whereas  $R_H$  at high temperature is essentially unchanged with time. This suggests that the source of the time dependence resides in the surface channel. In passing,  $R_H(T)$  above 150 K is positive and demonstrates an activated behavior [shown by the dashed line in Fig. 1(d)], signifying the thermal excitation of holes with an effective activation energy of  $\sim 60$  meV. This is similar to what we observed in BTS [5].

To understand the nature of the time evolution, the Shubnikov–de Haas (SdH) oscillations were measured in the aforementioned 30- $\mu\text{m}$ -thick sample twice, 5 h after cleavage (called *p* state) and 725 h later (called *n* state), between which  $R_H$  changed sign (the sample was kept at 300 K in air). In BSTS, the oscillations do not fade out even after long exposure to air, as opposed to other TI materials like Sb-doped  $\text{Bi}_2\text{Se}_3$  [10]. The SdH oscillations were clearly observed in  $\rho_{xx}(B)$  in our samples, but they were not clear in  $\rho_{yx}(B)$ , so the following SdH analysis is restricted to  $\rho_{xx}(B)$ . Figures 2(a) and 2(b) show  $\frac{d\rho_{xx}}{dB}$  for both the *p* and *n* states, plotted as a function of  $B_{\perp}^{-1} [= (B \cos\theta)^{-1}]$ , where  $\theta$  is the angle between  $B$  and the  $C_3$  axis. Several equidistant maxima and minima are easily recognized, and importantly, the positions of maxima and minima depend solely on  $B_{\perp}$ , which signifies a 2D character of the observed oscillations. Insets show the Fourier transform of the oscillations at  $\theta = 0^\circ$ . Two frequencies are clearly seen in the *p* state, but the second one (60 T) is probably a harmonic of the primary frequency  $F = 30$  T. On the other hand, only the primary  $F = 50$  T is seen in the *n* state. The averaged Fermi wave number  $k_F$  is obtained by using the Onsager relation  $F = (\hbar c / 2\pi e) \pi k_F^2$ , resulting in  $k_F$  of  $3.0 \times 10^6$  and  $3.9 \times 10^6 \text{ cm}^{-1}$  for the *p* and *n* states, respectively. This corresponds to the surface hole (electron) concentration of  $7.2 \times 10^{11}$  ( $1.2 \times 10^{12}$ )  $\text{cm}^{-2}$  for a spin-filtered surface state. Fitting the standard Lifshitz-Kosevich theory [11] to the temperature dependences of the SdH amplitudes [Figs. 2(c) and 2(d)] gives the cyclotron mass  $m_c$  of  $(0.10 \pm 0.01)m_e$  for holes and  $(0.075 \pm 0.003)m_e$  for electrons ( $m_e$  is the free electron mass). Also, from the  $B$  dependence of the SdH amplitudes [insets of Figs. 2(c) and 2(d)] one can obtain the scattering time  $\tau$  of  $5.8 \times 10^{-14}$  s ( $4.2 \times 10^{-14}$  s) for holes (electrons) through the Dingle analysis.

From the measured values of  $k_F$  and  $m_c$ , one obtains the effective Fermi velocity  $v_F^* (= \hbar k_F / m_c)$  of  $3.5 \times 10^5$  m/s

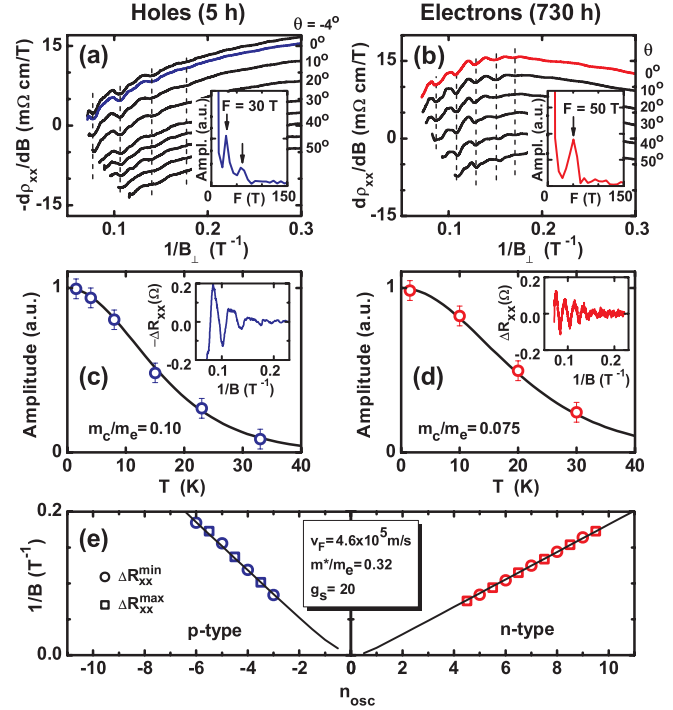


FIG. 2 (color online). (a),(b)  $\frac{d\rho_{xx}}{dB}$  vs  $B_{\perp}^{-1}$  measured in tilted magnetic fields in the *p* (5 h) and *n* (730 h) states. All curves are shifted for clarity. Insets show the Fourier transforms of the data at  $\theta = 0^\circ$ . (c),(d)  $T$  dependences of SdH amplitudes for  $\theta = 0^\circ$  shown in (a) and (b) and their theoretical fittings; insets show  $\Delta R_{xx}$  vs  $B_{\perp}^{-1}$  after subtracting a smooth background. (e) Landau-level fan diagram obtained from the oscillations in  $\Delta R_{xx}$  at 1.5 K and  $\theta = 0^\circ$ ; minima and maxima in  $\Delta R_{xx}$  correspond to  $n_{\text{osc}}$  and  $n_{\text{osc}} + \frac{1}{2}$ , respectively.

and  $6.0 \times 10^5$  m/s for holes and electrons, respectively. Now we discuss that this difference between the two  $v_F^*$  bears crucial information regarding the Dirac cone: If the surface state consists of ideal Dirac fermions, the Fermi velocity is independent of  $\mathbf{k}$  and is particle-hole symmetric. However, the energy dispersions of the surface states in Bi-based TI materials generally deviate from the ideal Dirac cone, and it can be described as [12]

$$E(k) = E_{\text{DP}} + v_F \hbar k + \frac{\hbar^2}{2m^*} k^2, \quad (1)$$

where  $E_{\text{DP}}$  is the energy at the Dirac point (DP),  $v_F$  is the Fermi velocity at the DP, and  $m^*$  is an effective mass that accounts for the curvature in  $E(k)$ . The effective Fermi velocity  $v_F^*$  reflects the local curvature in  $E(k)$  and can be expressed as  $v_F^*(k) = (\partial E / \partial k) / \hbar = v_F + \hbar k / m^*$ . The *p* and *n* states correspond to the situations where the Fermi energy  $E_F$  is below or above the DP, respectively, and the time evolution of  $R_H$  is a manifestation of the time-dependent change of the surface chemical potential. By using the  $k_F$  and  $v_F^*$  values obtained for the *p* and *n* states, we can solve simultaneous equations to obtain  $v_F = 4.6 \times 10^5$  m/s and  $m^* = 0.32m_e$ . This means that the time evolution of the transport properties allowed us to do a



“spectroscopy” of the surface state to determine its dispersion, from which we can further estimate the position of  $E_F$  to lie 80 meV below (140 meV above) the DP in the  $p$  ( $n$ ) state. Finally, the mean free path  $\ell_s = v_F^* \tau$  is about 20 nm (40 nm) and the surface mobility  $\mu_s^{\text{SDH}} = (e\ell_s)/(\hbar k_F)$  is about  $1.0 \times 10^3 \text{ cm}^2/\text{Vs}$  ( $9.8 \times 10^2 \text{ cm}^2/\text{Vs}$ ) in the  $p$  ( $n$ ) state.

To infer the Dirac nature of the surface state from the SdH oscillations [13,14], Fig. 2(e) shows the Landau-level (LL) fan diagram, which presents the values of  $B^{-1}$  at the  $n_{\text{osc}}$ th minima in the  $\rho_{xx}$  oscillations as a function of  $n_{\text{osc}}$  [14]. In the case of ideal Dirac particles, the diagram for holes (electrons) intersects the  $n_{\text{osc}}$  axis at  $-0.5$  ( $0.5$ ), reflecting the  $\pi$  Berry phase [13–15]. However, in recent SdH studies of TIs [5,6,10,16–18] exact  $\pi$  Berry phase has rarely been reported and this deviation has been a puzzle. The Zeeman coupling of the spins to the magnetic field can be a source of this discrepancy [10], and in addition, the deviation of  $E(k)$  from the ideal linear dispersion also causes the Berry phase to shift from  $\pi$  [14]. We therefore followed the scheme of Ref. [14] to see if the LL fan diagram obtained for BSTS can be understood by considering these additional factors: The solid lines in Fig. 2(e) show the theoretical LLs for the nonideal Dirac fermions [14] with the band parameters already obtained ( $v_F = 4.6 \times 10^5 \text{ m/s}$  and  $m^* = 0.32m_e$ ) and a surface  $g$  factor  $g_s = 20$  (which is the sole fitting parameter). Those lines agree reasonably well with the experimental data for both the  $p$  and  $n$  states, supporting not only the Dirac nature of the observed surface state but also the conjecture that the holes and electrons reside on the same Dirac cone.

Now we discuss the mechanism for the time evolution of the transport properties in BSTS. At low temperature, the Fermi level is pinned to the IB in the bulk [5], so the observed development most likely comes from a change in the surface as schematically shown in Figs. 3(a) and 3(b). To understand the  $p$  state where holes dominate the Hall response, one must assume that an upward band-bending occurs just after cleavage, putting the Fermi level below the DP and simultaneously creating a hole accumulation layer (AL) near the surface [Fig. 3(a)]. The air exposure apparently causes  $n$ -type doping on the surface as was reported for  $\text{Bi}_2\text{Se}_3$  [19], leading to a downward band-bending [Fig. 3(b)].

In the above picture, there must be three transport channels in the  $p$  state: surface Dirac holes, bulk IB, and the surface AL due to the band bending. Hence, one may wonder if the SdH oscillations observed in the  $p$  state might actually be due to the AL, rather than the Dirac holes. Fortunately, one can see that this is not the case, by analyzing the nonlinear  $B$  dependence of  $\rho_{yx}$ . In the following, we discuss the analyses of the  $\rho_{yx}(B)$  data, starting from the simpler case of the  $n$  state.

As in BTS [5], the  $\rho_{yx}(B)$  curves in the  $n$  state of BSTS can be well fitted with a simple two-band model described

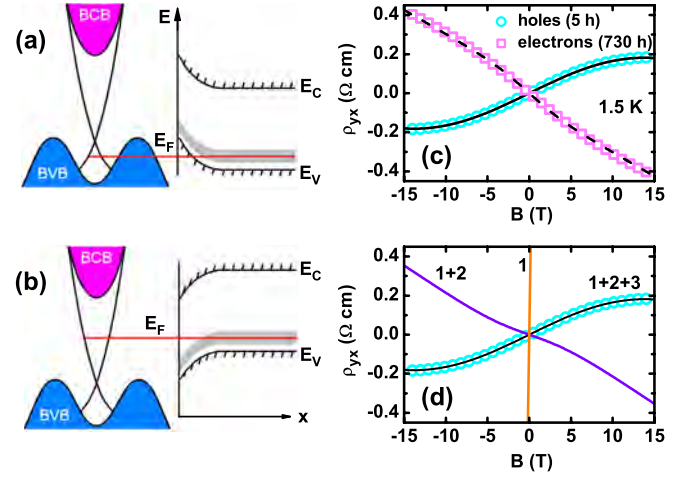


FIG. 3 (color online). (a),(b) Schematic picture of the bulk and surface states and the surface band bending for the  $p$  and  $n$  states, respectively.  $E_C$  ( $E_V$ ) is the conduction-band bottom (valence-band top); shaded band depicts the impurity band. (c)  $\rho_{yx}(B)$  data at 1.5 K in the  $p$  and  $n$  states. The dashed (solid) line is the fitting of  $\rho_{yx}(B)$  in the  $n$  state ( $p$  state) using the two-band (three-band) model. (d) Decomposition of the three-band  $\rho_{yx}(B)$  fitting in the  $p$  state (see text).

in Ref. [5]. The dashed line in Fig. 3(c) is a result of such fitting to the 1.5-K data, where the fitting parameters are the bulk electron density  $n_b = 2.3 \times 10^{16} \text{ cm}^{-3}$ , the bulk mobility  $\mu_b = 190 \text{ cm}^2/\text{Vs}$ , and the surface mobility  $\mu_s = 1250 \text{ cm}^2/\text{Vs}$  (the surface electron density was fixed at  $1.2 \times 10^{12} \text{ cm}^{-2}$  from the SdH data). These parameters give the residual bulk conductivity  $\sigma_b$  of  $0.73 \Omega^{-1} \text{ cm}^{-1}$ , and the surface contribution to the total conductance can be estimated as  $G_s/(G_s + \sigma_b t) \approx 0.1$ , where  $G_s \approx 2.4 \times 10^{-4} \Omega^{-1}$  is the sheet conductance of the surface and  $t = 30 \mu\text{m}$  is the thickness.

In the  $p$  state, the AL must also be taken into account, so we tried a three-band analysis in which we assumed that the bulk carriers are the same as in the  $n$  state. The solid line in Fig. 3(c) shows a result of the fitting to the 1.5-K data, where the fitting parameters are the AL mobility  $\mu_{s'} = 770 \text{ cm}^2/\text{Vs}$ , the AL sheet conductance  $G_{s'} = 2.2 \times 10^{-3} \Omega^{-1}$ , and the Dirac-hole mobility  $\mu_s = 1170 \text{ cm}^2/\text{Vs}$  (the Dirac-hole density was fixed at  $7.2 \times 10^{11} \text{ cm}^{-2}$  from the SdH data). To understand the relative importance of the three channels, it is instructive to examine the individual contributions to the total  $\rho_{yx}$ : as shown in Fig. 3(d), the putative  $\rho_{yx}(B)$  due solely to the surface Dirac holes (curve 1) is strongly modified when the residual bulk contribution is added (curve 1 + 2), but it is still different from the measured  $\rho_{yx}(B)$ ; only when the third contribution of the AL is added (curve 1 + 2 + 3), the  $\rho_{yx}(B)$  behavior is well reproduced.

Based on the above analysis, one can see that it is impossible to interpret the SdH oscillations in the  $p$  state to originate from the AL: if the SdH oscillations were due



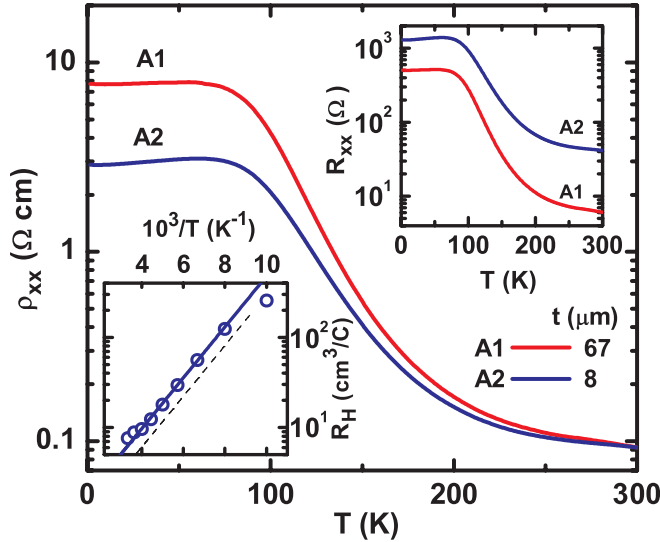


FIG. 4 (color online).  $\rho_{xx}(T)$  data of a BSTS sample in 0 T before and after reducing its thickness. Upper inset: plot of  $R_{xx}(T)$  for the same data set. Lower inset: high- $T$  activation behavior in  $R_H(T)$  for the 8- $\mu\text{m}$  sample, compared with that in the first sample [Fig. 1(d), inset] shown as a dashed line.

to the AL, the third transport channel must be the surface Dirac holes; however, the sheet carrier density  $n_{s'}$  of the third channel is estimated as  $n_{s'} = G_{s'}/(e\mu_{s'}) \approx 1.8 \times 10^{13} \text{ cm}^{-2}$ , which is too large for Dirac holes for which  $k_F \lesssim 5 \times 10^6 \text{ cm}^{-1}$  [20] and hence  $n_{s'}$  must be  $\lesssim 2 \times 10^{12} \text{ cm}^{-2}$ . Therefore, one can safely conclude that the SdH oscillations are due to the Dirac holes.

Last, we show that the surface conductance in BSTS can be estimated by simply changing the thickness. Figure 4 shows the  $\rho_{xx}(T)$  data of a different sample, measured first in 67- $\mu\text{m}$  thickness, and later cleaved to 8- $\mu\text{m}$  thick [21]. The overall behavior of  $\rho_{xx}(T)$  is similar between the two curves, but a striking difference lies in their low- $T$  saturation values  $\rho_1^{\text{sat}}$  (for 67  $\mu\text{m}$ ) and  $\rho_2^{\text{sat}}$  (for 8  $\mu\text{m}$ ): it is lower in the thinner sample, implying a larger relative surface contribution. Note that the resistance  $R_{xx}$  duly increases upon reducing the thickness, as shown in the upper inset of Fig. 4. Instructively, the difference in  $\rho_{xx}$  disappears at high  $T$  where the bulk conduction dominates. From the observed difference in  $\rho_i^{\text{sat}}$  one can estimate the surface and bulk contributions to the total conductivity by using  $\rho_i^{\text{sat}} = [(G_s/t_i) + \sigma_b]^{-1}$ . We obtain  $G_s \approx 1.8 \times 10^{-4} \Omega^{-1}$  and  $\sigma_b \approx 0.1 \Omega^{-1} \text{ cm}^{-1}$ , and this  $\sigma_b$  is much smaller than that in the 30- $\mu\text{m}$ -thick sample examined in Fig. 1. This is probably because the number of acceptors is smaller in this second sample [22], as can be inferred in the high-temperature  $R_H$  behavior [lower inset of Fig. 4]. The obtained values of  $G_s$  and  $\sigma_b$  allows us to calculate the fraction of the surface contribution to the total conductance,  $G_s/(G_s + \sigma_b t_i)$ , for the 67- and 8- $\mu\text{m}$  thick samples to be 0.2 and 0.7, respectively. Therefore, when the thickness of a BSTS sample is reduced to  $\lesssim 10 \mu\text{m}$ , one can

achieve a bulk TI crystal where the topological surface transport is dominant over the bulk transport.

In summary, we show that one can achieve a surface-dominated transport in the new TI compound  $\text{Bi}_{1.5}\text{Sb}_{0.5}\text{Te}_{1.7}\text{Se}_{1.3}$ . The surface band bending and its time dependence makes it possible to observe the SdH oscillations of both Dirac holes and electrons, with which we could determine the surface band dispersion across the Dirac point. In addition, by analyzing the nonlinear  $\rho_{yx}(B)$  curves, we could identify the role of the surface accumulation layer in the transport properties. Obviously, this material offers a well-characterized playground for studying the topological surface state.

This work was supported by JSPS (NEXT Program and KAKENHI 19674002), MEXT (Innovative Area “Topological Quantum Phenomena” KAKENHI), and AFOSR (AOARD 10-4103).

- [1] L. Fu and C.L. Kane, *Phys. Rev. B* **76**, 045302 (2007).
- [2] J.E. Moore and L. Balents, *Phys. Rev. B* **75**, 121306(R) (2007).
- [3] M.Z. Hasan and C.L. Kane, *Rev. Mod. Phys.* **82**, 3045 (2010).
- [4] X.L. Qi and S.C. Zhang, *arXiv:1008.2026v1* [Rev. Mod. Phys. (to be published)].
- [5] Z. Ren *et al.*, *Phys. Rev. B* **82**, 241306(R) (2010).
- [6] J. Xiong *et al.*, *arXiv:1101.1315*.
- [7] Since the antisite defects occur between Bi and Te, reducing the Te:Se ratio would suppress the antisite; at the same time, Se in the outermost layer is prone to vacancy creations, which is suppressed by Sb doping.
- [8] S. Nakajima, *J. Phys. Chem. Solids* **24**, 479 (1963).
- [9] The sample was suspended on gold wires in order to ensure that both surfaces were in the same condition.
- [10] J.G. Analytis *et al.*, *Nature Phys.* **6**, 960 (2010).
- [11] D. Shoenberg, *Magnetic Oscillations in Metals* (Cambridge University Press, Cambridge, 1984).
- [12] D. Culcer *et al.*, *Phys. Rev. B* **82**, 155457 (2010).
- [13] G.P. Mikitik and Yu. V. Sharlai, *Phys. Rev. Lett.* **82**, 2147 (1999).
- [14] A.A. Taskin and Y. Ando, *arXiv:1103.3096* [Phys. Rev. B (to be published)].
- [15] Y. Zhang *et al.*, *Nature (London)* **438**, 201 (2005).
- [16] D.X. Qu *et al.*, *Science* **329**, 821 (2010).
- [17] B. Sacépé *et al.*, *arXiv:1101.2352*.
- [18] C. Brüne *et al.*, *Phys. Rev. Lett.* **106**, 126803 (2011).
- [19] J.G. Analytis *et al.*, *Phys. Rev. B* **81**, 205407 (2010).
- [20] S.-Y. Xu *et al.*, *arXiv:1007.5111*; D. Hsieh *et al.*, *Nature (London)* **460**, 1101 (2009).
- [21] The cleaved 8- $\mu\text{m}$ -thick sample showed a gradual increase in  $\rho_{xx}$  similar to the 30- $\mu\text{m}$ -thick sample presented in Fig. 1, so we only used relaxed samples (in which the AL is absent) for the thickness-dependence study.
- [22] Unfortunately the SdH oscillations were not observed in this sample, probably due to a lower surface mobility.



# Optimizing $\text{Bi}_{2-x}\text{Sb}_x\text{Te}_{3-y}\text{Se}_y$ solid solutions to approach the intrinsic topological insulator regime

Zhi Ren, A. A. Taskin, Satoshi Sasaki, Kouji Segawa, and Yoichi Ando

*Institute of Scientific and Industrial Research, Osaka University, Ibaraki, Osaka 567-0047, Japan*

(Received 14 June 2011; revised manuscript received 31 August 2011; published 6 October 2011)

To optimize the bulk-insulating behavior in the topological insulator materials having a tetradymite structure, we have synthesized and have characterized single-crystal samples of  $\text{Bi}_{2-x}\text{Sb}_x\text{Te}_{3-y}\text{Se}_y$  solid solution at various compositions. We have elucidated that there are a series of intrinsic compositions where the acceptors and donors compensate each other and present a maximal bulk-insulating behavior. At such compositions, the resistivity can become as large as several  $\Omega\text{ cm}$  at low temperatures, and one can infer the role of the surface-transport channel in the nonlinear Hall effect. In particular, the composition of  $\text{Bi}_{1.5}\text{Sb}_{0.5}\text{Te}_{1.7}\text{Se}_{1.3}$  achieves the lowest bulk carrier density and appears to be best suited for surface-transport studies.

DOI: [10.1103/PhysRevB.84.165311](https://doi.org/10.1103/PhysRevB.84.165311)

PACS number(s): 73.25.+i, 74.62.Dh, 72.20.My, 73.20.At

## I. INTRODUCTION

The three-dimensional (3D) topological insulator (TI)<sup>1–5</sup> possesses spin-momentum-locked gapless surface states that are expected to host a variety of interesting quantum phenomena.<sup>6,7</sup> While a number of materials has been identified to be 3D TIs,<sup>8–18</sup> most of the known TI materials are poor insulators in the bulk, and finding ways to achieve a bulk-insulating state is an important current theme.<sup>19–25</sup> Recently, a large bulk resistivity together with clear quantum oscillations from the surface state were observed in a ternary tetradymite TI material  $\text{Bi}_2\text{Te}_2\text{Se}$  (BTS).<sup>26,27</sup> In this material, the chalcogens (Te and Se) are separated into different lattice sites, forming the ordered Te-Bi-Se-Bi-Te quintuple layers. This ordering provides a chemical environment suitable for reducing defect formations.<sup>26</sup> As a result, the chalcogen-ordered tetradymite TI is a promising material for approaching the intrinsic TI regime where the bulk carriers are negligible. Since the residual bulk carrier density in BTS was found to be on the order of  $10^{17}\text{ cm}^{-3}$ ,<sup>26</sup> it was desirable to find an appropriate route to further improve the bulk-insulating properties of the chalcogen-ordered tetradymite TI material.

In this respect, the tetradymite solid solution  $\text{Bi}_{2-x}\text{Sb}_x\text{Te}_{3-y}\text{Se}_y$  (BSTS) is interesting because it is known that some special combinations of  $x$  and  $y$  in this solid-solution system yield very low conductivity.<sup>28</sup> Except for a narrow composition region close to  $\text{Sb}_2\text{Se}_3$ , BSTS takes the same rhombohedral structure as its three end members  $\text{Bi}_2\text{Te}_3$ ,  $\text{Bi}_2\text{Se}_3$ , and  $\text{Sb}_2\text{Te}_3$ , all known to be TIs.<sup>11–14</sup> Hence, BSTS is naturally expected to be a TI as long as its structure is rhombohedral. Note that the BTS compound, where a perfect chalcogen ordering is presumably achieved, can be regarded as a member of this family ( $x = 0$ ,  $y = 1$ ).

Originally, the BSTS solid solution attracted attention because of its promising thermoelectric properties for near-room-temperature applications.<sup>29</sup> Decades of effort were devoted to optimizing the thermoelectric performance through tuning the composition and/or doping in the degenerate regime, resulting in a dimensionless figure of merit  $ZT$  ( $=S^2T/\rho\kappa$ , where  $S$  is the thermopower,  $\rho$  is the electrical resistivity, and  $\kappa$  is the thermal conductivity) close to 1. By contrast, nearly no effort was made to obtain insulating behavior in this family; nevertheless, because two prevailing types of charged defects that exist in BSTS [(Bi,Sb)/Te antisite defects and the

Se vacancy defects] introduce carriers of opposite signs, a careful tuning of  $x$  and  $y$  would, in principle, substantially cancel the bulk carriers and allow one to maximize the bulk-insulating properties. In fact, based on a systematic study of polycrystalline BSTS samples at room temperature, Teramoto and Takayanagi inferred<sup>28</sup> that a series of such intrinsic compositions exist and that the values of  $x$  and  $y$  for such compositions are linearly coupled. Unfortunately, the temperature dependence of the resistivity was not measured in their experiment, so it was not clear to what extent an insulating state was actually realized.

In the present paper, we perform a systematic study of the transport properties of the BSTS solid solution for a wide range of compositions and temperature, with the aim of maximizing the insulating property. It was found that the compositions suggested in Ref. 28 do not exactly correspond to the optimal compositions for insulating behavior. Instead, we determined a series of optimized compositions, where the relationship between  $x$  and  $y$  is obviously nonlinear. The BSTS crystals at the optimized compositions with  $0 \leq x \leq 1$  were found to present a large bulk resistivity exceeding  $1\text{ }\Omega\text{ cm}$  at low temperatures, and their transport properties at high temperatures signify the existence of a small activation gap. This result gives evidence for the existence of a series of BSTS solid solutions where the electron and hole carriers are nearly compensated. In particular, it appears that, at  $(x,y) = (0.5,1.3)$  ( $\text{Bi}_{1.5}\text{Sb}_{0.5}\text{Te}_{1.7}\text{Se}_{1.3}$ ), the compensation is maximally realized. Although the chances of observing the Shubnikov–de Haas (SdH) oscillations in BSTS samples are not very high, one can use the nonlinear Hall effect, which is always observed at low temperature, as a tool to infer the role of the surface-transport channel.

## II. EXPERIMENTAL DETAILS

The single crystals of  $\text{Bi}_{2-x}\text{Sb}_x\text{Te}_{3-y}\text{Se}_y$  were grown by melting stoichiometric amounts of high-purity elements [Bi, Sb, and Te were 6N (99.9999%), while Se was 5N (99.999%)] in sealed evacuated quartz tubes at  $850^\circ\text{C}$  for 48 h with intermittent shaking to ensure a homogeneity of the melt, followed by cooling slowly to  $550^\circ\text{C}$ , and then annealing at that temperature for 4 d. The resulting crystals have a typical domain size of up to several centimeters and are easily cleaved along the (111) plane to reveal a shiny surface. The

crystal structure of each sample was investigated by x-ray diffraction (XRD) analysis with Cu  $K\alpha$  emission, which was performed on powders obtained by crushing the crystals. Lattice parameters were refined by a least-squares fitting to the XRD data with the consideration of the zero shifts. All the samples used for transport measurements were confirmed to be single domain by using x-ray Laue analysis, and they were cut into thin bar-shaped specimens with a typical thickness of 100  $\mu\text{m}$ . The in-plane resistivity  $\rho_{xx}$  and the Hall resistivity  $\rho_{yx}$  were measured by using the standard six-probe method in a Physical Properties Measurement System (PPMS-9, Quantum Design, Inc.) down to 1.8 K, shortly after the electrical contacts were prepared by using room-temperature-cured silver paste.

### III. INTRINSIC COMPOSITIONS

Figures 1(a)–1(c) present how the compositions of the solid solution were optimized for the insulating behavior. Initially,

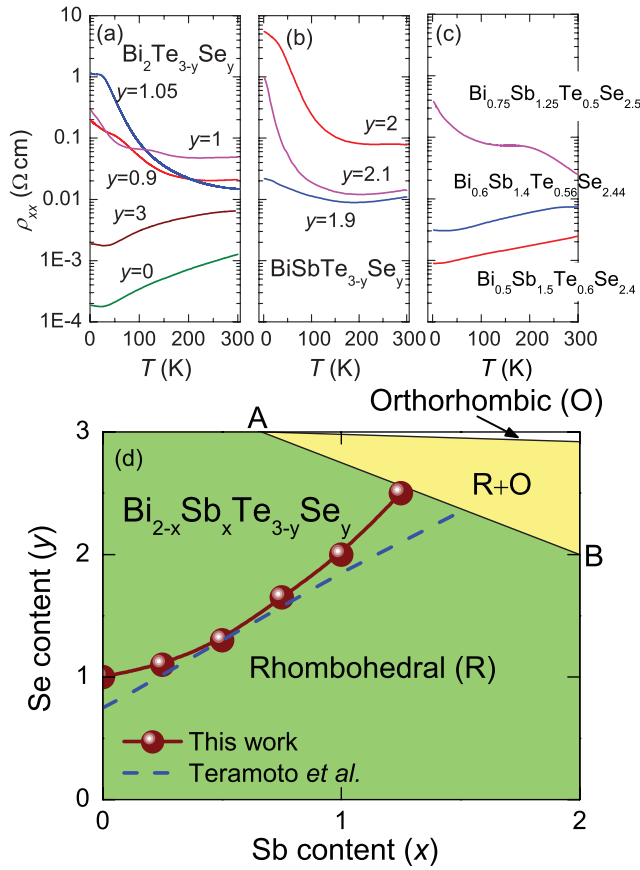


FIG. 1. (Color online) (a) and (b) Temperature dependences of  $\rho_{xx}$  for BSTS samples with fixed  $x$ 's and different  $y$ 's, showing how the compositions were optimized for the insulating behavior; panel (a) is for  $x = 0$  (Bi<sub>2</sub>Te<sub>3-y</sub>Se<sub>y</sub>) and panel (b) is for  $x = 1$  (BiSbTe<sub>3-y</sub>Se<sub>y</sub>). (c)  $\rho_{xx}(T)$  data used for optimizing the composition along the structural phase boundary [line AB in panel (d)]. (d) Composition-structure diagram of the BSTS system. The circles denote the intrinsic compositions determined in the present paper, while the dashed line denotes those suggested in Ref. 28. This diagram was determined by first fixing the Sb content  $x$  and optimizing the Se content  $y$  for that  $x$ ; the possible error in the optimized  $y$  value for a given  $x$  is the step size in the optimization process and is represented by the symbol size.

we synthesized and characterized samples for the intrinsic compositions suggested in Ref. 28. However, it turned out that, except for the  $(x, y) = (0.5, 1.3)$  case, all those samples were only poorly insulating or even metallic, with a nearly  $T$ -independent Hall coefficient signifying the existence of electron carriers with a density of  $10^{18}$ – $10^{19}\text{ cm}^{-3}$ , which indicated that there were too many Se vacancies that were not sufficiently compensated by the (Bi,Sb)/Te antisite defects. Therefore, we tried to optimize the composition by increasing the Se content  $y$  while fixing the Sb content  $x$ . The examples for  $x = 0$  and 1 are shown in Figs. 1(a) and 1(b). Also, we have performed a similar optimization along the structural phase boundary [line AB in Fig. 1(d)] in which one must simultaneously vary the values of  $x$  and  $y$ . As shown in Fig. 1(c), the composition  $(x, y) = (1.5, 2.4)$  suggested in Ref. 28 yielded only metallic samples; moving to  $(x, y) = (1.4, 2.44)$  was not sufficient, and finally, at  $(x, y) = (1.25, 2.5)$ , we found an insulating behavior.

The summary of the optimized compositions is shown in the composition-structure diagram [Fig. 1(d)] together with the linear intrinsic composition line suggested in Ref. 28. The possible errors in our experiment, which mostly come from the finite step size in the optimization process, are represented by the symbol size. Obviously, the relationship between  $x$  and  $y$  in the true intrinsic compositions is not linear but shows an upward curvature in this diagram. It should be noted that the authors of Ref. 28 used polycrystalline samples and only measured the conductivity at room temperature;<sup>28</sup> therefore, it is not surprising that the present result does not agree with their conclusion.

### IV. CRYSTAL STRUCTURE

Figure 2(a) shows the powder XRD patterns for a series of BSTS solid solutions at the optimized compositions, together with the Bi<sub>2</sub>Te<sub>3</sub> data, which are shown for comparison. The patterns for all the samples are essentially the same and can be well indexed with the rhombohedral structure (space group  $R\bar{3}m$ ), confirming that the solid solutions maintain the same crystal structure as their binary end members Bi<sub>2</sub>Te<sub>3</sub>, Bi<sub>2</sub>Se<sub>3</sub>, and Sb<sub>2</sub>Te<sub>3</sub>. The refined lattice parameters are summarized in Table I. As the system moves toward Sb<sub>2</sub>Se<sub>3</sub>, both the  $a$  and the  $c$  lattice parameters tend to decrease, which is reasonable because the ionic radius of Sb (Se) is smaller than that of Bi (Te).

It is important to note that the (107) and (0012) peaks, both of which are characteristic of the compounds with the BTS-type chalcogen ordering, are present in all BSTS samples, as can be seen in the magnified plot [Fig. 2(b)]. This indicates that the ordering of the chalcogen layers is preserved to some extent despite a large change in stoichiometry. To understand this observation, it is useful to recall the structure of the tetradymite, which is composed of stacked  $A_2^V B_3^{VI}$  ( $A^V = \text{Bi, Sb}; B^{VI} = \text{Te, Se}$ ) quintuple layers. Within the quintuple layer, the atoms are arranged in the sequence of  $B^{VI}(1) - A^V - B^{VI}(2) - A^V - B^{VI}(1)$ , where  $B^{VI}(1)$  and  $B^{VI}(2)$  are two inequivalent crystallographic sites. Because Se has a larger electronegativity than Te, the Se atoms preferentially occupy the  $B^{VI}(2)$  site and the remaining  $(y - 1)\text{Se} + (3 - y)\text{Te}$  atoms are distributed randomly in the  $B^{VI}(1)$  site when  $y$  is larger

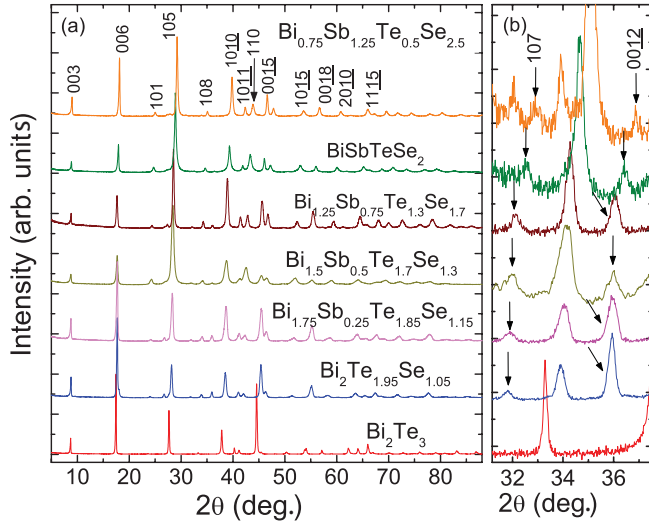


FIG. 2. (Color online) (a) Power XRD patterns for a series of BSTS samples at optimized compositions. The pattern for  $\text{Bi}_2\text{Te}_3$  is also shown for comparison. All diffraction peaks can be indexed based on the rhombohedral structure with the  $R\bar{3}m$  space group. (b) An enlarged view of the data near the (108) peak. Arrows mark the (107) and (0012) peaks related to the ordering of the chalcogen layers.

than 1.<sup>30</sup> Such an asymmetric arrangement of the chalcogen layers bears a similarity to that in BTS and accounts for the XRD results.

## V. RESISTIVITY

Figure 3(a) shows the typical temperature dependences of  $\rho_{xx}$  for the optimized compositions. It should be noted that the  $\rho_{xx}$  value was found to be sample dependent and could vary by a factor of 3 within the same composition, probably due to different levels of defect concentrations. Nevertheless, the activated behavior was essentially reproducible within the same batch, and the variation in terms of the activation energy was about 10%. The magnitude of  $\rho_{xx}$  at room temperature in Fig. 3(a) ranges from 25 to 140 m $\Omega$  cm, which is generally larger than that found in BTS.<sup>26</sup> Except for the  $(x,y) = (1.25,2.5)$  composition, which has the largest Se

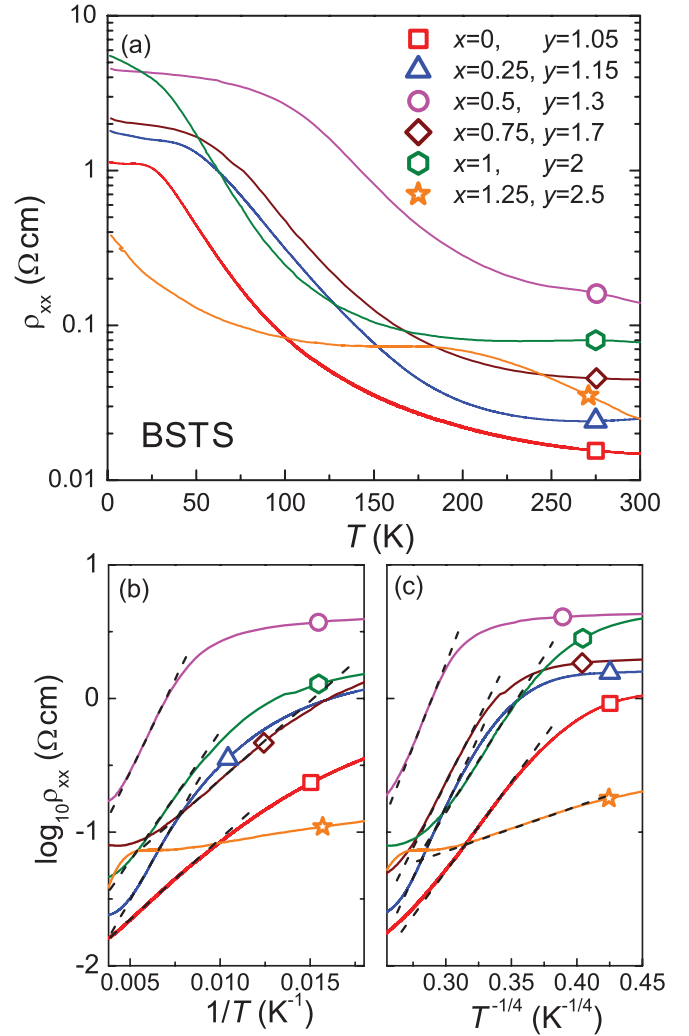


FIG. 3. (Color online) (a) Temperature dependences of  $\rho_{xx}$  for a series of BSTS samples at optimized compositions. Note that the vertical axis is in the logarithmic scale. (b) and (c) are the Arrhenius plot [ $\log_{10} \rho_{xx}$  vs  $1/T$ ] and the 3D-variable-range-hopping (VRH) plot [ $\log_{10} \rho_{xx}$  vs  $T^{-1/4}$ ] of the  $\rho_{xx}(T)$  data, respectively. Dashed lines represent linear fittings to the regions where the activation and the VRH behaviors can be recognized.

content, the overall temperature dependence of  $\rho_{xx}$  is similar and can be divided into three regimes:

TABLE I. Important parameters obtained for the optimized compositions.  $\Delta$  and  $\Delta^*$  are the thermal activation energies determined from the temperature dependences of  $\rho_{xx}$  and  $R_H$ , respectively. The effective acceptor concentration  $N_A^{\text{eff}}$  is estimated from the relation  $R_H^{-1} \approx e\sqrt{N_A^{\text{eff}} N_V} \exp(-\Delta^*/k_B T)$ , where  $N_V = 5.2 \times 10^{18} \text{ cm}^{-3}$  (Ref. 26) was assumed. Note that, among the samples with the same composition,  $\Delta$  and  $\Delta^*$  vary by  $\sim 10\%$ , and  $N_A^{\text{eff}}$  could vary by a factor of 3, probably due to different levels of defect concentrations.

Composition	$a$ (Å)	$c$ (Å)	$\rho_{xx}^{300 \text{ K}}$ (m $\Omega$ cm)	$\rho_{xx}^{1.8 \text{ K}}$ ( $\Omega$ cm)	$R_H^{300 \text{ K}}$ (cm <sup>3</sup> /C)	$R_H^{1.8 \text{ K}}$ (cm <sup>3</sup> /C)	$\Delta$ (meV)	$\Delta^*$ (meV)	$N_A^{\text{eff}}$ (cm <sup>-3</sup> )
$\text{Bi}_2\text{Te}_{1.95}\text{Se}_{1.05}$	4.28	29.86	14	1.1	2.6	-200	22	33	$9 \times 10^{18}$
$\text{Bi}_{1.75}\text{Sb}_{0.25}\text{Te}_{1.85}\text{Se}_{1.15}$	4.26	29.84	25	2.1	2.3	-610	43	60	$5 \times 10^{19}$
$\text{Bi}_{1.5}\text{Sb}_{0.5}\text{Te}_{1.7}\text{Se}_{1.3}$	4.24	29.83	140	4.5	2.7	-910	53	65	$6 \times 10^{19}$
$\text{Bi}_{1.25}\text{Sb}_{0.75}\text{Te}_{1.3}\text{Se}_{1.7}$	4.20	29.58	44	2.2	2.7	-370	38	48	$2 \times 10^{19}$
$\text{BiSbTeSe}_2$	4.16	29.41	77	5.5	2.4	802	30	22	$1 \times 10^{18}$
$\text{Bi}_{0.75}\text{Sb}_{1.25}\text{Te}_{0.5}\text{Se}_{2.5}$	4.12	29.16	25	0.38	-10.6	207			



(i) *Activated regime.* In the temperature range above  $\sim 100$  K, the  $\rho_{xx}(T)$  data can be fitted with the Arrhenius law,

$$\rho_{xx} \sim \exp(\Delta/k_B T), \quad (1)$$

where  $\Delta$  is the activation energy and  $k_B$  is the Boltzmann constant. In Fig. 3(b), we show the Arrhenius plot of the data together with linear fittings to obtain  $\Delta$ . The  $\Delta$  values are summarized in Table I, and they vary from 22 to 53 meV; however, since the temperature range of this activated behavior is not very wide, the obtained  $\Delta$  should not be taken too literally.

(ii) *Variable-range hopping (VRH) regime.* Below the temperature range of the activated behavior mentioned above, the  $\rho_{xx}(T)$  appears to be better described by the 3D-VRH behavior,

$$\rho_{xx} \sim \exp[(T/T_0)^{-1/4}], \quad (2)$$

where  $T_0$  is a constant that depends on the density of states at the Fermi level  $E_F$ . For example, in the data for  $\text{Bi}_2\text{Te}_{1.95}\text{Se}_{1.05}$  (marked by squares in Fig. 3), the VRH behavior holds for 60–140 K, while the activated behavior holds for 110–300 K. However, it should be noted that the temperature range where this VRH behavior appears to hold can have a significant overlap with the activated temperature range. For example, in the case of  $\text{Bi}_{1.25}\text{Sb}_{0.75}\text{Te}_{1.3}\text{Se}_{1.7}$  (marked by diamonds in Fig. 3) where the distinction is the most ambiguous, the activation behavior and the VRH behavior appear to hold in similar ranges, 85–140 and 90–170 K, respectively. Hence, the distinction between the two transport mechanisms can be a subtle issue, and it probably depends on the level of disorder in the sample.

(iii) *Saturation regime.* At low temperatures,  $\rho_{xx}$  tends to saturate, rather than to diverge as expected for intrinsic semiconductors, implying the existence of some extended states at  $E_F$  in the zero-temperature limit. In this regime, the magnetic-field dependence of the Hall resistivity  $\rho_{yx}$  is generally nonlinear (as will be described in detail later), which points to the existence of two or more transport channels. In the BTS compound, it was elucidated<sup>26</sup> that the topological surface state and a degenerate bulk impurity band both contribute to the low-temperature saturated resistivity. In addition, our recent study of the  $\text{Bi}_{1.5}\text{Sb}_{0.5}\text{Te}_{1.7}\text{Se}_{1.3}$  compound has identified<sup>31</sup> the third contribution of the accumulation layer (which is caused by the surface band bending and is topologically trivial) in samples where the Hall coefficient is positive at low temperatures.

## VI. HALL COEFFICIENT

To further characterize the transport properties, we have performed the Hall measurements. Figure 4(a) shows the temperature dependences of the low-field Hall coefficient  $R_H$ , defined as  $R_H = \rho_{yx}/B$  near  $B = 0$ , for the same series of samples. Above  $\sim 150$  K,  $\rho_{yx}$  is always linear in  $B$  so that  $\rho_{yx}/B$  is magnetic-field independent, and the resulting  $R_H$  is positive and shows a thermal-activation behavior in all the BSTS samples except  $\text{Bi}_{0.75}\text{Sb}_{1.25}\text{Te}_{0.5}\text{Se}_{2.5}$ . The positive and activated  $R_H(T)$  behavior indicates that the dominant charge carriers are thermally excited holes in the bulk valence band. By contrast, the high-temperature  $R_H$  in  $\text{Bi}_{0.75}\text{Sb}_{1.25}\text{Te}_{0.5}\text{Se}_{2.5}$

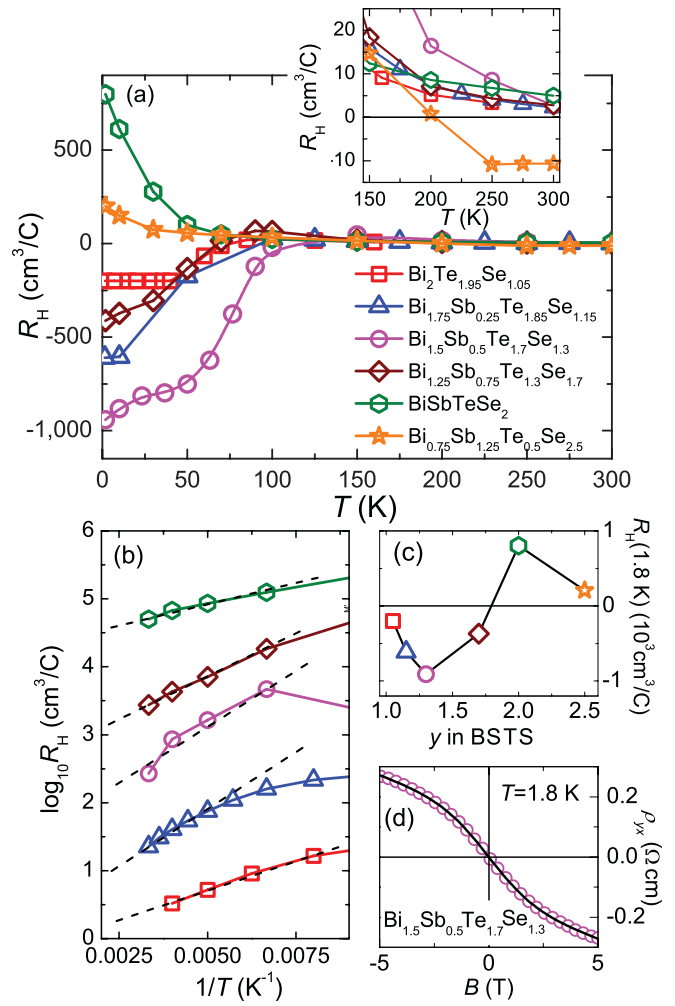


FIG. 4. (Color online) (a) Temperature dependences of the low-field Hall coefficient  $R_H$  for a series of BSTS samples at optimized compositions. The inset shows an enlarged view of the data between 150 and 300 K. (b) Arrhenius plot of  $R_H(T)$  at high temperatures for a series of samples except  $\text{Bi}_{0.75}\text{Sb}_{1.25}\text{Te}_{0.5}\text{Se}_{2.5}$  where the activation behavior was not clearly observed; the data are shifted vertically for clarity. Dashed lines are the Arrhenius-law fittings to extract the activation energy  $\Delta^*$ . (c) The value of  $R_H$  at 1.8 K plotted as a function of the Se content  $y$ . (d) Magnetic-field dependence of  $\rho_{yx}$  for the  $\text{Bi}_{1.5}\text{Sb}_{0.5}\text{Te}_{1.7}\text{Se}_{1.3}$  sample at 1.8 K; the solid line is a two-band-model fitting (Ref. 26) to the data. The obtained fitting parameters give a surface conductance of  $1.4 \times 10^{-4} \Omega^{-1}$  and a bulk conductivity of  $0.21 \Omega^{-1} \text{ cm}^{-1}$ ; since the measured sample was  $120\text{-}\mu\text{m}$  thick, the surface contribution was 5% of the total conductance.

is negative and only weakly dependent on temperature, which indicates that the electron carriers created by Se vacancies in this compound are degenerate near room temperature. Thus, the sign change in the high-temperature  $R_H$  at the largest Se content  $y$  in our series of samples reflects a change in the dominant defects from the Bi(Sb)/Te antisites (acceptors) to the Se vacancies (donors). Note that, in those samples, both acceptors and donors are expected to exist, and the observed charge-carrier concentration is likely to be determined by their competition.

From the Arrhenius plot of  $R_H(T)$  [Fig. 4(b)], one obtains the effective acceptor concentration  $N_A^{\text{eff}}$  together with the effective activation energy  $\Delta^*$ , both are summarized in Table I. It should be noted that, among the samples with the same composition, the variation in  $\Delta^*$  was within  $\sim 10\%$ , while  $N_A^{\text{eff}}$  could vary up to a factor of 3, reflecting the variation in the resistivity behavior within the same batch mentioned in Sec. V. One can see that the  $\Delta^*$  values are not much different from the  $\Delta$  values derived from the  $\rho_{xx}(T)$  data for the same samples, and the difference is less than 30%. This small difference can probably be ascribed to the temperature dependence of the mobility. Intriguingly,  $N_A^{\text{eff}}$  and  $\Delta^*$  seem to be correlated; namely, larger  $N_A^{\text{eff}}$  is accompanied by larger  $\Delta^*$ . However, the origin of this behavior is not clear at the moment.

At lower temperatures below 100 K,  $\rho_{yx}(B)$  is no longer a linear function of  $B$ , and  $R_H$  becomes very much dependent on composition. Figure 4(c) shows this variation in terms of the  $R_H$  value at 1.8 K plotted vs  $y$ .<sup>32</sup> The largest  $|R_H|$  was observed in  $\text{Bi}_{1.5}\text{Sb}_{0.5}\text{Te}_{1.7}\text{Se}_{1.3}$ , where  $R_H = -910 \text{ cm}^3/\text{C}$  at 1.8 K. This value could naively correspond to a very low carrier density of  $7 \times 10^{15} \text{ cm}^{-3}$ ; however, as we have demonstrated for BTS,<sup>26</sup> such a naive estimate based on the low-field  $R_H$  is not reliable when there are multiple transport channels that cause  $\rho_{yx}(B)$  to become nonlinear. Indeed,  $\rho_{yx}(B)$  was found to be nonlinear in  $\text{Bi}_{1.5}\text{Sb}_{0.5}\text{Te}_{1.7}\text{Se}_{1.3}$  [Fig. 4(d)], and an accurate estimate of the bulk and surface carrier densities is difficult without employing additional information from SdH oscillations.<sup>26,33</sup> Nevertheless, by using the simple two-band model to consider both the bulk and the surface-transport channels<sup>26</sup> [note that the accumulation layer<sup>31</sup> is irrelevant here since the slope of  $\rho_{yx}(B)$  is negative], one can make a reasonable fitting to the data [solid line in Fig. 4(d)], which yields the bulk carrier density  $1.8 \times 10^{16} \text{ cm}^{-3}$ , the bulk mobility  $73 \text{ cm}^2 \text{ V}^{-1} \text{ s}^{-1}$ , the surface carrier density  $1.5 \times 10^{11} \text{ cm}^{-2}$ , and the surface mobility  $2900 \text{ cm}^2 \text{ V}^{-1} \text{ s}^{-1}$ . (In the fitting procedure, the parameters were constrained by the measured  $\rho_{xx}$  value in 0 T.) Based on this fitting result, one can estimate the contribution of the surface transport to the total conductance to be  $\sim 5\%$ , which is reasonably large considering the thickness (120  $\mu\text{m}$ ) of the measured sample.

## VII. DISCUSSIONS

For the transport studies of the topological surface states, it is desirable that their SdH oscillations be observed. In the present series of BSTS samples, we did not observe clear SdH oscillations below 9 T. Most likely, whether the SdH oscillations can be observed depends crucially on the homogeneity and the value of the surface carrier density  $n_s$ ,<sup>34</sup> which may vary between samples and, even in the same single crystal, between different cleaves. The chances of observing the SdH oscillations were roughly 10% in our BSTS samples. On such lucky occasions, we were able to see both Dirac holes and electrons on the surface of  $\text{Bi}_{1.5}\text{Sb}_{0.5}\text{Te}_{1.7}\text{Se}_{1.3}$  samples, and the result was reported in Ref. 31. It should be emphasized, however, that, even though SdH oscillations are not always observed, one can achieve a surface-dominated transport by making sufficiently thin samples of BSTS.<sup>31</sup>

As we have already discussed in Sec. VI, the low-field  $R_H$  value in BSTS does not simply reflect the bulk carrier density, but it is also influenced by the contribution of the surface carriers, which presumably have a higher mobility than the bulk carriers. In view of this situation, the nontrivial composition dependence of  $R_H$  observed at 1.8 K [Fig. 4(c)] can be interpreted in two ways: One possibility is that it may signify the sign change in the surface carriers as the Se concentration  $y$  is increased. This is possible because the surface band structure of BTS is similar<sup>18</sup> to that of  $\text{Bi}_2\text{Te}_3$  where the Dirac point is located below the top of the valence band,<sup>13</sup> whereas, with increasing  $y$ , the surface band structure is expected to approach that of  $\text{Bi}_2\text{Se}_3$  where the Dirac point is isolated in the bulk gap;<sup>12</sup> therefore, if the chemical potential is pinned to the impurity band located just above the bulk valence band,<sup>26</sup> the nature of the surface carriers could change from Dirac electrons to Dirac holes. The other possibility is that the change in  $R_H$  is a reflection of the change in the nature of the degenerate bulk carriers in the impurity band. This is also possible because, at low  $y$ , the chemical potential is likely to be located below the center of the acceptor impurity band, whereas, with increasing  $y$ , the increasing amount of donors (due to Se vacancies) would cause the acceptor impurity band to be gradually filled and move the chemical potential to above the center of the impurity band. To further address this issue, systematic studies employing the SdH oscillations would be necessary.

## VIII. CONCLUSION

In this paper, in the BSTS solid solution, we have elucidated the existence of the intrinsic compositions where the acceptors due to the (Bi,Sb)/Te antisite defects and the donors due to the Se vacancy defects compensate each other and realize a maximally bulk-insulating state. The powder XRD patterns suggest that, at those compositions optimized for the insulating behavior, the crystal structure has an ordering of chalcogen layers in which the Se atoms preferentially occupy the middle of the quintuple layer and the remaining Se and Te atoms randomly occupy the outermost layers. Except for  $\text{Bi}_{0.75}\text{Sb}_{1.25}\text{Te}_{0.5}\text{Se}_{2.5}$ , which is close to the structural instability, all the BSTS samples at the optimized compositions show large  $\rho_{xx}$  values exceeding  $1 \text{ } \Omega \text{ cm}$  at low temperatures together with an activated behavior at high temperatures signifying the existence of an activation gap for the bulk carriers. The  $B$  dependence of  $\rho_{yx}$  at low temperatures points to the role of the surface-transport channel, and the nontrivial composition dependence of the low-field  $R_H$  reflects either the change in the surface band structure or the change in the bulk carriers in the impurity band. The  $|R_H|$  value at 1.8 K was found to be the largest in  $\text{Bi}_{1.5}\text{Sb}_{0.5}\text{Te}_{1.7}\text{Se}_{1.3}$ , and this composition appears to have achieved the lowest bulk carrier density.

## ACKNOWLEDGMENTS

This work was supported by JSPS (NEXT Program), MEXT (Innovative Area “Topological Quantum Phenomena” KAKENHI Grant No. 22103004), and AFOSR (AOARD Grant No. 10-4103).

- <sup>1</sup>L. Fu, C. L. Kane, and E. J. Mele, *Phys. Rev. Lett.* **98**, 106803 (2007).
- <sup>2</sup>J. E. Moore and L. Balents, *Phys. Rev. B* **75**, 121306(R) (2007).
- <sup>3</sup>R. Roy, *Phys. Rev. B* **79**, 195322 (2009).
- <sup>4</sup>L. Fu and C. L. Kane, *Phys. Rev. B* **76**, 045302 (2007).
- <sup>5</sup>X.-L. Qi, T. L. Hughes, and S.-C. Zhang, *Phys. Rev. B* **78**, 195424 (2008).
- <sup>6</sup>M. Z. Hasan and C. L. Kane, *Rev. Mod. Phys.* **82**, 3045 (2010).
- <sup>7</sup>X. L. Qi and S. C. Zhang, *Rev. Mod. Phys.* (to be published).
- <sup>8</sup>D. Hsieh, D. Qian, L. Wray, Y. Xia, Y. S. Hor, R. J. Cava, and M. Z. Hasan, *Nature (London)* **452**, 970 (2008).
- <sup>9</sup>A. A. Taskin and Y. Ando, *Phys. Rev. B* **80**, 085303 (2009).
- <sup>10</sup>A. Nishide, A. A. Taskin, Y. Takeichi, T. Okuda, A. Kakizaki, T. Hirahara, K. Nakatsuji, F. Komori, Y. Ando, and I. Matsuda, *Phys. Rev. B* **81**, 041309(R) (2010).
- <sup>11</sup>H.-J. Zhang, C.-X. Liu, X.-L. Qi, X. Dai, Z. Fang, and S.-C. Zhang, *Nat. Phys.* **5**, 438 (2009).
- <sup>12</sup>Y. Xia, D. Qian, D. Hsieh, L. Wray, A. Pal, H. Lin, A. Bansil, D. Grauer, Y. S. Hor, R. J. Cava, and M. Z. Hasan, *Nat. Phys.* **5**, 398 (2009).
- <sup>13</sup>Y. L. Chen, J. G. Analytis, J.-H. Chu, Z. K. Liu, S.-K. Mo, X. L. Qi, H. J. Zhang, D. H. Lu, X. Dai, Z. Fang, S. C. Zhang, I. R. Fisher, Z. Hussain, and Z.-X. Shen, *Science* **325**, 178 (2009).
- <sup>14</sup>D. Hsieh, Y. Xia, D. Qian, L. Wray, F. Meier, J. H. Dil, J. Osterwalder, L. Patthey, A. V. Fedorov, H. Lin, A. Bansil, D. Grauer, Y. S. Hor, R. J. Cava, and M. Z. Hasan, *Phys. Rev. Lett.* **103**, 146401 (2009).
- <sup>15</sup>T. Sato, K. Segawa, H. Guo, K. Sugawara, S. Souma, T. Takahashi, and Y. Ando, *Phys. Rev. Lett.* **105**, 136802 (2010).
- <sup>16</sup>K. Kuroda, M. Ye, A. Kimura, S. V. Eremeev, E. E. Krasovskii, E. V. Chulkov, Y. Ueda, K. Miyamoto, T. Okuda, K. Shimada, H. Namatame, and M. Taniguchi, *Phys. Rev. Lett.* **105**, 146801 (2010).
- <sup>17</sup>Y. L. Chen, Z. K. Liu, J. G. Analytis, J.-H. Chu, H. J. Zhang, B. H. Yan, S.-K. Mo, R. G. Moore, D. H. Lu, I. R. Fisher, S.-C. Zhang, Z. Hussain, and Z.-X. Shen, *Phys. Rev. Lett.* **105**, 266401 (2010).
- <sup>18</sup>S. Y. Xu, L. A. Wray, Y. Xia, R. Shankar, A. Petersen, A. Fedorov, H. Lin, A. Bansil, Y. S. Hor, D. Grauer, R. J. Cava, and M. Z. Hasan, e-print arXiv:1007.5111.
- <sup>19</sup>D.-X. Qu, Y. S. Hor, J. Xiong, R. J. Cava, and N. P. Ong, *Science* **329**, 821 (2010).
- <sup>20</sup>J. G. Analytis, R. D. McDonald, S. C. Riggs, J.-H. Chu, G. S. Boebinger, and I. R. Fisher, *Nat. Phys.* **10**, 960 (2010).
- <sup>21</sup>J. G. Checkelsky, Y. S. Hor, M.-H. Liu, D.-X. Qu, R. J. Cava, and N. P. Ong, *Phys. Rev. Lett.* **103**, 246601 (2009).
- <sup>22</sup>N. P. Butch, K. Kirshenbaum, P. Syers, A. B. Sushkov, G. S. Jenkins, H. D. Drew, and J. Paglione, *Phys. Rev. B* **81**, 241301 (2010).
- <sup>23</sup>J. G. Analytis, J. H. Chu, Y. Chen, F. Corredor, R. D. McDonald, Z. X. Shen, and I. R. Fisher, *Phys. Rev. B* **81**, 205407 (2010).
- <sup>24</sup>K. Eto, Z. Ren, A. A. Taskin, K. Segawa, and Y. Ando, *Phys. Rev. B* **81**, 195309 (2010).
- <sup>25</sup>Z. Ren, A. A. Taskin, S. Sasaki, K. Segawa, and Y. Ando, *Phys. Rev. B* **84**, 075316 (2011).
- <sup>26</sup>Z. Ren, A. A. Taskin, S. Sasaki, K. Segawa, and Y. Ando, *Phys. Rev. B* **82**, 241306(R) (2010).
- <sup>27</sup>J. Xiong, A. C. Petersen, D. X. Qu, R. J. Cava, and N. P. Ong, e-print arXiv:1101.1315.
- <sup>28</sup>I. Teramoto and S. Takayanagi, *J. Phys. Chem. Solids* **19**, 124 (1961).
- <sup>29</sup>L. R. Testardi, J. N. Bierly, Jr., and F. J. Donahoe, *J. Phys. Chem. Solids* **23**, 1209 (1962); C. H. Champness, P. T. Chiang, and P. Parekh, *Can. J. Phys.* **43**, 653 (1965); H. W. Jeon, H. P. Ha, D. B. Hyun, and J. D. Shim, *J. Phys. Chem. Solids* **52**, 579 (1991).
- <sup>30</sup>S. Nakajima, *J. Phys. Chem. Solids* **24**, 479 (1963).
- <sup>31</sup>A. A. Taskin, Z. Ren, S. Sasaki, K. Segawa, and Y. Ando, *Phys. Rev. Lett.* **107**, 016801 (2011).
- <sup>32</sup>In our recent study of  $\text{Bi}_{1.5}\text{Sb}_{0.5}\text{Te}_{1.7}\text{Se}_{1.3}$ , we observed that, in very thin samples, the low-temperature  $R_H$  can be positive immediately after the cleavage, and it changes sign with time (Ref. 31). All the samples measured in the present paper were relatively thick ( $\sim 100\ \mu\text{m}$ ) and did not show clear time evolution in  $R_H$ .
- <sup>33</sup>A. A. Taskin, K. Segawa, and Y. Ando, *Phys. Rev. B* **82**, 121302(R) (2010).
- <sup>34</sup>When  $n_s$  is inhomogeneous, the SdH oscillation frequency varies across the sample, and the oscillations are smeared; also, when  $n_s$  is too small, the SdH oscillation frequency becomes too low to be detected in our limited magnetic-field range.



# Fermi level tuning and a large activation gap achieved in the topological insulator $\text{Bi}_2\text{Te}_2\text{Se}$ by Sn doping

Zhi Ren, A. A. Taskin, Satoshi Sasaki, Kouji Segawa, and Yoichi Ando\*

*Institute of Scientific and Industrial Research, Osaka University, Ibaraki, Osaka 567-0047, Japan*

(Received 20 February 2012; published 3 April 2012)

We report the effect of Sn doping on the transport properties of the topological insulator  $\text{Bi}_2\text{Te}_2\text{Se}$  studied in a series of  $\text{Bi}_{2-x}\text{Sn}_x\text{Te}_2\text{Se}$  crystals with  $0 \leq x \leq 0.02$ . The undoped stoichiometric compound ( $x = 0$ ) shows an  $n$ -type metallic behavior with its Fermi level pinned to the conduction band. In the doped compound, it is found that Sn acts as an acceptor and leads to a downshift of the Fermi level. For  $x \geq 0.004$ , the Fermi level is lowered into the bulk forbidden gap and the crystals present a resistivity considerably larger than  $1 \Omega \text{ cm}$  at low temperatures. In those crystals, the high-temperature transport properties are essentially governed by thermally activated carriers whose activation energy is 95–125 meV, which probably signifies the formation of a Sn-related impurity band. In addition, the surface conductance directly obtained from the Shubnikov–de Haas oscillations indicates that a surface-dominated transport can be achieved in samples with several  $\mu\text{m}$  thickness.

DOI: [10.1103/PhysRevB.85.155301](https://doi.org/10.1103/PhysRevB.85.155301)

PACS number(s): 73.25.+i, 74.62.Dh, 72.20.My, 73.20.At

## I. INTRODUCTION

In a three-dimensional (3D) topological insulator (TI), a band inversion due to strong spin-orbit coupling induces gapless surface states (SSs) consisting of spin helical Dirac fermions,<sup>1–5</sup> which are expected to give rise to a number of topological quantum phenomena.<sup>6,7</sup> Whereas such surface-sensitive probes as angle-resolved photoemission spectroscopy (ARPES) and scanning tunneling microscopy have been successfully applied to investigate the topological SSs,<sup>8–19</sup> the transport study of the SSs remains a challenge due to the presence of the parallel bulk conducting channel that usually dominates the transport properties.<sup>20–28</sup> Recently, the ternary tetradymite  $\text{Bi}_2\text{Te}_2\text{Se}$  (BTS) has become a prototype TI material for studying the peculiar spin and charge transport of the SSs,<sup>29,30</sup> because carefully prepared BTS crystals not only present a very low bulk conduction but also show clear Shubnikov–de Haas (SdH) oscillations that reflect a high mobility of surface Dirac electrons. Given the lack of a truly bulk-insulating state in any of the known TI materials so far,<sup>31–33</sup> further improvement of BTS is worth pursuing.

The first synthesis of BTS was made while optimizing the continuous solid solutions between  $\text{Bi}_2\text{Te}_3$  and  $\text{Bi}_2\text{Se}_3$  for thermoelectric applications.<sup>34</sup> Nevertheless, unlike other members in the  $\text{Bi}_2\text{Te}_{3-x}\text{Se}_x$  ( $0 < x < 3$ ) family, the Te and Se atoms in BTS occupy distinct crystallographic sites, forming quintuple layers arranged in the sequential order Te–Bi–Se–Bi–Te along the  $c$  axis.<sup>35</sup> Such chalcogen ordering is believed to provide structural basis for reducing bulk carriers and achieving high surface mobility.<sup>29</sup> Unfortunately, similarly to  $\text{Bi}_2\text{Se}_3$ , the BTS crystals grown from the stoichiometric melts show  $n$ -type metallic conduction with the electron density  $n_e$  of  $\sim 10^{19} \text{ cm}^{-3}$ .<sup>36</sup> When the chalcogen stoichiometry is altered in the starting composition, one obtains<sup>29,36</sup> metallic or insulating crystals at different positions along the boule, which is due to the inevitable phase separation during the solidification process, according to a newly established phase diagram of the  $\text{Bi}_2\text{Te}_3$ – $\text{Bi}_2\text{Se}_3$  system.<sup>37</sup> Therefore, it is desirable to explore an alternative route to obtain BTS crystals with a large bulk resistivity while keeping the chalcogen stoichiometry, which would be useful for achieving a high surface-carrier mobility.

In this paper, we show that the above objective can be accomplished by hole doping through a Bi-site substitution, which has already been proven to be effective in tuning the carrier type and density for both of the binary end members,  $\text{Bi}_2\text{Te}_3$  and  $\text{Bi}_2\text{Se}_3$ .<sup>10,22,23,28</sup> It is found that, in analogy to its role in  $\text{Bi}_2\text{Te}_3$ ,<sup>10,38–40</sup> the group IV element Sn acts as an acceptor in BTS, which allows us to tune the Fermi level ( $E_F$ ) of this material. In particular, the  $\text{Bi}_{2-x}\text{Sn}_x\text{Te}_2\text{Se}$  crystals with  $x \geq 0.004$  show low-temperature resistivity reaching several  $\Omega \text{ cm}$ , indicating that  $E_F$  is tuned into the bulk band gap; their transport properties at high temperatures signify a large activation gap, which probably comes from a Sn-related impurity band. In about half of those samples, we observed SdH oscillations originating from the topological surface state below 14 T. Our analysis of the SdH oscillations gives direct evidence that one can achieve a surface-dominated transport in a bulk Sn-doped BTS crystal with a thickness of several  $\mu\text{m}$ .

## II. EXPERIMENTAL DETAILS

The single crystals of  $\text{Bi}_{2-x}\text{Sn}_x\text{Te}_2\text{Se}$  were grown by melting high-purity elemental shots of Bi (99.9999%), Sn (99.99%), Te (99.9999%), and Se (99.999%) with a nominal ratio of Bi:Sn:Te:Se =  $(2-x):x:2:1$  ( $x = 0, 0.002, 0.004, 0.006, 0.01, 0.02$ ) in sealed evacuated quartz tubes at  $850^\circ\text{C}$  for 48 h with periodical shaking to ensure homogeneity, followed by cooling slowly to  $500^\circ\text{C}$  and then annealing at that temperature for 4 days. The resulting crystals are easily cleaved along the (111) plane, revealing a shiny mirrorlike surface. The x-ray diffraction (XRD) analysis, which was performed on powders obtained by crushing the crystals, confirmed the samples to be single phase with chalcogen-ordered tetradymite structure.

For transport characterizations, the crystals were cut into bar-shaped samples with a typical thickness of  $100 \mu\text{m}$  after they were checked to be single domain by x-ray Laue analysis. The electrical leads were attached to the samples using room-temperature-cured silver paste in a six-probe configuration. The in-plane resistivity  $\rho_{xx}$  and the Hall coefficient  $R_H$  were measured in a Quantum Design physical properties



measurement system (PPMS-9) down to 1.8 K. The magnetic field was applied along the  $C_3$  axis which is perpendicular to the cleaved surface. For each  $x$  value, the data were taken on several crystals obtained from different parts of the boule in order to check for sample-to-sample variation. In addition, selected samples were cleaved down to a few micrometers by using Kapton tapes and then brought to a 14-T magnet for the detection of SdH oscillations using an ac measurement technique, in which two lock-in amplifiers were employed to collect the signals in both the longitudinal ( $\rho_{xx}$ ) and transverse ( $\rho_{yx}$ ) channels simultaneously. The measurements were carried out by sweeping the magnetic field between  $\pm 14$  T at a rate of 0.3 T/min, during which the temperature was stabilized to within  $\pm 5$  mK.

### III. RESULTS

#### A. Resistivity

Figure 1(a) shows typical data for the temperature dependencies of  $\rho_{xx}$  in  $\text{Bi}_{2-x}\text{Sn}_x\text{Te}_2\text{Se}$  crystals with different  $x$  values, together with the data for an insulating sample grown from the starting composition  $\text{Bi}_2\text{Te}_{1.95}\text{Se}_{1.05}$  which we abbreviate as  $\text{BTS}_{1.05}$ . The undoped stoichiometric BTS crystal ( $x = 0$ ) shows a metallic behavior in the whole temperature range; correspondingly, the Hall coefficient  $R_H$  [inset of Fig. 2(a)] is negative and nearly temperature independent, giving an electron carrier density of  $\sim 1.5 \times 10^{19} \text{ cm}^{-3}$  at 1.8 K. This result is in agreement with the previous study,<sup>36</sup> which indicated that  $E_F$  is pinned to the conduction band for this composition. Upon doping with Sn, a drastic change in both the resistivity value and its temperature dependence was observed. It is worth noting that an insulating behavior of  $\rho_{xx}$  is already established even for 0.1% of Sn doping to the Bi site ( $x = 0.002$ ). For  $x \geq 0.004$ , the  $\rho_{xx}$  values reach a few  $\Omega \text{ cm}$ , which is usually larger than that achieved in  $\text{BTS}_{1.05}$ .<sup>29</sup>

It should be noted that there is a marked difference in the  $\rho_{xx}(T)$  behavior between the Sn-doped BTS ( $x \geq 0.004$ ) and the  $\text{BTS}_{1.05}$  samples. First, in the high-temperature region,  $\rho_{xx}$  in Sn-doped BTS samples increases more steeply with decreasing temperature, as can be seen more clearly in the Arrhenius plot shown in Fig. 1(b). The magnitude of  $\rho_{xx}$  at room temperature in Sn-doped BTS samples varies from 80 to 110 m $\Omega \text{ cm}$ , which is considerably larger than that in  $\text{BTS}_{1.05}$ .<sup>29</sup> Also, the high-temperature slope in the Arrhenius plot, which is almost doping independent, corresponds to an activation gap  $\Delta$  of approximately 120 meV; this is nearly three times larger than that found for the  $\text{BTS}_{1.05}$  sample ( $\Delta \simeq 45$  meV). Second, in the low-temperature region, while  $\rho_{xx}(T)$  of the  $\text{BTS}_{1.05}$  sample becomes nearly flat, the Sn-doped BTS samples show a more strongly temperature-dependent  $\rho_{xx}(T)$  behavior with a weak upturn below  $\sim 10$  K, whose origin is not clear at present.

In addition to the above observations, the Sn-doped BTS samples were found to show a higher degree of homogeneity. As an example, Fig. 1(c) shows the  $\rho_{xx}(T)$  data for four samples obtained from different parts of a boule for  $x = 0.006$ . One can see that all the samples show qualitatively similar temperature dependence of  $\rho_{xx}$ . Although the  $\rho_{xx}$  values still

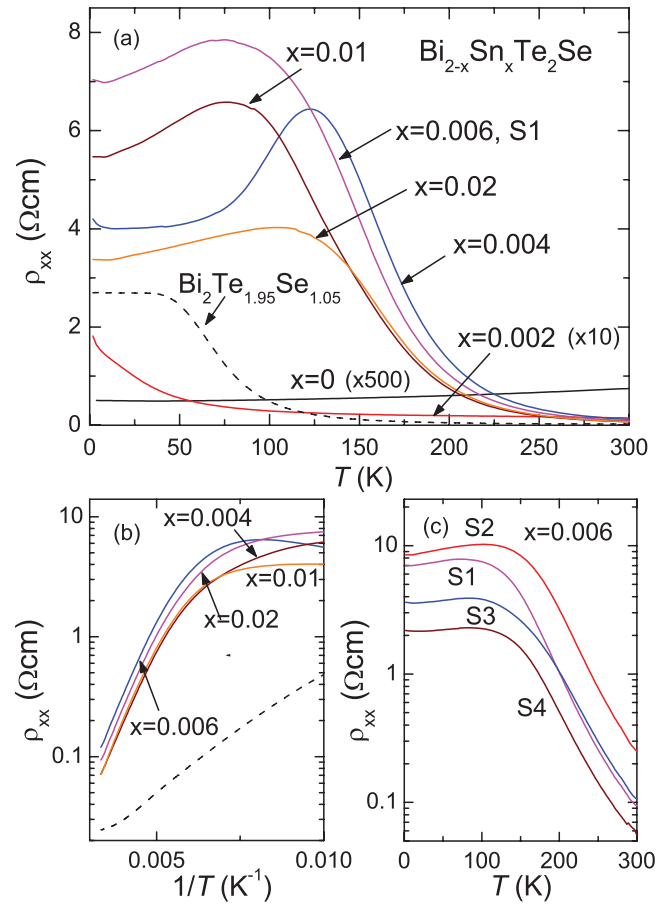


FIG. 1. (Color online) (a) Temperature dependencies of  $\rho_{xx}$  for  $\text{Bi}_{2-x}\text{Sn}_x\text{Te}_2\text{Se}$  single-crystal samples with various  $x$ . Note that the data with  $x = 0$  and  $x = 0.002$  have been magnified by a factor of 500 and 10, respectively. For comparison, the data for an insulating sample grown from the starting composition  $\text{Bi}_2\text{Te}_{1.95}\text{Se}_{1.05}$  are also included (dashed line). (b) Arrhenius plot of the  $\rho_{xx}(T)$  data for the temperature range between 100 and 300 K. (c)  $\rho_{xx}(T)$  data for four representative samples with  $x = 0.006$  obtained from different parts of a boule. The data are labeled in numerical order, where S1 and S4 represent first-to-freeze and the end parts, respectively. Note that the vertical axis is in logarithmic scale.

vary between samples by a factor of 4, it is notable that all of them are larger than 1  $\Omega \text{ cm}$  at low temperature.

#### B. Hall coefficient

To further investigate the doping effect of Sn in BTS, we measured the Hall resistivity  $\rho_{yx}$ . Figure 2(a) shows the temperature dependencies of the Hall coefficient  $R_H$  for the same series of  $\text{BTS}_{1.05}$  and  $\text{Bi}_{2-x}\text{Sn}_x\text{Te}_2\text{Se}$  samples; here we follow our previous definition of  $R_H$  as  $R_H = \rho_{yx}/B$  near  $B = 0$ .<sup>31</sup> It turns out that 0.1% of Sn doping results in an increase in  $|R_H|$  by nearly one order of magnitude, to  $\sim -4 \text{ cm}^3/\text{C}$  at 1.8 K [Fig. 2(a) inset]. Assuming a one-band model, this gives  $n_e \simeq 1.6 \times 10^{18} \text{ cm}^{-3}$ , implying that one Sn atom substituted for a Bi atom in BTS introduces approximately one hole, which is much the same as that in the case of  $n$ -type  $\text{Bi}_2\text{Te}_3$ .<sup>10</sup> While  $R_H$  is negative for  $x = 0$  and 0.002 [Fig. 2(a) inset], it becomes positive at  $x = 0.004$  [Fig. 2(a) main panel],

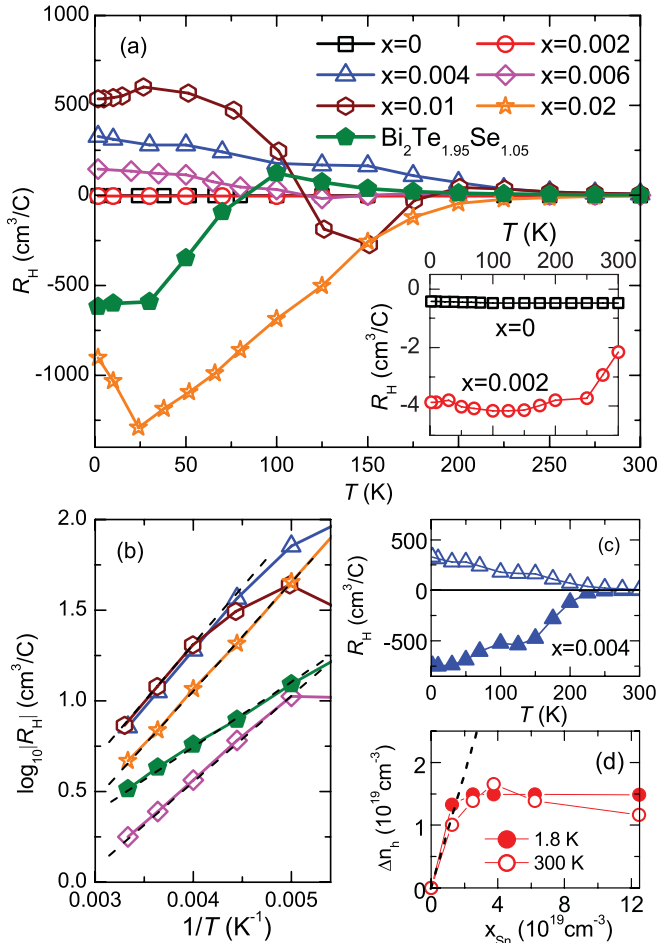


FIG. 2. (Color online) (a) Temperature dependencies of the low-field Hall coefficient  $R_H$  for a series of  $\text{Bi}_{2-x}\text{Sn}_x\text{Te}_2\text{Se}$  samples, together with the data for the  $\text{BTS}_{1.05}$  sample. The inset shows a magnified view of the data with  $x = 0$  and  $x = 0.002$ . (b) Arrhenius plot of  $R_H(T)$  at high temperature for a series of samples except for  $x = 0$  and  $0.002$  where no activation behavior was observed. Dashed lines are the Arrhenius-law fittings to extract the activation energy  $\Delta^*$ . (c)  $R_H(T)$  data for two different samples with  $x = 0.004$ , showing both  $n$ -type and  $p$ -type behavior. (d) The density of introduced holes  $[\Delta n_h = n(x) - n(0)]$  by Sn doping plotted as a function of the density of Sn dopant atoms. The estimation of the carrier density is based on a one-band model for simplicity. The dashed line corresponds to the ideal situation where each Sn atom donates one hole.

suggesting that an  $n$ -to- $p$  type transition occurs as a result of Sn doping between  $x = 0.002$  and  $0.004$ . In fact, in the case of  $x = 0.004$ , both  $n$ - and  $p$ -type samples with a large  $|R_H|$  were found in the same batch [Fig. 2(c)], placing this composition at the verge of such a transition. Somewhat unexpectedly,  $R_H$  becomes negative again at a higher doping of  $x = 0.02$  [Fig. 2(a)], whose origin is not clear. In the following, we focus on the temperature dependence of  $R_H$  for the samples with  $x \geq 0.004$ .

Above  $\sim 200$  K,  $R_H$  of those samples shows a thermally activated behavior, indicating that  $E_F$  is lowered into the bulk band gap. The effective activation gap  $\Delta^*$ , which is obtained from the Arrhenius plot of  $R_H(T)$  shown in Fig. 2(b), is 115, 95, 125, and 110 meV for the samples with  $x = 0.004$ ,

0.006, 0.01, and 0.02, respectively. Actually, the  $\Delta^*$  values for all the measured crystals fall within 95–125 meV for those compositions. These  $\Delta^*$  values are not far from the  $\Delta$  values derived from the  $\rho_{xx}(T)$  data, and their difference is likely due to the temperature dependence of the carrier mobility. More importantly, the  $\Delta^*$  values are much larger than that found in the  $\text{BTS}_{1.05}$  sample ( $\sim 65$  meV), implying that the Sn doping brings  $E_F$  closer to the middle of the band gap. At low temperatures, the  $|R_H|$  values of those Sn-doped samples become large, sometimes exceeding  $1000 \text{ cm}^3/\text{C}$  which would correspond to the carrier density of only  $6 \times 10^{15} \text{ cm}^{-3}$  in a one-band model.

### C. Surface quantum oscillations

Although Sn doping is expected to introduce impurity scattering, it turned out that the surface mobility remains reasonably high so that SdH oscillations can still be observed. As a matter of fact, traces of SdH oscillations were detected in nearly 50% of the Sn-doped BTS samples measured in the 14-T magnet. Among those successful cases, the data taken on an  $n$ -type sample with  $x = 0.004$  (thickness  $t = 6 \mu\text{m}$ )<sup>41</sup> showed the simplest pattern of the oscillations. In the following, we present the analysis of this simplest case.

Figure 3(a) shows the magnetic-field dependence of the transverse conductivity  $G_{yx}$  of this sample at 1.6 K, which was calculated from  $\rho_{xx}$  and  $\rho_{yx}$ . SdH oscillations are already visible in the raw data for magnetic field above 10 T. After removing a smooth background, one can clearly see that the oscillatory part of  $G_{yx}$ ,  $\Delta G_{yx}$ , exhibits periodic maxima and minima as a function of  $1/B$  [Fig. 3(a) inset], establishing the existence of a well defined Fermi surface (FS). In Fig. 3(b), we plot the  $1/B$  values corresponding to the maxima (closed circles) and the minima (open circles) of  $\Delta G_{yx}$  as a function of the Landau level index  $n$ , following the index assignment scheme in Ref. 42. From the linear fitting of the data with the slope fixed at the oscillation frequency obtained from the Fourier transform ( $F = 116$  T), we obtain a finite intercept  $\beta = 0.4 \pm 0.1$ . Since the slope is fixed in this analysis, the error in  $\beta$  is relatively small; the main source of the error is the uncertainty in determining the positions of maxima and minima in the data shown in the inset of Fig. 3(a), and the error of  $\pm 0.1$  in  $\beta$  is a conservative estimate. The obtained  $\beta$  of  $0.4 \pm 0.1$  is reasonably close to the value  $\beta = 0.5$  expected for massless Dirac fermions, which points to the topological SS origin of the SdH oscillations. Using the Onsager relation  $F = (\hbar c/2\pi e)A$ , where  $A$  is the extremal FS cross-section area, we find the Fermi wave vector  $k_F = 5.9 \times 10^6 \text{ cm}^{-1}$ , which corresponds to the surface carrier density  $n_s = 2.8 \times 10^{12} \text{ cm}^{-2}$  for a spin-nondegenerate surface state. It is worth noting that if one assumes that the SdH oscillations originate from a bulk FS, the bulk carrier density implied by  $F$  is of the order of  $10^{18} \text{ cm}^{-3}$ , which is totally inconsistent with the large  $R_H$  value observed at 1.8 K ( $\sim -100 \text{ cm}^3/\text{C}$ ). Hence, one can conclude that the SdH oscillations are certainly coming from the surface. From the obtained  $k_F$  value and the Fermi velocity  $v_F \simeq 4.6 \times 10^5 \text{ m/s}$ ,<sup>29</sup>  $E_F$  is estimated to be  $\sim 170$  meV above the Dirac point, pointing to the electron character of the surface carriers.

By fitting the temperature dependence of the oscillation amplitude with the standard Lifshitz-Kosevich (LK) theory

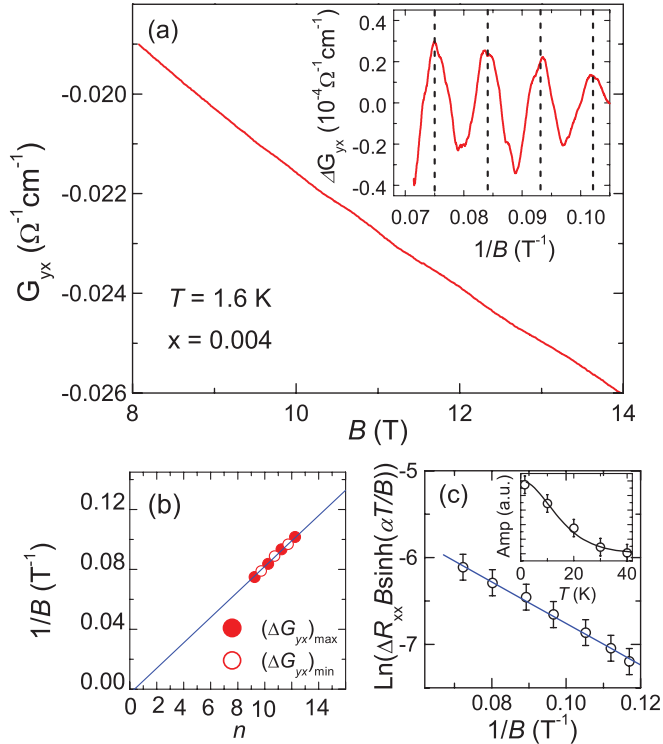


FIG. 3. (Color online) (a) Transverse conductance  $G_{yx}$  for an  $n$ -type sample with  $x = 0.004$  at 1.6 K plotted as a function of magnetic field  $B$  applied along the  $C_3$  axis. The inset shows the oscillatory component of  $G_{yx}$ ,  $\Delta G_{yx}$ , plotted as a function of  $1/B$ . The dashed lines are a guide to the eyes. (b) Landau-level fan diagram for oscillations in  $\Delta G_{yx}$ . Maxima and minima correspond to  $n + 1/4$  and  $n + 3/4$ , respectively. The linear fitting with the slope of  $F = 116$  T fixed by the oscillation frequency intersects the axis at  $\beta = 0.4 \pm 0.1$ . (c) Dingle plot for the oscillations in  $\Delta R_{xx}$ , yielding  $T_D = 12.5$  K; inset shows the temperature dependence of the SdH amplitudes. The solid line represents the fitting by the LK theory, giving  $m_c = 0.13m_e$ .

[inset of Fig. 3(c)], we obtained the cyclotron mass  $m_c = 0.13m_e$ , where  $m_e$  is the free electron mass. Once  $m_c$  is known, the Dingle plot [Fig. 3(c)] gives the Dingle temperature  $T_D = 12.5$  K, which corresponds to the surface quantum mobility  $\mu_s^{\text{SdH}}$  of  $\sim 1300$  cm<sup>2</sup>/Vs. This  $\mu_s^{\text{SdH}}$  value is roughly twice as large as that reported for thick BTS<sub>1.05</sub> samples.<sup>29</sup> Surprisingly, according to these results, the ratio of the estimated surface conductance to the total conductance, given by  $G_s/\sigma t$ , is calculated to be about 1.8 in this sample; here, the surface sheet conductance  $G_s = en_s\mu_s^{\text{SdH}} \simeq 5.8 \times 10^{-4} \Omega^{-1}$ , the measured overall conductivity  $\sigma$  was  $0.64 \Omega^{-1}\text{cm}^{-1}$  at 1.6 K, and  $t = 6 \mu\text{m}$ .<sup>43</sup> Obviously, it is unphysical to have  $G_s/\sigma t > 1$ , and this result implies that the actual surface transport is hindered by steps between terraces created upon cleaving, giving an effective surface conductance that is smaller than the intrinsic one given by  $n_s$  and  $\mu_s^{\text{SdH}}$ . Note that a similar problem was reported in Ref. 42. In any case, the SdH oscillations give a direct estimate of the surface transport parameters, which indicate that a surface-dominated transport can be achieved in Sn-doped BTS crystals with several  $\mu\text{m}$  thickness. The remaining bulk contribution is most likely the degenerate transport through the impurity band which is located in the bulk band gap; to

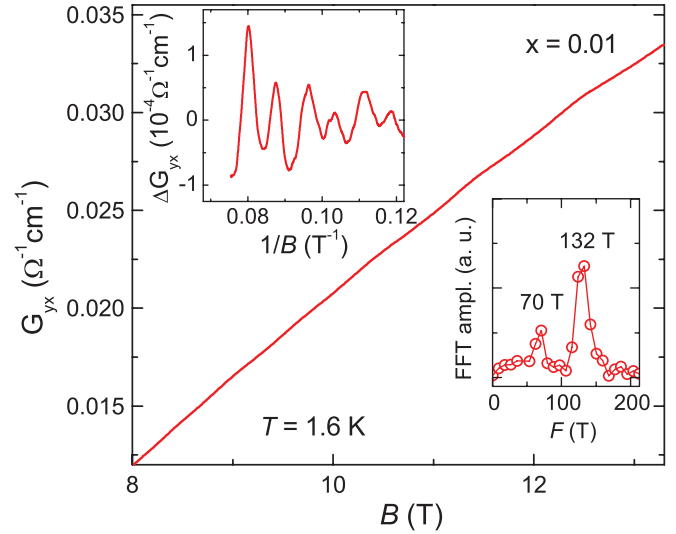


FIG. 4. (Color online)  $G_{yx}$  for a sample with  $x = 0.01$  at 1.6 K plotted as a function of  $B$  applied along the  $C_3$  axis. The upper inset shows the oscillatory component  $\Delta G_{yx}$  plotted as a function of  $1/B$ . The lower inset shows the Fourier transform of  $\Delta G_{yx}(B^{-1})$ , revealing two prominent frequencies.

further reduce the bulk contribution, one needs to achieve the Anderson localization in this impurity-band transport.

Apart from this simplest case, the patterns of the observed SdH oscillations were complicated. One such example, which was observed in a sample with  $x = 0.01$ , is shown in Fig. 4. As can be seen in the lower inset, the Fourier transform of  $\Delta G_{yx}(B^{-1})$  reveals two well-resolved peaks at  $F_1 = 70$  T and  $F_2 = 132$  T, reflecting the beating visible in the oscillation data (upper inset). The  $k_F$  values calculated from the Onsager relation are  $4.6 \times 10^6$  and  $6.3 \times 10^6$  cm<sup>-1</sup> for  $F_1$  and  $F_2$ , respectively. These correspond to  $n_s$  of  $1.7 \times 10^{12}$  and  $3.2 \times 10^{12}$  cm<sup>-2</sup>, respectively. Unfortunately, as was pointed out in Ref. 28, the multicomponent nature of the oscillations prevents us from reliably extracting the cyclotron mass or the Dingle temperature for each component. Also, the Landau-level fan diagram is not very reliable for extracting  $\beta$  in the multicomponent case.

#### IV. DISCUSSION

From the above results, it is clear that Sn acts as an acceptor in BTS. Ideally, one would expect that the total number of holes introduced by Sn doping,  $\Delta n_h$ , increases linearly with increasing  $x$ . However, as can be seen in Fig. 2(d),  $\Delta n_h$  becomes nearly constant for  $x \geq 0.004$ , which deviates significantly from the ideal situation. Therefore, there must be some additional effects that lead to deactivation of Sn dopants. In this respect, a similar problem was noted in previous studies of Sn doping in Bi<sub>2</sub>Te<sub>3</sub>,<sup>38–40</sup> and two possibilities have been proposed to explain the apparent discrepancy.

One possibility considered for Bi<sub>2</sub>Te<sub>3</sub> is that a part of the Sn atoms are built into the lattice in such a way that a seven-layer lamellar structure, i.e., Te-Bi-Te-Sn-Te-Bi-Te, is formed.<sup>38</sup> If a similar structure exists in Sn-doped BTS as well, it would be Se-Bi-Te-Sn-Te-Bi-Se. It is important to note that, in contrast to those occupying the Bi site, the Sn atoms in this structure

do not bring any charge to the lattice, and thus the discrepancy is reconciled. However, no additional diffraction peaks except for those corresponding to the chalcogen-ordered tetradymite structure were observed in the XRD data even for the sample with the highest Sn-doping concentration (data not shown), suggesting that the seven-layer lamellae, if they exist, are randomly distributed in the lattice.

Another, more plausible possibility is that at high Sn-doping concentration, the wave functions of the Sn acceptors overlap significantly, leading to the formation of an impurity band (IB).<sup>39,40</sup> Within this picture, increasing Sn content results in an increase in the density of states (DOS) of the IB instead of hole doping. In Sn-doped Bi<sub>2</sub>Te<sub>3</sub>, this Sn-related IB was shown to be located at 15 meV below the top of the upper valence band.<sup>39</sup> However, in the case of Sn-doped BTS, this Sn-related IB is most likely located within the bulk band gap, because the activation energy was found to be much larger in Sn-doped BTS than in BTS<sub>1.05</sub>, which naturally points to the appearance of a new IB to pin the chemical potential in Sn-doped BTS. Note that while there may also be IBs due to Se vacancies and Bi/Te antisite defects in Sn-doped BTS, it is most likely that  $E_F$  is pinned to the Sn-related IB due to its large DOS. The fact that the activation energy of  $\sim 120$  meV is essentially unchanged for a range of Sn concentrations ( $x = 0.004$ – $0.02$ ) is also consistent with this picture. Further studies are called for to clarify the details of the IBs in Sn-doped BTS.

## V. CONCLUSION

We performed a systematic study of the transport properties of a series of Bi<sub>2–x</sub>Sn<sub>x</sub>Te<sub>2</sub>Se single crystals with  $0 \leq x \leq 0.02$ . It is found that Sn behaves as an acceptor, which enables us to tune the Fermi level that is located in the conduction band in the undoped stoichiometric compound. For  $\geq 0.004$ ,  $E_F$  is successfully tuned into the bulk band gap, and the resistivity becomes as large as several  $\Omega$  cm at low temperatures. The transport properties at high temperatures show a thermally activated behavior with a large activation gap, which is probably related to the formation of a Sn-related impurity band. The analysis of the SdH oscillations observed in a 6- $\mu$ m-thick sample indicates that a surface-dominated transport can be achieved in Sn-doped BTS single crystals with several  $\mu$ m thickness. This, along with the large activation gap, makes the Sn-doped BTS system well suited for future applications of topological insulators.

## ACKNOWLEDGMENTS

This work was supported by JSPS (NEXT Program), MEXT (Innovative Area “Topological Quantum Phenomena” KAKENHI 22103004), and AFOSR (AOARD 104103 and 124038).

\*y\_ando@sanken.osaka-u.ac.jp

- <sup>1</sup>L. Fu, C. L. Kane, and E. J. Mele, *Phys. Rev. Lett.* **98**, 106803 (2007).
- <sup>2</sup>J. E. Moore and L. Balents, *Phys. Rev. B* **75**, 121306(R) (2007).
- <sup>3</sup>R. Roy, *Phys. Rev. B* **79**, 195322 (2009).
- <sup>4</sup>L. Fu and C. L. Kane, *Phys. Rev. B* **76**, 045302 (2007).
- <sup>5</sup>X.-L. Qi, T. L. Hughes, and S.-C. Zhang, *Phys. Rev. B* **78**, 195424 (2008).
- <sup>6</sup>M. Z. Hasan and C. L. Kane, *Rev. Mod. Phys.* **82**, 3045 (2010).
- <sup>7</sup>X. L. Qi and S. C. Zhang, *Rev. Mod. Phys.* **83**, 1057 (2010).
- <sup>8</sup>D. Hsieh, D. Qian, L. Wray, Y. Xia, Y. S. Hor, R. J. Cava, and M. Z. Hasan, *Nature (London)* **452**, 970 (2008).
- <sup>9</sup>A. Nishide, A. A. Taskin, Y. Takeichi, T. Okuda, A. Kakizaki, T. Hirahara, K. Nakatsuji, F. Komori, Y. Ando, and I. Matsuda, *Phys. Rev. B* **81**, 041309(R) (2010).
- <sup>10</sup>Y. L. Chen, J. G. Analytis, J.-H. Chu, Z. K. Liu, S.-K. Mo, X. L. Qi, H. J. Zhang, D. H. Lu, X. Dai, Z. Fang, S. C. Zhang, I. R. Fisher, Z. Hussain, and Z.-X. Shen, *Science* **325**, 178 (2009).
- <sup>11</sup>T. Sato, K. Segawa, H. Guo, K. Sugawara, S. Souma, T. Takahashi, and Y. Ando, *Phys. Rev. Lett.* **105**, 136802 (2010).
- <sup>12</sup>K. Kuroda, M. Ye, A. Kimura, S. V. Ereemeev, E. E. Krasovskii, E. V. Chulkov, Y. Ueda, K. Miyamoto, T. Okuda, K. Shimada, H. Namatame, and M. Taniguchi, *Phys. Rev. Lett.* **105**, 146801 (2010).
- <sup>13</sup>Y. L. Chen, Z. K. Liu, J. G. Analytis, J.-H. Chu, H. J. Zhang, B. H. Yan, S.-K. Mo, R. G. Moore, D. H. Lu, I. R. Fisher, S.-C. Zhang, Z. Hussain, and Z.-X. Shen, *Phys. Rev. Lett.* **105**, 266401 (2010).
- <sup>14</sup>S. Y. Xu, L. A. Wray, Y. Xia, R. Shankar, A. Petersen, A. Fedorov, H. Lin, A. Bansil, Y. S. Hor, D. Grauer, R. J. Cava, and M. Z. Hasan, e-print [arXiv:1007.5111](https://arxiv.org/abs/1007.5111).

- <sup>15</sup>T. Arakane, T. Sato, S. Souma, K. Kosaka, K. Nakayama, M. Komatsu, T. Takahashi, Z. Ren, K. Segawa, and Y. Ando, *Nature Commun.* **3**, 636 (2012).
- <sup>16</sup>P. Roushan, J. Seo, C. V. Parker, Y. S. Hor, D. Hsieh, D. Qian, A. Richardella, M. Z. Hasan, R. J. Cava, and A. Yazdani, *Nature (London)* **460**, 1106 (2009).
- <sup>17</sup>Z. Alpichshev, J. G. Analytis, J. H. Chu, I. R. Fisher, Y. L. Chen, Z. X. Shen, A. Fang, and A. Kapitulnik, *Phys. Rev. Lett.* **104**, 016401 (2010).
- <sup>18</sup>P. Cheng, C. L. Song, T. Zhang, Y. Y. Zhang, Y. L. Wang, J. F. Jia, J. Wang, Y. Y. Wang, B. F. Zhu, X. Chen, X. C. Ma, K. He, L. L. Wang, X. Dai, Z. Fang, X. C. Xie, X. L. Qi, C. X. Liu, S. C. Zhang, and Q. K. Xue, *Phys. Rev. Lett.* **105**, 076801 (2010).
- <sup>19</sup>T. Hanaguri, K. Igarashi, M. Kawamura, H. Takagi, and T. Sasagawa, *Phys. Rev. B* **82**, 081305(R) (2010).
- <sup>20</sup>A. A. Taskin and Y. Ando, *Phys. Rev. B* **80**, 085303 (2009).
- <sup>21</sup>D.-X. Qu, Y. S. Hor, J. Xiong, R. J. Cava, and N. P. Ong, *Science* **329**, 821 (2010).
- <sup>22</sup>J. G. Analytis, R. D. McDonald, S. C. Riggs, J.-H. Chu, G. S. Boebinger, and I. R. Fisher, *Nature Phys.* **10**, 960 (2010).
- <sup>23</sup>Y. S. Hor, A. Richardella, P. Roushan, Y. Xia, J. G. Checkelsky, A. Yazdani, M. Z. Hasan, N. P. Ong, and R. J. Cava, *Phys. Rev. B* **79**, 195208 (2009).
- <sup>24</sup>J. G. Checkelsky, Y. S. Hor, M.-H. Liu, D.-X. Qu, R. J. Cava, and N. P. Ong, *Phys. Rev. Lett.* **103**, 246601 (2009).
- <sup>25</sup>N. P. Butch, K. Kirshenbaum, P. Syers, A. B. Sushkov, G. S. Jenkins, H. D. Drew, and J. Paglione, *Phys. Rev. B* **81**, 241301 (2010).
- <sup>26</sup>J. G. Analytis, J. H. Chu, Y. Chen, F. Corredor, R. D. McDonald, Z. X. Shen, and I. R. Fisher, *Phys. Rev. B* **81**, 205407 (2010).



- <sup>27</sup>K. Eto, Z. Ren, A. A. Taskin, K. Segawa, and Y. Ando, *Phys. Rev. B* **81**, 195309 (2010).
- <sup>28</sup>Z. Ren, A. A. Taskin, S. Sasaki, K. Segawa, and Y. Ando, *Phys. Rev. B* **84**, 075316 (2011).
- <sup>29</sup>Z. Ren, A. A. Taskin, S. Sasaki, K. Segawa, and Y. Ando, *Phys. Rev. B* **82**, 241306(R) (2010).
- <sup>30</sup>J. Xiong, A. C. Petersen, D. X. Qu, Y. S. Hor, R. J. Cava, and N. P. Ong, *Physica E* **44**, 917 (2012).
- <sup>31</sup>Z. Ren, A. A. Taskin, S. Sasaki, K. Segawa, and Y. Ando, *Phys. Rev. B* **84**, 165311 (2011).
- <sup>32</sup>A. A. Taskin, Z. Ren, S. Sasaki, K. Segawa, and Y. Ando, *Phys. Rev. Lett.* **107**, 016801 (2011).
- <sup>33</sup>C. Brune, C. X. Liu, E. G. Novik, E. M. Hankiewicz, H. Buhmann, Y. L. Chen, X. L. Qi, Z. X. Shen, S. C. Zhang, and L. W. Molenkamp, *Phys. Rev. Lett.* **106**, 126803 (2011).
- <sup>34</sup>N. Fuschillo, J. N. Bierly, and F. J. Donahoe, *J. Phys. Chem. Solids* **8**, 430 (1959).
- <sup>35</sup>S. Nakajima, *J. Phys. Chem. Solids* **24**, 479 (1963).
- <sup>36</sup>S. Jia, H. W. Ji, E. Climent-Pascual, M. K. Fuccillo, M. E. Charles, J. Xiong, N. P. Ong, and R. J. Cava, *Phys. Rev. B* **84**, 235206 (2011).
- <sup>37</sup>O. B. Sokolov, S. Ya. Skipidarov, N. I. Duvankov, and G. G. Shabunina, *J. Cryst. Growth* **262**, 442 (2004).
- <sup>38</sup>J. Horák, P. Lošťák, and J. Guerts, *Phys. Status Solidi B* **167**, 459 (1991).
- <sup>39</sup>V. A. Kulbachinskii, M. Inoue, M. Sasaki, H. Negishi, W. X. Gao, K. Takase, Y. Gimán, P. Lostak, and J. Horak, *Phys. Rev. B* **50**, 16921 (1994).
- <sup>40</sup>C. M. Jaworski, V. Kulbachinskii, and J. P. Heremans, *Phys. Rev. B* **80**, 233201 (2009).
- <sup>41</sup>In  $\text{Bi}_{1.5}\text{Sb}_{0.5}\text{Te}_{1.7}\text{Se}_{1.3}$  samples with the thickness of several  $\mu\text{m}$ , we observed (Ref. 32) that the low-temperature  $R_H$  undergoes a sign change with time and that the SdH frequency accordingly shows a drastic change. However, for the present sample, only a slight time evolution in  $R_H$  and the SdH frequency was observed.
- <sup>42</sup>J. Xiong, Y. K. Luo, Y. H. Koo, S. Jia, R. J. Cava, and N. P. Ong, e-print [arXiv:1111.6031](https://arxiv.org/abs/1111.6031).
- <sup>43</sup>It should be noted that in the present experiment, the bottom surface of the sample was glued to a Kapton tape, so the top and bottom surfaces were in different environments. This means that the surface chemical potentials (and hence the surface carrier densities) for the top and bottom surfaces were most likely different; nevertheless, only a single frequency was observed in the SdH oscillations, suggesting that only one surface was responsible for the oscillations. We therefore considered only one surface in this calculation of  $G_s$ .



# Electrochemical synthesis and superconducting phase diagram of $\text{Cu}_x\text{Bi}_2\text{Se}_3$

M. Kriener,<sup>1,\*</sup> Kouji Segawa,<sup>1</sup> Zhi Ren,<sup>1</sup> Satoshi Sasaki,<sup>1</sup> Shohei Wada,<sup>1</sup> Susumu Kuwabata,<sup>2</sup> and Yoichi Ando<sup>1,†</sup>

<sup>1</sup>*Institute of Scientific and Industrial Research, Osaka University, Osaka 567-0047, Japan*

<sup>2</sup>*Department of Applied Chemistry, Osaka University, Osaka 565-0871, Japan*

(Received 6 June 2011; revised manuscript received 12 July 2011; published 8 August 2011)

The superconducting  $\text{Cu}_x\text{Bi}_2\text{Se}_3$  is an electron-doped topological insulator and is a prime candidate of the topological superconductor which still awaits discovery. The electrochemical intercalation technique for synthesizing  $\text{Cu}_x\text{Bi}_2\text{Se}_3$  offers good control of restricting Cu into the van der Waals gap and yields samples with shielding fractions of up to  $\sim 50\%$ . We report essential details of this synthesis technique and present the established superconducting phase diagram of  $T_c$  vs  $x$ , along with a diagram of the shielding fraction vs  $x$ . Intriguingly, those diagrams suggest that there is a tendency to spontaneously form small islands of optimum superconductor in this material.

DOI: [10.1103/PhysRevB.84.054513](https://doi.org/10.1103/PhysRevB.84.054513)

PACS number(s): 74.25.Dw, 74.62.-c, 82.45.Vp, 65.40.gk

## I. INTRODUCTION

Topological insulators (TIs) are attracting great interest since they realize a new state of matter; namely, the bulk of such materials is insulating, but in contrast to conventional band insulators, their bulk wave functions exhibit a nontrivial  $Z_2$  topology leading to gapless and hence conductive surface states.<sup>1–3</sup> Those topological surface states are interesting because they exhibit a Dirac-like energy dispersion (similar to that in graphene) and a helical spin polarization, both of which hold promise for various energy-saving device applications.<sup>4–6</sup> Soon after the theoretical predictions of candidate materials,<sup>7,8</sup> a series of promising materials were experimentally discovered to be three-dimensional (3D) TIs,<sup>9–21</sup> stimulating the search for a superconducting analog, i.e., a topological superconductor, which is characterized by a full energy gap in the bulk and the existence of gapless surface Andreev bound states.<sup>22–27</sup> Such a topological superconductor is predicted to be a key to realizing a fault-tolerant topological quantum computing,<sup>22</sup> and the discovery of a concrete example of the topological superconductor would have a large impact on future technology. In this context, there is an intriguing prediction that when superconductivity is achieved by doping a topological insulator, it may realize a topological superconducting state.<sup>28</sup>

Recently, Hor *et al.*<sup>29</sup> reported superconductivity in the electron-doped TI material  $\text{Cu}_x\text{Bi}_2\text{Se}_3$  for  $0.1 \leq x \leq 0.3$ , where the layered TI compound  $\text{Bi}_2\text{Se}_3$  was intercalated with Cu. Their samples showed superconductivity below critical temperatures  $T_c \leq 3.8$  K. In a subsequent study on these samples,<sup>30</sup> it was further found that the topological surface states remain intact upon Cu intercalation. Thus,  $\text{Cu}_x\text{Bi}_2\text{Se}_3$  is the first promising candidate material to be a topological superconductor, and it is very important to elucidate the nature of its superconducting state. However, the samples prepared by Hor *et al.* showed superconducting shielding fractions of only less than 20% and the resistivity never really disappeared below  $T_c$ .<sup>29,30</sup> Therefore, some doubts remained about the bulk nature of the superconducting phase in  $\text{Cu}_x\text{Bi}_2\text{Se}_3$ , and preparations of higher quality samples were strongly called for.

In our recent experiments,<sup>31</sup> we succeeded in synthesizing  $\text{Cu}_x\text{Bi}_2\text{Se}_3$  samples with shielding fractions of up to 50% (depending on the Cu concentration) by applying a different sample preparation method than the standard melt-growth

method employed in Ref. 29. In our high-quality samples, besides observing zero resistivity, we were able to measure the specific-heat anomaly in the superconducting phase, which indicated that the superconductivity in this material is a bulk feature and, moreover, appears to have a full energy gap,<sup>31</sup> which is a prerequisite to topological superconductivity.<sup>23</sup> In this paper, we describe in detail the newly applied preparation method of  $\text{Cu}_x\text{Bi}_2\text{Se}_3$  to employ electrochemical intercalation, and present the electronic phase diagram of  $T_c$  vs Cu concentration  $x$ . We also show how the superconducting shielding fraction of the electrochemically prepared samples changes with  $x$ , which bears an intriguing implication of intrinsically inhomogeneous superconductivity.

## II. SAMPLE PREPARATIONS

Pristine  $\text{Bi}_2\text{Se}_3$  has a layered crystal structure ( $R\bar{3}m$ , space group 166) consisting of stacked Se–Bi–Se–Bi–Se quintuple layers. The rhombohedral [111] direction is denoted as the  $c$  axis and the (111) plane as the  $ab$  plane. The neighboring quintuple layers are only weakly van der Waals bonded to each other. Cu is known to enter  $\text{Bi}_2\text{Se}_3$  either as an intercalant in the van der Waals gaps or as a substitutional defect to replace Bi. In the former case,  $\text{Cu}^+$  is formed and acts as a donor, whereas in the latter case, it creates two holes by replacing three Bi  $6p$  electrons by one Cu  $4s$  electron upon forming a  $\sigma$  bond. Therefore, Cu acts as an ambipolar dopant for  $\text{Bi}_2\text{Se}_3$ .<sup>32,33</sup> The melt-growth method employed by Hor *et al.*<sup>29</sup> cannot avoid the formation of substitutional Cu defects; in contrast, our electrochemical method has a distinct advantage to promote only the intercalation of Cu.

For the present experiments, we first grew single crystals of pristine  $\text{Bi}_2\text{Se}_3$  by melting stoichiometric amounts of high-purity elemental shots of Bi (99.9999%) and Se (99.999%) at 850 °C for 96 h in sealed evacuated quartz glass tubes, followed by a slow cooling to 550 °C over 72 h and annealing at that temperature for 48 h. Before the electrochemical intercalation procedure, those melt-grown  $\text{Bi}_2\text{Se}_3$  single crystals were cleaved and cut into rectangular pieces. They were wound by 50- $\mu\text{m}$  thick, bare Cu wire and acted as the working electrode (WE). A 0.5-mm thick Cu stick was used both as the counter (CE) and reference electrode (RE) in our simplified setup sketched in Fig. 1(a).

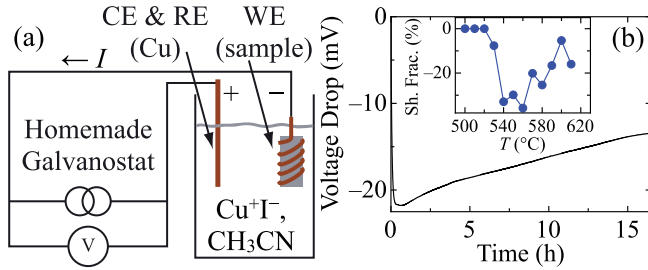
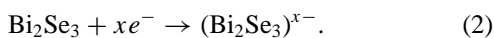
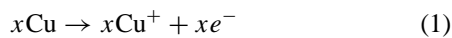


FIG. 1. (Color online) (a) Sketch of our simplified electrochemical intercalation setup. The counter electrode (CE) is also used as reference electrode (RE). The current direction is indicated. (b) Typical time dependence of the voltage drop measured between working and counter electrodes. The inset summarizes the development of the diamagnetism (plotted in terms of the shielding fraction) in a sample with  $x = 0.31$  upon annealing at different temperatures.

Since Hor *et al.*<sup>29</sup> reported that  $\text{Cu}_x\text{Bi}_2\text{Se}_3$  samples are sensitive to air, the pristine  $\text{Bi}_2\text{Se}_3$  samples were transferred into a glove box and the electrochemical intercalation of Cu was done in an inert atmosphere. To provide the electrical wiring required for electrochemical intercalation processes as sketched in Fig. 1(a), our glove box was specially modified for air-tight electrical connections. For the intercalation, we used a saturated solution of CuI powder (99.99%) in acetonitrile  $\text{CH}_3\text{CN}$ . A current of  $10 \mu\text{A}$  was applied to the electrodes for a suitable time period to give the desired Cu concentration  $x$ . The typical time dependence of the voltage drop between the standard and working electrodes observed for our samples is shown in Fig. 1(b). Its absolute value was usually between  $-10$  and  $-30$  mV. The whole process was controlled by a computer which was also used to determine the total transferred charge.

After the intercalation had finished, the Cu concentration  $x$  in the sample was determined from its weight change: we measured the weight before and after the intercalation process with a high-precision balance with a resolution of  $0.1 \mu\text{g}$ , and the possible error in  $x$  was less than  $\pm 0.01$ . Note that this direct measurement of the Cu concentration is expected to be more accurate than most of the chemical analysis methods.<sup>34</sup> Nevertheless, we have also employed the inductively coupled plasma atomic-emission spectroscopy (ICP-AES) analysis, which is a destructive method but is good at giving absolute numbers, to confirm that the  $x$  values determined from the weight change is indeed reliable, as will be described later.

For a consistency check of our electrochemical intercalation process, we have calculated the total charge transferred during the intercalation. The experimentally determined Faraday number for our samples was usually up to 15% smaller than the theoretical Faraday constant,  $96485 \text{ C/mol}$ . In this regard, it was reported<sup>32,33</sup> that a simple physical attachment of Cu metal to  $\text{Bi}_2\text{Se}_3$  crystal results in a perceptible diffusion of  $\text{Cu}^+$  into the van der Waals gaps of  $\text{Bi}_2\text{Se}_3$ . This reaction can be described as the following oxidation and reduction formulas in an electrochemical viewpoint:



The occurrence of electron transfer from Cu to  $\text{Bi}_2\text{Se}_3$  implies that the redox potential of  $\text{Cu}^{+/0}$  is more negative than that

of  $(\text{Bi}_2\text{Se}_3)^{0/x-}$ . Since we are using a Cu wire to hold the sample and to make the electrical contact, it is possible that this wire became the source of an additional  $\text{Cu}^+$  intercalation to the sample(s). This reaction should not be included into the charge balance, and hence the difference between the estimated and the theoretical Faraday numbers is naturally expected. This inference is supported by our observation that the sample mass increased even without applying a current, though at a much lower reaction rate.

It is most likely that the electrochemical intercalation is induced by reduction of  $\text{Bi}_2\text{Se}_3$  without reduction of  $\text{Cu}^+$ , yielding  $(\text{Cu}^+)_x(\text{Bi}_2\text{Se}_3)^{x-}$ . This implies that doping of electrons with the nominal fraction of  $x$  should take place upon  $\text{Cu}^+$  intercalation. The reaction at the counter electrode seems to be oxidation of Cu metal rather than that of  $\text{I}^-$  to  $\text{I}_2$  or  $\text{I}_3^-$ , because the former redox potential is more negative than the latter one in an aqueous medium.

It is important to note that the as-intercalated samples *do not* superconduct yet. It turned out that the samples have to be annealed in order to establish superconductivity. For this purpose, the samples were sealed under vacuum in quartz glass tubes and put into a muffle furnace. For the determination of the optimum annealing temperature, one sample with  $x = 0.31$  was annealed subsequently for 2 h at different temperatures starting at  $500^\circ\text{C}$ . After each annealing run, the diamagnetic response was checked, and the result is shown in the inset of Fig. 1(b). A trace of diamagnetism indicating the appearance of a superconducting phase was detected after annealing at  $530^\circ\text{C}$ , and the annealing temperature of  $560^\circ\text{C}$  was found to yield the largest shielding fraction. When the sample was annealed at higher temperatures than  $560^\circ\text{C}$ , the shielding fraction was found to be reduced irreversibly. (The onset  $T_c$  was essentially independent of the annealing temperature.) Therefore, the samples used for determining the phase diagram presented here were treated in the following way: they were heated up to  $540^\circ\text{C}$  in 1 h, and then the temperature was gradually increased to  $560^\circ\text{C}$  in 40 min to avoid any overheating; the samples were kept at  $560^\circ\text{C}$  for 2 h and eventually quenched by dropping the quartz glass tubes into cold water.<sup>35</sup> We will come back later to the question of what is happening during the annealing process to activate the superconductivity.

To confirm the accuracy of the  $x$  values determined by the mass change (and also to make sure that the Cu content does not change appreciably during the annealing process), we measured the  $x$  values of eight of our samples in the post-annealed state by using the ICP-AES analysis (the sample mass was between 15 and 38 mg). For this destructive analysis, the whole sample was dissolved in nitric acid  $\text{HNO}_3$ . The Cu concentrations obtained from the ICP-AES analyses for the eight samples agreed with those obtained from the mass change within  $\pm 0.014$ ,<sup>36</sup> giving confidence in the  $x$  values reported in this paper.

In addition to the ICP-AES analysis, we have employed the electron-probe microanalyzer (EPMA) to check the distribution of Cu within the sample after the annealing. For this analysis, one sample with  $x = 0.31$  was cleaved and subsequently scanned over distances of  $10 \mu\text{m}$  and  $1 \text{ mm}$ , as sketched in Fig. 2(c). The intensity of the characteristic x-ray of each element is plotted vs the scan position for the two different scan lengths in Figs. 2(a) and 2(b). One can see that

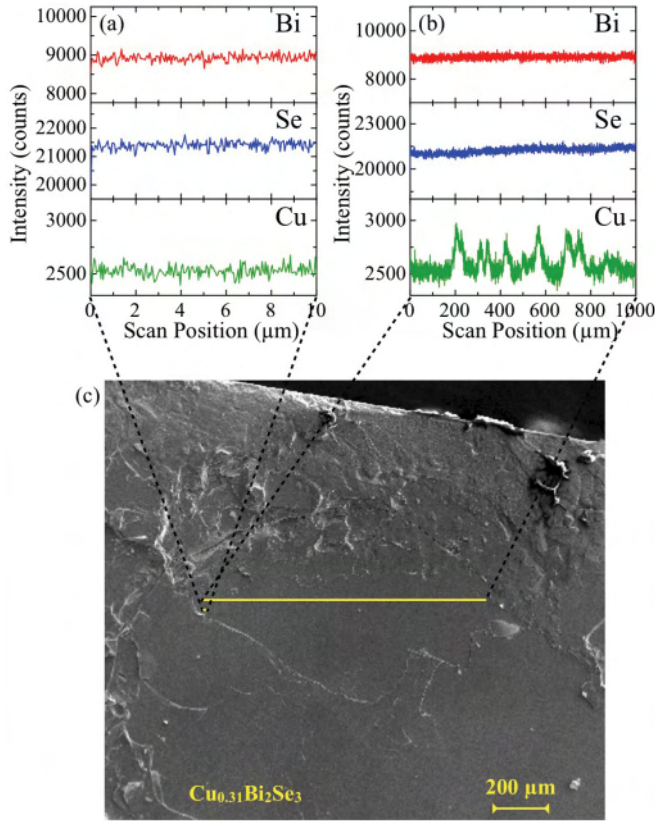


FIG. 2. (Color online) EPMA analyses of the cleaved surface of a sample with  $x = 0.31$ . Panels (a) and (b) summarize scans along two lines of  $10\ \mu\text{m}$  and  $1\ \text{mm}$  lengths, respectively, sketched in panel (c). One can see that the local Cu concentration is uniform on the  $\mu\text{m}$  scale, but it is inhomogeneous on the sub-mm scale.

the distributions of Bi and Se are essentially homogeneous on any length scale, as evidenced by the constant intensity of the respective characteristic x-ray. On the other hand, the distribution of Cu shows a variation of up to  $\sim 20\%$  on the sub-mm length scale [Fig. 2(b)], although on the  $10\text{-}\mu\text{m}$  length scale the Cu distribution is usually homogeneous [Fig. 2(a)]. Since the averaged Cu concentration of this sample determined from the mass change was 0.31, the spatial variation of  $\sim 20\%$  corresponds to the variation in  $x$  of  $\sim 0.06$ .

### III. SAMPLE CHARACTERIZATIONS

The superconducting samples were characterized by measuring the dc magnetization  $M$  and transport properties. To take the magnetization data, a commercial SQUID magnetometer (Quantum Design, MPMS) was used with the magnetic field applied parallel to the  $ab$  plane. The samples were cooled down in zero-magnetic field (zero-field cooled, ZFC) to the lowest accessible temperature  $T = 1.8\ \text{K}$ ; then a small dc field of  $B = 0.2\ \text{mT}$  was applied and the magnetization was measured upon increasing temperature. After passing through  $T_c$ , defined as the onset of the drop in the  $M(T)$  curves, data were again taken upon decreasing the temperature back to  $1.8\ \text{K}$  (field cooled, FC). The superconducting shielding fraction of a sample was estimated from its magnetic moment at  $T = 1.8\ \text{K}$  after ZFC. The resistivity  $\rho_{xx}$  and the Hall coef-

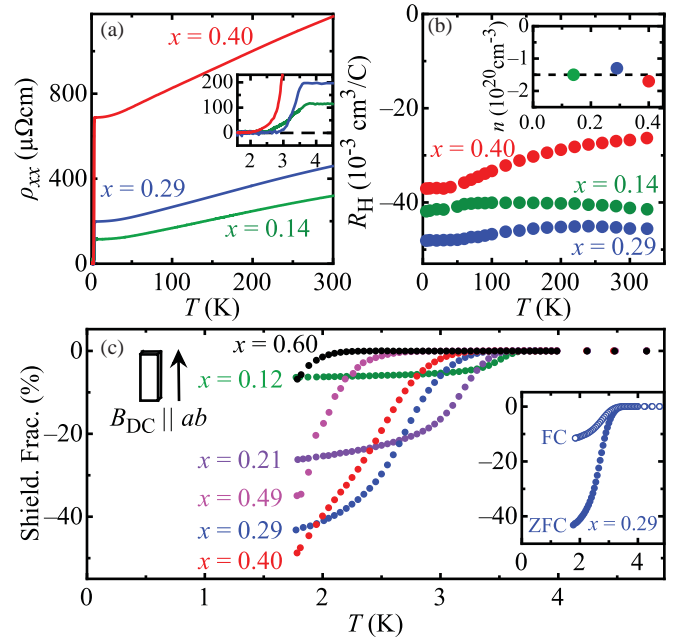


FIG. 3. (Color online) (a) Temperature-dependent resistivity of  $\text{Cu}_x\text{Bi}_2\text{Se}_3$  for  $x = 0.14, 0.29$ , and  $0.40$ . The inset gives an enlargement around the superconducting transition. (b) Temperature dependence of the Hall coefficient  $R_H$  and the  $x$ -dependence of the charge-carrier concentration  $n$  (inset). (c) Temperature dependence of the superconducting shielding fraction in  $B = 0.2\ \text{mT}$  after ZFC for various Cu concentrations  $0.12 \leq x \leq 0.60$ . For  $x = 0.29$ , the ZFC and FC data are exemplarily shown in the inset.

ficient  $R_H$  were measured by a standard six-probe technique, where the electrical current was applied in the  $ab$  plane.

With our electrochemical intercalation technique, we have successfully synthesized samples which superconduct above  $1.8\ \text{K}$  for Cu concentrations of  $0.09 \leq x \leq 0.64$ . Figure 3(a) shows the resistivity data of  $\text{Cu}_x\text{Bi}_2\text{Se}_3$  for three selected Cu concentrations  $x = 0.14, 0.29$ , and  $0.40$  measured in zero field. All those samples exhibit a metallic temperature dependence above  $T_c$  and show zero resistance below  $T_c$ , see the expanded view in the inset of Fig. 3(a). With increasing Cu concentration, the absolute value of  $\rho_{xx}$  increases; especially, between  $x = 0.29$  and  $0.40$ , a strong rise in the absolute value is observed, which implies that a high Cu concentration enhances the disorder in the samples. Figure 3(b) summarizes the temperature dependences of  $R_H$  for the three samples, which are generally weak. The inset shows the  $x$ -dependence of the charge-carrier concentration  $n$  determined from the low-temperature value of  $R_H$ . It is striking that, despite the factor of three difference in the Cu concentration, the change in  $n$  is very small:  $n = 1.5 \times 10^{20}$ ,  $1.3 \times 10^{20}$ , and  $1.7 \times 10^{20}\ \text{cm}^{-3}$  for  $x = 0.14, 0.29$ , and  $0.40$ , respectively. Furthermore, those values correspond to only  $\sim 2\%$  of electron doping. This is totally inconsistent with the expectation that there should be electron carriers with the nominal fraction of  $x$  in  $\text{Cu}_x\text{Bi}_2\text{Se}_3$ . Therefore, there must be some side reaction taking place in  $\text{Cu}_x\text{Bi}_2\text{Se}_3$  to significantly reduce the actual electron carriers. In this regard, a similar problem was previously noted in a study of Cu intercalation into  $\text{Bi}_2\text{Te}_3$ , and it was proposed that  $\text{Cu}^+$  reacts with the matrix to form a four-layer lamellar



structure Cu–Te–Bi–Te that annihilates electrons.<sup>37</sup> If a similar reaction occurs in  $\text{Cu}_x\text{Bi}_2\text{Se}_3$ , it would be



The formation of this type of structural defects can indeed explain the small  $n$  values observed in  $\text{Cu}_x\text{Bi}_2\text{Se}_3$ .

Figure 3(c) summarizes the temperature dependences of the shielding fraction in samples with various  $x$  values. The onset temperatures of superconductivity in the magnetization data are slightly lower than the onset of the resistivity transition in respective samples, which is usual for disordered superconductors. The right inset of Fig. 3(c) shows the ZFC and FC data for  $x = 0.29$ , and other samples exhibited similar differences between the two. We note that samples with  $x \geq 0.70$  were also prepared, but they did not show any superconducting transition above 1.8 K; however, it is possible that they exhibit superconductivity at lower temperatures.

#### IV. PHASE DIAGRAM AND DISCUSSIONS

Figure 4(a) shows the phase diagram of  $T_c$  vs  $x$  based on our measurements of more than 40 samples, and Fig. 4(b) summarizes the shielding fraction of those samples at 1.8 K. The lowest  $x$  value at which we found superconductivity was 0.09, where  $T_c$  was already 3.45 K; however, in spite of this relatively high  $T_c$ , the superconducting signal was very weak with a shielding fraction of only around 1%. For slightly larger  $x$  values around 0.12–0.15, the maximum values of  $T_c$  are found, but the shielding fractions were less than 20%, which is in agreement with the earlier report by Hor *et al.*<sup>29</sup> Intriguingly,  $T_c$  gradually decreases with increasing  $x$  down to  $T_c \approx 2.2$  K for  $x = 0.64$ , which is the highest Cu concentration for which we could clearly confirm the superconductivity.

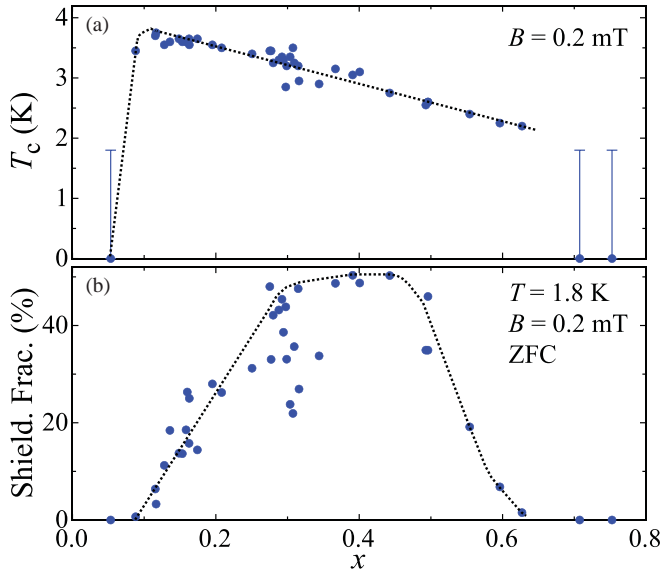


FIG. 4. (Color online) Cu concentration  $x$  dependence of (a) the critical temperature and (b) the shielding fraction at 1.8 K. These  $T_c$  data were extracted from the onset of superconductivity in magnetization measurements, the shielding-fraction data from the ZFC magnetization at  $T = 1.8$  K, see Fig. 3(c).

Although  $T_c$  seems to be quite robust and reproducible, the shielding fraction exhibits a scattering among different samples even with similar  $x$  values, as can be seen in Fig. 4(b). Nevertheless, there is a clear trend that samples with maximal shielding fractions are obtained only for  $0.3 \leq x \leq 0.5$  and the shielding fraction is reduced systematically (almost linearly) as  $x$  becomes smaller than  $x \approx 0.3$ . This trend, together with the EPMA result that the actual Cu concentration varies on a sub-mm scale, suggests that  $\text{Cu}_x\text{Bi}_2\text{Se}_3$  has a tendency to phase segregate and that there is a spontaneous formation of small islands in which the local Cu concentration is essentially the optimum value for superconductivity. In view of the fact that the  $T_c$  of this material is uncharacteristically high for a low-carrier-density superconductor<sup>38</sup> with  $n \sim 10^{20} \text{ cm}^{-3}$ , the present observation seems to imply that the inhomogeneous nature of the superconductivity may partly be responsible for the anomalously high  $T_c$ .<sup>39</sup> Furthermore, the unexpected drop of the shielding fraction for  $x > 0.5$  suggests that the inhomogeneity may be necessary for the occurrence of superconductivity in this material.

If  $\text{Cu}_x\text{Bi}_2\text{Se}_3$  indeed has a tendency toward phase segregation to spontaneously form small superconducting islands, it naturally explains why a high-temperature annealing is necessary for activating the superconductivity: It allows Cu atoms to move and promotes the formation of superconducting islands. If annealed at too high a temperature, the material seems to melt partly, the crystal structure degrades, and eventually the superconductivity is destroyed irreversibly. Indeed, the melting temperature of  $\text{Cu}_x\text{Bi}_2\text{Se}_3$  appears to be systematically reduced with  $x$ , and our test sample with  $x = 1.4$ , which was initially rectangular shaped, became sphere-like after annealing at 560 °C. (Note that the melting point of pure  $\text{Bi}_2\text{Se}_3$  is 706 °C.) Therefore, the optimal annealing temperature corresponds to the one that maximally promotes the motion of Cu atoms while avoiding degradation of the matrix due to partial melting.

#### V. SUMMARY

In summary, we have synthesized superconducting  $\text{Cu}_x\text{Bi}_2\text{Se}_3$  by an electrochemical intercalation method, which yields samples with much higher superconducting shielding fractions compared to those prepared by the melt-growth technique previously employed. The superconductivity was observed for  $0.09 \leq x \leq 0.64$ , which is much wider than previously reported, and the transition temperature  $T_c$  was found to show an unexpected monotonic decrease with  $x$ . Also, the largest attainable shielding fraction was found to be strongly dependent on  $x$ , and its  $x$  dependence suggests that  $\text{Cu}_x\text{Bi}_2\text{Se}_3$  has a tendency to phase segregate and form small superconducting islands.

#### ACKNOWLEDGMENTS

We acknowledge the technical support from the Comprehensive Analysis Center, Institute of Scientific and Industrial Research, Osaka University, for the ICP-AES and the EPMA analyses. This work was supported by JSPS (NEXT Program), MEXT (Innovative Area “Topological Quantum Phenomena” KAKENHI 22103004), and AFOSR (AOARD 10-4103).

\*mkriener@sanken.osaka-u.ac.jp

†Corresponding author: y\_ando@sanken.osaka-u.ac.jp

- <sup>1</sup>L. Fu, C. L. Kane, and E. J. Mele, *Phys. Rev. Lett.* **98**, 106803 (2007).
- <sup>2</sup>J. E. Moore and L. Balents, *Phys. Rev. B* **75**, 121306(R) (2007).
- <sup>3</sup>R. Roy, *Phys. Rev. B* **79**, 195322 (2009).
- <sup>4</sup>M. Z. Hasan and C. L. Kane, *Rev. Mod. Phys.* **82**, 3045 (2010).
- <sup>5</sup>J. E. Moore, *Nature* **464**, 194 (2010).
- <sup>6</sup>X. Qi and S. Zhang, Topological insulators and superconductors, e-print [arXiv:1008.2026v1](https://arxiv.org/abs/1008.2026v1) (to be published).
- <sup>7</sup>L. Fu and C. L. Kane, *Phys. Rev. B* **76**, 045302 (2007).
- <sup>8</sup>H.-J. Zhang, C.-X. Liu, X.-L. Qi, X. Dai, Z. Fang, and S.-C. Zhang, *Nat. Phys.* **5**, 438 (2009).
- <sup>9</sup>D. Hsieh, D. Qian, L. Wray, Y. Xia, Y. S. Hor, R. J. Cava, and M. Z. Hasan, *Nature* **452**, 970 (2008).
- <sup>10</sup>A. A. Taskin and Y. Ando, *Phys. Rev. B* **80**, 085303 (2009).
- <sup>11</sup>A. Nishide, A. A. Taskin, Y. Takeichi, T. Okuda, A. Kakizaki, T. Hirahara, K. Nakatsuji, F. Komori, Y. Ando, and I. Matsuda, *Phys. Rev. B* **81**, 041309(R) (2010).
- <sup>12</sup>Y. L. Chen, J. G. Analytis, J.-H. Chu, Z. K. Liu, S.-K. Mo, X. L. Qi, H. J. Zhang, D. H. Lu, X. Dai, Z. Fang, S. C. Zhang, I. R. Fisher, Z. Hussain, and Z.-X. Shen, *Science* **325**, 178 (2009).
- <sup>13</sup>D. Hsieh, Y. Xia, D. Qian, L. Wray, F. Meier, J. H. Dil, J. Osterwalder, L. Patthey, A. V. Fedorov, H. Lin, A. Bansil, D. Grauer, Y. S. Hor, R. J. Cava, and M. Z. Hasan, *Phys. Rev. Lett.* **103**, 146401 (2009).
- <sup>14</sup>Y. Xia, D. Qian, D. Hsieh, L. Wray, A. Pal, H. Lin, A. Bansil, D. Grauer, Y. S. Hor, R. J. Cava, and M. Z. Hasan, *Nat. Phys.* **5**, 398 (2009).
- <sup>15</sup>T. Sato, K. Segawa, H. Guo, K. Sugawara, S. Souma, T. Takahashi, and Y. Ando, *Phys. Rev. Lett.* **105**, 136802 (2010).
- <sup>16</sup>K. Kuroda, M. Ye, A. Kimura, S. V. Ereemeev, E. E. Krasovskii, E. V. Chulkov, Y. Ueda, K. Miyamoto, T. Okuda, K. Shimada, H. Namatame, and M. Taniguchi, *Phys. Rev. Lett.* **105**, 146801 (2010).
- <sup>17</sup>Y. L. Chen, Z. K. Liu, J. G. Analytis, J.-H. Chu, H. J. Zhang, B. H. Yan, S.-K. Mo, R. G. Moore, D. H. Lu, I. R. Fisher, S.-C. Zhang, Z. Hussain, and Z.-X. Shen, *Phys. Rev. Lett.* **105**, 266401 (2010).
- <sup>18</sup>Z. Ren, A. A. Taskin, S. Sasaki, K. Segawa, and Y. Ando, *Phys. Rev. B* **82**, 241306(R) (2010).
- <sup>19</sup>S. Xu, L. Wray, Y. Xia, R. Shankar, A. Petersen, A. Fedorov, H. Lin, A. Bansil, Y. Hor, D. Grauer, R. Cava, and M. Hasan, Discovery of several large families of Topological Insulator classes with backscattering-suppressed spin-polarized single-Dirac-cone on the surface, e-print [arXiv:1007.5111v1](https://arxiv.org/abs/1007.5111v1).
- <sup>20</sup>J. Xiong, A. C. Petersen, Dongxia Qu, R. J. Cava, and N. P. Ong, Quantum oscillations in a topological insulator Bi<sub>2</sub>Te<sub>2</sub>Se with large bulk resistivity, e-print [arXiv:1101.1315](https://arxiv.org/abs/1101.1315).
- <sup>21</sup>A. A. Taskin, Z. Ren, S. Sasaki, K. Segawa, and Y. Ando, *Phys. Rev. Lett.* **107**, 016801 (2011).
- <sup>22</sup>L. Fu and C. L. Kane, *Phys. Rev. Lett.* **100**, 096407 (2008).
- <sup>23</sup>A. P. Schnyder, S. Ryu, A. Furusaki, and A. W. W. Ludwig, *Phys. Rev. B* **78**, 195125 (2008).
- <sup>24</sup>X.-L. Qi, T. L. Hughes, S. Raghu, and S.-C. Zhang, *Phys. Rev. Lett.* **102**, 187001 (2009).
- <sup>25</sup>X.-L. Qi, T. L. Hughes, and S.-C. Zhang, *Phys. Rev. B* **81**, 134508 (2010).
- <sup>26</sup>J. Linder, Y. Tanaka, T. Yokoyama, A. Sudbø, and N. Nagaosa, *Phys. Rev. Lett.* **104**, 067001 (2010).
- <sup>27</sup>M. Sato, *Phys. Rev. B* **81**, 220504(R) (2010).
- <sup>28</sup>L. Fu and E. Berg, *Phys. Rev. Lett.* **105**, 097001 (2010).
- <sup>29</sup>Y. S. Hor, A. J. Williams, J. G. Checkelsky, P. Roushan, J. Seo, Q. Xu, H. W. Zandbergen, A. Yazdani, N. P. Ong, and R. J. Cava, *Phys. Rev. Lett.* **104**, 057001 (2010).
- <sup>30</sup>L. A. Wray, S.-Y. Xu, Y. Xia, Y. S. Hor, D. Qian, A. V. Fedorov, H. Lin, A. Bansil, R. J. Cava, and M. Z. Hasan, *Nat. Phys.* **6**, 855 (2010).
- <sup>31</sup>M. Kriener, K. Segawa, Z. Ren, S. Sasaki, and Y. Ando, *Phys. Rev. Lett.* **106**, 127004 (2011).
- <sup>32</sup>L. P. Caywood and G. R. Miller, *Phys. Rev. B* **2**, 3209 (1970).
- <sup>33</sup>A. Vaško, L. Tichý, J. Horák, and J. Weissenstein, *Appl. Phys.* **5**, 217 (1974).
- <sup>34</sup>For example, the wavelength dispersive X-ray spectroscopy (WDS) analysis, which is a non-destructive method and is often employed in the chemical content analysis, is sensitive to relative differences, but it is not good at giving absolute numbers.
- <sup>35</sup>As for the optimization of the annealing time, we have annealed several samples that were already annealed at 560 °C for 2 h for various additional durations of time at the same temperature; annealing for a few additional hours did not improve the shielding fraction, and a long-term annealing (more than a day) usually resulted in a decrease in the shielding fraction. Separately, we found that an annealing for less than 1 h did not establish superconductivity. We therefore settled on the 2-h annealing procedure to minimize the sample preparation time.
- <sup>36</sup>The detailed results of the ICP-AES analyses are the following: the  $x$  values of the eight samples determined from the mass change were 0.117, 0.128, 0.266, 0.286, 0.293, 0.295, 0.308, and 0.318; for these samples, the  $x$  values determined by the ICP-AES analyses were 0.114, 0.128, 0.279, 0.300, 0.299, 0.282, 0.303, and 0.319, respectively; therefore, the differences between the two were 0.003, 0.000, −0.013, −0.014, −0.006, 0.013, 0.005, and −0.001.
- <sup>37</sup>J. Bludská, S. Karamazov, J. Navrátil, I. Jakubec, and J. Horák, *Solid State Ionics* **171**, 251 (2004).
- <sup>38</sup>M. L. Cohen, in *Superconductivity*, edited by R. D. Parks (Marcel Dekker, New York, 1969), Vol. 1, chap. 12.
- <sup>39</sup>I. Martin, D. Podolsky, and S. A. Kivelson, *Phys. Rev. B* **72**, 060502(R) (2005).

# Topological transition in $\text{Bi}_{1-x}\text{Sb}_x$ studied as a function of Sb doping

Fumitaka Nakamura,<sup>1</sup> Yuka Kousa,<sup>2</sup> Alexey A. Taskin,<sup>3</sup> Yasuo Takeichi,<sup>1</sup> Akinori Nishide,<sup>1</sup> Akito Kakizaki,<sup>1</sup> Marie D'Angelo,<sup>4</sup> Patrick Lefevre,<sup>5</sup> Francois Bertran,<sup>5</sup> Amina Taleb-Ibrahimi,<sup>5</sup> Fumio Komori,<sup>1</sup> Shin-ichi Kimura,<sup>6</sup> Hiroshi Kondo,<sup>2</sup> Yoichi Ando,<sup>3,\*</sup> and Iwao Matsuda<sup>1,†</sup>

<sup>1</sup>*Institute for Solid State Physics, University of Tokyo, Kashiwa, Chiba 277-8581, Japan*

<sup>2</sup>*Faculty of Science and Technology, Keio University, Yokohama, Kanagawa 223-8522, Japan*

<sup>3</sup>*Institute of Scientific and Industrial Research, Osaka University, Ibaraki, Osaka 567-0047, Japan*

<sup>4</sup>*Institut des Nanosciences de Paris, Université Pierre et Marie Curie-Paris 6, CNRS-UMR 7588, 4 place Jussieu, F-75252 Paris, France*

<sup>5</sup>*Cassiopee Beamline, synchrotron SOLEIL/CNRS, BP 48, F-91192 Gif-Sur-Yvette, France*

<sup>6</sup>*UVSOR Facility, Institute for Molecular Science, Okazaki 444-8585, Japan*

(Received 1 June 2011; revised manuscript received 11 October 2011; published 6 December 2011)

Spin- and angle-resolved photoemission spectroscopy measurements were performed on  $\text{Bi}_{1-x}\text{Sb}_x$  samples at  $x = 0.04, 0.07$ , and  $0.21$  to study the change of the surface band structure from nontopological to topological. Energy shift of the  $T$  and  $L_s$  bulk bands with Sb concentration is quantitatively evaluated. An edge state becomes topologically nontrivial at  $x = 0.04$ . An additional trivial edge state appears at the  $L$  band gap that forms at  $x > 0.04$  and apparently hybridize with the nontrivial edge state. A scenario for the topological transition mechanism is presented. Related issues of self-energy and temperature dependence of the surface state are also considered.

DOI: [10.1103/PhysRevB.84.235308](https://doi.org/10.1103/PhysRevB.84.235308)

PACS number(s): 73.20.-r, 79.60.-i

## I. INTRODUCTION

Bismuth-antimony alloy has long been studied for its thermoelectronic properties,<sup>1</sup> and recently it has been vigorously investigated as a topological insulator.<sup>2</sup> A topological insulator is a material realizing a nontrivial topology in the valence-band wave function. While an energy gap is present for the bulk bands, the edge state is gapless and carries spin current that is topologically protected from scattering by a nonmagnetic impurity.<sup>3-5</sup> Three-dimensional materials are theoretically characterized with eight time-reversal-invariant momenta, and they are classified with four topological invariants,<sup>6</sup>  $\nu_0; (\nu_1 \nu_2 \nu_3)$ . A (111)-crystal surface of  $\text{Bi}_{1-x}\text{Sb}_x$  ( $x > 0.07$ ) or an Sb crystal is in the topologically nontrivial 1;(111) class, while a Bi crystal is in the topologically trivial 0;(000) class. Doping of Sb atoms into a semimetal Bi crystal results in a quantum phase transition to a topologically insulating  $\text{Bi}_{1-x}\text{Sb}_x$  crystal. Recent photoemission experiments have proven its nature as a topological insulator by observing the odd number of band crossings of the edge states at the Fermi level.<sup>2,7</sup> Bulk band energy shift with Sb doping is crucial for Bi to be a topological insulator, but only “indirect” experiments concerning topological insulators, such as transport measurements, have been performed using Sb doping of Bi.<sup>8</sup> Therefore, direct observation of the bulk band shift and the associated evolution of edge-state band dispersions using, for example, photoemission spectroscopy, is needed for comprehensive understanding.

In the present research, we systematically measured the evolution of the electronic structure of  $\text{Bi}_{1-x}\text{Sb}_x$  at different Sb concentrations ( $x = 0.04, 0.07$ , and  $0.21$ ) by momentum- and spin-resolved photoemission spectroscopy to trace the topological transition from Rashba-split trivial surface states to topological surface states. Shifts of the bulk bands with  $x$  are quantitatively evaluated. Changes of the surface-state band structure are experimentally determined. The  $\Sigma_2$  band becomes topologically nontrivial, connecting the bulk  $T$

valence band and the bulk  $L_a$  conduction band at around  $x = 0.04$ . The additional  $\Sigma'_1$  band appears in the  $L$  gap above  $x = 0.04$ . Surface band structures of the topological  $\text{Bi}_{1-x}\text{Sb}_x$  insulator are likely a result of hybridization between nontrivial edge states and trivial surface states, as proposed in previous theoretical research.<sup>9</sup> In the present article, the related issues of quasiparticle lifetime and the thermal effect of the surface state are also discussed.

## II. EXPERIMENTS

High-resolution momentum- and spin-resolved photoemission spectroscopy experiments were performed at the CASSIOPEE beamline (SOLEIL, France) and at the BL-19A beamline (KEK-PF, Japan), respectively. Angle-resolved photoemission spectroscopy (ARPES) measurements were performed with a hemispherical photoelectron spectrometer (VG Scienta R4000) at an energy resolution of 18 meV and an angular resolution of  $\pm 0.1^\circ$ . Linearly and circularly polarized light at photon energies ranging from 14 to 32 eV were used. The spectra were detected under  $7 \times 10^{-9}$  Pa at 4 K, if not specified in the article. Spin- and angle-resolved photoemission spectroscopy (SARPES) measurements were done with a He-I  $\alpha$  source and with a hemispheric analyzer (SPECS Phoibos150) equipped with a home-made, high-yield, very-low-energy electron diffraction (VLEED) spin polarimeter.<sup>10,11</sup> The energy and angle resolutions of the analyzer were 50 meV and  $\pm 1^\circ$ , respectively. The spectra were detected under  $3 \times 10^{-8}$  Pa at 130 K. The effective Sherman function was  $S_{\text{eff}} = 0.29 \pm 0.04$ , which was calibrated in advance with the spin polarization of secondary electrons from Ni(110).  $\text{Bi}_{1-x}\text{Sb}_x$  crystals were grown from a stoichiometric mixture of 99.9999% purity Bi and Sb elements by a zone-melting method.  $\text{Bi}_{1-x}\text{Sb}_x$  samples with  $x = 0.04, 0.07$ , and  $0.21$  were used in this experiment. The crystals were cleaved along the (111) plane below 130 K. The Sb composition of the surface



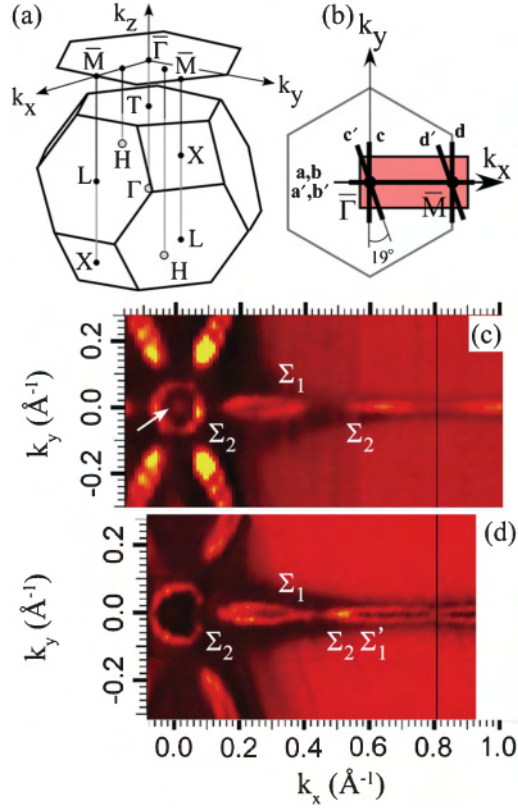


FIG. 1. (Color online) (a) Three-dimensional Brillouin zone and its projection onto the (111) surface. High-symmetry points in the (surface) Brillouin zones are indicated. (b) The surface Brillouin zone (SBZ) is depicted for the measured region in (c) and (d). Thick lines, labeled alphabetically, are the directions of angle-resolved photoemission data shown in the following figures. (c) and (d) are Fermi surfaces of  $\text{Bi}_{1-x}\text{Sb}_x$  at (c)  $x = 0.04$  and (d)  $x = 0.21$ , taken at  $h\nu = 29$  eV. The black solid line corresponds to the zone boundary. Circularly polarized light was used in (c), and linearly polarized light in (d).

was checked with electron-probe microanalysis (EPMA), showing lateral compositional homogeneity over the length scale of the photon beam size for the ARPES measurements. The crystal orientations were determined by *ex situ* x-ray diffraction, *in situ* low-energy electron diffraction (LEED), and by photoemission Fermi surface mapping. Figure 1 shows the normalized photoemission intensity distribution at the Fermi level ( $\pm 5$  meV) of  $\text{Bi}_{1-x}\text{Sb}_x$  for  $x = 0.04$  [Fig. 1(c)] and  $x = 0.21$  [Fig. 1(d)], obtained with photon energy  $h\nu = 29$  eV. The spectral features indicated by arrows and labels are described below.

### III. RESULTS AND DISCUSSION

#### A. Sb dependence of $\text{Bi}_{1-x}\text{Sb}_x$ electronic structure of bulk and surface-state bands

Figures 2(a) and 2(b) show a series of ARPES spectra and the gray-scale band diagram of  $\text{Bi}_{1-x}\text{Sb}_x$  ( $x = 0.04$ ) taken along the  $\bar{\Gamma}$ - $\bar{M}$  direction, or  $k_x$  axis. The measurement directions for Fig. 2 are indicated in Fig. 1(b). Prominent peaks at  $\bar{\Gamma}$  are assigned to the bulk band (b), and the spectral tail, extending to the Fermi level ( $E_F$ ), has created intensity in the

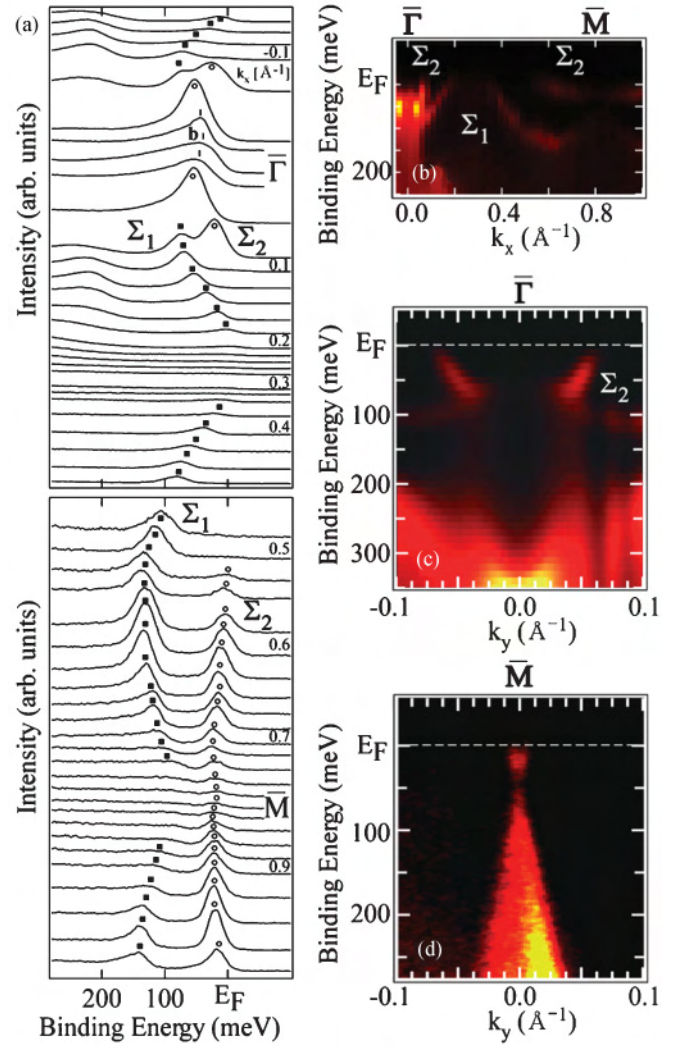


FIG. 2. (Color online) A collection of ARPES spectra of  $\text{Bi}_{1-x}\text{Sb}_x$  ( $x = 0.04$ ). The data, taken along the  $a$ ,  $b$ ,  $c$ , and  $d$  lines in the SBZ in Fig. 1(b), are presented in (a), (b), (c), and (d), respectively. Data were obtained at  $h\nu = 29$  eV (circularly polarized light). Peak positions of the edge state (surface state) and bulk bands are marked with symbols.

photoemission Fermi surface as indicated by the white arrow in Fig. 1(c). The assignment of the bulk band was confirmed by observing band dispersion along the  $k_z$  direction by changing photon energy. Figure 2(c) displays the photoemission band diagram along the  $k_y$  axis around  $\bar{\Gamma}$ . The  $\Sigma_1$  and  $\Sigma_2$  states, identified in the figures, lose photoemission intensity as they disperse in the bulk band region at  $\bar{\Gamma}$ . This is due to matching of the surface state with the bulk state, forming surface resonance. This causes the lifetime of a hole, created by photoemission process, to be short, resulting in suppression of photoemission intensity. These spectral features indicate that the maximum of the bulk valence band ( $T$  band<sup>1</sup>) at  $\bar{\Gamma}$  is located nearly at  $E_F$ .

Along the  $\bar{\Gamma}$ - $\bar{M}$  direction, as shown in Figs. 2(a) and 2(b), two surface states  $\Sigma_1$  and  $\Sigma_2$  around  $\bar{\Gamma}$  shift to lower binding energy ( $E_B$ ) as  $k_x$  increases, and they cross  $E_F$ . Then  $\Sigma_1$  and  $\Sigma_2$  reappear at  $E_F$  at  $k_x \sim 0.35$  and  $0.5 \text{ \AA}^{-1}$ , respectively.



The  $\Sigma_2$  band moves to higher binding energy as it approaches  $\bar{M}$ , while the  $\Sigma_1$  band presents a shallow bottom around  $k_x \sim 0.6 \text{ \AA}^{-1}$ . As shown in Fig. 1(c), Fermi surfaces of the  $\Sigma_2$  band are a hexagonal electron pocket at  $\bar{\Gamma}$  and oval electron pockets along the  $\bar{\Gamma}$ – $\bar{M}$  axis, while those of the  $\Sigma_1$  band are oval hole pockets also along the  $\bar{\Gamma}$ – $\bar{M}$  axis. At the  $\bar{M}$  point, as shown in Fig. 2(d), a Dirac cone with a large Fermi velocity is observed with the energy gap.<sup>12</sup> The lower band can be assigned to the bulk  $L_s$  band. Since the binding energy of the  $\Sigma_2$  band shown in Fig. 2(a) is about 25 meV, which is lower than the gap at 50 meV, the upper band of the Dirac cone is likely the bulk  $L_a$  band, which is connected with the dispersion curve of the  $\Sigma_2$  band. The matching of the edge state with the bulk state is ascertained by reduction of its photoemission intensity at  $\bar{M}$ .

Figure 3(a) shows a sequence of ARPES spectra of  $\text{Bi}_{1-x}\text{Sb}_x$  ( $x = 0.21$ ) taken along the  $\bar{\Gamma}$ – $\bar{M}$  ( $k_x$ ) direction. In contrast to

Fig. 2(a), one finds little intensity near  $E_F$  at  $\bar{\Gamma}$  in Fig. 3(a). Absence of the bulk band indicates a larger energy gap at  $\bar{\Gamma}$ , and thus the dispersion curve of the  $\Sigma_2$  surface state is much clearer, as shown in Fig. 3(b). Dispersions of the  $\Sigma_1$  and  $\Sigma_2$  bands along the  $\bar{\Gamma}$ – $\bar{M}$  axis in Fig. 3(a) are similar to those of the  $x = 0.04$  sample in Fig. 2(a). Additionally, the  $\Sigma'_1$  band was observed as having peak shoulders near the  $\bar{M}$  point. Its existence was verified by detailed comparisons among the ARPES spectra and by peak fitting with Voigt functions. Figure 4(a) shows ARPES spectra at  $\bar{M}$  of  $\text{Bi}_{1-x}\text{Sb}_x$  crystals at  $x = 0.04$  and  $x = 0.21$ , indicating that both peaks are of the same width. On the other hand, at  $k_x = 0.7 \text{ \AA}^{-1}$  [Fig. 4(b)], the spectral width of the  $x = 0.21$  sample is broader than that of the  $x = 0.04$  one. This indicates existence of two edge states in the  $x = 0.21$  spectrum, which is not inconsistent with the observation of a single peak at time-reversal-invariant momentum ( $\bar{M}$ ). To trace the two edge states  $\Sigma_2$  and  $\Sigma'_1$  near  $E_F$ , the ARPES spectra of the  $x = 0.21$  crystal around  $\bar{M}$  are curve fitted with Voigt functions. The Gaussian width was set at 18 meV, corresponding to the total experimental resolution. The Lorentzian width was determined from the ARPES spectra of the  $x = 0.04$  sample [Fig. 4(c)] and from the spectrum of the  $x = 0.21$  sample at the  $\bar{M}$  point. The Fermi-Dirac function is also included in the fit. As shown in Fig. 4(d), each spectrum is well fitted. The  $\Sigma'_1$  band appears and merges with the  $\Sigma_2$  band at the  $\bar{M}$  point. In Fig. 1(d), Fermi surfaces of a hexagonal electron pocket at  $\bar{\Gamma}$  and oval hole pockets are assigned to  $\Sigma_2$  and  $\Sigma_1$ , respectively. The oval Fermi surfaces of electron pockets near  $\bar{M}$  originate from the  $\Sigma_2$  and  $\Sigma'_1$  bands.

Figure 5(a) compares the energy spectra at the  $\bar{\Gamma}$  point of the three-dimensional BZ ( $\bar{\Gamma}$  of SBZ) between the  $\text{Bi}_{1-x}\text{Sb}_x$   $x = 0.04$  and 0.21 samples. As described above, a peak at  $x = 0.04$  is assigned to the bulk  $T$  band, and it shows an energy shift of at least 120 meV ( $\pm 30$  meV) toward higher binding energy at  $x = 0.21$ . Figure 5(b) displays ARPES spectra at the  $\bar{M}$  point of SBZ for the  $\text{Bi}_{1-x}\text{Sb}_x$   $x = 0.04$  and 0.21 samples, also showing higher  $E_B$  shift of the spectral bulk band edge with higher Sb concentration. The energy change corresponds to that of the  $L_s$  band. Figure 5(c) shows evolution of the bulk band structure of the  $\text{Bi}_{1-x}\text{Sb}_x$  alloy as a function of Sb concentration  $x$ , estimated in the transport research<sup>1</sup> and evaluated by previous and present photoemission research.<sup>2</sup> Sb doping of the Bi crystal first reduces the energy gap between the two different parity bands  $L_s$  and  $L_a$  at the  $L$  point, and shifts the  $T$  band to higher binding energy. Corresponding symmetry points are labeled in Fig. 1(a). Around  $x = 0.04$ , the  $L_s$  and  $L_a$  bands cross each other and the gap reopens with inverted ordering. Then the top of the valence band at  $T$  comes down further in energy and crosses the bottom of the conduction band at  $x = 0.07$ . At this point, the indirect gap becomes positive, and the alloy has become an insulator. At  $x = 0.09$ , the  $T$  valence band clears the  $L_s$  valence band, and the alloy is a direct-gap insulator at the  $L$  points. As  $x$  is increased further, the gap increases until it reaches its maximum value at  $x = 0.18$ . At that point, the valence band at  $H$  crosses the  $L_s$  valence band. For  $x = 0.22$ , the  $H$  band crosses the  $L_a$  conduction band, and the alloy becomes a semimetal again. As indicated in the band diagram

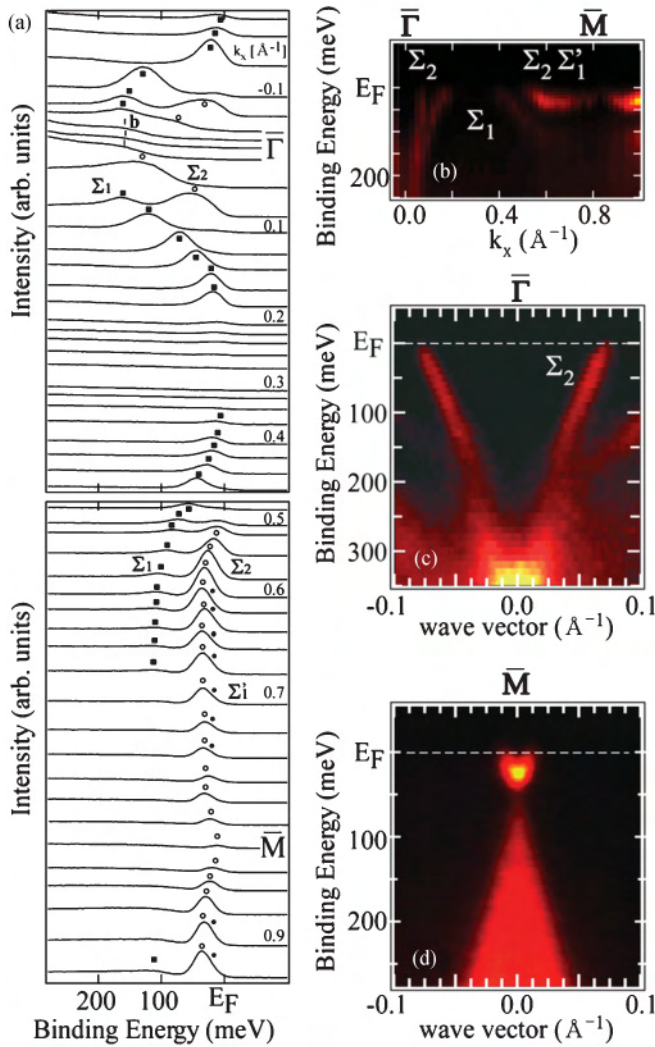


FIG. 3. (Color online) A collection of ARPES spectra of  $\text{Bi}_{1-x}\text{Sb}_x$  ( $x = 0.21$ ). The data, taken along  $a'$ ,  $b'$ ,  $c'$ , and  $d'$  lines in the SBZ in Fig. 1(b), are presented in (a), (b), (c), and (d), respectively. Data were obtained at  $h\nu = 29$  eV (linearly polarized light). Peak positions of the edge state (surface state) and bulk bands are marked with symbols.

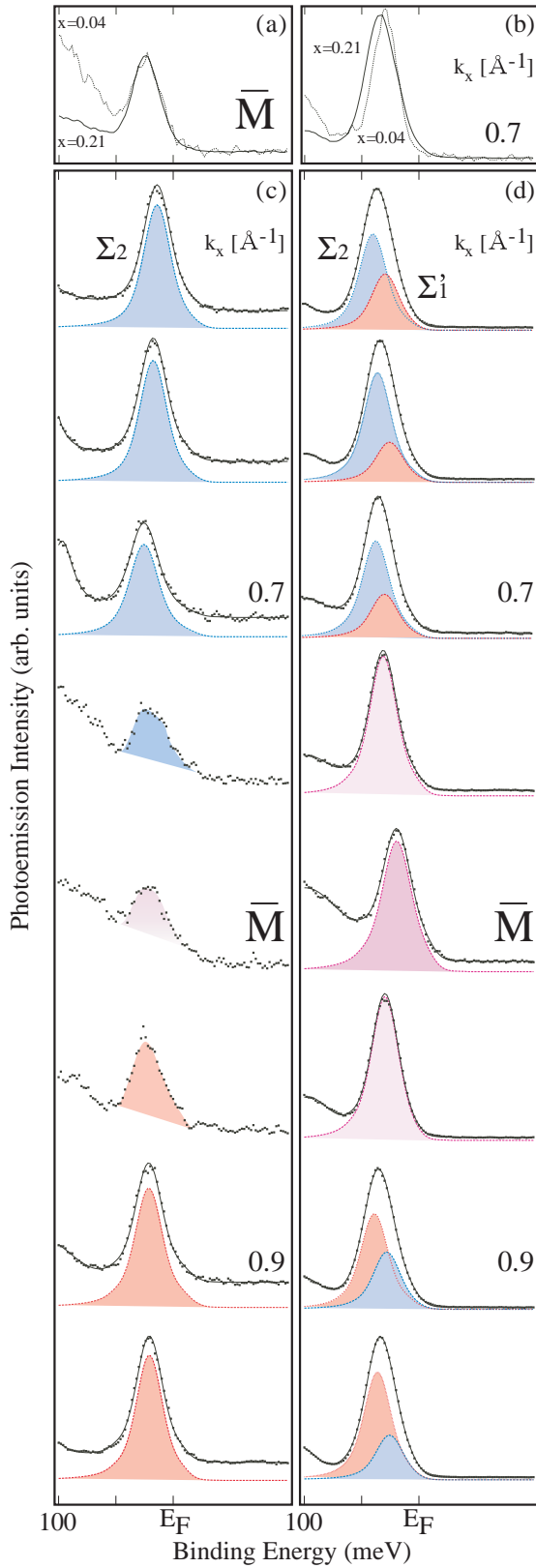


FIG. 4. (Color online) (a) and (b) show ARPES spectra of  $\text{Bi}_{1-x}\text{Sb}_x$  at (a) the  $\bar{M}$  point and (b)  $k_x = 0.7 \text{ \AA}^{-1}$  for the  $x = 0.04$  and  $0.21$  samples, measured at  $h\nu = 29 \text{ eV}$  (linearly polarized light). (c) and (d) show a collection of ARPES spectra with the fitted Voigt functions around the  $\bar{M}$  point from (c) Fig. 2 and (d) Fig. 3.

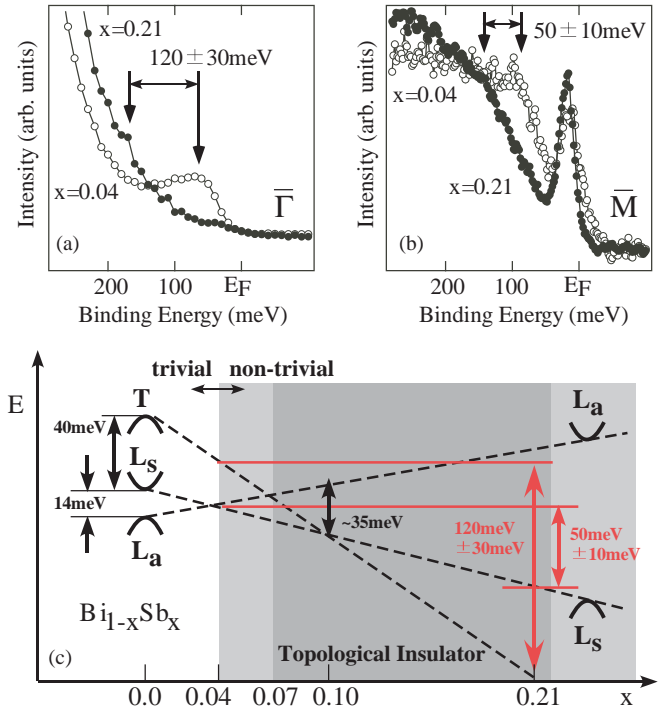


FIG. 5. (Color online) (a) ARPES spectra of  $\text{Bi}_{1-x}\text{Sb}_x$  at  $\bar{\Gamma}$  for the  $x = 0.04$  and  $0.21$  samples, measured at  $h\nu = 23 \text{ eV}$  (linearly polarized light). (b) ARPES spectra of  $\text{Bi}_{1-x}\text{Sb}_x$  at the  $\bar{M}$  point for the  $x = 0.04$  and  $0.21$  samples, measured at  $h\nu = 29 \text{ eV}$  (circularly polarized light). (c) Schematic representation<sup>6</sup> of the bulk band energy evolution of  $\text{Bi}_{1-x}\text{Sb}_x$  as a function of  $x$ . The energy differences of the bulk bands, evaluated by the present and previous research,<sup>2</sup> are overlapping.

in Fig. 1(a),  $\text{Bi}_{1-x}\text{Sb}_x$  becomes a topological insulator at  $x = 0.07$ – $0.22$ .

Based on these results, Fig. 6 summarizes the electronic structure of the  $\text{Bi}_{1-x}\text{Sb}_x(111)$  surface at (a)  $x = 0.04$  and (b)  $x = 0.21$ . Around  $x = 0.04$ , the  $L_a$  and  $L_s$  bands are likely to close the energy gap and form a Dirac-cone dispersion. The bulk is metallic. Two metallic surface-state bands  $\Sigma_1$  and  $\Sigma_2$  exist in the bulk band gap. The  $\Sigma_2$  band connects to the bulk band at the electron side of the Dirac cone.<sup>12</sup> On the other hand, at  $x = 0.21$  the bulk is insulating and three metallic surface-state bands  $\Sigma_1$ ,  $\Sigma_2$ , and  $\Sigma'_1$  are identified within the bulk band gap. There exist five  $E_F$  crossings of the surface-state band. The odd-number nature classifies  $\text{Bi}_{1-x}\text{Sb}_x$  ( $x = 0.21$ ) as topologically nontrivial, and thus the material is a topological insulator. These results are consistent with previous photoemission research with different Sb compositions.<sup>2,7,11,13</sup>

### B. Spin-polarized surface band structure at $x = 0.07$

It has been reported for  $\text{Bi}_{1-x}\text{Sb}_x(111)$  at  $x = 0.0$  and  $0.12$  that edge states (surface states) of  $\text{Bi}_{1-x}\text{Sb}_x(111)$  are spin split, and that spin-polarized surface band structure occurs over the surface Brillouin zone.<sup>7,11,14</sup> Along the  $\bar{\Gamma}$ – $\bar{M}$  axis, one spin-up and one spin-down surface-state bands of the Rashba effect were detected for a pure Bi(111) surface,<sup>14</sup>

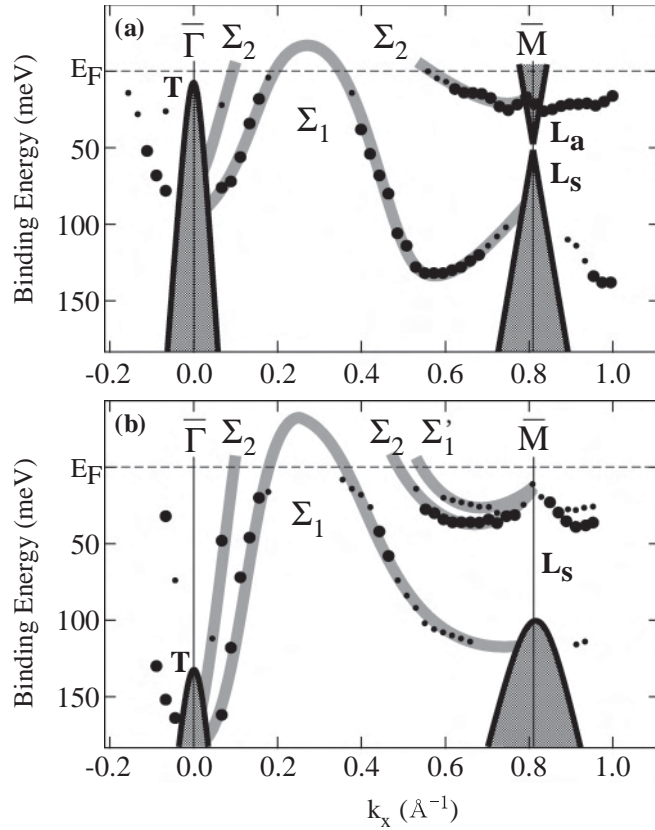


FIG. 6. Spin-integrated photoemission band diagram of  $\text{Bi}_{1-x}\text{Sb}_x$  crystals at (a)  $x = 0.04$  and (b)  $x = 0.21$ , determined from ARPES spectra in Figs. 2 and 3. The small and large symbols represent the rather distinctive and the weak spectral features, respectively. The shaded region is the bulk band structure projected onto the SBZ. The edge state and bulk bands are labeled.

while three spin-polarized edge-state bands, i.e., two spin-up and one spin-down, were observed for  $x = 0.12$  by spin- and angle-resolved photoemission spectroscopy (SARPES) measurements.<sup>7,11</sup> In order to trace the evolution of the spin structure during the topological transition, SARPES measurements were performed on the  $\text{Bi}_{1-x}\text{Sb}_x(111)$  surface at an intermediate Sb concentration of  $x = 0.07$ . Figure 7 shows a series of spin-up and spin-down SARPES measurements along the  $\bar{\Gamma}$ – $\bar{M}$  direction. Around  $\bar{\Gamma}$ , spin-up  $\Sigma_1$  and spin-down  $\Sigma_2$  bands are identified at positive wave vector ( $k$ ). Spin characteristics of the two bands are inverted at the opposite  $k$  side of  $\bar{\Gamma}$  or in the negative wave-vector region. Near  $\bar{M}$ , one spin-down band,  $\Sigma_2$ , can be identified at  $k$  values smaller than the  $\bar{M}$  point. The band takes the opposite spin orientation as it passes the  $\bar{M}$  point. The previous spin-resolved photoemission research of  $\text{Bi}_{1-x}\text{Sb}_x$  at  $x = 0.12$  observed both the  $\Sigma_2$  and  $\Sigma'_1$  bands around  $\bar{M}$  with comparable photoemission intensity. The dispersion of the  $\Sigma_2$  band for  $x = 0.07$  suggests that the Dirac point of the surface state, namely, the crossing between the  $\Sigma_2$  and  $\Sigma'_1$  bands, accidentally coincides with the Fermi energy; this means that the  $\Sigma'_1$  band is located above  $E_F$  and is invisible in the present data for  $x = 0.07$ .

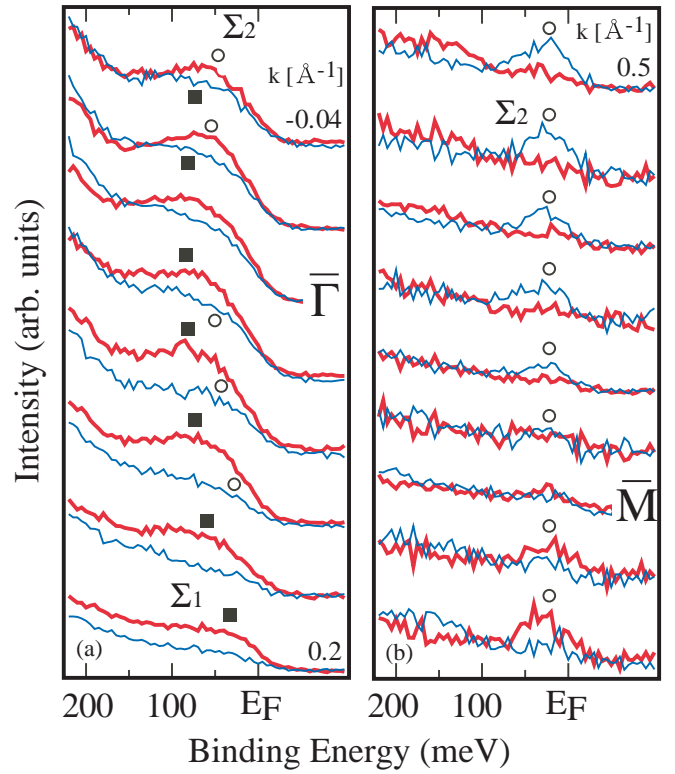


FIG. 7. (Color online) A sequence of SARPES spectra of  $\text{Bi}_{1-x}\text{Sb}_x$  ( $x = 0.07$ ) along the  $\bar{\Gamma}$ – $\bar{M}$  direction. Spin-up and spin-down SARPES data spectra around  $\bar{\Gamma}$  and  $\bar{M}$  are shown in (a) and (b), respectively. Peak positions of the edge-state (surface-state) bands are marked with symbols.

### C. A scenario of the topological transition

From these results, a scenario of the topological transition mechanism of  $\text{Bi}_{1-x}\text{Sb}_x$  may be summarized as shown in Fig. 8. For pure Bi ( $x = 0.0$ ), surface-state bands with opposite spin orientations  $\Sigma_1$  and  $\Sigma_2$  disperse separately within the bulk band gap, as shown in Fig. 8(a). The  $\Sigma_1$  and  $\Sigma_2$  bands connect bulk valence bands of the  $T$  band and the  $L_a$  band at  $\bar{\Gamma}$  and at  $\bar{M}$ , respectively. Around  $x = 0.04$ , the bulk  $L_a$  and  $L_s$  bands

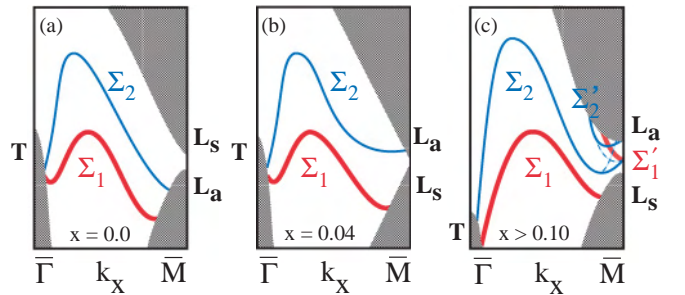


FIG. 8. (Color online) A sequence of surface electronic structure during the topological transition of  $\text{Bi}_{1-x}\text{Sb}_x(111)$  from the surface Rashba phase to the quantum spin-Hall phase. (a)  $x = 0$ , trivial pure Bi semimetal with trivial surface states  $\Sigma_1$  and  $\Sigma_2$ . (b)  $x = 0.04$ . (c)  $x > 0.10$ , topological insulator with a nontrivial edge state  $\Sigma_2$  and trivial edge states  $\Sigma_1$ ,  $\Sigma'_1$ , and  $\Sigma'_2$ , with spin-selective hybridization. The original band dispersions are shown as broken lines.



touch each other, forming a Dirac cone, and then an energy gap is formed between the conduction-band minimum of the  $L_a$  band and the valence-band maximum of the  $L_s$  band.<sup>12</sup> At this stage the  $\Sigma_2$  band, being topologically nontrivial, connects the bulk  $T$  valence band at  $\bar{\Gamma}$  and the bulk  $L_a$  conduction band at  $\bar{M}$ . The change of the surface electronic structure matches the transition mechanism based on the theoretical simulation.<sup>9</sup> Above  $x = 0.04$ , trivial surface-state bands ( $\Sigma'_1$  and  $\Sigma'_2$ ) split from the  $L_a$  band, are created within the band gap, and are spin polarized due to the Rashba effect. The nontrivial  $\Sigma_2$  band hybridizes with the trivial  $\Sigma'_2$  band of the same spin orientation. The spin-polarized band structure at  $x \geq 0.07$  is schematically depicted in Fig. 8(c), which reproduces the band diagram of Fig. 6(b). Detailed dispersion curves of the  $\Sigma'_1$  and  $\Sigma_2$  bands around the  $\bar{M}$  point have been determined for  $\text{Bi}_{1-x}\text{Sb}_x$  crystals at  $x = 0.1$ ,<sup>2,13</sup> and also observed at  $x = 0.12$  and  $0.13$ .<sup>7,11</sup> The hybridization between the trivial and nontrivial edge states was proposed by theoretical research.<sup>9</sup> The present research suggests that the existence of the trivial states  $\Sigma'_1$  and  $\Sigma'_2$  is likely related to the opening of the inverted gap at the  $L$  point.

Creation of a surface state within the bulk band gap has been a long-standing issue in surface science, and there exist various models such as Tamm and Shockley surface states.<sup>15</sup> Recently, a generalized theory was formulated based on the Green-function method.<sup>15</sup> In the linear crystal model, the surface state is formed by the condition

$$|\beta/\alpha_0| < 1, \quad (1)$$

where  $\beta$  is the resonance integral (matrix element) of the unperturbed bulk Hamiltonian and  $\alpha_0$  is the matrix element of a surface potential. When Eq. (1) is satisfied, the surface energy level lies below (above) the lower (upper) bulk band edge. Based on the model, the magnitude of the surface potential of the  $\text{Bi}_{1-x}\text{Sb}_x(111)$  surface seemingly becomes large with increasing Sb concentration  $x$ . The model also suggests that the appearance of the trivial surface states  $\Sigma'_1$  and  $\Sigma'_2$  may depend on surface conditions after crystal cleavage. Theoretical calculations with proper treatment of the surface layer are likely needed to reproduce the band diagrams in Fig. 8(c).

#### D. Electron-electron interaction of the surface state

High-resolution photoemission results allow us to obtain information on the electron self-energy  $\Sigma_{\text{self}}$  that is closely related to the surface band structure. The momentum width of a photoemission-band dispersion curve corresponds to the imaginary part of the electron self energy,<sup>16,17</sup>  $\text{Im} \Sigma_{\text{self}}$ . Figure 9 shows an example of (a) the photoemission band diagram of the  $\Sigma_1$  band and (b) the momentum distribution curve (MDC) at  $E_B = 50$  meV for the  $\text{Bi}_{1-x}\text{Sb}_x$  ( $x = 0.21$ ) crystal. The MDC data is curve fitted with a Voigt function using the Lorentzian widths as fitting parameters, as shown in Fig. 9(b). The Gaussian width corresponds to the instrumental resolution and it matches the angular resolution of the electron spectrometer,  $\pm 0.11^\circ$ . The Lorentzian widths (half-width at half-maximum) corresponds to the momentum width that, by multiplication with the band velocity, converts to  $|\text{Im} \Sigma_{\text{self}}|$ .

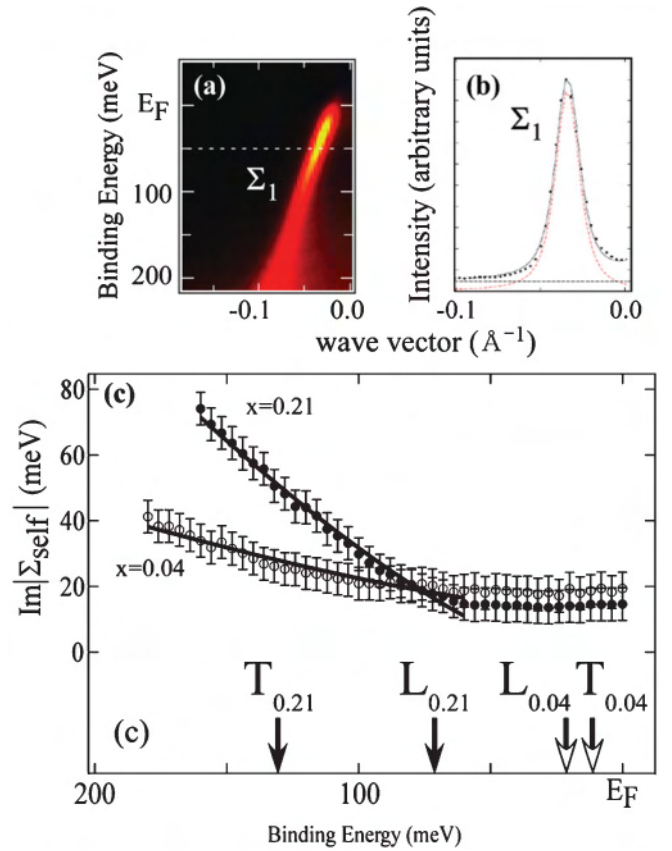


FIG. 9. (Color online) Analysis of the electron self-energy  $\Sigma_{\text{self}}$  of the  $\Sigma_1$  band. (a) Photoemission band diagram of  $\text{Bi}_{1-x}\text{Sb}_x$  ( $x = 0.21$ ) of  $k_x = 0.2 \text{ \AA}^{-1}$  taken at  $h\nu = 29 \text{ eV}$ . The angle scan was taken along an axis rotated  $19^\circ$  with respect to the  $k_y$  axis, as shown in Fig. 1(b). (b) Momentum distribution curve at  $E_B = 50 \text{ meV}$ , indicated by a broken line in (a). The data were fitted with a Voigt function to obtain the half-width at half-maximum of the peak. (c) Energy dependence of  $|\text{Im} \Sigma_{\text{self}}|$  of  $\text{Bi}_{1-x}\text{Sb}_x$  at  $x = 0.04$  and  $0.21$ . The bulk band ( $T$  and  $L$ ) edges of each Sb concentration are indicated.

Figure 9(c) shows the dependence of  $\text{Im} \Sigma_{\text{self}}$  obtained by this procedure with binding energy for  $\text{Bi}_{1-x}\text{Sb}_x$  crystals of the  $x = 0.04$  and  $0.21$  samples. In both cases, a constant  $|\text{Im} \Sigma_{\text{self}}|$  of 10–20 meV was obtained from an  $E_F$ -to- $E_B$  range of 60 meV, followed by  $(E_B)^2$  dependence for  $E_B > 60 \text{ meV}$ .

The self-energy of surface-state electrons originates from various process, i.e., electron-phonon coupling, electron-impurity scattering, and electron-electron interaction.<sup>18–21</sup> Electron-electron interaction at a surface is composed of two parts: surface-to-bulk transition and surface-to-surface transition. To consider the former case, edges of the  $T$  band and the  $L$  band with each Sb concentration are marked in Fig. 9(c). The absence of a systematic energy change at the bulk band maximum indicates that the effect of the surface-to-bulk transition is weak enough to be neglected. The electron-phonon coupling induces discontinuous energy dependence at the Debye energy, and the bulk band transition begins at  $E_B$  of the bulk band edge. As shown in Fig. 9(c), no steplike dependence was observed. On the other hand,  $|\text{Im} \Sigma_{\text{self}}|$  of the electron-impurity scattering



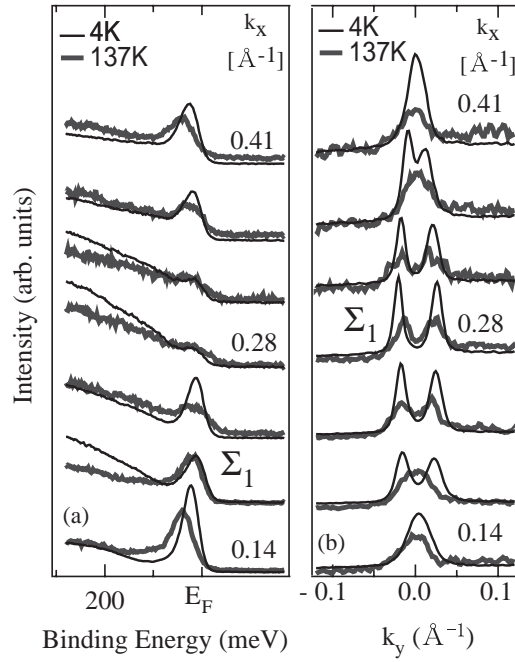


FIG. 10. (a) Energy distribution curves and (b) momentum distribution curves at  $E_F$  for  $\text{Bi}_{1-x}\text{Sb}_x$  ( $x = 0.21$ ) taken at 137 and 4 K ( $h\nu = 29$  eV, linearly polarized light).

has no energy dependence, and that of the electron-electron interaction between the surface-state electrons shows quadratic energy dependence (modified by a logarithmic factor in two-dimensional systems<sup>18</sup>), which were measured in Fig. 9(c). Therefore, the self-energy of the surface-state band of  $\text{Bi}_{1-x}\text{Sb}_x$  is dominated by these two process: the electron-impurity scattering below  $E_B \sim 60$  meV and the surface state electron-electron interaction above  $E_B \sim 60$  meV. The self-energy of the two-dimensional electron-electron interaction,  $|\text{Im } \Sigma_{\text{el-el}}|$ , has been analytically formulated<sup>20,22</sup> as  $|\text{Im } \Sigma_{\text{el-el}}| = \beta(E_B)^2[\frac{1}{4} + \ln 2 + \frac{1}{2} |\ln(E_B/\mu)|]$ , where  $\mu$  is the Fermi energy for the two-dimensional (surface-state) band. The observed  $|\text{Im } \Sigma_{\text{self}}|$  data were fitted by the  $|\text{Im } \Sigma_{\text{el-el}}|$  function [Fig. 9(c)]. Estimating  $\mu \sim 200$  meV from the experimental edge-state band dispersions, one crudely obtains  $\beta \sim 0.8 \text{ eV}^{-1}$  for  $x = 0.04$  and  $\beta \sim 2.7 \text{ eV}^{-1}$  for  $x = 0.21$ . It is important to note that the logarithmic correction factor dominates only at  $E_F$ , and it contributes to several percent in the fitted  $E_B$  range. Thus, the choice of  $\mu$  does not alter the present evaluation of the coefficient  $\beta$ . The  $\beta$  value gives a measure of the electron-electron interaction strength and is related to the bandwidth ( $W$ ) and on-site Coulomb repulsion energy ( $U$ ) as  $2\beta \sim (\pi U^2)/(2W^3)$  within the Born approximation.<sup>18</sup> The width of the  $\Sigma_1$  band is estimated to be  $W \sim 0.2$  eV for  $x = 0.04$  and  $0.21$ . From these values, the Coulomb interaction can be estimated to be  $U \sim 0.1$  eV for  $x = 0.04$  and  $U \sim 0.2$  eV for  $x = 0.21$ . Compared to surface and bulk states of correlated materials,<sup>18,20,23</sup> the Coulomb interaction of the  $\text{Bi}_{1-x}\text{Sb}_x$  surface state is much smaller, indicating that electrons at the surface have little electron correlation effect.

### E. Temperature dependence of the edge-state band

Finally, we discuss the temperature dependence of the energy position of the edge-state band. Clear  $E_F$  crossings of the  $\Sigma_1$  band were observed in the present photoemission experiment, as shown in Figs. 1–3, whereas those seen in previous research<sup>7,11</sup> were rather obscure. Besides the difference in the Sb concentrations in the samples, the main difference between the experiments was the measurement temperature:  $\sim 130$  and  $\sim 4$  K for the previous and the present measurements, respectively. Thus, temperature dependence of the ARPES spectra is examined. Figure 10 shows a series of (a) energy distribution curves and (b) momentum distribution curves ( $E_F$ ) for  $\text{Bi}_{1-x}\text{Sb}_x$  ( $x = 0.21$ ) taken at 4 and 137 K. At  $k_x = 0.14$  and  $0.41 \text{ \AA}^{-1}$  in Fig. 10(a), the  $E_B$  positions of the  $\Sigma_1$  state at 137 K are higher than those at 4 K. On the other hand, two peaks in MDCs in Fig. 10(b) indicate two  $E_F$  crossings along the  $k_y$  axis. The  $\Sigma_1$  band at 137 K has a smaller  $k_y$  range of the double MDC peaks, or smaller Fermi surface, than that at 4 K. The heating and cooling process of the sample was repeated several times to confirm the spectral change with temperature. Then from 4 to 137 K the  $\Sigma_1$  band was estimated, via EDC and MDC data, to move from  $18 \pm 4$  meV to higher  $E_B$ . The direction of the  $E_B$  shift with temperature is consistent with the energy position of the band reported at different temperatures,<sup>7,11</sup> as described above. The thermal effect may originate from physisorption of the residual gas or a change in lattice parameter with temperature.<sup>24</sup>

## IV. CONCLUSIONS

The spin-polarized electronic structure of  $\text{Bi}_{1-x}\text{Sb}_x$  was investigated by spin- and angle-resolved photoemission spectroscopy measurements at Sb concentrations of  $x = 0.04$ ,  $0.07$ , and  $0.21$ . The energy shift of the  $T$  and  $L_s$  bulk band edge with  $x$  was quantitatively evaluated. The topological transition of the surface band structure is likely to be associated with the appearance of a trivial edge state at the  $L$  band gap that hybridizes with the nontrivial edge state. A self-energy analysis of the edge state found negligible electron correlation effects at the surface. The energy position of the edge state was found to move to lower binding energy by cooling.

## ACKNOWLEDGMENTS

Shuichi Murakami, Toru Hirahara, and S.-J. Tang are gratefully acknowledged for valuable comments and discussions. Hidetoshi Miyazaki is sincerely appreciated for the experiments at beamline BL5U (UVSOR). This work was partly supported by PICS/CNRS, by JSPS (KAKENHI Grants No. 18360018 and No. 19340078, and the Next-Generation World-Leading Researchers Program), by MEXT (Innovative Area “Topological Quantum Phenomena,” KAKENHI Grant No. 22103004), and by AFOSR (Grant No. AOARD-10-4103). Parts of this work were performed by the Use-of-UVSOR Facility Program (BL5U, 2010) of the Institute for Molecular Science.

\*y\_ando@sanken.osaka-u.ac.jp

†imatsuda@issp.u-tokyo.ac.jp

- <sup>1</sup>B. Lenoir, M. Cassax, J.-P. Michenaud, H. Scherrer, and S. Scherrer, *J. Phys. Chem. Solids* **57**, 89 (1996).
- <sup>2</sup>D. Hsieh, D. Qian, L. Wray, Y. Xia, Y. S. Hor, R. J. Cava, and M. Z. Hasan, *Nature (London)* **452**, 970 (2008).
- <sup>3</sup>C. L. Kane and E. J. Mele, *Phys. Rev. Lett.* **95**, 226801 (2005).
- <sup>4</sup>C. L. Kane and E. J. Mele, *Phys. Rev. Lett.* **95**, 146802 (2005).
- <sup>5</sup>B. A. Bernevig and S. C. Zhang, *Phys. Rev. Lett.* **96**, 106802 (2006).
- <sup>6</sup>L. Fu and C. L. Kane, *Phys. Rev. B* **76**, 045302 (2007).
- <sup>7</sup>A. Nishide, A. A. Taskin, Y. Takeichi, T. Okuda, A. Kakizaki, T. Hirahara, K. Nakatsuji, F. Komori, Y. Ando, and I. Matsuda, *Phys. Rev. B* **81**, 041309(R) (2010).
- <sup>8</sup>E. I. Rogacheva *et al.*, *Appl. Phys. Lett.* **94**, 202111 (2009).
- <sup>9</sup>H. J. Zhang, C. X. Liu, X. L. Qi, X. Y. Deng, X. Dai, S. C. Zhang, and Z. Fang, *Phys. Rev. B* **80**, 085307 (2009).
- <sup>10</sup>T. Okuda, Y. Takeichi, Yuuki Maeda, A. Harasawa, I. Matsuda, T. Kinoshita, and A. Kakizaki, *Rev. Sci. Instrum.* **79**, 123117 (2008).
- <sup>11</sup>A. Nishide, Y. Takeichi, T. Okuda, A. A. Taskin, T. Hirahara, K. Nakatsuji, F. Komori, A. Kakizaki, Y. Ando, and I. Matsuda, *New J. Phys.* **12**, 065011 (2010).
- <sup>12</sup>P. A. Wolff, *J. Phys. Chem. Solids* **25**, 1057 (1964).
- <sup>13</sup>D. Hsieh, Y. Xia, L. Wray, D. Qian, A. Pal, J. H. Dil, J. Osterwalder, F. Meier, G. Bihlmayer, C. L. Kane, Y. S. Hor, R. J. Cava, and M. Z. Hasan, *Science* **323**, 919 (2009).
- <sup>14</sup>Yu. M. Koroteev, G. Bihlmayer, J. E. Gayone, E. V. Chulkov, S. Blugel, P. M. Echenique, and Ph. Hofmann, *Phys. Rev. Lett.* **93**, 046403 (2004).
- <sup>15</sup>S. G. Davison and M. Steslicka, *Basic Theory of Surface State* (Oxford University Press, New York, 1992).
- <sup>16</sup>P. V. Bogdanov, A. Lanzara, S. A. Kellar, X. J. Zhou, E. D. Lu, W. J. Zheng, G. Gu, J.-I. Shimoyama, K. Kishio, H. Ikeda, R. Yoshizaki, Z. Hussain, and Z. X. Shen, *Phys. Rev. Lett.* **85**, 2581 (2000).
- <sup>17</sup>X. J. Zhou *et al.*, *Phys. Rev. Lett.* **95**, 117001 (2005).
- <sup>18</sup>T. Valla, A. V. Fedorov, P. D. Johnson, and S. L. Hulbert, *Phys. Rev. Lett.* **83**, 2085 (1999).
- <sup>19</sup>S. R. Park, W. S. Jung, C. Kim, D. J. Song, C. Kim, S. Kimura, K. D. Lee, and N. Hur, *Phys. Rev. B* **81**, 041405(R) (2010).
- <sup>20</sup>M. Higashiguchi, K. Shimada, M. Arita, Y. Miura, N. Tobita, X. Cui, Y. Aiura, H. Namatame, and M. Taniguchi, *Surf. Sci.* **601**, 4005 (2007).
- <sup>21</sup>V. M. Silkin, T. Balasubramanian, E. V. Chulkov, A. Rubio, and P. M. Echenique, *Phys. Rev. B* **64**, 085334 (2001).
- <sup>22</sup>C. Hodges, H. Smith, and J. W. Wilkins, *Phys. Rev. B* **4**, 302 (1971).
- <sup>23</sup>M. Higashiguchi, K. Shimada, K. Nishiura, X. Cui, H. Namatame, and M. Taniguchi, *Phys. Rev. B* **72**, 214438 (2005).
- <sup>24</sup>S.-J. Tang, H.-T. Jeng, C.-S. Hsue, Ismail, P. T. Sprunger, and E. W. Plummer, *Phys. Rev. B* **77**, 45405 (2008).

# Observations of two-dimensional quantum oscillations and ambipolar transport in the topological insulator $\text{Bi}_2\text{Se}_3$ achieved by Cd doping

Zhi Ren, A. A. Taskin, Satoshi Sasaki, Kouji Segawa, and Yoichi Ando

*Institute of Scientific and Industrial Research, Osaka University, Ibaraki, Osaka 567-0047, Japan*

(Received 10 April 2011; revised manuscript received 24 June 2011; published 9 August 2011)

We present a defect-engineering strategy to optimize the transport properties of the topological insulator  $\text{Bi}_2\text{Se}_3$  to show a high bulk resistivity and clear quantum oscillations. Starting with a  $p$ -type  $\text{Bi}_2\text{Se}_3$  obtained by combining Cd doping and a Se-rich crystal-growth condition, we were able to observe a  $p$ -to- $n$ -type conversion upon gradually increasing the Se vacancies by post annealing. With the optimal annealing condition, where a high level of compensation is achieved, the resistivity exceeds  $0.5\ \Omega\text{cm}$  at 1.8 K and we observed two-dimensional Shubnikov–de Haas oscillations composed of multiple frequencies in magnetic fields below 14 T.

DOI: [10.1103/PhysRevB.84.075316](https://doi.org/10.1103/PhysRevB.84.075316)

PACS number(s): 73.25.+i, 74.62.Dh, 72.20.My, 73.20.At

## I. INTRODUCTION

The three-dimensional (3D) topological insulator (TI) realizes a novel quantum state of matter where a nontrivial  $Z_2$  topology of the wave function of the bulk valence band leads to the emergence of a “topological” surface state consisting of helically spin-polarized Dirac fermions.<sup>1–3</sup> The peculiar spin texture of the surface state holds promise for novel spintronics and fault-tolerant topological quantum computing, so there is a rush of research to address this surface state.<sup>4,5</sup> However, most of the known TI materials are poorly insulating in the bulk, making it difficult to probe the surface state by transport experiments. For example,  $\text{Bi}_2\text{Se}_3$  is considered to be a promising TI material because it has a relatively large ( $\sim 0.3$  eV) bulk band gap and a nearly perfect Dirac cone as its topological surface state<sup>6,7</sup>; however, no matter whether it is in the form of bulk crystal,<sup>7,8</sup> nanoribbon,<sup>9</sup> or epitaxial thin film,<sup>10</sup>  $\text{Bi}_2\text{Se}_3$  always accompanies a lot of Se vacancies (usually  $\sim 10^{19}\ \text{cm}^{-3}$ ) that act as electron donors, and as a result, the residual bulk carriers hinder the transport studies of the surface state of this material.

To achieve a bulk-insulating state in  $\text{Bi}_2\text{Se}_3$ , doping holes to compensate for the residual electrons is a viable strategy. While this was done through low-level substitution of  $\text{Ca}^{2+}$  for  $\text{Bi}^{3+}$ ,<sup>11</sup> the resulting disorder was so strong that no Shubnikov–de Haas (SdH) oscillation from the surface state was observed<sup>12</sup> in  $\text{Bi}_{2-x}\text{Ca}_x\text{Se}_3$ . A different strategy was to partially substitute Sb for Bi, which apparently reduces the Se vacancies; indeed, with a relatively large ( $\sim 12\%$ ) Sb substitution, surface SdH oscillations were successfully observed in  $n$ -type  $\text{Bi}_{2-x}\text{Sb}_x\text{Se}_3$ , but a very high magnetic field ( $\sim 60$  T) was required for the observation.<sup>13</sup> It is to be noted that, with the Sb doping, one can never cross the band gap to reach the  $p$ -type regime, and, hence, the tuning of the chemical potential to the Dirac point is impossible. This is a pity because  $\text{Bi}_2\text{Se}_3$  is attractive for its isolation of the Dirac point from the bulk bands. Therefore, it is desirable to find a suitable  $p$ -type dopant to access the Dirac point while keeping the mobility to be sufficiently high for the surface state to be studied by the SdH oscillations.

In this paper, we show that tactful defect engineering in  $\text{Bi}_2\text{Se}_3$  employing Cd doping in combination with Se-vacancy tuning provides a useful means to control the chemical potential across the band gap. In the literature,<sup>14</sup> whereas Cd in

$\text{Bi}_2\text{Se}_3$  was shown to behave as an acceptor, Cd-doped  $\text{Bi}_2\text{Se}_3$  crystals always remained  $n$  type due to the low solubility of Cd atoms in  $\text{Bi}_2\text{Se}_3$ ; however, it has been elucidated<sup>15–17</sup> that increasing the Se content in the Bi-Se melt for the crystal growth can suppress the formation of Se vacancies and greatly reduce the residual bulk carrier density to the level of  $\sim 10^{17}\ \text{cm}^{-3}$ . Therefore, even though the solubility of Cd is low, one could achieve a  $p$ -type behavior by combining Cd doping and a Se-rich growth condition. Actually, we obtained a  $p$ -type sample with this strategy and, furthermore, starting from the  $p$ -type sample, we could gradually increase the Se vacancies by careful post annealing and achieve a high level of compensation, at which the sample becomes optimally bulk insulating and presents two-dimensional (2D) SdH oscillations below 14 T.

## II. EXPERIMENTAL DETAILS

The single crystals of Cd-doped  $\text{Bi}_2\text{Se}_3$  were grown by using elemental shots of Bi (99.9999%), Cd (99.99%), and Se (99.999%) as starting materials. To maximize the Cd content in the crystal, excess Cd and a mixture of Bi and Se with a ratio of Bi:Se = 32:68 were melted in a sealed evacuated quartz tube at 750 °C for 48 h with intermittent shaking to ensure a homogeneity, followed by cooling slowly to 550 °C and then annealing at the same temperature for one week. The resulting crystals are easily cleaved along the basal plane, revealing a silvery mirrorlike surface. The x-ray diffraction measurements confirmed the crystal to be single phase with the proper  $\text{Bi}_2\text{Se}_3$  structure. The actual Cd content was determined by the inductively coupled plasma atomic-emission spectroscopy (ICP-AES) to be 0.0020(2). The as-grown crystals were examined by x-ray Laue analysis and cut into single-domain, thin bar-shaped samples with typical dimensions of  $3 \times 1 \times 0.2\ \text{mm}^3$ .

For each annealing experiment, samples weighing about 4.2 mg were sealed in evacuated quartz tubes and annealed at a given temperature for one week, followed by quenching into cold water. All the samples used in this work were taken from the same part of the same batch, and the variation of the Cd content was confirmed to be negligible by the ICP-AES analysis. To avoid possible surface contamination, the surface layer of the annealed crystals was removed using adhesive tapes before transport measurements.

It is worth mentioning that, in our annealing experiments, we took precautions to minimize the uncertainty in the annealing temperature. For each annealing run, we placed the quartz tube at the same position of the same furnace so that the temperature gradients in the furnace as well as the thermocouple calibration errors do not affect the annealing result. Also, the environment temperature was kept constant during this experiment to minimize the temperature fluctuations between different annealing runs. As a result, the annealing temperature  $T_{\text{anneal}}$  was very reproducible and its variation between different runs with nominally the same  $T_{\text{anneal}}$  was within  $\pm 1^\circ\text{C}$ .

The in-plane resistivity  $\rho_{xx}$  and the Hall coefficient  $R_H$  were measured in a quantum design physical properties measurement system (PPMS-9) down to 1.8 K, for which the electrical contacts were prepared by using room-temperature-cured silver paste. In addition, one of the high-resistivity samples was brought to a 14-T magnet for detailed SdH oscillation measurements using an ac six-probe method, in which four lock-in amplifiers were employed to measure both the primary and the second-harmonic signals in the longitudinal and transverse channels at a frequency of 19 Hz. The SdH oscillation data were taken by sweeping the magnetic fields between  $\pm 14$  T with the rate of 0.3 T/min, during which the temperature was stabilized to within  $\pm 5$  mK.

### III. RESULTS AND DISCUSSIONS

#### A. $p$ -type $\text{Bi}_{2-x}\text{Cd}_x\text{Se}_3$

The temperature dependence of the in-plane resistivity  $\rho_{xx}$  of a  $\text{Bi}_{1.998}\text{Cd}_{0.002}\text{Se}_3$  crystal grown in the Se-rich condition is shown in Fig. 1(a), together with the data for a pristine  $\text{Bi}_2\text{Se}_3$  sample grown with the same Bi/Se ratio. The pristine  $\text{Bi}_2\text{Se}_3$  crystal shows an essentially metallic behavior with a weak resistivity upturn below  $\sim 30$  K, which is typical for low-carrier-density<sup>15–17</sup>  $\text{Bi}_2\text{Se}_3$ ; indeed, the Hall coefficient  $R_H$  in this sample at 1.8 K corresponds to the bulk electron density  $n_e \sim 7 \times 10^{17} \text{ cm}^{-3}$ , which is very small for  $\text{Bi}_2\text{Se}_3$ . On the other hand, in  $\text{Bi}_{1.998}\text{Cd}_{0.002}\text{Se}_3$ , the resistivity upturn is absent and the  $\rho_{xx}$  value is lower, suggesting a higher carrier density. In fact, as shown in Fig. 1(b),  $R_H$  in the  $\text{Bi}_{1.998}\text{Cd}_{0.002}\text{Se}_3$  crystal is positive and its value at 1.8 K corresponds to the hole density  $n_h \sim 9 \times 10^{18} \text{ cm}^{-3}$ , implying that the Cd doping has created  $\sim 9.7 \times 10^{18} \text{ cm}^{-3}$  of holes ( $\sim 0.8$  hole per Cd atom) that outnumbers the electrons coming from Se vacancies.<sup>14</sup> The reason for the smaller number of doped holes compared to the Cd concentration is most likely that a small portion of Cd atoms occupies the interstitial site and acts as donors. In Fig. 1(b),  $R_H$  is only weakly dependent on temperature and the Hall resistivity  $\rho_{yx}$  is perfectly linear in  $B$  (as shown in the inset), reflecting the metallic nature of the as-grown  $\text{Bi}_{1.998}\text{Cd}_{0.002}\text{Se}_3$  sample, which is due to a single type of carriers (i.e., the bulk holes). The Hall mobility  $\mu_H (= R_H/\rho_{xx})$ , also shown in Fig. 1(b), increases with decreasing temperature, reaching  $\sim 1600 \text{ cm}^2/\text{Vs}$  at 1.8 K.

#### B. $p$ -to- $n$ -type conversion by post annealing

Annealing the as-grown  $\text{Bi}_{1.998}\text{Cd}_{0.002}\text{Se}_3$  crystals in evacuated quartz tubes has a drastic effect on its transport properties.

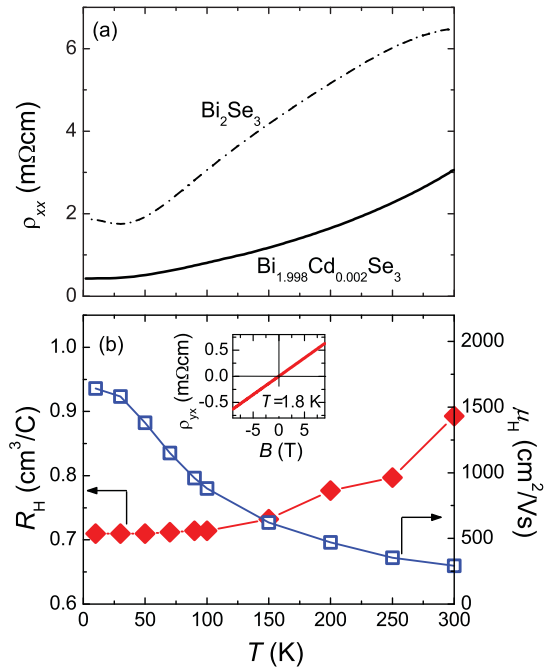


FIG. 1. (Color online) (a) Temperature dependences of  $\rho_{xx}$  of an as-grown  $\text{Bi}_{1.998}\text{Cd}_{0.002}\text{Se}_3$  crystal (solid line) and a pristine  $\text{Bi}_2\text{Se}_3$  crystal (dashed-dotted line) grown in the same Se-rich condition. The pristine sample is  $n$  type with  $n_e \sim 7 \times 10^{17} \text{ cm}^{-3}$ , while the Cd-doped sample is  $p$  type with  $n_h \sim 9 \times 10^{18} \text{ cm}^{-3}$ . Note that the low-temperature resistivity upturn in the pristine sample is absent in the Cd-doped sample. (b) Temperature dependences of  $R_H$  (left axis) and  $\mu_H$  (right axis) for the Cd-doped sample; inset shows the magnetic field dependence of  $\rho_{yx}$  in this sample at 1.8 K.

Figure 2(a) shows how the temperature dependence of  $\rho_{xx}$  changes upon annealing in a narrow temperature window between  $573^\circ\text{C}$  and  $590^\circ\text{C}$ . One can see that  $\rho_{xx}(T)$  evolves *nonmonotonically* with the annealing temperature  $T_{\text{anneal}}$ , namely,  $\rho_{xx}$  initially increases with  $T_{\text{anneal}}$  until  $T_{\text{anneal}}$  exceeds  $577^\circ\text{C}$ , after which  $\rho_{xx}$  decreases as  $T_{\text{anneal}}$  is further increased. Notably,  $\rho_{xx}$  of the sample annealed at  $577^\circ\text{C}$  show a high value of  $0.5 \text{ }\Omega\text{cm}$  at 1.8 K, which is three orders of magnitude larger than that of the as-grown sample. Figure 2(b) shows the typical temperature dependences of low-field  $R_H$  data (defined as  $R_H = \rho_{yx}/B$  for  $B \approx 0$ ) for different  $T_{\text{anneal}}$ , which indicates that more and more electron carriers are introduced as  $T_{\text{anneal}}$  is increased, and the sign change from  $p$  type to  $n$  type occurs around  $T_{\text{anneal}} = 577^\circ\text{C}$ .

Since the drastic change in the transport properties occurs in a very narrow temperature window ( $573$ – $580^\circ\text{C}$ ), one may wonder about the reproducibility of the result. As a matter of fact, the observed change was quite reproducible, as demonstrated in Figs. 3 and 4. Figures 3(a)–3(d) show the  $\rho_{xx}(T)$  data for at least two samples annealed at the same temperature, where one can see that the behavior for each  $T_{\text{anneal}}$  is essentially reproducible. Figures 4(a)–4(d) show the corresponding  $R_H(T)$  data for the same sets of samples; here, except for the case of  $T_{\text{anneal}} = 577^\circ\text{C}$  [Fig. 4(c)], we observed reasonable reproducibility [Figs. 4(a), 4(b), and 4(d)]. For  $T_{\text{anneal}} = 577^\circ\text{C}$ , two of the three samples (A and B) showed a sign change in  $R_H$  from negative to positive upon



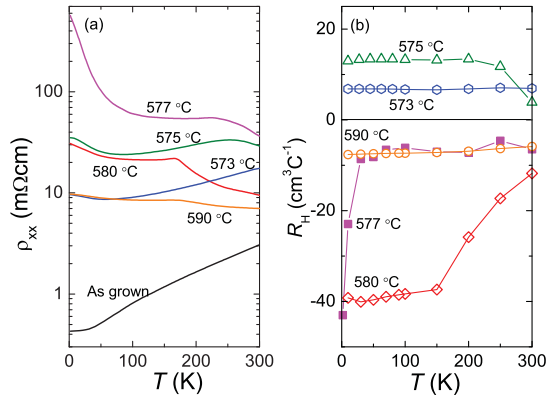


FIG. 2. (Color online) (a) Temperature dependences of  $\rho_{xx}$  for  $\text{Bi}_{1.998}\text{Cd}_{0.002}\text{Se}_3$  crystals annealed at different temperatures in evacuated quartz tubes. The data for the as-grown crystal are also shown for comparison. The low-temperature resistivity values span three orders of magnitude. (b) Temperature dependences of  $R_H$  for the same series of samples. As the annealing temperature is increased, the crystal becomes less  $p$  type and is eventually converted to  $n$  type. This conversion occurs with the annealing temperature of  $\sim 577^\circ\text{C}$ .

lowering temperature from 300 K, whereas the  $R_H$  of sample C remained negative in the whole temperature range. Actually, this variation in the behavior of  $R_H$  indicates that the  $T_{\text{anneal}} = 577^\circ\text{C}$  samples are at the verge of the  $p$ -to- $n$ -type conversion.

Figures 4(e)–4(h) show the  $\rho_{yx}(B)$  curves measured in sample “A” of each  $T_{\text{anneal}}$ . One can clearly see that the curve in Fig. 4(g) for  $T_{\text{anneal}} = 577^\circ\text{C}$  is nonlinear, indicating that there are at least two bands contributing to the transport. In topological-insulator samples with a large bulk resistivity, these kinds of nonlinear  $\rho_{yx}(B)$  curves are indications of the surface channels making noticeable contributions.<sup>18–22</sup> Therefore, the consistently high resistivity [Fig. 3(c)] together with the complex behaviors of the Hall signal are likely to be a signature of a high level of compensation achieved in the samples annealed at  $577^\circ\text{C}$ ; in other words, in those samples, the acceptors and donors are nearly equal in number and their delicate balance can easily change the sign of  $R_H$ . It is to be emphasized that our data demonstrate that this high level of

compensation is reproducibly achieved with  $T_{\text{anneal}} = 577^\circ\text{C}$ . In samples annealed at other temperatures, the  $\rho_{yx}(B)$  behavior is almost linear [Figs. 4(e), 4(f), and 4(h)], suggesting that the contribution of the surface to the transport properties is minor. In passing, the collection of  $\rho_{xx}(T)$  and  $R_H(T)$  data shown in Fig. 2 for varying  $T_{\text{anneal}}$  are for sample “A” of each  $T_{\text{anneal}}$  shown in Figs. 3 and 4.

### C. Defect chemistry

The above observation that a drastic change in the transport properties of  $\text{Bi}_{1.998}\text{Cd}_{0.002}\text{Se}_3$  occurs in a very narrow temperature window might seem surprising. However, this behavior can be readily understood by examining the defect chemistry associated with the annealing. In the present system, there are mainly two different types of charged defects, the aliovalent substitutional defect  $\text{Cd}'_{\text{Bi}}$  and the vacancy defect  $\text{V}_{\text{Se}}^{\bullet\bullet}$ .<sup>11,14</sup> The former acts as an acceptor and the latter acts as a donor. Therefore, the effective charge-carrier density is determined by their competition and can be expressed as  $n_{\text{eff}} = [\text{Cd}'_{\text{Bi}}] - 2[\text{V}_{\text{Se}}^{\bullet\bullet}]$ , where positive (negative)  $n_{\text{eff}}$  denotes the hole (electron) density. In an as-grown sample, the  $\text{Cd}'_{\text{Bi}}$  defects are dominant and  $n_{\text{eff}}$  is positive; accordingly, the chemical potential lies in the valence band. When annealed in evacuated quartz tubes, a portion of selenium goes into the gas phase  $\text{Se}_2$  in equilibrium with the solid phase,<sup>23</sup> resulting in the formation of more  $\text{V}_{\text{Se}}^{\bullet\bullet}$  defects while leaving  $\text{Cd}'_{\text{Bi}}$  unaffected (because the  $T_{\text{anneal}}$  employed in this paper is much lower than the melting temperature of  $710^\circ\text{C}$ ). The equilibrated vapor pressure of  $\text{Se}_2$  increases with increasing  $T_{\text{anneal}}$ ,<sup>23</sup> creating more  $\text{V}_{\text{Se}}^{\bullet\bullet}$  and eventually changing  $n_{\text{eff}}$  from positive to negative.

To be more quantitative, one may assume that the increase in the Se-vacancy concentration upon annealing,  $\Delta[\text{V}_{\text{Se}}^{\bullet\bullet}]$ , is directly reflected in the increase in the number of  $\text{Se}_2$  molecules in the quartz tube, which determines the  $\text{Se}_2$  vapor pressure  $P_{\text{Se}_2}$ ; in constant volume, one expects a linear relation between  $\Delta[\text{V}_{\text{Se}}^{\bullet\bullet}]$  and  $P_{\text{Se}_2}$  if the  $\text{Se}_2$  vapor behaves as an ideal gas. According to Ref. 23, the equilibrated  $\text{Se}_2$  vapor pressure  $P_{\text{Se}_2}$  of  $\text{Bi}_2\text{Se}_3$  is related to the absolute temperature  $T$  via

$$\log P_{\text{Se}_2}[\text{atm}] = A - B/T[\text{K}], \quad (1)$$

where  $A = 7.81 \pm 0.50$  and  $B = 10870 \pm 640$  for the temperature range of  $527^\circ\text{C}$  to  $627^\circ\text{C}$ . From this  $T$  dependence of  $P_{\text{Se}_2}$ , one can infer that  $\Delta[\text{V}_{\text{Se}}^{\bullet\bullet}]$  is very sensitive to the change in  $T_{\text{anneal}}$ . For example, changing  $T_{\text{anneal}}$  by just  $1^\circ\text{C}$  near  $577^\circ\text{C}$  results in a variation of  $\sim 3.5\%$  in  $\Delta[\text{V}_{\text{Se}}^{\bullet\bullet}]$ ; therefore, the expected change in  $\Delta[\text{V}_{\text{Se}}^{\bullet\bullet}]$  upon changing  $T_{\text{anneal}}$  from  $575^\circ\text{C}$  to  $580^\circ\text{C}$  is as much as  $\sim 18\%$ . It is thus expected that a sign change in  $n_{\text{eff}}$  occurs abruptly in the vicinity of  $T_{\text{anneal}} = 577^\circ\text{C}$ , where  $n_{\text{eff}} \approx 0$  (namely,  $[\text{Cd}'_{\text{Bi}}] \approx [\text{V}_{\text{Se}}^{\bullet\bullet}]$ ), and results in a drastic change in the transport properties as we observed.

### D. Surface quantum oscillations

From the above results, it is clear that the highest level of compensation is achieved in samples annealed at  $577^\circ\text{C}$ . We therefore measured the sample C of  $T_{\text{anneal}} = 577^\circ\text{C}$  in a 14-T magnet using a rotation sample holder to investigate its SdH oscillations in detail. Before the high-field measurements, to

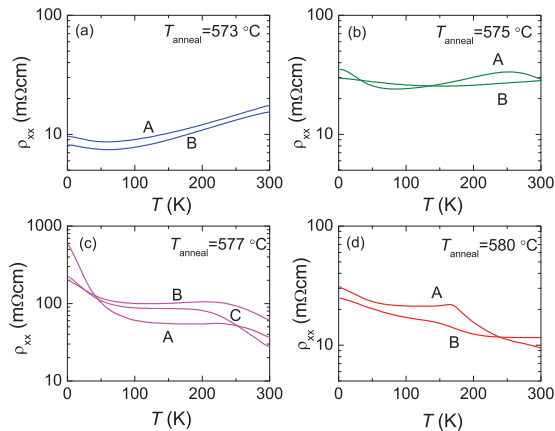


FIG. 3. (Color online) (a)–(d) Reproducibility of the  $\rho_{xx}(T)$  data in samples annealed at the same temperature, demonstrated for four different values of  $T_{\text{anneal}}$  indicated in each panel.

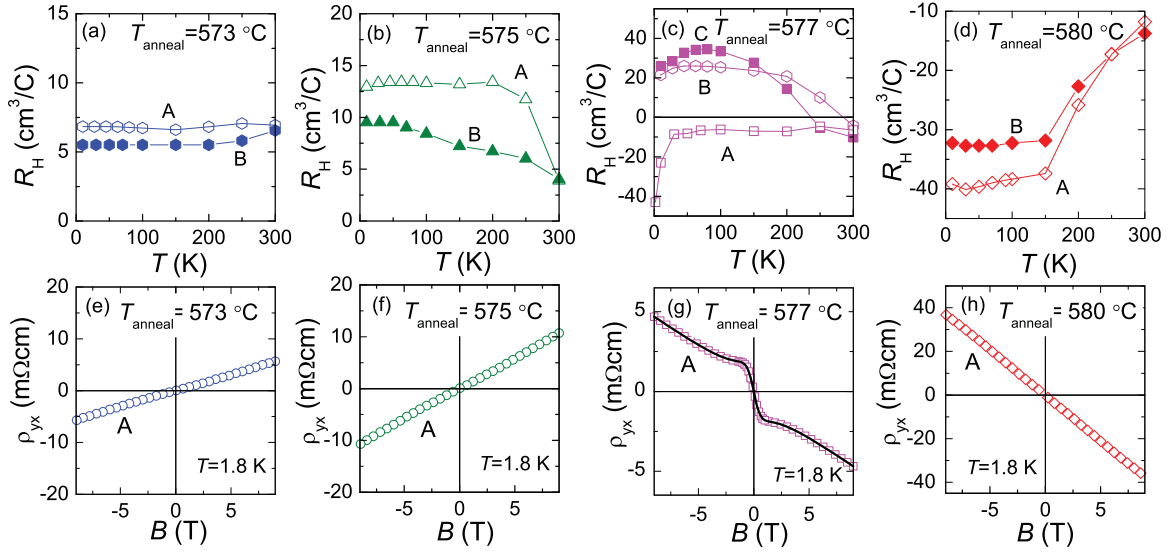


FIG. 4. (Color online) (a)–(d) Reproducibility of the  $R_H(T)$  data in samples annealed at the same temperature, demonstrated for four different values of  $T_{\text{anneal}}$  indicated in each panel. (e)–(h) Magnetic-field dependences of  $\rho_{yx}$  measured in sample “A” of each  $T_{\text{anneal}}$ . The solid line in (g) is the two-band-model fitting to the data.

protect the surface state from aging, the top surface of the sample was covered with  $\text{Al}_2\text{O}_3$  in the following way: First, the crystal was cleaved on both surfaces with adhesive tapes to reveal fresh surfaces, mounted on a sample holder with General Electric (GE) varnish, and transferred into the sputtering chamber; second, the top surface was cleaned by bias sputtering with Ar ions for 13 min and then, without breaking the vacuum, a 540-nm-thick  $\text{Al}_2\text{O}_3$  film was deposited by the rf magnetron sputtering. After this process, gold wires were bounded to the side faces by spot welding. Probably because of the sample heating during the spot welding, the  $\rho_{xx}$  value of this sample became even larger than that shown in Fig. 3(c). Also, the sign of  $R_H$  at low temperature changed to negative after the process, showing the Hall response similar to that of the sample A. The  $R_H(T)$  behavior of this sample C after the  $\text{Al}_2\text{O}_3$ -coverage process is shown in Fig. 5(a), and its  $\rho_{yx}(B)$  curve at 1.4 K is shown in Fig. 5(b).

In our measurements using an ac lock-in technique, we simultaneously recorded the primary and the second-harmonic signals during the magnetic-field sweeps. Figure 5(c) shows the magnetic-field ( $B$ ) dependences of the primary signal ( $\rho_{xx}$ ) and the second-harmonic signal (denoted  $\Delta\rho_{xx}$ ) measured at 1.4 K in magnetic fields along the  $C_3$  axis. One can see that the second-harmonic signal ( $\Delta\rho_{xx}$ ) shows pronounced oscillations, while in the primary signal ( $\rho_{xx}$ ), the oscillations are hardly visible. To understand the nature of the oscillations, we show in Fig. 5(d) the plots of  $\Delta\rho_{xx}$  and  $d^2\rho_{xx}/dB^2$  (second derivative of the primary signal) versus the inverse magnetic field  $1/B$ ; a comparison between the two curves indicates that they present essentially the same peak and dip positions. While the waveforms are quite complicated, the Fourier transform (FT) spectrum of  $\Delta\rho_{xx}(B^{-1})$  shown in Fig. 5(e) presents three well-defined peaks at  $F_1 = 11\text{ T}$ ,  $F_2 = 27\text{ T}$ , and  $F_3 = 33\text{ T}$ , indicating that the observed oscillations are SdH oscillations with multiple frequencies.

Note that the second-harmonic in ac measurements is a distortion of the input sine wave, and its occurrence is an

indication of a nonlinear response. In the present case, the SdH oscillations are apparently giving rise to a peculiar non-ohmicity. This makes the second-harmonic signal to be useful for observing the SdH oscillations with a high sensitivity, although the detailed mechanism is not clear at the moment.

Figure 6(a) shows how the SdH oscillations observed in  $\Delta\rho_{xx}$  change when the magnetic field is rotated by plotting  $\Delta\rho_{xx}$  versus  $1/(B \cos \theta)$ , where  $\theta$  is the angle between  $B$  and the  $C_3$  axis. One can see that the oscillatory features are essentially dependent on the perpendicular component of the magnetic field. Also, as shown in Fig. 6(b), the angular dependences of all three frequencies in the FT spectra are consistent with  $1/\cos \theta$ . These results strongly suggest that the present SdH oscillations signify 2D Fermi surface(s). We note that the SdH oscillations in this sample disappeared after keeping the sample in ambient atmosphere for a week, which suggests that the SdH oscillations were coming from the surface. (This observation also suggests that the  $\text{Al}_2\text{O}_3$  coverage, while useful for slowing the aging of the surface of  $\text{Bi}_2\text{Se}_3$ , does not provide a perfect protection.) Furthermore, one can estimate the bulk mobility of this sample to be  $\sim 40\text{ cm}^2/\text{Vs}$  from the values of  $\rho_{xx}$  and  $R_H$ , and such a mobility is too low to give rise to SdH oscillations of the bulk carriers below 14 T. All told, one can reasonably conclude that the observed SdH oscillations are of the surface origin.

From the SdH oscillation data, the Fermi wave vector  $k_F$  can be calculated via the Onsager relation  $F = (\hbar c/2\pi e)\pi k_F^2$ , yielding  $k_F = 0.018, 0.029$ , and  $0.032\text{ \AA}^{-1}$  for  $F_1$ ,  $F_2$ , and  $F_3$ , respectively. These are of the same order as the value  $k_F = 0.031\text{ \AA}^{-1}$  reported for the topological surface state in  $n$ -type  $\text{Bi}_{2-x}\text{Sb}_x\text{Se}_3$ .<sup>13</sup> However, because of the multicomponent nature of the oscillations that leads to complicated waveforms, it is difficult to reliably extract the cyclotron mass  $m_c$  nor the Dingle temperature for each component using the Lifshitz-Kosevich theory.<sup>24</sup> This makes it impossible to identify the origins of the three oscillation frequencies, but possible reasons for the multiple components in the present

case include the following: (i) harmonics of a fundamental frequency are observed, (ii) chemical potentials of the top and bottom surfaces are not identical and give two frequencies associated with the topological surface states, and (iii) a trivial 2D electron gas<sup>25</sup> created by the band bending at the surface presents additional SdH oscillations. Note that, in the case of the present sample used for the detailed SdH measurements, the top surface was covered by  $\text{Al}_2\text{O}_3$  and the bottom surface was covered by the GE varnish, so the conditions of the two surfaces were very different. To resolve the origins of those multiple frequencies, an experiment involving the gate control of the surface chemical potential to trace the energy dispersion of each branch (as was done<sup>26</sup> for exfoliated  $\text{Bi}_2\text{Se}_3$ ) would be desirable.

### E. Nonlinear $\rho_{yx}(B)$ behavior

Although we could not extract the surface mobility from the SdH oscillations in the present case, we can still estimate the relevant parameters of the surface and the bulk transport channels by analyzing the nonlinear  $\rho_{yx}(B)$  behavior [Fig. 5(b)] with the simple two-band model described in Ref. 18. The solid line in Fig. 5(b) is the result of the two-band-model fitting, from which we obtained the bulk electron density  $n_b = 7 \times 10^{17} \text{ cm}^{-3}$ , the bulk mobility  $\mu_b = 17 \text{ cm}^2/\text{Vs}$ , the

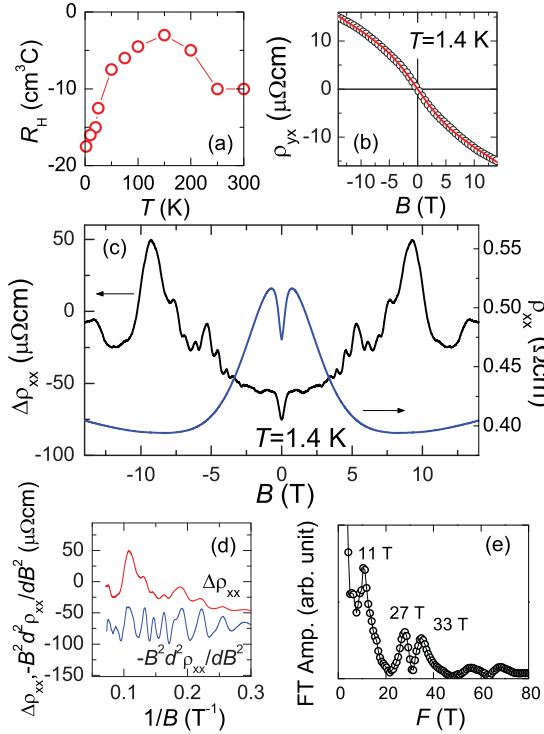


FIG. 5. (Color online) (a)  $R_H(T)$  data of the sample C of  $T_{\text{anneal}} = 577^\circ\text{C}$  after the  $\text{Al}_2\text{O}_3$ -coverage process. (b)  $\rho_{yx}(B)$  data of the same sample measured at 1.4 K; the solid line is the result of the two-band-model fitting. (c) Magnetic-field dependences of the primary signal ( $\rho_{xx}$ ) and the second-harmonic signal ( $\Delta\rho_{xx}$ ) measured at 1.4 K in magnetic fields along the  $C_3$  axis. (d) Plots of  $\Delta\rho_{xx}(B)$  and  $d^2\rho_{xx}/dB^2$  vs the inverse magnetic field  $1/B$ . Clear SdH oscillations can be seen in both data, and good agreements in the positions of peaks and dips between the two curves are evident. (e) The FT spectrum of  $\Delta\rho_{xx}$  show three prominent frequencies.

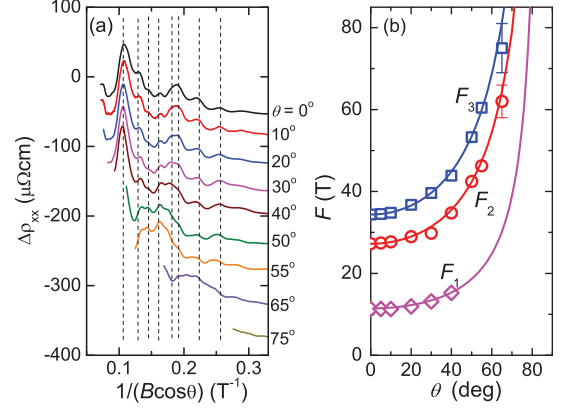


FIG. 6. (Color online) (a) The  $\Delta\rho_{xx}$  data for varying magnetic-field directions, plotted as a function of  $1/(B \cos \theta)$ ; dashed lines mark the positions of the peaks. (b) The three prominent frequencies in the FT spectra of the SdH oscillations plotted as a function of  $\theta$ . All the frequencies vary as  $1/\cos \theta$ , as indicated by the solid lines.

surface electron density  $n_s = 1.8 \times 10^{12} \text{ cm}^{-2}$ , and the surface mobility  $\mu_s = 1.2 \times 10^3 \text{ cm}^2/\text{Vs}$ . The observed frequencies of the SdH oscillations, 11, 27, and 33 T, correspond to the surface carrier densities of  $2.5 \times 10^{11}$ ,  $6.7 \times 10^{11}$ , and  $8.1 \times 10^{11} \text{ cm}^{-2}$  in spin-filtered surface states, respectively, and it is interesting that the sum of these numbers,  $1.7 \times 10^{12} \text{ cm}^{-2}$ , appears to be consistent with the  $n_s$  value obtained from the two-band analysis. Also, it is assuring that the surface mobility  $\mu_s$  obtained from the two-band analysis,  $\sim 1200 \text{ cm}^2/\text{Vs}$ , is reasonably large and is consistent with our observation of the SdH oscillations in moderate magnetic fields.

In passing, the  $\rho_{yx}(B)$  data of the sample A shown in Fig. 4(g) can also be fitted with the two-band model. The result of the fitting, shown by the solid line in Fig. 4(g), yields the bulk electron density  $n_b = 1.3 \times 10^{18} \text{ cm}^{-3}$ , the bulk mobility  $\mu_b = 15 \text{ cm}^2/\text{Vs}$ , the surface electron density  $n_s = 2.0 \times 10^{11} \text{ cm}^{-2}$ , and the surface mobility  $\mu_s = 1.0 \times 10^4 \text{ cm}^2/\text{Vs}$  for this sample.

## IV. CONCLUSION

In conclusion, we demonstrate that, with tactful defect engineering, one can optimize the transport properties of the topological insulator  $\text{Bi}_2\text{Se}_3$  to show a high bulk resistivity and clear quantum oscillations. Specifically, by employing a Se-rich crystal-growth condition, we achieved the  $p$ -type state in  $\text{Bi}_2\text{Se}_3$  by Cd doping; we then employed careful post annealing to tune the Se vacancies and achieved a high level of compensation, where the acceptors and donors nearly cancel each other and the sample presents a high  $\rho_{xx}$  value exceeding  $0.5 \Omega\text{cm}$  at 1.8 K and shows 2D SdH oscillations consisting of multiple components below 14 T.

## ACKNOWLEDGMENTS

We thank T. Minami for technical assistance. This work was supported by JSPS (NEXT Program and KAKENHI 19674002), MEXT (Innovative Area “Topological Quantum Phenomena” KAKENHI 22103004), and AFOSR (AOARD 10-4103).

- <sup>1</sup>L. Fu and C. L. Kane, *Phys. Rev. B* **76**, 045302 (2007).
- <sup>2</sup>J. E. Moore and L. Balents, *Phys. Rev. B* **75**, 121306(R) (2007).
- <sup>3</sup>R. Roy, *Phys. Rev. B* **79**, 195322 (2009).
- <sup>4</sup>M. Z. Hasan and C. L. Kane, *Rev. Mod. Phys.* **82**, 3045 (2010).
- <sup>5</sup>X. L. Qi and S. C. Zhang, e-print [arXiv:1008.2026](#).
- <sup>6</sup>H. J. Zhang, C. X. Liu, X. L. Qi, X. Dai, Z. Fang, and S. C. Zhang, *Nat. Phys.* **5**, 438 (2009).
- <sup>7</sup>Y. Xia, D. Qian, D. Hsieh, L. Wray, A. Pal, H. Lin, A. Bansil, D. Grauer, Y. S. Hor, R. J. Cava, and M. Z. Hasan, *Nat. Phys.* **5**, 398 (2009).
- <sup>8</sup>K. Eto, Z. Ren, A. A. Taskin, K. Segawa, and Y. Ando, *Phys. Rev. B* **81**, 195309 (2010).
- <sup>9</sup>H. Peng, K. Lai, D. Kong, S. Meister, Y. Chen, X. L. Qi, S. C. Zhang, Z. X. Shen, and Y. Cui, *Nat. Mater.* **9**, 225 (2010).
- <sup>10</sup>X. Chen, X. C. Ma, K. He, J. F. Jia, and Q. K. Xue, *Adv. Mater. (Weinheim)* **23**, 1162 (2011).
- <sup>11</sup>Y. S. Hor, A. Richardella, P. Roushan, Y. Xia, J. G. Checkelsky, A. Yazdani, M. Z. Hasan, N. P. Ong, and R. J. Cava, *Phys. Rev. B* **79**, 195208 (2009).
- <sup>12</sup>J. G. Checkelsky, Y. S. Hor, M. H. Liu, D. X. Qu, R. J. Cava, and N. P. Ong, *Phys. Rev. Lett.* **103**, 246601 (2009).
- <sup>13</sup>J. G. Analytis, R. D. McDonald, S. C. Riggs, J. H. Chu, G. S. Boebinger, and I. R. Fisher, *Nat. Phys.* **6**, 960 (2010).
- <sup>14</sup>J. Horák, L. Koudelka, J. Kilkorka, and L. Šiška, *Phys. Status Solidi* **111**, 575 (1982).
- <sup>15</sup>H. Köhler and A. Fabricius, *Phys. Status Solidi B* **71**, 487 (1975).
- <sup>16</sup>J. G. Analytis, J. H. Chu, Y. Chen, F. Corredor, R. D. McDonald, Z. X. Shen, and I. R. Fisher, *Phys. Rev. B* **81**, 205407 (2010).
- <sup>17</sup>N. P. Butch, K. Kirshenbaum, P. Syers, A. B. Sushkov, G. S. Jenkins, H. D. Drew, and J. Paglione, *Phys. Rev. B* **81**, 241301(R) (2010).
- <sup>18</sup>Z. Ren, A. A. Taskin, S. Sasaki, K. Segawa, and Y. Ando, *Phys. Rev. B* **82**, 241306(R) (2010).
- <sup>19</sup>H. Steinberg, D. R. Gardner, Y. S. Lee, and P. Jarillo-Herrero, *Nano Lett.* **10**, 5032 (2010).
- <sup>20</sup>D.-X. Qu, Y. S. Hor, J. Xiong, R. J. Cava, and N. P. Ong, *Science* **329**, 821 (2010).
- <sup>21</sup>N. Bansal, Y. S. Kim, M. Brahlek, E. Edrey, and S. Oh, e-print [arXiv:1104.5709](#).
- <sup>22</sup>A. A. Taskin, Z. Ren, S. Sasaki, K. Segawa, and Y. Ando, *Phys. Rev. Lett.* **107**, 016801 (2011).
- <sup>23</sup>M. L. Cafaro, G. Bardi, and V. Oiancente, *J. Chem. Eng. Jpn.* **29**, 78 (1984).
- <sup>24</sup>D. Shoenberg, *Magnetic Oscillations in Metals* (Cambridge University Press, Cambridge, 1984).
- <sup>25</sup>M. Bianchi, D. D. Guan, S. N. Bao, J. L. Mi, B. B. Iversen, P. D. C. King, and P. Hofmann, *Nat. Commun.* **1**, 128 (2010).
- <sup>26</sup>B. Sacépé, J. B. Oostinga, J. Li, A. Ubaldini, N. J. G. Couto, E. Giannini, and A. F. Morpurgo, e-print [arXiv:1101.2352](#).



# Berry phase of nonideal Dirac fermions in topological insulators

A. A. Taskin and Yoichi Ando

*Institute of Scientific and Industrial Research, Osaka University, Ibaraki, Osaka 567-0047, Japan*

(Received 16 March 2011; revised manuscript received 27 April 2011; published 12 July 2011)

A distinguishing feature of Dirac fermions is the Berry phase of  $\pi$  associated with their cyclotron motions. Since this Berry phase can be experimentally assessed by analyzing the Landau-level fan diagram of the Shubnikov–de Haas (SdH) oscillations, such an analysis has been widely employed in recent transport studies of topological insulators to elucidate the Dirac nature of the surface states. However, the reported results have usually been unconvincing. Here we show a general scheme for describing the phase factor of the SdH oscillations in realistic surface states of topological insulators, and demonstrate how one can elucidate the Dirac nature in real experimental data.

DOI: [10.1103/PhysRevB.84.035301](https://doi.org/10.1103/PhysRevB.84.035301)

PACS number(s): 73.25.+i, 73.20.At, 71.70.Di, 72.20.My

## I. INTRODUCTION

During the last three decades, the Berry phase<sup>1</sup> has become an important concept in condensed matter physics,<sup>2</sup> playing a fundamental role in various phenomena such as electric polarization,<sup>3</sup> orbital magnetism,<sup>4,5</sup> anomalous Hall effects,<sup>6</sup> etc. The Berry phase (or geometrical phase) in solids<sup>7</sup> is determined by topological characteristics of the energy bands in the Brillouin zone (BZ) and represents a fundamental property of the system.<sup>8</sup> For example, a nonzero Berry phase, which can be measured directly in magnetotransport experiments, reflects the existence of a singularity in the energy bands such as a band-contact line in three-dimensional (3D) bulk states or a Dirac point in a two-dimensional (2D) surface state.<sup>9</sup> Also, the Berry phase of  $\pi$  is responsible for the peculiar “antilocalization” effects in carbon nanotubes or graphene.<sup>10</sup> Recently, the  $\pi$  Berry phase has been observed in the Shubnikov–de Haas (SdH) oscillations in graphene,<sup>11,12</sup> giving one of the key pieces of evidence for the Dirac nature of quasiparticles in the 2D carbon sheet.

The 3D topological insulator<sup>13–16</sup> (TI) also supports spin-polarized 2D Dirac fermions on its surface,<sup>17</sup> which can be distinguished from ordinary charge carriers by a nonzero Berry phase. Recently, several groups have reported observations of the SdH oscillations coming from the 2D surface states of TIs.<sup>18–25</sup> In those studies, a finite Berry phase has been reported, but it usually deviates from the exact  $\pi$  value. For example, in the new TI material  $\text{Bi}_2\text{Te}_2\text{Se}$  (BTS),<sup>21</sup> where a large contribution of the surface transport to the total conductivity has been observed, the apparent Berry phase extracted from the SdH-oscillation data was  $0.44\pi$ . So far, the Zeeman coupling of the spin to the magnetic field has been considered<sup>20</sup> as a possible source of such a discrepancy. Here, we show that in addition to the Zeeman term, the deviation of the dispersion relation  $E(k)$  from an ideal linear dispersion<sup>26</sup> can shift the Berry phase from  $\pi$ . We further show how the real experimental data for nonideal Dirac fermions can be understood by taking into account those additional factors.

## II. ENERGY DISPERSION OF SURFACE STATES

The energy dispersion of the surface states in TIs can be directly measured in angle-resolved photoemission spectroscopy (ARPES) experiments. As an example, Fig. 1 shows

the dispersion of the surface state (together with the bulk state) in BTS reported by Xu *et al.*<sup>27</sup> One can easily recognize that  $E(k)$  is not an ideal Dirac-like dispersion, but it can be fitted reasonably well for the two high-symmetry axes with

$$E(k) = v_F \hbar k + \frac{\hbar^2}{2m} k^2, \quad (1)$$

with a single Fermi velocity  $v_F = 3.4 \times 10^5$  m/s and an effective mass  $m$  which slightly varies with the direction in the surface BZ as shown by the solid lines in Fig. 1 [ $m/m_0 = 0.15$  (0.125) for the  $\bar{\Gamma} \rightarrow \bar{M}$  ( $\bar{\Gamma} \rightarrow \bar{K}$ ) direction with  $m_0$  the free-electron mass].

Similar fittings can be obtained for other TIs owing to the progress in ARPES studies of these materials.<sup>17,24,28,29</sup>

## III. BERRY PHASE IN QUANTUM OSCILLATIONS

It is commonly accepted that quantum oscillations observed in 3D metals can be well understood within Lifshits–Kosevich<sup>30</sup> (the de Haas–van Alphen effect) and Adams–Holstein<sup>31</sup> (the SdH effect) theories. Recently this approach has been generalized to describe magnetic oscillations in graphene, which is a 2D system with a Dirac-like spectrum of charge carriers.<sup>32,33</sup> There are two most prominent features that distinguish such systems from materials with a parabolic spectrum: First, rather weak magnetic fields are sufficient to bring the system into a regime where only a few Landau levels are occupied. Second, Dirac quasiparticles acquire the Berry phase of  $\pi$  in the cyclotron motion, changing the phase of quantum oscillations.

In the SdH effect, the oscillating part of  $\rho_{xx}$  follows

$$\Delta\rho_{xx} \sim \cos \left[ 2\pi \left( \frac{F}{B} - \gamma \right) \right], \quad (2)$$

where  $F$  is the oscillation frequency and  $2\pi\gamma$  is the phase factor ( $0 \leq \gamma < 1$ ). This is the same  $\gamma$  as in the Onsager semiclassical quantization condition<sup>34</sup>

$$A_N = \frac{2\pi e}{\hbar} B(N + \gamma), \quad (3)$$

when the  $N$ th Landau level (LL) is crossing the Fermi energy  $E_F$  ( $A_N$  is the area of an electron orbit in the  $k$  space).  $\gamma$  is

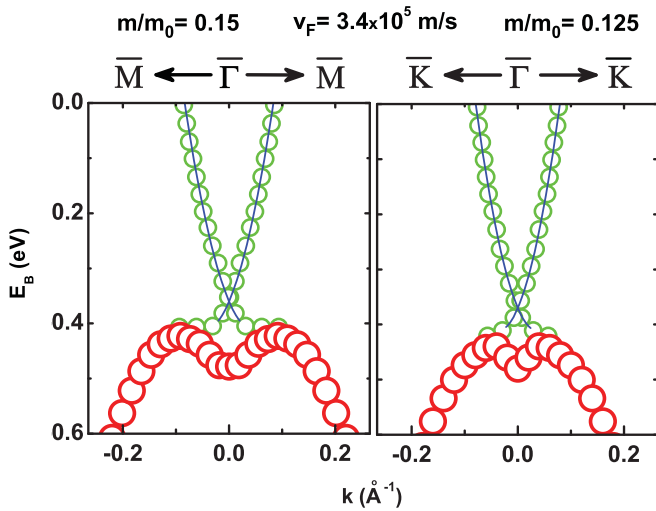


FIG. 1. (Color online) Experimental band dispersions (symbols) in  $\text{Bi}_2\text{Te}_2\text{Se}$  measured by ARPES in Ref. 27 and the fitting of Eq. (1) to the surface state (solid line). Large symbols depict the bulk state.

directly related to the Berry phase through<sup>9</sup>

$$\gamma - \frac{1}{2} = -\frac{1}{2\pi} \oint_{\Gamma} \vec{\Omega} d\vec{k}, \quad (4)$$

where  $\vec{\Omega}(\vec{k}) = i \int d\vec{k} u_{\vec{k}}^*(\vec{r}) \vec{\nabla}_{\vec{k}} u_{\vec{k}}(\vec{r})$  is the Berry connection,  $u_{\vec{k}}(\vec{r})$  is the amplitude of the Bloch wave function, and  $\Gamma$  is a closed electron orbit [the intersection of the Fermi surface  $E(\vec{k}) = E_F$  with the plane  $k_z = \text{const}$ ]. For spinless quasiparticles, it is known<sup>9,34</sup> that the Berry phase is zero for a parabolic energy dispersion ( $\gamma = \frac{1}{2}$ ) and  $\pi$  for a linear energy dispersion ( $\gamma = 0$ ).

Experimentally,  $\gamma$  can be obtained from an analysis of the Landau-level fan diagram. There are three quantities which are often used as abscissa for plotting a LL fan diagram: (i) The Landau level index  $N$ , which determines the energy  $E_N$  of the  $N$ th LL. (ii) The filling factor  $\nu \equiv \frac{N_s S}{N_\phi}$ , where  $N_s$  is the density of charge carriers,  $S$  is the area of the sample,  $N_\phi = \frac{BS}{\Phi_0}$  is the number of flux quanta, and  $\Phi_0 = \frac{h}{e}$  is the flux quantum. (iii) An integer number  $n$  which marks the  $n$ th minimum of the oscillations in  $\rho_{xx}$ . Although all three quantities are related to each other, the most straightforward way to plot a LL fan diagram from the  $\rho_{xx}$  oscillations in a 2D system<sup>18</sup> is to assign an integer  $n$  to a minimum of  $\rho_{xx}$  (or a half integer to a maximum of  $\rho_{xx}$ ). From Eq. (2), one can see that the first minimum in  $\rho_{xx}$  is always in the range of  $0 < \frac{F}{B_1} \leq 1$ . Thus, the plot of  $F/B_n$  vs  $n$ , which makes a straight line with a unit slope for periodic oscillations, is uniquely defined and cuts the  $n$  axis between 0 and 1 depending on the phase of the oscillations,  $\gamma$ .

The ordinate  $1/B_n$  in a LL fan diagram is determined by the Landau quantization of the cyclotron motion of electrons in a magnetic field. In 2D systems, upon sweeping  $B$ ,  $\rho_{xx}$  shows a maximum (or a sharp peak in the quantum Hall effect<sup>18</sup>) each time that  $E_N(B)$  crosses the Fermi level. Thus, the position of the maximum in  $\rho_{xx}$  that corresponds to the  $N$ th LL,  $1/B_n$ ,

is given by

$$2\pi \left( \frac{F}{B_n} - \gamma \right) = 2\pi N. \quad (5)$$

On the other hand, the  $n$ th minimum in  $\rho_{xx}$  occurs at  $1/B_n$  when  $2\pi \left( \frac{F}{B_n} - \gamma \right) = 2\pi n - \pi$ , so the positions of the maxima and minima are shifted by  $\frac{1}{2}$  on the  $n$  axis.

The Onsager relation<sup>34</sup> gives  $F$  in terms of the Fermi wave vector  $k_F$  as  $F = (\hbar/2\pi e)\pi k_F^2$ , and this  $k_F$  can be calculated from Eq. (1) as

$$k_F^2 = 2 \left( \frac{mv_F}{\hbar} \right)^2 \left( 1 + \frac{E_F}{mv_F^2} - \sqrt{1 + \frac{2E_F}{mv_F^2}} \right). \quad (6)$$

Also, when  $E_F$  is at the  $N$ th LL, there is a relation

$$E_N(B_N) = E_F. \quad (7)$$

From Eqs. (5)–(7), one obtains

$$\gamma = \frac{mv_F^2}{\hbar \omega_c} \left( 1 + \frac{E_N}{mv_F^2} - \sqrt{1 + \frac{2E_N}{mv_F^2}} \right) - N, \quad (8)$$

where  $\omega_c = eB/m$  is the cyclotron frequency.

In the general case,  $\gamma$  is a function of  $B$ , meaning that oscillations in  $\rho_{xx}$  are quasiperiodic in  $1/B$ . In order to calculate  $\gamma$  one needs to find the eigenvalues  $E_N$  for a given Hamiltonian.

#### IV. MODEL HAMILTONIAN

For the (111) surface state of the  $\text{Bi}_2\text{Se}_3$ -family TI compounds, the Hamiltonian for nonideal Dirac quasiparticles in perpendicular magnetic fields can be written as<sup>35</sup>

$$\hat{H} = v_F(\Pi_x \sigma_y - \Pi_y \sigma_x) + \frac{\Pi^2}{2m} - \frac{1}{2} g_s \mu_B B \sigma_z, \quad (9)$$

where the Landau gauge  $\mathbf{A} = (0, By, 0)$  for the vector potential is used,  $\Pi = \hbar \mathbf{k} + e\mathbf{A}$ ,  $\sigma_i$  are the Pauli matrices,  $\mu_B$  is the Bohr magneton, and  $g_s$  is the surface  $g$ -factor. Note that this Hamiltonian is essentially the same as for a conventional 2D electron gas (2DEG) with Bychkov-Rashba spin-orbit interaction term.<sup>36</sup> The only difference is that in TIs the parabolic term in Eq. (1) is a small perturbation in comparison with the linear one. The LL energies are given by<sup>35–37</sup>

$$E_N^{(\pm)} = \hbar \omega_c N \pm \sqrt{2\hbar v_F^2 e B N + \left( \frac{1}{2} \hbar \omega_c - \frac{1}{2} g_s \mu_B B \right)^2}, \quad (10)$$

where the “+” and “−” branches are for electrons and holes, respectively. The obtained eigenvalues  $E_N$  define the exact positions of maxima in  $\rho_{xx}$  and, thus, the phase of oscillations through Eq. (8).

In two extreme cases, for nonmagnetic fermions ( $g_s = 0$ ), Eq. (8) gives the expected results. First, for a linear dispersion (ideal Dirac fermions),  $m \rightarrow \infty$  leads to  $E_N = \pm \sqrt{2\hbar e v_F^2 B N}$  and  $\gamma \rightarrow \frac{E_N^2}{2\hbar e v_F^2 B} - N$ , giving  $\gamma = 0$  (Berry phase is  $\pi$ ). Second, for a parabolic dispersion,  $v_F \rightarrow 0$  leads to  $E_N = \hbar \omega_c (N + \frac{1}{2})$  and  $\gamma \rightarrow \frac{E_N}{\hbar \omega_c} - N$ , giving  $\gamma = \frac{1}{2}$  (Berry phase is zero). This gives confidence that the expression for  $\gamma$  given

in Eq. (8) is generally valid for the topological surface state with a nonideal Dirac cone described by Eq. (1).

### V. LANDAU-LEVEL FAN DIAGRAM FOR NONIDEAL DIRAC FERMIONS

Let us first consider how the LL fan diagram will be modified when both linear and parabolic terms are present in the Hamiltonian [Eq. (9)]. For the moment, the Zeeman coupling of the electron spin to the magnetic field is assumed to be negligible ( $g_s = 0$ ). Figure 2(a) shows the calculated positions of maxima and minima in  $\rho_{xx}$  for oscillations with  $F = 60$  T and  $v_F = 3 \times 10^5$  m/s as  $m/m_0$  is varied. One can see that upon decreasing  $m/m_0$ , the calculated lines on the LL fan diagram are gradually shifting upward from the ideal Dirac line that crosses the  $n$  axis at exactly  $\frac{1}{2}$ . Moreover, the lines are not straight anymore, which is reflected in the dependence of  $\gamma$  vs  $N$  shown in the inset. With decreasing  $N$  (increasing  $B$ ),  $\gamma$  becomes larger, reflecting the change in the phase of oscillations at high fields.

A similar change in the LL fan diagram occurs if we modify another parameter,  $v_F$ . As shown in Fig. 2(b), the calculated lines are gradually shifting upward from the ideal Dirac line as

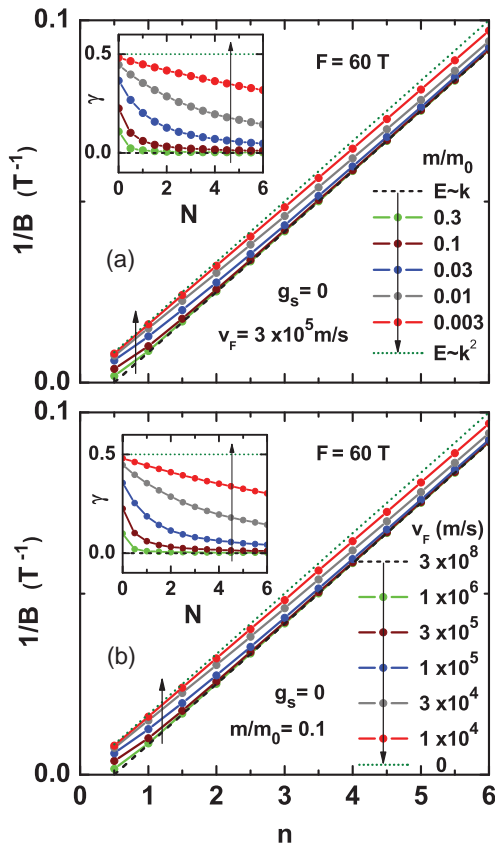


FIG. 2. (Color online) (a) Landau level fan diagram calculated for  $F = 60$  T,  $v_F = 3 \times 10^5$  m/s,  $g_s = 0$ , and different  $m/m_0$ . Arrows show the direction of decreasing  $m/m_0$ . The dashed and dotted lines are the expected behaviors for an ideal Dirac dispersion and a parabolic dispersion, respectively. (b) Landau level fan diagram calculated for  $F = 60$  T,  $m/m_0 = 0.1$ ,  $g_s = 0$ , and different  $v_F$ . Arrows show the direction of decreasing  $v_F$ . Insets show the calculated  $\gamma(N)$ .

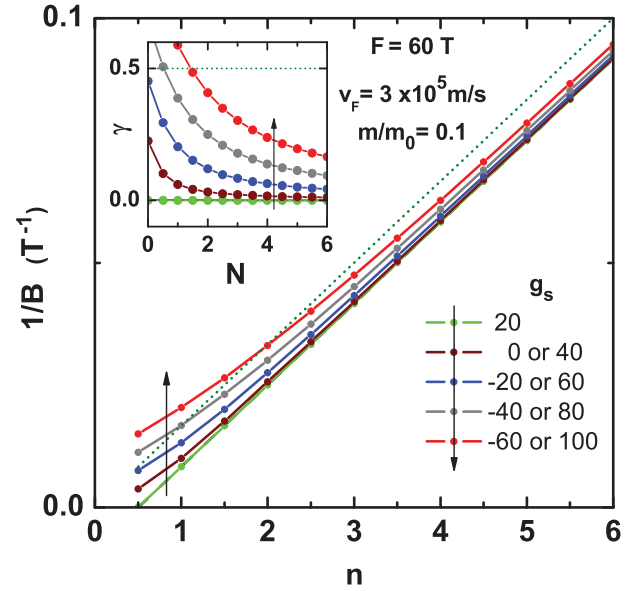


FIG. 3. (Color online) Landau-level fan diagram calculated for  $F = 60$  T and different  $g_s$ , keeping  $v_F = 3 \times 10^5$  m/s and  $m/m_0 = 0.1$  constant. Arrows show the direction of changing  $g_s$ . The dotted line is the expected behavior for a parabolic dispersion. Inset shows the calculated  $\gamma(N)$ .

$v_F$  is decreased. The results shown in Fig. 2 can be understood as a competition between linear and quadratic terms in the Hamiltonian [Eq. (9)]. Note that for the whole range of the parameters  $v_F$  and  $m/m_0$ , the positions of maxima and minima in  $\rho_{xx}$  lie between two straight lines (shown as dotted and dashed lines in Fig. 2) corresponding to  $\gamma = 0$  and  $\gamma = \frac{1}{2}$ .

Let us now take the Zeeman term into consideration. Figure 3 shows the LL fan diagram calculated with  $F = 60$  T,  $v_F = 3 \times 10^5$  m/s, and  $m/m_0 = 0.1$ , while  $g_s$  is varied. To understand the effect of the Zeeman coupling, it is important to recognize the following two points: (i) The Zeeman term in Eq. (10) would tend to cancel the  $\frac{1}{2}\hbar\omega_c$  term when  $g_s$  is positive. In fact, when  $\frac{1}{2}\hbar\omega_c = \frac{1}{2}g_s\mu_B B$  (i.e.,  $g_s = 2m_0/m$ ) is satisfied, the effect of the finite effective mass is canceled and the LL fan diagram becomes identical to that for the linear dispersion (ideal Dirac) case. In the present simulations, we use  $m/m_0 = 0.1$ , so that this cancellations occurs when  $g_s = 20$ . (ii) A pair of  $g_s$  values that give the same  $|\frac{1}{2}\hbar\omega_c - \frac{1}{2}g_s\mu_B B|$  are effectively the same in determining the behavior of the LL fan diagram. The result of our calculations shown in Fig. 3 is a demonstration of these two points. Since the Zeeman effect is more pronounced at higher fields, the LL fan diagram in Fig. 3 is strongly modified from a straight line when the quantum limit is approached, i.e., close to  $N = 0$ .

### VI. THE CASE OF BTS

Let us examine the real data measured in the BTS sample,<sup>21</sup> in the light of the above considerations. Figure 4 shows the LL fan diagram for oscillations in  $d\rho_{xx}/dB$  measured at  $T = 1.6$  K in magnetic fields perpendicular to the (111) plane.<sup>21</sup> In Ref. 21, the data were simply fitted with a straight line, and the least-squares fitting gave a slope of  $F = 64$  T with the intersection of the  $n$  axis at  $0.22 \pm 0.12$ ; this result implies a

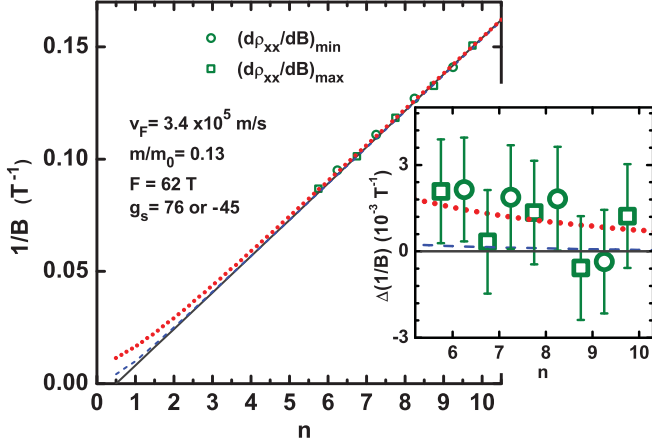


FIG. 4. (Color online) Landau-level fan diagram for oscillations in  $d\rho_{xx}/dB$  measured at  $T = 1.6$  K and  $\theta \simeq 0^\circ$  reported in Ref. 21 for BTS. Minima and maxima in  $d\rho_{xx}/dB$  correspond to  $n + \frac{1}{4}$  and  $n + \frac{3}{4}$ , respectively. Solid (dark gray) line is the calculated diagram for an ideal Dirac cone with  $v_F = 3.4 \times 10^5$  m/s and  $F = 62$  T; dashed (blue) line includes the effect of the actual dispersion with  $m/m_0 = 0.13$ ; dotted (red) line further includes the Zeeman effect, where  $g_s = 76$  or  $-45$  was determined from a least-squares fitting to the data. Inset shows the experimental data and calculations after subtracting the contribution from an ideal Dirac cone,  $(1/B)_{\text{Dirac}}$ , where  $\Delta(1/B) \equiv (1/B) - (1/B)_{\text{Dirac}}$ .

finite Berry phase, but it was not exactly equal to  $\pi$ , which remained a puzzle.<sup>21</sup> Now, we analyze this LL fan diagram by considering the nonideal Dirac dispersion as well as the Zeeman effect. The ARPES data<sup>27</sup> for the surface state of BTS (Fig. 1) give  $v_F = 3.4 \times 10^5$  m/s and the averaged effective mass  $m/m_0 = 0.13$ . We fix the oscillation frequency  $F$  at 62 T obtained from the Fourier-transform analysis of the  $d\rho_{xx}/dB$  oscillations.<sup>21</sup>

In Fig. 4, the calculated diagram for an ideal Dirac cone is shown by the solid (dark gray) line, whereas that for the nonideal Dirac cone with the effective-mass term is shown by the dashed (blue) line. One can see that the difference is small, which indicates that the effective mass of  $0.13m_0$  is not light enough to significantly alter the LL fan diagram. One may also see that these two lines undershoot the actual data points at smaller  $n$ , which is even more clearly seen in the inset, where the experimental data and the calculations are shown after subtracting the contribution from an ideal Dirac cone. By further including the Zeeman effect, we can greatly improve the analysis, as shown by the dotted (red) line; here,  $g_s$  is taken as the only fitting parameter and a least-squares fitting to the data was performed. The best value of  $g_s$  is 76 or  $-45$ .

The inset of Fig. 4 makes it clear that it is the slight deviation of the experimental points from the ideal Dirac line that causes a simple straight-line fitting of the LL fan diagram to intersect the  $n$  axis not exactly at 0.5. Since the Berry phase in real situations is not a fixed value but is dependent on the magnetic field, the simple straight-line analysis of the LL fan diagram should not be employed for the determination of the Berry phase. Obviously, the SdH oscillations of the topological surface states are best understood by the analysis which considers both the deviation of the energy spectrum

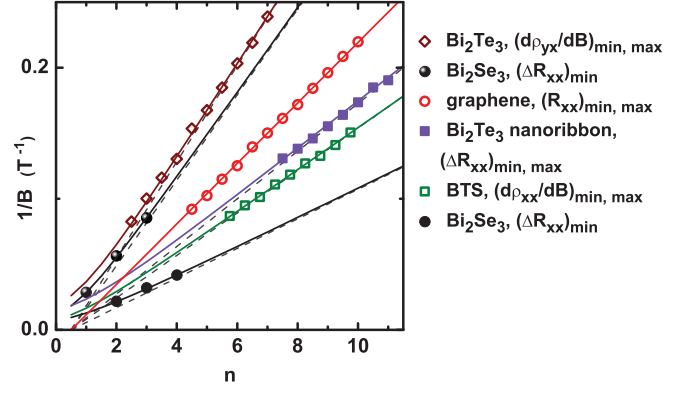


FIG. 5. (Color online) Landau-level fan diagrams for SdH oscillations observed in various TIs and graphene. Symbols are obtained from the published experimental data in the literature. Solid lines are calculations taking into account the nonideal dispersions of the surface states (determined by  $m/m_0$ ) and the Zeeman coupling to an external magnetic field (determined by  $g_s$ ). Dashed lines are calculations for ideal Dirac fermions ( $m/m_0 = \infty$  and  $g_s = 0$ ). Open diamonds are  $(d\rho_{yx}/dB)_{\text{min,max}}$  in  $\text{Bi}_2\text{Te}_3$  from Ref. 18; filled circles are  $(\Delta R_{xx})_{\text{min}}$  in  $\text{Bi}_2\text{Se}_3$  from Ref. 20; open circles are  $(R_{xx})_{\text{min,max}}$  in graphene from Ref. 11; filled squares are  $(\Delta R_{xx})_{\text{min,max}}$  in a  $\text{Bi}_2\text{Te}_3$  nanoribbon from Ref. 25; open squares are  $(d\rho_{xx}/dB)_{\text{min,max}}$  in BTS from Ref. 21.

of the Dirac-like charge carriers from the ideal linear dispersion and their strong coupling with an external magnetic field.

## VII. OTHER MATERIALS

Similar analyses can be performed for other TIs in which the quantum oscillations coming from the 2D topological surface states have been observed. Figure 5 shows the LL fan diagrams for the SdH oscillations published to date for TI materials,<sup>18,20,21,25,38</sup> together with the data obtained in graphene,<sup>11</sup> which provides a good reference for studies of Dirac fermions. We digitized the published experimental data in the literature and determined ourselves the positions of minima  $1/B_{\text{min}}$  and maxima  $1/B_{\text{max}}$  of the oscillating parts of the resistivity (resistance), Hall resistivity, or their derivatives with respect to  $B$ . The data obtained for various materials are plotted as functions of  $n$  in Fig. 5. Note that, to avoid ambiguities, we considered only those data that show oscillations with a single frequency.<sup>38</sup>

The parameters of the surface states used in our fan-diagram analyses have been obtained from the published ARPES data by fitting them in the same way as for BTS (see Fig. 1). Table I shows  $v_F$  and  $m/m_0$  for the  $\text{Bi}_2\text{Se}_3/\text{Bi}_2\text{Te}_3$  family and graphene. These parameters were fixed during the fitting of the data shown in Fig. 5. The only parameter that could

TABLE I. Parameters of the surface states from ARPES.

Material	$v_F$ (m/s)	$m/m_0$	Ref.	Remark
$\text{Bi}_2\text{Se}_3$	$3.0 \times 10^5$	0.25	[28]	Averaged
$\text{Bi}_2\text{Te}_2\text{Se}$	$3.4 \times 10^5$	0.13	[21]	Averaged
$\text{Bi}_2\text{Te}_3$	$3.7 \times 10^5$	3.8	[29]	Near Dirac point
Graphene	$1 \times 10^6$	$\infty$	[11]	Calculations



TABLE II. Parameters used for the calculations shown in Fig. 5.

Material	Ref.	$F$ (T)	$E_F$ (eV)	$g_s$
Bi <sub>2</sub> Se <sub>3</sub>	[20]	30.7	0.074	55 or -39
Bi <sub>2</sub> Se <sub>3</sub>	[20]	88.6	0.143	55 or -39
Bi <sub>2</sub> Te <sub>2</sub> Se	[21]	62.0	0.152	76 or -45
Bi <sub>2</sub> Te <sub>3</sub>	[18]	27.3	0.074	65 or -65
Bi <sub>2</sub> Te <sub>3</sub> , nanoribbon	[25]	54.7	0.101	65 or -65
Graphene	[11]	43.3	0.239	0

vary in our calculations was  $g_s$ . Note that the frequency of oscillations  $F$  (and, thus, the Fermi energy  $E_F$ ) is essentially determined by the periodicity of the observed oscillations. Table II summarizes the parameters thus obtained. The results of our calculations are shown in Fig. 5 by solid lines. Dashed lines depict the behavior expected for ideal Dirac cones ( $m/m_0 = \infty$ ) and negligible Zeeman coupling ( $g_s = 0$ ) for the TI data. One can clearly see in Fig. 5 that only graphene shows the ideal behavior in the LL fan diagram: a straight line that crosses the  $n$  axis at 0.5. All TI materials, despite their essentially Dirac-like nature of the surface state, present LL fan diagrams that deviate from the ideal behavior. (The deviations from the dashed lines are most clearly seen in strong magnetic fields.)

In view of the good agreements between the data and the fittings for all the materials analyzed in Fig. 5, one

may conclude that the advanced analysis considering both the curvature of the Dirac cone and the Zeeman effect can reasonably describe the SdH oscillation data obtained for TIs and confirm the Dirac nature in their surface states.

## VIII. SUMMARY

We derived the formula for the phase  $\gamma$  of the SdH oscillations coming from the surface Dirac fermions of realistic topological insulators with a nonideal dispersion given by Eq. (1). We also calculated how the curvature in the dispersion as well as the effect of Zeeman coupling affect the Landau-level fan diagram of the SdH oscillations for realistic parameters. Finally, we demonstrated that the Landau-level fan diagrams obtained from recently reported SdH oscillations in topological insulators can actually be understood to signify the essentially Dirac nature of the surface states, along with a relatively large Zeeman effect in those narrow-gap materials.

## ACKNOWLEDGMENTS

We thank G. P. Mikitik for helpful discussions. This work was supported by JSPS (NEXT Program), MEXT (Innovative Area “Topological Quantum Phenomena” KAKENHI Grant No. 22103004), and AFOSR (AOARD Grant No. 10-4103).

<sup>1</sup>M. V. Berry, *Proc. R. Soc. London, Ser. A* **392**, 45 (1984).

<sup>2</sup>A. Shapere and F. Wilczek, *Geometrical Phase in Physics* (World Scientific, Singapore, 1989).

<sup>3</sup>R. D. King-Smith and David Vanderbilt, *Phys. Rev. B* **47**, 1651(R) (1993).

<sup>4</sup>D. Xiao, J. Shi, and Q. Niu, *Phys. Rev. Lett.* **95**, 137204 (2005).

<sup>5</sup>T. Thonhauser, D. Ceresoli, D. Vanderbilt, and R. Resta, *Phys. Rev. Lett.* **95**, 137205 (2005).

<sup>6</sup>N. Nagaosa, J. Sinova, S. Onoda, A. H. MacDonald, and N. P. Ong, *Rev. Mod. Phys.* **82**, 1539 (2010).

<sup>7</sup>J. Zak, *Phys. Rev. Lett.* **62**, 2747 (1989).

<sup>8</sup>D. Xiao, M. C. Chang, and Q. Niu, *Rev. Mod. Phys.* **82**, 1957 (2010).

<sup>9</sup>G. P. Mikitik and Yu. V. Sharlai, *Phys. Rev. Lett.* **82**, 2147 (1999).

<sup>10</sup>T. Ando, T. Nakanishi, and R. Saito, *J. Phys. Soc. Jpn.* **67**, 2857 (1998).

<sup>11</sup>K. S. Novoselov, A. K. Geim, S. V. Morozov, D. Jiang, M. I. Katsnelson, I. V. Grigorieva, S. V. Dubonos, and A. A. Firsov, *Nature (London)* **438**, 197 (2005).

<sup>12</sup>Y. Zhang, Y.-W. Tan, H. L. Stormer, and P. Kim, *Nature (London)* **438**, 201 (2005).

<sup>13</sup>L. Fu, C. L. Kane, and E. J. Mele, *Phys. Rev. Lett.* **98**, 106803 (2007).

<sup>14</sup>J. E. Moore and L. Balents, *Phys. Rev. B* **75**, 121306(R) (2007).

<sup>15</sup>R. Roy, *Phys. Rev. B* **79**, 195321 (2009).

<sup>16</sup>X.-L. Qi, T. L. Hughes, and S.-C. Zhang, *Phys. Rev. B* **78**, 195424 (2008).

<sup>17</sup>M. Z. Hasan and C. L. Kane, *Rev. Mod. Phys.* **82**, 3045 (2010).

<sup>18</sup>D.-X. Qu, Y. S. Hor, J. Xiong, R. J. Cava, and N. P. Ong, *Science* **329**, 821 (2010).

<sup>19</sup>A. A. Taskin, K. Segawa, and Y. Ando, *Phys. Rev. B* **82**, 121302(R) (2010).

<sup>20</sup>J. G. Analytis, R. D. McDonald, S. C. Riggs, J.-H. Chu, G. S. Boebinger, and I. R. Fisher, *Nature Phys.* **10**, 960 (2010).

<sup>21</sup>Z. Ren, A. A. Taskin, S. Sasaki, K. Segawa, and Y. Ando, *Phys. Rev. B* **82**, 241306(R) (2010).

<sup>22</sup>J. Xiong, A. C. Petersen, Dongxia Qu, R. J. Cava, and N. P. Ong, e-print [arXiv:1101.1315](https://arxiv.org/abs/1101.1315).

<sup>23</sup>B. Sacépé, J. B. Oostinga, J. Li, A. Ubaldini, N. J. G. Couto, E. Giannini, and A. F. Morpurgo, e-print [arXiv:1101.2352](https://arxiv.org/abs/1101.2352).

<sup>24</sup>C. Brüne, C. X. Liu, E. G. Novik, E. M. Hankiewicz, H. Buhmann, Y. L. Chen, X. L. Qi, Z. X. Shen, S. C. Zhang, and L. W. Molenkamp, *Phys. Rev. Lett.* **106**, 126803 (2011).

<sup>25</sup>F. Xiu, L. He, Y. Wang, L. Cheng, L.-T. Chang, M. Lang, G. Huang, X. Kou, Y. Zhou, X. Jiang, Z. Chen, J. Zou, A. Shailos, and K. L. Wang, *Nature Nano.* **6**, 216 (2011).

<sup>26</sup>D. Culcer, E. H. Hwang, T. D. Stanescu, and S. Das Sarma, *Phys. Rev. B* **82**, 155457 (2010).

<sup>27</sup>S. Y. Xu, L. A. Wray, Y. Xia, R. Shankar, A. Petersen, A. Fedorov, H. Lin, A. Bansil, Y. S. Hor, D. Grauer, R. J. Cava, and M. Z. Hasan, e-print [arXiv:1007.5111v1](https://arxiv.org/abs/1007.5111v1).

<sup>28</sup>Y. Xia, D. Qian, D. Hsieh, L. Wray, A. Pal, H. Lin, A. Bansil, D. Grauer, Y. S. Hor, R. J. Cava, and M. Z. Hasan, *Nature Phys.* **5**, 398 (2009).

- <sup>29</sup>Y. L. Chen, J. G. Analytis, J.-H. Chu, Z. K. Liu, S.-K. Mo, X. L. Qi, H. J. Zhang, D. H. Lu, X. Dai, Z. Fang, S. C. Zhang, I. R. Fisher, Z. Hussain, and Z.-X. Shen, *Science* **325**, 178 (2009).
- <sup>30</sup>I. M. Lifshits and A. M. Kosevich, *Zh. Eksp. Teor. Fiz.* **29**, 730 (1955) [*Sov. Phys. JETP* **2**, 636 (1956)].
- <sup>31</sup>E. Adams and T. Holstein, *J. Phys. Chem. Solids* **10**, 254 (1959).
- <sup>32</sup>S. G. Sharapov, V. P. Gusynin, and H. Beck, *Phys. Rev. B* **69**, 075104 (2004).
- <sup>33</sup>V. P. Gusynin and S. G. Sharapov, *Phys. Rev. B* **71**, 125124 (2005).
- <sup>34</sup>D. Shoenberg, *Magnetic Oscillations in Metals* (Cambridge University Press, Cambridge, 1984).
- <sup>35</sup>Z. Wang, Z.-G. Fu, S.-X. Wang, and P. Zhang, *Phys. Rev. B* **82**, 085429 (2010).
- <sup>36</sup>Y. A. Bychkov and E. I. Rashba, *Pis'ma Zh. Eksp. Teor. Fiz.* **39**, 66 (1984) [*JETP Lett.* **39**, 78 (1984)].
- <sup>37</sup>B. Seradjeh, J. Wu, and P. Phillips, *Phys. Rev. Lett.* **103**, 136803 (2009).
- <sup>38</sup>We did not include the data reported in Refs. 19 and 24, because the SdH oscillations observed in  $\text{Bi}_{0.91}\text{Sb}_{0.09}$  (Ref. 19) and in a strained epitaxial film of HgTe (Ref. 24) clearly show multiple frequencies.

# Additional Evidence for the Surface Origin of the Peculiar Angular-Dependent Magnetoresistance Oscillations Discovered in a Topological Insulator $\text{Bi}_{1-x}\text{Sb}_x$

A A Taskin, Kouji Segawa and Yoichi Ando<sup>1</sup>

Institute of Scientific and Industrial Research, Osaka University  
Ibaraki, Osaka 567-0047, Japan

E-mail: y\_ando@sanken.osaka-u.ac.jp

**Abstract.** We present detailed data on the unusual angular-dependent magnetoresistance oscillation phenomenon recently discovered in a topological insulator  $\text{Bi}_{0.91}\text{Sb}_{0.09}$ . Direct comparison of the data taken before and after etching the sample surface gives compelling evidence that this phenomenon is essentially originating from a surface state. The symmetry of the oscillations suggests that it probably comes from the (111) plane, and obviously a new mechanism, such as a coupling between the surface and the bulk states, is responsible for this intriguing phenomenon in topological insulators.

## 1. Introduction

Topological insulators [1-3] are an emerging class of materials that host a new quantum-mechanical state of matter [4-7] where an insulating bulk state supports an intrinsically metallic surface state that is “topologically protected”, meaning that it is stable against any disorder that does not break time-reversal symmetry. Recently, angle-resolved photoemission spectroscopy (ARPES) studies on a cleaved trigonal surface of  $\text{Bi}_{1-x}\text{Sb}_x$  have revealed that the energy dispersions of its surface states possess the distinctive character to qualify this material as a topological insulator [8-10]. However, to directly probe the unique properties of the surface states and to elucidate whether they could really be exploited on a macroscopic level, transport and magnetic studies of high-quality single crystals are indispensable. Unfortunately, in “real-life” samples of topological insulators available today, there is always some bulk conductivity due to residual carriers, and separating the contributions from two-dimensional (2D) and three-dimensional (3D) states turns out to be challenging [11-13].

In this context, we have recently succeeded in observing both the de Haas-van Alphen (dHvA) oscillations [14] and the Shubnikov-de Haas (SdH) oscillations [15] in high-quality bulk single crystals of  $\text{Bi}_{1-x}\text{Sb}_x$  alloy in the “insulating” regime ( $0.07 \leq x \leq 0.22$ ), which is the first material to be known as a 3D topological insulator. These observations became possible by growing highly pure and homogeneous single crystals of this alloy and achieving the bulk carrier density of the order of  $10^{16} \text{ cm}^{-3}$ . The dHvA and SdH oscillations signified a previously-unknown Fermi surface (FS) with a clear 2D character that coexists with a 3D bulk FS [14,15]. Since  $\text{Bi}_{1-x}\text{Sb}_x$  is a 3D material, the observed 2D FS is naturally assigned to the “surface”, which could be internal surfaces such as twin boundaries.

<sup>1</sup> To whom any correspondence should be addressed.

Furthermore, we have extended our measurements to the angular dependence of the magnetoresistance (MR), which was successfully applied to the studies of quasi-2D organic conductors in the 1980s and lead to the discovery of the celebrated angular-dependent magnetoresistance oscillations (AMRO) [16-18]. Intriguingly, in our angular-dependent MR studies, we found oscillatory angular dependences in both the resistivity  $\rho_{xx}$  and the Hall resistivity  $\rho_{yx}$  [15]. The oscillations observed at lower fields were elucidated to be essentially a manifestation of the SdH oscillations, whereas the ones observed at higher fields were obviously of novel origin [15]. We proposed that the latter originates from the topological surface state on the cleaved (111) surface of  $\text{Bi}_{1-x}\text{Sb}_x$ , where the coupling between the surface and bulk states are probably playing a key role in the peculiar MR oscillation phenomenon [15].

In this paper, we present additional evidence to demonstrate that the “high-field” oscillations are most likely due to the exposed surface, by directly comparing the oscillations before and after the sample surface was chemically etched.

## 2. Experimental

High-quality  $\text{Bi}_{0.91}\text{Sb}_{0.09}$  single crystals were grown from a stoichiometric mixture of high-purity (6N) Bi and Sb elements by a zone melting method. The resistivity was measured by a standard four-probe method on a rectangular sample, where the current was directed along the  $C_1$  axis. Continuous rotations of the sample in constant magnetic fields were used to measure the angular dependence of the MR within the trigonal-binary ( $C_3$ - $C_2$ ) crystallographic plane. Magnetic fields up to 16 T were applied using a dc superconducting magnet in a  $^4\text{He}$  cryostat. All the data shown here were taken at the lowest temperature of 1.5 K. To obtain a fresh surface on the  $\text{Bi}_{1-x}\text{Sb}_x$  single crystals, we applied the following chemical etching procedure:

- 1) Keep for several minutes in the 1:4:9 mixture of  $\text{HNO}_3$ ,  $\text{CH}_3\text{COOH}$ , and  $\text{H}_2\text{O}$ .
- 2) Rinse in distilled water.
- 3) Keep for several minutes in the diluted (50 mol-%)  $\text{HCl}$ .
- 4) Rinse in distilled water and dry.

## 3. Results

### 3.1. Angular-Dependent MR Oscillations

Figures 1(a) and 1(b) show the angular dependences of the transverse MR and the Hall resistivity,

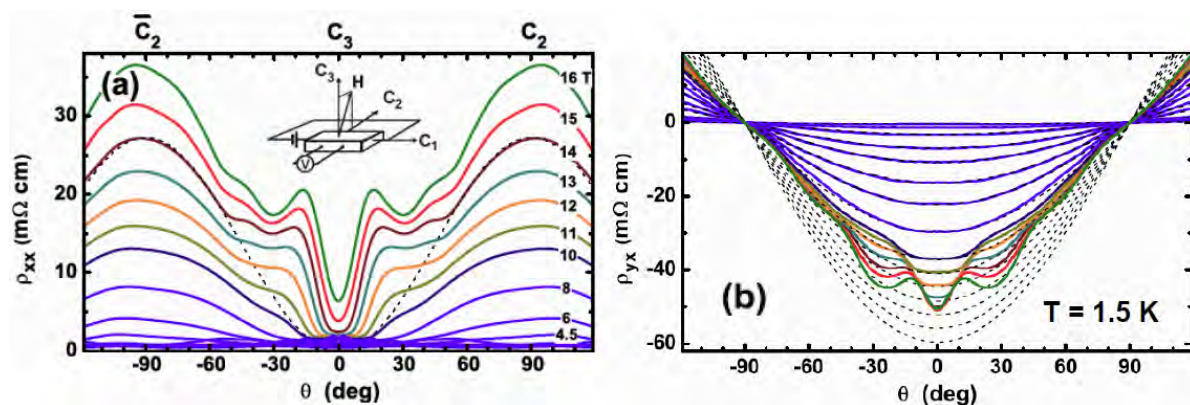


Figure 1. (a) Angular dependences of  $\rho_{xx}$  measured in the trigonal-binary ( $C_3$ - $C_2$ ) plane in constant magnetic fields. The dashed line is the MR background  $\sim (1 - \cos^2\theta)$  for  $B = 14$  T. Inset depicts the measurement geometry, where  $\theta = 0^\circ$  corresponds to the  $C_3$  axis. (b) Angular dependences of  $\rho_{yx}$  measured in the same conditions as in (a). The dashed lines are the expected angular dependences of the Hall effect plotted for all magnetic fields.



respectively, measured in magnetic fields rotated within the trigonal-binary ( $C_3$ - $C_2$ ) plane perpendicular to the current. The magnetic-field strength was kept constant during each rotation. As can be seen in Figs. 1(a) and 1(b), both  $\rho_{xx}$  and  $\rho_{yx}$  present an oscillatory behavior as a function of the rotation angle  $\theta$ . As we have elaborated in our previous paper [15], two different types of oscillations can be distinguished: The first type [though not very clearly seen in Fig. 1] consists of oscillations appearing at lower fields, while the second one becomes prominent at higher fields ( $B \geq 10$  T). The former “low-field” oscillations were demonstrated [15] to be essentially due to the SdH oscillations originating from the 2D state residing on the (2,-1,-1) plane, which was unambiguously observed in the  $\rho_{xx}(B)$  data for magnetic-field sweeps in fixed magnetic-field directions.

The focus of the present paper is the “high-field” oscillations, which develop on a smooth field-dependent background coming from the anisotropy of  $\rho_{xx}(B)$  along the different axes. An example of the fitting of the background for  $B = 14$  T is shown by the dashed line in Fig. 1(a). Because of a large MR background in strong magnetic fields, only largest peaks in  $\rho_{xx}(\theta)$  can be clearly seen in the raw data [Fig. 1(a)].

The  $\rho_{yx}(\theta)$  data shown in Fig. 1(b) also present pronounced angular-dependent oscillations at high fields. The “background” for  $\rho_{yx}(\theta)$  is simply the angular dependence of the Hall effect,  $R_H B \cos \theta$ , where  $R_H$  is the Hall coefficient. As can be clearly seen in Fig. 1(b), low-field  $\rho_{yx}(\theta)$  data follow this expected angular dependence very closely (we use  $R_H = -37 \text{ cm}^3/\text{C}$ , obtained from the Hall measurements), and the large deviation from this simple behavior is observed only in magnetic fields above 10 T. Figure 2 shows “pure” oscillations in  $\Delta\rho_{yx}(\theta)$  after subtracting the  $R_H B \cos \theta$  contribution from  $\rho_{yx}(\theta)$ . One can clearly see a set of peaks, which are marked by short vertical ticks in Fig. 2. They are symmetric with respect to the  $C_3$  axis and show a rather complicated magnetic-field dependence.

### 3.2. Surface-Condition Dependence

The data shown in Figs. 1 and 2 were taken on a refreshed surface immediately after chemically etching the sample. To investigate the effect of etching, we had conducted the same angular-dependent MR measurements on the same sample before etching. Incidentally, this sample was characterized 7 months before those measurements, and it was kept in a desiccator, exposing its surface to dry air for 7 months. Our intention was to see how such an “old” sample behaves. Intriguingly, the angular-dependent MR oscillations were smeared, as shown in Fig. 3 for  $\rho_{xx}$ . Figure 4 presents a direct comparison of the oscillations in  $\rho_{xx}$  and  $\rho_{yx}$  before and after etching. It is evident that the refreshed surface yields more pronounced oscillations, which gives direct evidence that the peculiar angular-

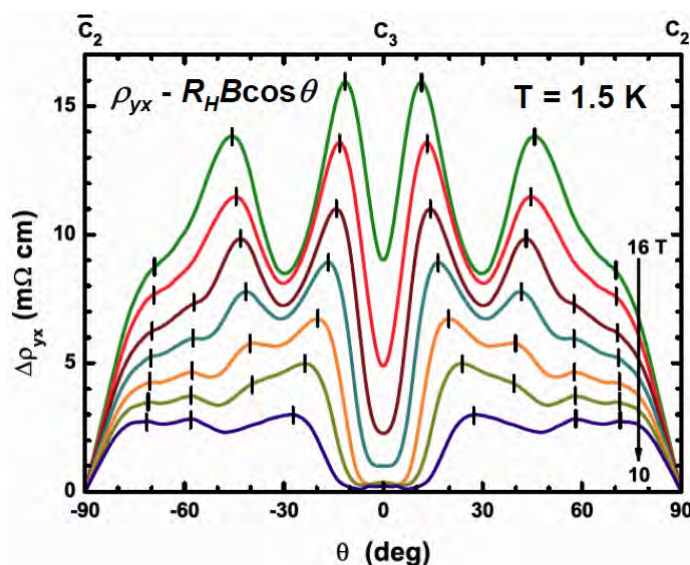


Figure 2. “High-field” angular-dependent oscillations in  $\Delta\rho_{yx}(\theta)$  obtained by subtracting the expected  $R_H B \cos \theta$  behavior from the  $\rho_{yx}$  data shown in Fig. 1(b). Ticks mark the positions of distinguishable peaks.

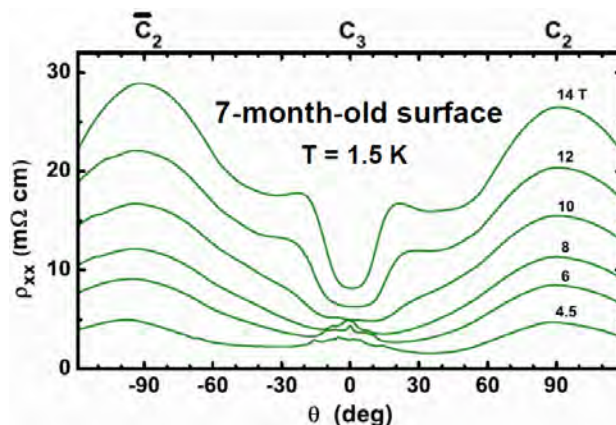


Figure 3. Angular dependences of  $\rho_{xx}$  measured in the trigonal-binary ( $C_3$ - $C_2$ ) plane on the 7-month-old surface of the same  $\text{Bi}_{0.91}\text{Sb}_{0.09}$  sample before etching. Note that the angular-dependent MR oscillations are smeared compared to those shown in Fig. 1(a).

dependent oscillations are essentially originating from a surface state.

#### 4. Discussions

In the “high-field” oscillations, an important feature is that the amplitude of the peaks weakens as the magnetic field is rotated away from the  $C_3$  axis, which is somewhat reminiscent of the behavior of the ordinary AMRO in quasi-2D systems if the conduction planes lie perpendicular to the  $C_3$  axis [16-18]. Thus, it is probable that the “high-field” oscillations are coming from the (111) plane (which is perpendicular to the  $C_3$  axis), where surface states are seen in photoemission [8-10] and tunnelling [19] experiments. Another distinguishable feature of the “high-field” oscillations is that they survive up to rather high temperatures [15]. For example, even at 40 K there are still visible traces of oscillations while the SdH oscillations are already gone at this temperature [15], which is reminiscent of the behaviour of the ordinary AMRO in quasi-2D systems. In spite of these similarities to the quasi-2D AMRO, the peak positions of the “high-field” oscillations apparently shift with the magnetic field, which is not expected for the ordinary AMRO. Moreover, the existence of a finite coupling between

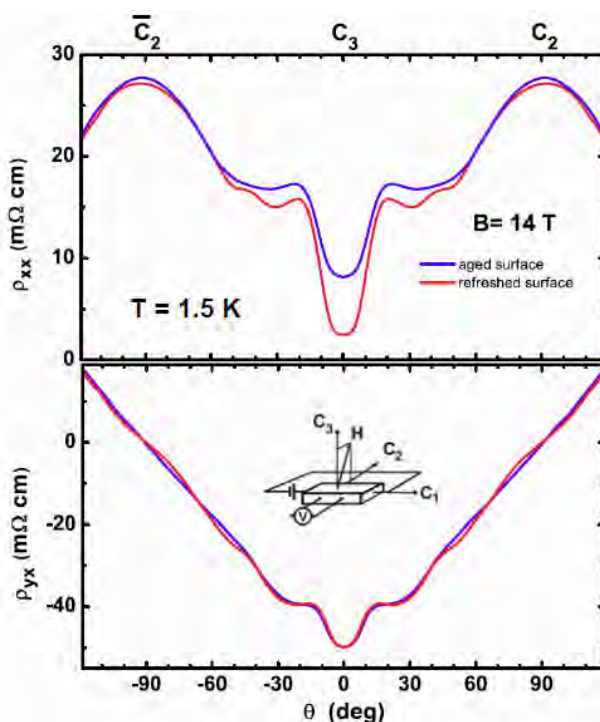


Figure 4. Direct comparison of the oscillations in  $\rho_{xx}$  and  $\rho_{yx}$  before and after etching the sample surface, measured on the same  $\text{Bi}_{0.91}\text{Sb}_{0.09}$  sample. It is evident that the refreshed surface yields more pronounced oscillations, which gives evidence for the surface origin of these oscillations.

conduction planes is essential for the quasi-2D AMRO [20], but there is no such inter-plane coupling for the surface states as long as the crystal is thick enough. Therefore, the observed “high-field” angular oscillations are a new phenomenon apparently specific to topological insulators.

## 5. Conclusion

We present detailed data on the angular-dependent MR oscillation phenomenon which was recently discovered in a topological insulator  $\text{Bi}_{0.91}\text{Sb}_{0.09}$ . Direct comparison of the data taken before and after etching the sample surface gives compelling evidence that this novel phenomenon is essentially originating from a surface state. The symmetry of the oscillations suggests that it probably comes from the (111) plane. In the surface state of a topological insulator, there is no “quasi two-dimensionality” that introduces a finite warping to the 2D cylindrical Fermi surface, whereas the existence of such a warping is essential for the ordinary AMRO to occur; therefore, it is likely that a new mechanism, such as a coupling between the surface and the bulk states, is responsible for this intriguing phenomenon in topological insulators.

## Acknowledgments

This work was supported by JSPS (KAKENHI Grant No. 19674002), MEXT (KAKENHI Grant No. 22103004), and AFOSR (AOARD Grant No. 10-4103).

## References

- [1] Qi X L and Zhang S C 2010 *Physics Today* **63** 33.
- [2] Moore J E 2010 *Nature* **464** 194.
- [3] Hasan M Z and Kane C L 2010 *arXiv*:1002.2895 (to be published in *Rev. Mod. Phys.*).
- [4] Fu L, Kane C L and Mele E J 2007 *Phys. Rev. Lett.* **98** 106803.
- [5] Fu L and Kane C L 2007 *Phys. Rev. B* **76** 045302.
- [6] Moore J E and Balents L 2007 *Phys. Rev. B* **75** 121306(R).
- [7] Qi X L, Hughes T L and Zhang S C 2008 *Phys. Rev. B* **78** 195424.
- [8] Hsieh D *et al.* 2008 *Nature* **452** 970.
- [9] Hsieh D *et al.* 2009 *Science* **323** 919.
- [10] Nishide A *et al.* 2010 *Phys. Rev. B* **81** 041309(R).
- [11] Eto K, Ren Z, Taskin A A, Segawa K and Ando Y 2010 *Phys. Rev. B* **81** 195309.
- [12] Peng H *et al.* 2010 *Nature Materials* **9** 225.
- [13] Checkelsky J G *et al.* 2009 *Phys. Rev. Lett.* **103** 246601.
- [14] Taskin A A and Ando Y 2009 *Phys. Rev. B* **80** 085303.
- [15] Taskin A A, Segawa K and Ando Y 2010 *Phys. Rev. B* **82** 121302(R).
- [16] Kartsovnik M V *et al.* 1988 *JETP Lett.* **48** 541.
- [17] Kajita K *et al.* 1989 *Solid St. Comm.* **70** 1189.
- [18] Yamaji K 1989 *J. Phys. Soc. Jpn.* **58** 1520.
- [19] Roushan P, Seo J, Parker C V, Hor Y S, Hsieh D, Qian D, Richardella A, Hasan M Z, Cava R J and Yazdani A 2009 *Nature* **460** 1106.
- [20] Cooper B K and Yakovenko V M 2006 *Phys. Rev. Lett.* **96** 037001.

## トポロジカル絶縁体の電子輸送現象

安 藤 陽 一

大阪大学産業科学研究所 ☎ 567-0047 大阪府茨木市美穂ヶ丘 8-1

(2010 年 12 月 13 日受理)

## Electrical Transport Properties of Topological Insulators

Yoichi ANDO

Institute of Scientific and Industrial Research, Osaka University  
Ibaraki, Osaka 567-0047

(Received December 13, 2010)

From a viewpoint of transport properties, topological insulators are the materials that are insulating in the bulk but are metallic at their edge. After briefly introducing the basic phenomena such as Dirac fermions and quantum spin Hall effect for topological insulators, we describe the details of the quantum oscillations originating from the surface state of a three-dimensional topological insulator  $\text{Bi}_{1-x}\text{Sb}_x$ , which was observed for the first time by our group. Intriguingly, this material was found to exhibit a novel angular-dependent magnetoresistance oscillation phenomenon, whose origin is still unknown but probably reflects a new physics in the surface transport properties of the topological insulator.

KEYWORDS : topological insulator, surface states, quantum oscillations, Dirac fermions, magnetoresistance

## 1. は じ め に

本稿ではトポロジカル絶縁体について、輸送現象を専門とする実験家の観点からその概要を解説すると共に、筆者のグループでこれまで行ってきた電子輸送特性の研究を紹介する。トポロジカル絶縁体は、輸送現象の観点からいえば、バルクはエネルギーギャップを持つ絶縁体だが、その“エッジ”（2次元系なら端、3次元系なら表面）はギャップレスの金属状態をもつ物質である<sup>1-3)</sup>。このためトポロジカル絶縁体は「新しい種類の固体物質」と考えることができる。トポロジカル絶縁体がこのような特異な性質を示すのは、強いスピン軌道相互作用によって価電子帯の電子波動関数のパリティが奇になることに由来する。数学では整数群を  $\mathbb{Z}$  で表し、それを偶数と奇数に分けた商群を  $\mathbb{Z}_2$  と表記するが、量子状態を持つパリティの偶奇性は波動関数を連続変形しても保存されるのでこれをトポロジカル不変量とみなすことができ、その偶奇性の分類を「 $\mathbb{Z}_2$  トポロジー」と呼ぶ。

普通の絶縁体（真空を含む）の量子状態は偶パリティを持つので、その属する  $\mathbb{Z}_2$  トポロジカルクラスは「偶」であるのに対して、トポロジカル絶縁体では強いスピン軌道相互作用の効果でバンド反転が起こり、 $\mathbb{Z}_2$  トポロジーに関して「奇」パリティの量子状態が実現している。トポロジーの異なる絶縁体波動関数の間では、一方から他方へ連続的に遷移することはできないので、その間で一度ギャップが閉じ、“絶縁体以外の状態”、つまり金属状態が現れることになる。これがトポロジカル絶縁体における金属的エッジ状態の起源である。

このエッジ状態は、上記のようなトポロジカルな理由によってその存在が保証されているため、“連続変形”に対応するような摂動に対して消失または局在することがない。普通の金属や半導体において、超高真空下の清浄表面にギャップレスの金属的表面状態が現れることがある（例えば、金やビスマスの表面に現れる Rashba 分裂した表面状態が最近注目を集めている<sup>4,5)</sup>）が、このような表面状態は、分子の吸着など周期ポテンシャルを乱す要因があると容易に局在してしまう。トポロジカル絶縁体の表面状態は、これらとは一線を画している。



## 2. 量子スピンホール効果

上記の  $Z_2$  トポロジーの理由で生じるエッジ状態を使えば、2次元のバルク絶縁体において、量子化されたスピンホール伝導率が現れる「量子スピンホール効果」を実現できることが、Kane と Mele によって理論的に示された<sup>6)</sup>。その理由は、エッジ状態の中で右へ進む電子と左へ進む電子が時間反転対称性の要請により、それぞれアップとダウンの異なるスピン状態を取る（これをヘリカルなスピン偏極と呼ぶ）ことにある [Fig. 1 (a), (b)]。このようなヘリカルにスピン偏極したエッジ状態は、平衡状態において無散逸のスピン流を運んでいると考えられる。その平衡を破って電流を流すと、無散逸スピン流のバランスが崩れて電流と垂直な方向にスピン偏極が現れ、これがスピンホール効果として観測されることが期待される。ヘリカルな1次元エッジ状態においては、散乱が（スピンを保存する限り）禁止されているため伝導はバリスティックになり、スピンホール伝導度が量子化される。

このような量子スピンホール絶縁体の具体例として、HgTe を CdTe で挟んだ量子井戸が Bernevig・Hughes・Zhang によって理論的に提案され<sup>7)</sup>、実際にゼロ磁場中における量子化されたエッジ状態の存在が König らによって実験的に確認された<sup>8)</sup>。この2次元トポロジカル絶縁体における1次元エッジ状態は、強磁場中の量子ホール系と同じように、基本的に無散逸で電流を運ぶことが

できると考えられており、今後の研究の発展が期待される。また、このような系における量子化されたスピンホール効果自体はまだ実証されておらず、今後の実験研究における重要な課題である。

## 3. ディラック電子性

ヘリカルなスピン偏極をしたエッジ状態においては、一般の運動量  $k$  においてスピンの自由度に関する縮退が解け、アップかダウンのいずれか一方のスピン状態しか取れない。運動量  $-k$  にはもう一方のスピン状態が対応する。また、 $k=0$  においては、クラマースの定理によりアップとダウンのスピン状態が縮退する。これは、 $+k$  と  $-k$  に分かれていたアップスピンとダウンスピンの2本の分散は  $k=0$  では交わる (Fig. 1 (b) 参照) ことを意味する。 $k=0$  の十分近くでそれぞれの分散が直線で近似できる場合、これは  $k=0$  に電荷中性点（ディラック点）を持つディラック電子系と見なすことができる。なお、このような理由によるディラック電子系の出現は、 $k=0$  の他にも、ブリルアン域の境界で  $+k$  と  $-k$  が等価になる点（このような点を時間反転不変運動量と呼ぶ）を表面状態の分散が通るときにも起こる。このように、ヘリカルにスピン偏極したディラック錐がブリルアン域の中で時間反転不変運動量を囲むように存在する (Fig. 1 (b)) のが、トポロジカル絶縁体の大きな特徴である。グラフェンにおけるディラック電子系はスピン縮退しているが、トポロジカル絶縁体のディラック電子系においてはスピンの「自由度」はなくなっており、スピンの向きが  $k$  によって自動的に決まってしまうところが特徴かつ重要である。

## 4. 3次元トポロジカル絶縁体

Kane と Mele による絶縁体における  $Z_2$  トポロジーの発見から2年後、量子状態の  $Z_2$  トポロジーによる分類は、2次元系に限らず3次元系でも可能であることが理論的に明らかになった<sup>9,10)</sup>。3次元系の場合、その“エッジ”状態である金属的表面状態は、2次元の場合のエッジ状態と同様、ヘリカルなスピン偏極をしている (Fig. 1 (c))。したがって、前節で述べた理由と同様にディラック電子系になっている。しかし、その表面状態では、電子の散乱は ( $k \rightarrow -k$  の後方散乱以外は) 禁止されていないので、量子スピンホール効果は起きない。その代わりに、3次元トポロジカル絶縁体は、上記のヘリカル・ディラック電子性に加えて、新奇な電気磁気効果<sup>11,12)</sup>、超伝導体との接合におけるマヨラナ型準粒子<sup>13)</sup> など、非常に興味深い物理を示すことが理論的に予想されており、いわば「新奇な量子現象の金鉱脈」として、

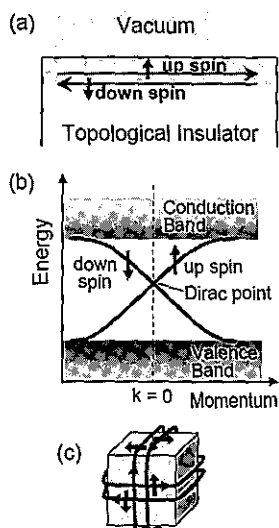


Fig. 1. (color online). Schematic pictures of (a) the helically spin-polarized edge state of a topological insulator in the real space, (b) the energy dispersion of the same state, and (c) the surface state of a 3D topological insulator and its spin polarization.

いま世界的に大きなブームが起きている<sup>1-3)</sup>。3次元トポロジカル絶縁体の具体例として、これまでに  $\text{Bi}_{1-x}\text{Sb}_x$  合金 (ただしエネルギーギャップが開いて絶縁体になる  $x=0.07-0.22$  の組成範囲のみ)<sup>14-16)</sup>,  $\text{Bi}_2\text{Se}_3$  や  $\text{Bi}_2\text{Te}_3$  等の tetradymite 構造をもつカルコゲナイド<sup>17-19)</sup>,  $\text{TlBiSe}_2$  等の3元カルコゲナイド<sup>20-24)</sup>, などが見つかった。いまのところ, トポロジカル絶縁体か否かの判定は, 角度分解光電子分光 (ARPES) による表面状態の解析によって行われている。

### 5. 3次元トポロジカル絶縁体の輸送現象による研究

トポロジカル絶縁体の表面状態に関わる輸送現象を観測するのは容易ではない。これは, 現在までに知られているトポロジカル絶縁体物質の単結晶試料には例外なくバルクのキャリアがドーピングされており, 電流の大半がバルクに流れてしまうためである。本節では, 我々が高品質  $\text{Bi}_{1-x}\text{Sb}_x$  単結晶を用いて行った表面状態に起因する輸送現象の観測について紹介する。

#### 5.1 $\text{Bi}_{1-x}\text{Sb}_x$ における表面電子系の量子振動の観測

表面2次元電子系の移動度や有効質量など電子系の詳細情報を得るには, 磁化の de Haas-van Alphen (dHvA) 振動や抵抗率の Shubnikov-de Haas (SdH) 振動などの量子振動効果を観測することが望ましい。筆者らのグループでは,  $\text{Bi}_{1-x}\text{Sb}_x$  単結晶中の組成の均一度を上げて高移動度を実現することにより, バルクキャリア濃度  $8 \times 10^{22} \text{ m}^{-3}$  の試料において, トポロジカル絶縁体中の2次元電子系に起因する量子振動を観測することに初めて成功した<sup>25)</sup>。試料中では縮退電子系として3次元電子系と2次元電子系が共存しているが, 量子振動の磁場方

向依存性を詳細に測定することにより, 両者の分離が可能になった。

Fig. 2 に我々が作製した高品質  $\text{Bi}_{1-x}\text{Sb}_x$  単結晶の抵抗率の温度依存性を  $x=0.00, 0.06, 0.09$  について示す。このうち  $x=0.09$  はバルク絶縁体組成であるため, 抵抗率はエネルギーギャップの存在を反映して 200 K 以下で絶縁体的に上昇するが, 50 K 以下では上昇が止まって金属的な振舞いを示す。過去にも絶縁体組成の  $\text{Bi}_{1-x}\text{Sb}_x$  において, このように低温で金属的な抵抗率の振舞いが現れることは観測されていたが, 当時は不純物バンドによる伝導だと考えられていた<sup>26)</sup>。Fig. 3 には  $\text{Bi}_{1-x}\text{Sb}_x$  単結晶の写真とブリルアン域の図, および  $x=0.09$  について磁場方向を系統的に変えながら 2 K で測定した dHvA 振動の生データを示す。顕著な量子振動が観測されることから, この試料中には明らかにフェルミ面が存在することがわかる。この試料について我々は dHvA 振動周期の詳細な角度依存性の測定を行い, フェルミ面の構造を決定した (Fig. 4)。○で示したブランチの角度依存性は, 2次元フェルミ面の存在を示すものである。さらに Fig. 5 に示すように, dHvA 振動の振幅の温度依存性を Lifshitz-Kosevich 公式<sup>27)</sup>を用いて解析してサイクロトロン質量  $m_c$  を決定し, その角度依存性を求めたところ,  $m_c$  が2次元フェルミ面に特徴的な  $1/\sin \theta$  の角度依存性を示して  $\theta=0^\circ$  で鋭く発散することが明らかになった。これは, 試料中に2次元電子系が存在することの確証を与えるものである。

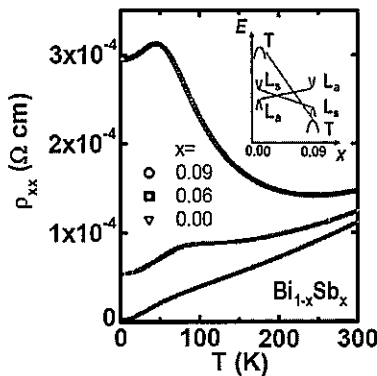


Fig. 2. (color online). Temperature dependences of the resistivity in high-quality  $\text{Bi}_{1-x}\text{Sb}_x$  single crystals in the semimetallic ( $x=0.00, 0.06$ ) and insulating ( $x=0.09$ ) regimes (Ref. 25, ©American Physical Society, 2009).

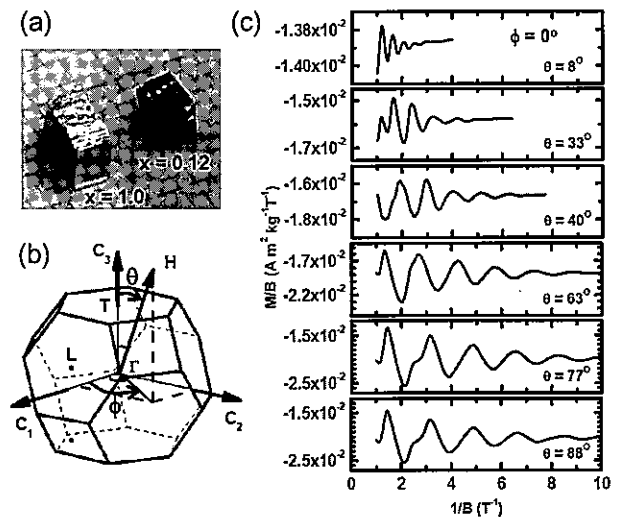


Fig. 3. (color online). (a) Photograph of  $\text{Bi}_{1-x}\text{Sb}_x$  single crystals. (b) 3D Brillouin zone and the definition of the magnetic-field angles. (c) Raw data of the dHvA oscillations for systematically varied magnetic-field directions measured for  $x=0.09$  (Ref. 25, ©American Physical Society, 2009).

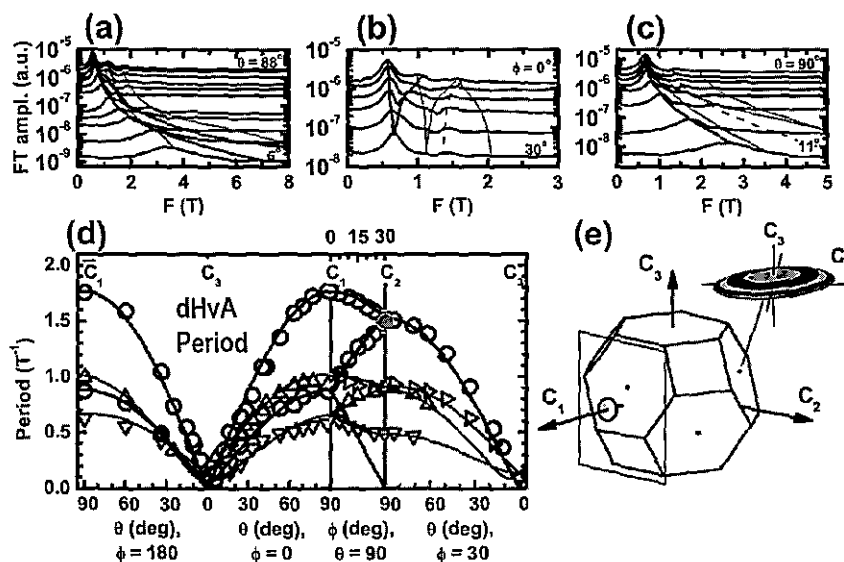


Fig. 4. (color online). (a-c) Change of the dHvA oscillation frequencies for the rotations in (a) binary, (b) trigonal, and (c) bisectrix planes. (d) Observed magnetic-field-direction dependences of the dHvA periods (= inverse frequency) for the three high-symmetry planes; thick (thin) lines are the calculated magnetic-field-direction dependences of the periods originating from the 2D (3D) Fermi surfaces. (e) Schematic picture of the Fermi surfaces determined from the dHvA oscillations; the 3D Fermi surfaces are located at the three equivalent L points in the Brillouin zone, while the 2D Fermi surfaces reside on the  $C_1$  planes (Ref. 25, ©American Physical Society, 2009).

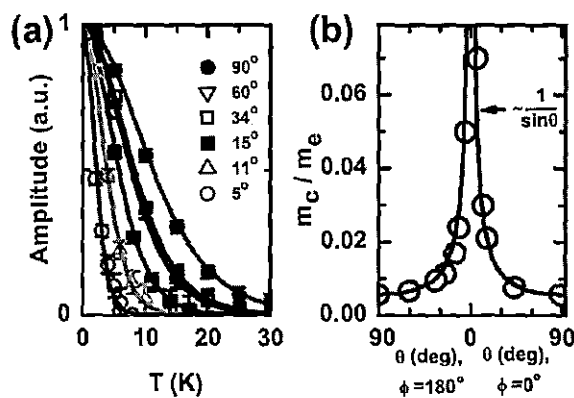


Fig. 5. (color online). (a) Temperature dependences of the amplitude of the dHvA oscillations for various field directions observed in  $\text{Bi}_{0.91}\text{Sb}_{0.09}$ , together with their fitting to the Lifshitz-Kosevich formula. (b) Obtained cyclotron mass,  $m_c$ , presents a sharp divergence at  $\theta = 0^\circ$  following the  $1/\sin \theta$  angular dependence (Ref. 25, ©American Physical Society, 2009).

ここで注意しておきたいのは、我々の実験では2次元フェルミ面は結晶の  $C_1$  面 [rhombohedral の結晶軸で  $(2\bar{1}\bar{1})$  面] 上のみ観測されていることである。ARPES の実験はヘキ開面である  $(111)$  面についてのみ行われて

おり<sup>15,16)</sup>、複雑な表面状態が観測されているが、この  $(111)$  面上の表面状態は dHvA 効果では見えていない。この原因は、 $(111)$  面上表面状態は吸着等の乱れによって移動度が低下してしまうためであろうと推測しているが、詳細は不明である。また興味深いことに、 $C_1$  面上で観測された dHvA 効果の振幅は通常の2次元電子系に期待されるものよりも数桁大きい。これは観測されている2次元電子系が結晶中の転移面のような内部表面に生じている可能性を示唆するが、詳細はまだ不明である。トポロジカル絶縁体中の刃状転位におけるトポロジカルなエッジ状態の出現は既に理論的に示されているので<sup>28)</sup>、積層欠陥の場合への拡張が望まれる。

上記の試料よりさらに品質改良したバルクキャリア濃度  $4 \times 10^{22} \text{ m}^{-3}$  の試料では、抵抗率にも明確な SdH 振動が観測された<sup>29)</sup>。Fig. 6 には抵抗率の磁場微分のデータと、これをフーリエ変換して得られる振動周波数の磁場角度依存性を示す。Fig. 6 の (b) に□と◇で示した  $f_2$  と  $f_3$  は共に3次元的な電子ポケットに対応する振動周波数で、○で示した  $f_1$  が2次元電子系に対応するが、この2次元電子系が存在する  $C_1$  面に平行な方向 ( $C_3$  軸方向) に磁場が近づくにつれて  $f_1$  が発散する様子がはっきり見て取れる。この試料では  $\theta = 0^\circ$  の近傍で  $f_1$  と  $f_2$

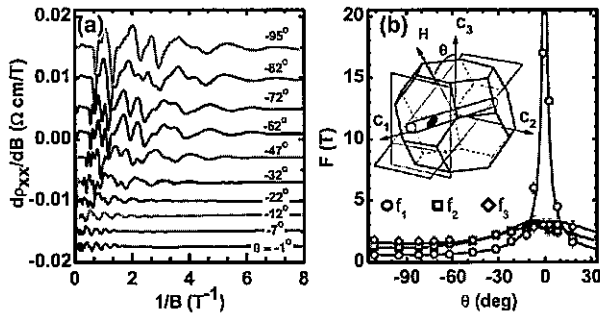


Fig. 6. (color online). SdH oscillations observed in the resistivity of a  $\text{Bi}_{0.91}\text{Sb}_{0.09}$  sample with the bulk carrier density  $4 \times 10^{16} \text{ cm}^{-3}$ : (a) Plots of  $d\rho_{xx}/dB$  vs  $1/B$  for various field directions: (b) magnetic-field-direction dependences of the three SdH frequencies obtained from the Fourier transform of the data (Ref. 29, ©American Physical Society, 2010).

の違いが非常に大きくなるので、両者の振幅の温度依存性を独立に解析することが可能で、これによりバルク電子系と2次元電子系の詳細を求めることができた。バルク電子系は  $\theta=3^\circ$  のとき、 $m_c=0.033 m_e$  ( $m_e$  は自由電子の質量)、平均自由行程 16 nm、移動度  $1.12 \text{ m}^2/\text{Vs}$  であるのに対して、2次元電子系では垂直磁場中で  $m_c=0.0057 m_e$ 、平均自由行程 150 nm、移動度  $5.5 \text{ m}^2/\text{Vs}$  が得られた。平均自由行程を比較すると、2次元電子の方がバルクよりも9倍も長いことは非常に特徴的である。これは、2次元電子系の起源が表面状態にあり、それがディラック電子系であるために有効質量が非常に軽く移動度も大きくなっているためであると考えれば納得がいく。この2次元電子系のフェルミ速度は  $8.4 \times 10^5 \text{ m/s}$  と求められるが、これは  $\text{Bi}_2\text{Se}_3$  や  $\text{Bi}_2\text{Te}_3$  の ARPES 測定によって求められた表面状態のディラック点におけるフェルミ速度 (約  $4 \times 10^5 \text{ m/s}$ ) と同じオーダーである。なお最近、表面ディラック電子系が示す SdH 振動は、 $\text{Bi}_2\text{Te}_3$  (Ref. 30),  $\text{Bi}_2\text{Se}_3$  (Ref. 31),  $\text{Bi}_2\text{Te}_2\text{Se}$  (Ref. 24) の3つの系についても相次いで観測されている。

## 5.2 $\text{Bi}_{1-x}\text{Sb}_x$ における特異な角度依存磁気抵抗振動現象

最近筆者らは、 $\text{Bi}_{1-x}\text{Sb}_x$  における特異な角度依存磁気抵抗振動現象を発見した<sup>29)</sup>。前節で紹介したバルクキャリア濃度  $4 \times 10^{22} \text{ m}^{-3}$  の高品質  $\text{Bi}_{0.91}\text{Sb}_{0.09}$  単結晶において、一定磁場中で試料を回転させながら抵抗率を測定したところ、Fig. 7 に示すように高磁場で特徴的な振動現象が観測された。低磁場領域でも抵抗率の角度依存振動が見られるが、これは基本的に SdH 振動が形を変えて現れたものである。これに対して高磁場で見える振動は SdH 効果では説明できない。また、この振動現象はホ

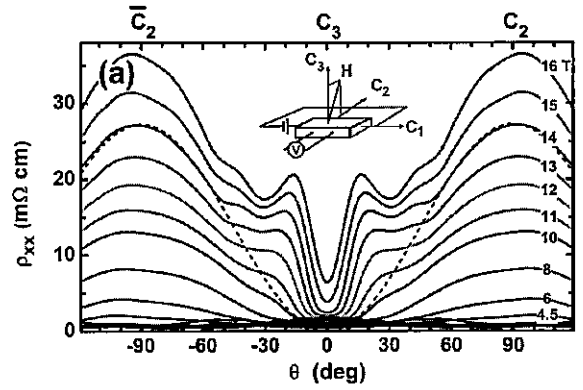


Fig. 7. (color online). Angular-dependent magnetoresistance oscillations observed in a high-quality  $\text{Bi}_{0.91}\text{Sb}_{0.09}$  single crystals at 1.5 K by continuously rotating the sample in constant magnetic fields (Ref. 29, ©American Physical Society, 2010).

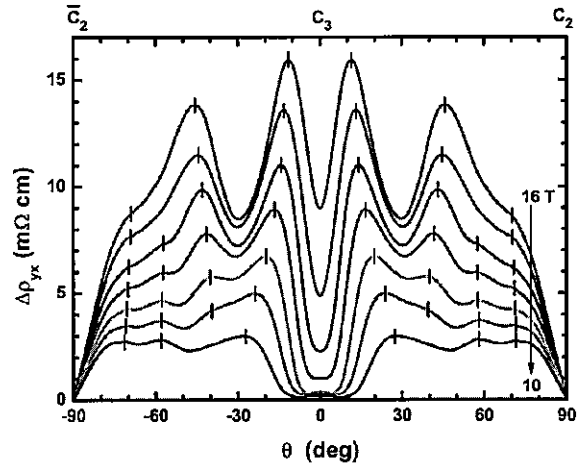


Fig. 8. (color online). Angular-dependent oscillations of the Hall resistivity obtained by subtracting the expected  $R_H B \cos \theta$  behavior from the raw  $\rho_{yx}$  data. Ticks mark the positions of distinguishable peaks (Ref. 29, ©American Physical Society, 2010).

ール抵抗率  $\rho_{yx}$  でも観測され、 $\rho_{yx}$  の生データから通常のホール抵抗率に対して期待される  $R_H B \cos \theta$  の成分をバックグラウンドとして差し引くと、Fig. 8 に示すように非常に顕著な振動が現れる。磁気抵抗の角度依存振動現象としては擬2次元系や擬1次元系における「梶田振動」(または「山地振動」と呼ばれる現象<sup>32-35)</sup>が有名だが、その際ピークを与える「魔法角」は磁場によって変化しない。これに対して  $\text{Bi}_{1-x}\text{Sb}_x$  で観測された磁気抵抗振動現象においては、Fig. 8 のデータから明らかに、ピークが現れる角度は外部磁場によって変化しているので、明らかに梶田振動とは別の起源を持つものであり、新奇な現象と考えられる。純粋な2次元系の物



理としては、このような角度依存振動効果が現れることは考えにくいので、おそらくトポロジカル絶縁体における表面2次元電子系とバルク3次元電子系の間の結合が起源になっているのではないかと推測しているが、詳細はまだ不明である。また、この角度依存振動の振幅がH//C<sub>3</sub>軸の付近で最も大きく、(111)面をエッチングして清浄化すると振動が顕著になる<sup>36)</sup>ことから、この振動に参与しているのは(111)面上の2次元電子系である可能性が高い。

## 6. まとめと今後の展望

トポロジカル絶縁体の研究はまだ始まったばかりの新しい分野である。本稿では詳しく触れなかったが、3次元トポロジカル絶縁体の表面に存在するヘリカルな2次元ディラック電子系に対しては様々な新しい量子現象が理論的に予想されている。例えば、超伝導を接合したときに近接効果でトポロジカル絶縁体表面に誘起される超伝導はトポロジカルな性質を持つと考えられており、そのエッジモードとしてマヨラナ型準粒子の出現<sup>13,37)</sup>が予想されている。このマヨラナ型準粒子はトポロジカル量子計算の量子ビットになると考えられており、応用上も重要である。また、表面状態がヘリカルなスピン偏極をしていることに起因する磁気抵抗効果<sup>38)</sup>なども議論されており、当然、このスピン偏極を利用したスピントロニクス素子も考えられるだろう。さらに、フェルミレベルがディラック点に来るように制御した上で強磁性絶縁体との交換相互作用などによって表面状態にギャップを開けることができれば、そのときの電磁応答を記述する方程式には磁場と電場が内積で直接結合した交差項が現れ、これが「トポロジカル電気磁気効果」を生むと予想されている<sup>11,12)</sup>。この場合に期待される現象として、半整数量子ホール効果<sup>11)</sup>、点電荷に対する鏡像磁気モノポールの出現<sup>12)</sup>、電場による磁場の直接誘起とその係数の微細構造定数( $e^2/hc$ )による量子化<sup>11)</sup>、などがあげられる。

このような新奇現象の検証・解明はこれからであるが、その実現において最も重要なのが、バルク絶縁性を確保した試料である。最近筆者らは、Bi<sub>2</sub>Te<sub>2</sub>Seという新しいトポロジカル絶縁体がバルク絶縁性を確保する上で非常に有望な物質であることを発見したが<sup>24)</sup>、バルクの伝導チャンネルが無視できるようなトポロジカル絶縁体試料も、そう遠くない日に得られるであろう。

なお、ここで紹介した筆者らによる研究は科研費の若手研究(S)と新学術領域研究「対称性の破れた凝縮系におけるトポロジカル量子現象」、およびAFOSR-AOARDの補助を受けて行われた。

## 文 献

- 1) X.L. Qi and S.-C. Zhang : *Physics Today* **63**, 33 (2010).
- 2) J.E. Moore : *Nature* **464**, 194 (2010).
- 3) M.Z. Hasan and C.L. Kane : arXiv : 1002.2895 (to be published in *Rev. Mod. Phys.* ).
- 4) M. Hoesch, M. Muntwiler, V.N. Petrov, M. Hengsberger, L. Patthey, M. Shi, M. Falub, T. Gerber and J. Osterwalder : *Phys. Rev. B* **69**, 241401 (R) (2004).
- 5) Ph. Hofmann : *Prog. Surf. Sci.* **81**, 191 (2006).
- 6) C.L. Kane and E.J. Mele : *Phys. Rev. Lett.* **95**, 146802 (2005).
- 7) B.A. Bernevig, T.L. Hughes and S.-C. Zhang : *Science* **314**, 1757 (2006).
- 8) M. König, S. Wiedmann, C. Brüne, A. Roth, H. Buhmann, L.W. Molenkamp, X.-L. Qi and S.-C. Zhang : *Science* **318**, 766 (2007).
- 9) L. Fu, C.L. Kane and E.J. Mele : *Phys. Rev. Lett.* **98**, 106803 (2007).
- 10) J.E. Moore and L. Balents : *Phys. Rev. B* **75**, 121306 (R) (2007).
- 11) X.-L. Qi, T.L. Hughes and S.-C. Zhang : *Phys. Rev. B* **78**, 195424 (2008).
- 12) X.-L. Qi, R. Li, J. Zang and S.-C. Zhang : *Science* **323**, 1184 (2009).
- 13) L. Fu and C.L. Kane : *Phys. Rev. Lett.* **100**, 096407 (2008).
- 14) L. Fu and C.L. Kane : *Phys. Rev. B* **76**, 045302 (2007).
- 15) D. Hsieh, D. Qian, L. Wray, Y. Xia, Y.S. Hor, R.J. Cava and M.Z. Hasan : *Nature* **452**, 970 (2008).
- 16) A. Nishide, A.A. Taskin, Y. Takeichi, T. Okuda, A. Kakizaki, T. Hirahara, K. Nakatsuji, F. Komori, Y. Ando and I. Matsuda : *Phys. Rev. B* **81**, 041309 (R) (2010).
- 17) H.-J. Zhang, C.-X. Liu, X.-L. Qi, X. Dai, Z. Fang and S.-C. Zhang : *Nat. Phys.* **5**, 438 (2009).
- 18) Y. Xia, D. Qian, D. Hsieh, L. Wray, A. Pal, H. Lin, A. Bansil, D. Grauer, Y.S. Hor, R.J. Cava and M.Z. Hasan : *Nat. Phys.* **5**, 398 (2009).
- 19) Y.L. Chen, J.G. Analytis, J.-H. Chu, Z.K. Liu, S.-K. Mo, X.L. Qi, H.J. Zhang, D.H. Lu, X. Dai, Z. Fang, S.C. Zhang, I.R. Fisher, Z. Hussain and Z.-X. Shen : *Science* **325**, 178 (2009).
- 20) T. Sato, K. Segawa, H. Guo, K. Sugawara, S. Souma, T. Takahashi and Y. Ando : *Phys. Rev. Lett.* **105**, 136802 (2010).
- 21) Y. Chen, Z. Liu, J.G. Analytis, J.-H. Chu, H. Zhang, S.-K. Mo, R.G. Moore, D. Lu, I. Fisher, S.-C. Zhang, Z. Hussain and Z.-X. Shen : arXiv : 1006.3843.
- 22) K. Kuroda, M. Ye, A. Kimura, S.V. Ereemeev, E.E. Krasovskii, E.V. Chulkov, Y. Ueda, K. Miyamoto, T. Okuda, K. Shimada, H. Namatame and M. Taniguchi : *Phys. Rev. Lett.* **105**, 146801 (2010).
- 23) S.-Y. Xu, L.A. Wray, Y. Xia, R. Shankar, A. Petersen, A. Fedorov, H. Lin, A. Bansil, Y.S. Hor, D. Grauer, R.J. Cava and M.Z. Hasan : arXiv : 1007.5111.
- 24) Z. Ren, A.A. Taskin, S. Sasaki, K. Segawa and Y. Ando :

- Phys. Rev. B **82**, 241306 (R) (2010).
- 25) A.A. Taskin and Y. Ando : Phys. Rev. B **80**, 085303 (2009).
- 26) B. Lenoir, M. Cassart, J.-P. Michenaud, H. Scerrer and S. Scherrer : J. Phys. Chem. Solids **57**, 89 (1996).
- 27) D. Shoenberg : "Magnetic Oscillations in Metals" (Cambridge Univ. Press, 1984).
- 28) Y. Ran, Y. Zhang and A. Vishwanath : Nat. Phys. **5**, 298 (2009).
- 29) A.A. Taskin, K. Segawa and Y. Ando : Phys. Rev. B **82**, 121302 (R) (2010).
- 30) D.Q. Qu, Y.S. Hor, J. Xiong, R.J. Cava and N.P. Ong : Science **329**, 821 (2010).
- 31) J.G. Analytis, R.D. McDonald, S.C. Riggs, J.-H. Chu, G.S. Boebinger and I.R. Fisher : Nat. Phys. **6**, 960 (2010).
- 32) K. Kajita, Y. Nishio, T. Takahashi, W. Sasaki, R. Kato, H. Kobayashi, A. Kobayashi and Y. Iye : Solid St. Comm. **70**, 1189 (1989).
- 33) K. Yamaji : J. Phys. Soc. Jpn. **58**, 1520 (1989).
- 34) G.M. Danner, W. Kang and P.M. Chaikin : Phys. Rev. Lett. **72**, 3714 (1994).
- 35) B.K. Cooper and V.M. Yakovenko : Phys. Rev. Lett. **96**, 037001 (2006).
- 36) A.A. Taskin, K. Segawa and Y. Ando : arXiv : 1009.4005.
- 37) J. Linder, Y. Tanaka, T. Yokoyama, A. Sudbø and N. Nagaosa : Phys. Rev. Lett. **104**, 067001 (2010).
- 38) T. Yokoyama, Y. Tanaka and N. Nagaosa : Phys. Rev. B **81**, 121401 (R) (2010).